UNIVERSITY OF CALIFORNIA

Santa Barbara

Applying Magnetic Resonance Spectroscopic Techniques to Elucidate Structure-Property Relationships in Silica-Based Surfaces

A dissertation submitted in partial satisfaction of the

requirements for the degree Doctor of Philosophy

in Chemistry

by

Tarnuma Tabassum

Committee in charge:

Professor Songi Han, Co-Chair

Professor Susannah L. Scott, Co-Chair

Professor Mahdi M. Abu-Omar

Professor Gabriel Ménard

Professor Baron G. Peters

September 2021

The dissertation of Tarnuma Tabassum is approved.

_____

Professor Baron G. Peters

_____

Professor Gabriel Ménard

_____

Professor Mahdi M. Abu-Omar

_____

Professor Susannah L. Scott, Committee Co-Chair

_____

Professor Songi Han, Committee Co-Chair

September 2021

Applying Magnetic Resonance Spectroscopic Techniques to Elucidate Structure-Property Relationships in Silica-Based Surfaces

by

Tarnuma Tabassum

ACKNOWLEDGEMENTS

When I was looking into PhD programs and furtively perusing through different websites, I came across this: "*It takes a village to raise a PhD*". I found it somewhat funny, not fully realizing how true this statement would turn out to be for me, since it took a whole host of wonderful scientists, researchers as well as supportive friends and family for my thesis to come to completion.

I am extremely grateful and fortunate to have had the opportunity to work with both my advisors, Professor Susannah L. Scott and Professor Songi Han. Susannah has been monumental in helping me develop my critical thinking, scientific thought processes, and I have learnt from her what it truly means to be a *good scientist*. I find her determination in pushing the boundaries of science and what we can learn from it truly remarkable. Songi has, over the years, taught me the magic of magnetic resonance spectroscopy. Her excitement, curiosity and wisdom in using these seemingly daunting techniques to unravel fascinating fundamental aspects in materials has inspired me. I am deeply touched whenever I realize how much she cares about the well-being of her students. Both my advisors are excellent communicators, and I am grateful to them for drilling into me the importance of communicating science effectively, otherwise, good science loses its meaning.

I am thankful to my committee member, Professor Mahdi Abu-Omar for his guidance, and I particularly remember the time that I had the opportunity of directly working with him through the Crossroads Fellowship. Mahdi made the process of generating lecture series for undergraduates a fun and enjoyable process, through his creativity and encouragement. I am grateful to my committee member, Professor Gabriel Ménard, for his guidance and mentorship, and the ease with which I have been able to have conversations with him. I am also fortunate to have been able to interact with Professor Baron Peters, who has guided me and helped me think about my materials using his theoretical insight.

My mentors over the years have also been brilliant and wonderful. I am particularly grateful to Professor Wei Chen, my undergraduate research advisor, for igniting that initial spark and turning my general interest in chemistry to something deeper. I am grateful to Professor Ilia Kaminker, for getting me truly invested in EPR (a technique I was completely unfamiliar with), and Professor Fan Zhang for teaching me the art of air-free synthesis. I thank Professor Sheetal Jain for fueling my interests in NMR, and for his wisdom both inside and outside of lab. I am thankful to Dr Asif Equbal for pushing me to dig a little deeper, Dr Long Qi for his inspiring and conscientious work ethic, and Dr Tom Casey for our discussions on career and life. I am grateful to the CNSI project scientists and technical managers, Dr Jerry Hu for all his help with NMR, wisdom, and chocolates that have fueled extended hours over at CNSI, Jaya Nolt for her willingness to help and kindness, and Shamon Walker for helping me getting acquainted with EPR when I first started. I also appreciate Richard Bock's finesse and skills with glass, without which my air-free experiments would be impossible.

One of the best parts about my thesis has been its collaborative nature, and I must thank both Susannah and Songi again for involving me in many different projects and trusting me, as well as agreeing to send me off to Germany and France for making my research

experience that much stronger. I am grateful to my collaborators in the Center for Catalysis Energy Innovation, Professor Michael Tsapatsis, Professor Wei Fan and Professor Omar Abdelrahman for introducing me to siliceous zeolites, their useful insights as well as sending us materials, multiple times. I am particularly grateful to Dr Stavros Caratzoulas whose insights through modeling have helped me bolster my experimental results. Their students, Matheus, Jason, Jacky and Han have been responsive and efficient collaborators.

I thank Professor Regina Palkovits for graciously welcoming me to her group in Aachen, Germany and encouraging me to dabble into a little bit of catalysis through the IRES program. Dr Ruiyan Sun and Dr Anja Fink have been instrumental in teaching me catalysis with patience and kindness. My IRES cohort, Marcus, Anthony, Zhiyu and Bryan were key in making my experience in Germany nothing short of being memorable.

I started to learn NMR fully when I went to France from the mentorship and guidance of Dr Régis Gauvin and Dr Laurent Delevoye. I thank Régis for welcoming me to Lille and French culture, his guidance and mentorship, his kindness and for teaching me the most important French words during my time there and afterwards. I am grateful to Laurent for sharing with me his knowledge, his sharp NMR skills and for his ability to come up with a joke in every possible situation. I thank Dr Nicolas Merle from the bottom of my heart for patiently teaching me organometallic syntheses, his endearing nature and for his kindness even when I contaminated his precious vacuum line. I had a really great time in France, and all three of them made it more fun and enriching. Debbie, Sarah-Belle and Isa were also great company and I miss our conversations over coffee.

I was also lucky to have experienced working on topics completely out of my repertoire. Thanks to Susannah, I participated in an interdisciplinary program with the Bren School, through which I experienced the energy, enthusiasm and brilliance of Professor Sangwon Suh. I enjoyed getting to know Dr Jun-Hee Jang, Dr Jiajia Zheng and Yang through this program as well as our insightful discussions. Thanks to Songi, I learned how to apply EPR to study materials other than catalysts. I am grateful to Professor Rachel Segalman, Professor Javier Read de Alaniz, Dr Nicole Schauser and Dr Hui Nie for our productive collaborations on polymer electrolytes. I also thank Professor Vlad Michaelis for his enthusiasm in applying EPR to study perovskites and our collaboration.

I am lucky to have been in two wonderful labs, and all past and present members have made this experience memorable. I thank Colin and his puppy Sebastian for making late-night grading just a little bit less tedious, Li for all her guidance on food and EXAFS collaborations, Hyunjin for his songs, which were exactly what you needed to listen to when you were having a bit of a frustrating day in lab and for his inspiring meticulousness, Jackie for our conversations, Ali for all those delicious baked goods and teaching me how to run the coolest NMR experiments, and Abby for her laughs and her guidance on using our *precious* glovebox. I also thank Jing, Garrett, Jiakai, Zach, Lijun and Youhong for being helpful, wonderful labmates and our insightful discussions. I also thank Salman, for our collaborations and whose theoretical insights I find awe-inspiring.

I joined the Han lab not really realizing how social it is, and I was very pleasantly surprised. I thank Miranda for her unwavering support throughout the years, for being the best travel companion in Germany and elsewhere, our efficient collaborations and our friendship, Mia for her relentless energy and engaging conversations, Kendrick for making me realize that Vietnamese food is delicious, Alisa for teaching me how to drive, Chung-Ta for his presence and good aura, Yann for bearing with my nonsensical whims, Cocoa for always encouraging me, and Kan for bearing with my puns, Tim for our EPR collaborations, Blake for teaching me that EPR can also be done at high fields and with lasers. I also thank Alicia, Ryan, Raj, Celeste, Michael, Kate, Audra, Thomas, Yanxian, Nikki, Neil and Julia for their helpfulness, support and all our interesting and insightful discussions.

I am grateful to my father, Nasir, for his relentless positivity and for motivating me to be a better scientist. I thank my mother, Bilkis, for encouraging me to be resilient, and for somehow always managing to pull me out of my lows. I am exceedingly thankful to both my parents for their love and support, and in particular, the patience they have shown me the many times I complained about my experiments not working. I am eternally thankful to Akchheta for all the laughter, love, comfort, jokes and food. Her continuous companionship, support, and willingness to participate in venting sessions throughout the years has been immense. I am grateful to my uncle Moshiul, aunt Tazeen and my cousin Tasneem for being supportive and for reminding me to take a deep breath every now and then. I am grateful to Kavita, for being an excellent running companion, for her delicious meals and for our friendship, David for the extensive driving lessons, Nora for always coming up with the best hiking locations, and Niva for being a ray of sunshine. I am glad I have such supportive friends back home and all over: Maisha, Nabilah, Dania, Bushra, Nooria, Sangeeta, Nabila, Tamjeed, and Alveed for the conversations, memes, laughter, fun and general reminders that it is okay to take it easy.

This thesis was supported by funding from the U.S. National Science Foundation (NSF) Award No. CHE-1800596; Catalysis Center for Energy Innovation, an Energy Frontier Research Center funded by the U.S. Department of Energy, Office of Science, Office of Basic Energy Sciences under Award No. DE-SC0001004; UC Santa Barbara's Mellichamp Academic Initiative in Sustainability. The experiments made use of the MRL Shared Experimental Facilities, supported by the MRSEC Program of the NSF under Award No. DMR-1720256.

VITA OF TARNUMA TABASSUM
September 2021

EDUCATION

Doctor of Philosophy in Chemistry, University of California, Santa Barbara, September 2021 (expected)
Bachelor of Arts in Chemistry, Mount Holyoke College, South Hadley, May 2015 (magna cum laude with high honors)

PUBLICATIONS

*S.K. Jain, *T. Tabassum, L. Li, L. Ren, W. Fan, M. Tsapatsis, S. Caratzoulas, S. Han, and S.L. Scott. "P-site Structural Diversity and Evolution in a Zeosil Catalyst". *J. Am. Chem. Soc.* 2021, *143*, 1968-1983.

H. Nie, N. S. Schauser, J. L. Self, T. Tabassum, S. Oh, Z. Geng, S. Jones, M. S. Zayas, V. G. Reynolds, M. L. Chabinyc, C. J. Hawker, S. Han, C. M. Bates, R.A Segalman, and J. Read de Alaniz. "Light-Switchable and Self-Healable Polymer Electrolytes Based on Dynamic Diarylethene and Metal-Ion Coordination." *J. Am. Chem. Soc.*, 2021, *143*, 1562–1569.

N. S. Schauser, D. Grzetic, T. Tabassum, G. Kliegle, M. L. Le, E. Susca, A. Segolene; T. J. Keller, K. Delaney, S. Han, R. Seshadri, G. Fredrickson, and R. Segalman. "The Role of Backbone Polarity on Aggregation and Conduction of Ions in Polymer Electrolytes". *J. Am. Chem. Soc.* 2020, *142*, 15, 7055–7065.

S.K. Jain, C.J. Yu, C. Wilson, T. Tabassum, D. Freedman, and S. Han, "Tracing dynamic nuclear polarization pathways using transition metal-nuclear spin rulers". *Chem*, 2021, *7*, 421-435.

M. Dorneles de Mello, G. Kumar, T. Tabassum, S.K. Jain, T. H. Chen, S. Caratzoulas, X. Li, D.G. Vlachos, S. Han, S.L. Scott, P.J. Dauenhauer. *Angew. Chem. Int. Ed*. 2020, *59*, 2–9.

Y. Li, A. Equbal, T. Tabassum., and S. Han. "^{1}H Thermal Mixing Dynamic Nuclear Polarization with BDPA as Polarizing Agents". *J. Phys. Chem. Lett.*, 2020, *11*, 9195-9202.

A. Equbal, Y. Li, T. Tabassum, and S. Han "Crossover from a Solid Effect to Thermal Mixing ^{1}H Dynamic Nuclear Polarization with Trityl-OX063". *J. Phys. Chem. Lett.*, 2020, *11*, 9, 3718–3723.

A. Chamas, H. Moon, J. Zheng, Y. Qiu, T. Tabassum, J. H. Jang, M. Abu-Omar, S. L. Scott, and S. Suh. "Degradation Rates of Plastics in the Environment". *ACS Sustainable Chem. Eng.* 2020, *8*, 3494-3511.

A. Willms, H., Schumacher, T. Tabassum, L. Qi, S.L. Scott, P.J. Hausoul, and M. Rose. "Solid Molecular Frustrated Lewis Pairs in a Polyamine Organic Framework for the Catalytic Metal-free Hydrogenation of Alkenes." *ChemCatChem,* 2018, *10,* 1835-1843.

"Stabilization of the P-site Distribution in P-zeosils through Increased Hydrophobicity". T.Tabassum, S.K. Jain. S. Caratzoulas, W. Fan, M. Tsapatsis, S. Han, and S.L. Scott. *Manuscript in preparation*.

"EPR Evidence for Silanol Clustering on Silica Surfaces". T.Tabassum**,** L. Li, S. A. Khan, I. Kaminker, S.K. Jain, B. Peters, W. Shen, S. L. Scott and S. Han. *Manuscript in preparation.*

PRESENTATIONS

"EPR Signatures of Grafted V(IV) Sites Reveal the Clustered Nature of Silanols on Partially Dehydroxylated Silica". T.Tabassum, L. Li, S. A. Khan, I. Kaminker, S.K. Jain, B. G. Peters, W. Shen, S. L. Scott and S. Han. Cardiff 2021 RSC ESR Interest Group 54th Annual Conference, April 2021.

"Probing the Nature of P-sites in siliceous P-zeolite Catalysts: *Using Advanced Solid-state NMR Methods*". T. Tabassum, S.K. Jain, S. Han, S. L. Scott. UCSB Catalysis Seminars, Santa Barbara, CA April 2020.

"EPR Silent Vanadium(IV) Clusters on Dehydroxylated Amorphous Silica", T. Tabassum, S. Han, S. L. Scott, 12th Amgen-Clorox Graduate Student Symposium, Santa Barbara, CA October 2019.

"Understanding Metal-Support Interactions using Electron Paramagnetic Resonance", T. Tabassum, S. Han, S. L. Scott, Chemical Sciences Student Seminar, Santa Barbara, CA November 2017.

AWARDS

Chateaubriand Fellow, Embassy of France in the United States (2019)
IRES AcalNet Fellow, NSF and DAAD (2018)
Crossroads Interdiscliplinary Fellow, UCSB Graduate Division (2018)
Mellichamp Academic Initiative in Sustainability Fellow, UCSB (2017)

ABSTRACT

Applying Magnetic Resonance Spectroscopic Techniques to Elucidate Structure-Property Relationships in Silica-Based Surfaces

by

Tarnuma Tabassum

Obtaining molecular-level structural information about heterogeneous catalysts and catalyst supports such as silicas and all-silica zeolites (zeosils) is critical for the rational design of new catalysts. Magnetic resonance techniques, including solid-state magic angle spinning nuclear magnetic resonance (MAS-NMR) and electron paramagnetic resonance (EPR) spectroscopies, are powerful and non-invasive tools, which were used to acquire detailed structural and dynamic information about these silica-based systems.

Thermal dehydroxylation reduces the number of silanol sites on silica surfaces and is typically used to increase the fraction of non-interacting silanols for well-defined active sites, however, several studies have suggested that pairs or clusters of silanols persist even upon extreme heat treatment. The spatial distribution of these silanols was investigated using VCl_4 as a paramagnetic probe molecule. EPR signals for the grafted V(IV) were absent at room temperature, but a Lorentzian lineshape characteristic of spin-spin coupled centers was observed below 20 K. The latter finding indicates strong electron spin-spin coupling and implies that the silanols are clustered. ^1H double-quantum single-quantum MAS NMR also

suggests that many silanols are closely spaced. Varying the V-loading combined with an analysis of the contribution of the coupled V(IV) component to the total EPR spectrum led to the finding that silanols are clustered in groups of 7 or more, and consequently cannot be described as isolated.

Zeosils modified with H_3PO_4, referred to as P-zeosils, selectively catalyze the dehydration of biomass-derived alcohols, but are unstable in the presence of water. The nature of the active P-sites in these catalysts, and how they are impacted by water is not known. The P-site distribution in a P-modified self-pillared pentasil (P-SPP) was probed using solid-state ^{31}P MAS NMR with frequency-selective detection, dynamic nuclear polarization-enhanced ^{29}Si-filtered ^{31}P detection and ^{31}P-^{31}P correlation experiments. The P-sites in the dehydrated material are surface-bound via hydrolytically sensitive P-O-Si linkages, while some are also oligomers containing hydrolytically robust P-O-P linkages. The P-sites evolve rapidly when exposed to water, even at room temperature. Initial cleavage of some P–O–Si linkages results in an evolving mixture of surface-bound mono- and oligonuclear P-sites with acidity due to the generation of POH groups. Eventually all are converted to H_3PO_4. The effect of the zeosil framework on the stability of the P-sites was determined by comparing the solid-state ^{31}P and ultrafast ^{1}H MAS-NMR of P-SPP to that of a hydrophobic P-modified BEA zeosil (P-BEA). P-BEA contains a higher fraction of hydrolytically-stable P-O-P bonds and a lower accessibility to water compared to P-SPP. Thus, both the water content and the framework play a role in the P-site distribution, which in turn impact the acidity and hence, catalytic activity of P-zeosils. However, elucidating the precise nature of the active P-sites under reaction conditions requires the use of *operando* NMR. At elevated temperatures (140 °C) and in the presence of 2-propanol, ^{31}P and ^{13}C *operando* MAS NMR spectra suggest the POH sites

are converted to phosphate esters. The ability to identify acidic sites in P-zeosils, and to describe their structure and stability, by combining insights using conventional and *operando* NMR, will play an important role in controlling the activity of microporous catalysts.

TABLE OF CONTENTS

LIST OF FIGURES

LIST OF TABLES

Chapter 1: Introduction

1.1 Characterization of solid acid catalysts and challenges

Highly porous solids, both amorphous and crystalline, are widely used as heterogeneous catalysts and catalyst supports. Catalytic activity depends in part on the nature of specific "active" sites which are attached to the external and internal surfaces, or located within the pore channels or cages.[1,2] The structures and dynamics of these active sites as well as their relationship to the surrounding environment are critical information for the rational design of new catalysts with improved activity, selectivity and stability. Obtaining molecular-level information is non-trivial, since the active sites are often present at low concentration, and exist as a distribution that evolves in response to the environment.[3] Consequently, it is important to characterize active sites under reaction conditions. A battery of physicochemical and spectroscopic techniques, such as magnetic resonance, vibrational, and X-ray spectroscopies, are generally deployed to understand the structure of the active sites in heterogeneous catalysts.

Magnetic resonance techniques, including nuclear magnetic resonance (NMR) and electron paramagnetic resonance (EPR) spectroscopies, are powerful, non-invasive tools for probing solid catalysts at the atomic/molecular level.[3,4] Dynamic nuclear polarization (DNP) merges the high sensitivity of EPR with the resolution of NMR.[5] NMR (sometimes in combination with DNP for improved sensitivity) probes the local chemical environments and dynamics of diamagnetic sites. EPR probes paramagnetic sites, which may be present in catalytic systems either as active sites or intermediates and are frequently associated with

transition metal ions. Furthermore, both NMR and EPR techniques can be used to study catalysts under reaction conditions.[6,7]

1.2 The role of silica in heterogeneous catalytic systems

Silica is widely used as a support in heterogeneous catalysis, due to its highly tunable properties, including surface area, pore volume, pore size and particle size.[8,9] Its surface is terminated by hydroxyl groups, also known as surface silanols. They are weakly Brønsted acidic, and may serve as anchoring sites for further chemical tailoring of the surface. In particular, a strategy to disperse metal precursors and form isolated, well-defined sites, is ligand protonolysis by isolated silanols. The latter are presumed to be formed by thermal pretreatment temperature of the silica, which causes the fraction of non-interacting silanols to increase.[10] Deactivation of metal sites due to aggregation of the grafted sites is suppressed by isolating the sites.[11–13] Generating spatially isolated silanols is therefore believed to be a prerequisite for creating well-defined functionalized silica surfaces. Typically, IR[14–16] and 1D NMR (^{1}H and ^{29}Si)[17–19] spectral signatures are presented as evidence for the predominance of isolated silanols on thermally pretreated SiO_2. Although these techniques can differentiate between hydrogen-bonded and non-hydrogen-bonded silanols, they are not sensitive to spatial proximity of more than two silanols, or silanols that are not hydrogen-bonded but still close to one another.

Knowledge about the surface silanol distribution is imperative in understanding their reactivities towards metal complexes. Studies probing the surface of SiO_2 indirectly have suggested that truly isolated silanols may not be generated even upon extreme thermal treatment, and have proposed silanol pairs[20,21] and clusters.[22–24] Nevertheless, the vast

majority of studies still assume the predominance of isolated silanols on silicas thermally treated above 700 °C.[25–28] Thus, more direct approaches that investigate the proximity of silanols, covering longer range distances than IR, NMR or EXAFS, are required.

The silanol distribution is also an important factor in determining the behavior of orthophosphoric acid (H_3PO_4), which is used in combination with silica to generate industrially important catalysts such as "solid phosphoric acids" (SPAs).[29–31] The SPAs have been used since the 1930s in large-scale catalytic processes such as propene oligomerization and benzene alkylation.[31] The active sites in SPAs are suggested to be free phosphoric acid oligomers,[32] but their interactions with the silica surface may shift oligomerization equilibria, thereby altering catalytic activity. Moderate Brønsted acidity can be installed in siliceous (all-silica) zeolites (*aka* zeosils) by infusing them with H_3PO_4. P-zeosils catalyze two noteworthy reactions: the Diels-Alder coupling of carbohydrate-derived 2,5-dimethylfuran with ethylene to give *p*-xylene,[33] and the tandem dehydration-ring opening of tetrahydrofuran to give 1,3-butadiene.[34] Surface and/or pore confinement in a siliceous materials may promote the condensation of H_3PO_4 with itself (leading to oligomeric sites containing P-O-P linkages) and/or the silica framework (forming P-O-Si linkages). Thus, acquiring direct evidence on the environment-dependent speciation of the P-sites is a necessary step towards establishing structure-activity relationships for P-based solid acid catalysts.

Many reactions relevant to degradation of biomass derivatives to obtain high value chemicals generate water, which is known to play an important role in enhancing or suppressing catalytic activity as well as stability of the catalyst (and in particular, zeosil) framework.[35,36] For instance, Brønsted acidic zeolites functionalized with organosilanes that cap silanol defects have been used as a strategy to increase hydrolytic stability compared to

their hydrophilic unfunctionalized analogs.[37,38] Thus, elucidating the effect of water on the zeosil framework is critical in controlling P-site distribution and stability. Furthermore, investigating structure-property relationships of P-zeosils and reaction mechanisms in dehydration reactions requires characterization tools with molecular level precision, and the ability to study catalysts under reaction conditions, i.e., at elevated temperatures and pressures.

1.3 Nuclear interactions in solid state NMR

Obtaining an NMR spectrum depends on the Zeeman splitting of the nuclear spin energy levels in the presence of an external magnetic field and a perturbation using radio frequency (RF) pulses. The gap between the nuclear spin energy levels is sensitive to spin-spin and spin-lattice interactions. Most of these interactions, such as dipole-dipole coupling among spatially proximal spins (both homo- and hetero-nuclear), and quadrupolar coupling between the nuclear quadrupole moment (for nuclear spins, $I>1/2$) and the surrounding electric field gradient, depend on internuclear distances and orientations. The chemical shift anisotropy, which is reflective of the symmetry and/or the mobility of $I=1/2$ nuclei, also affects the energy gap of the nuclear spins.

Molecular tumbling averages orientation-dependent interactions, leading to sharp peaks in the solution-state NMR spectrum. NMR signals for heterogeneous catalysts are typically much broader, due to orientation-dependent internal spin interactions in the solid state. This results in lower resolution, as well as a loss of sensitivity. If multiple sites are present, their isotropic chemical shifts may overlap due to the broadening. To average these strong interactions, solid samples are typically spun at thousands of Hz at an angle of 54.74°

with respect to the external magnetic field B_0. This is known as Magic Angle Spinning (MAS). It results in narrower linewidths by attenuating orientation-dependent interactions (or even eliminating them, when the spinning frequency is faster than the magnitude of the anisotropic interactions, at *ultra-fast* spinning frequencies), thereby simplifying the analysis of complex spectra. Improved resolution aids in attributing signals to sites with similar characteristic chemical shifts.

Anisotropic interactions contain structural and dynamic information on the systems that are lost by using MAS. Spinning at a frequency lower than the magnitude of the coupling interactions results in a spinning sideband pattern, Figure 1.1a, from which information about chemical shift anisotropy and quadrupolar coupling can be extracted. These parameters are correlated with the symmetry and the mobility, respectively, of the nuclei. To extract more information, sophisticated RF pulse sequences can be used to reintroduce interactions selectively during the evolution of the spin-states. For instance, frequency-selective NMR techniques such as $^{\text{RESPIRATION}}$CP provide the opportunity of acquiring site-specific information on multiple types of sites even when the spectrum is crowded by spectral overlap of the isotropic chemical shifts and their spinning sidebands (Figure 1.1b).[39] This involves applying the RF pulse at the frequency (chemical shift) the specific site of interest, which results in suppression of the other peaks visible in the spectrum.

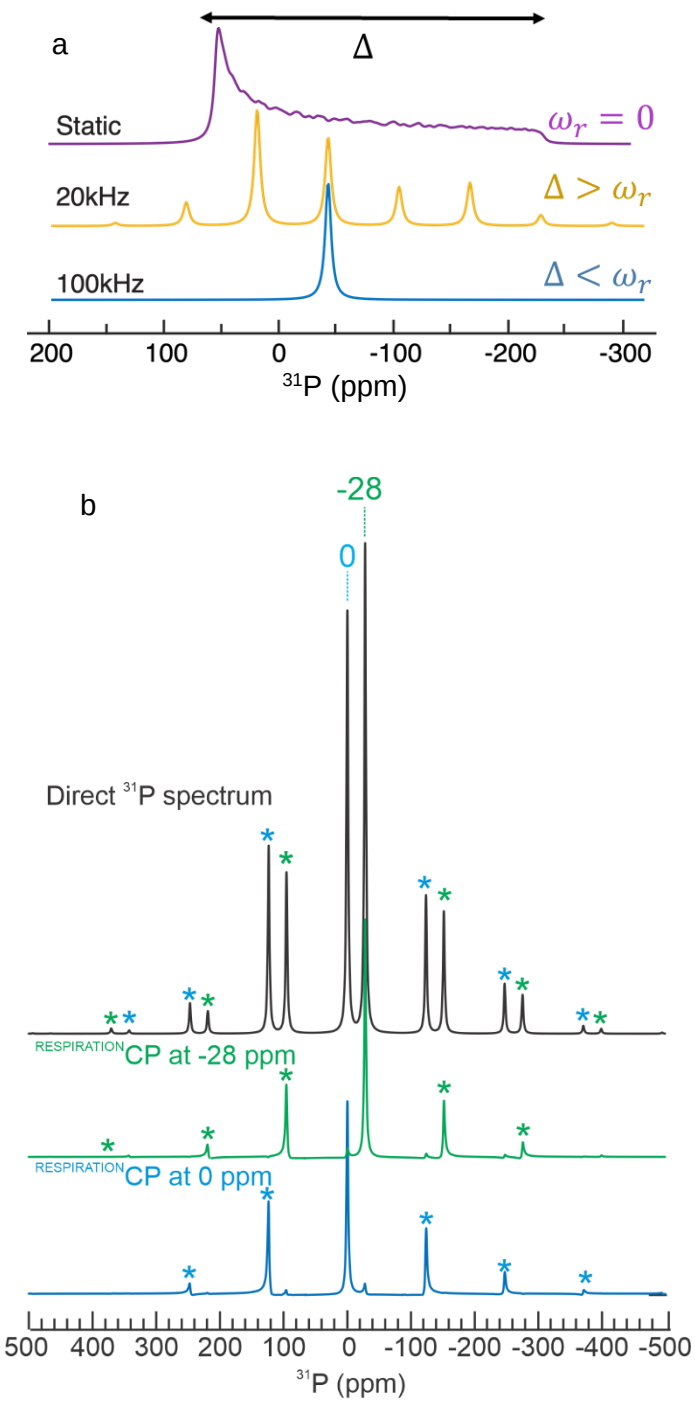

Figure 1.1 Simulated ^{31}P MAS NMR spectra. a) The effect of MAS at different spinning frequencies is shown. An isotropic chemical shift of -43 ppm and chemical shift anisotropy (Δ) of -160 ppm were considered. b) The direct ^{31}P MAS NMR spectrum (black) showing two sites and their corresponding sidebands, indicated with asterisks (*). $^{\text{RESPIRATION}}$CP spectra,

acquired by setting the RF frequency at 0 (blue) and -28 ppm (green) gives the selective sideband pattern for ^{31}P spins corresponding to the two signals.

In favorable cases, solid-state NMR spectroscopy can be used for *in-situ* analysis. Since it is sensitive to the chemical environment of the nuclei in the reacting system,[40,41] it does not require separation of molecules in complex mixtures.[42,43] However, observing multiphase systems, at elevated temperatures and pressures, is challenging for solid-state MAS NMR experiments, in which samples spin at several thousand Hz in a strong magnetic field. The development of *operando* MAS NMR technology has made it possible to probe catalytic systems over a wide range of pressures, temperatures and chemical environments.[6,44,45] Time-resolved interactions between molecules and active sites can reveal the nature of the active sites under catalytic conditions,[46–48] and allows monitoring of chemical transformations if/when side-products, such as water, are generated.

Despite its many advantages, the intrinsically low sensitivity of NMR is further aggravated in solid catalysts when NMR-active nuclei have low gyromagnetic ratios, low natural abundance, or make up a small fraction of the bulk solid material. DNP, which merges both NMR and EPR, combats these sensitivity issues by enhancing the polarization of NMR-active nuclei via unpaired electron spins with much larger gyromagnetic ratios (γ) (Figure 1.2).[5] Unpaired electrons are typically present as exogenously introduced stable organic radicals. The technique relies on saturation of the EPR signal by microwave irradiation, and subsequent transfer of polarization to less sensitive nuclei of interest. DNP has shown improvements in sensitivity of up to 2-3 orders of magnitude, shortening experimental times

dramatically and broadening the scope of NMR spectroscopy to allow correlation experiments with insensitive nuclei.[5]

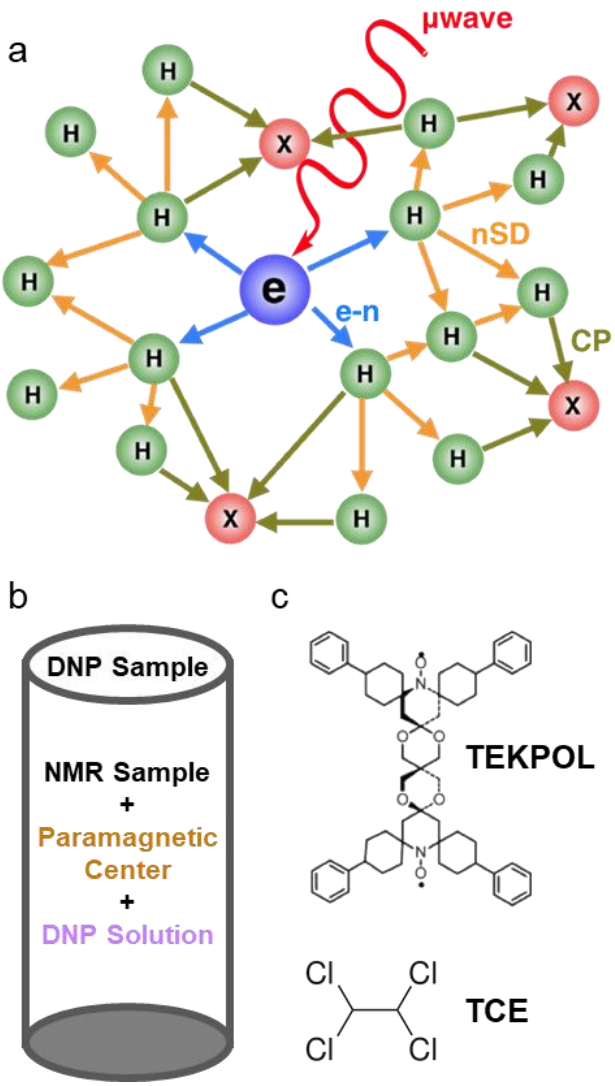

Figure 1.2. Dynamic nuclear polarization of solid catalysts. (a) Microwave irradiation (μwave) excites electrons, which transfer their polarization to nearby protons (H) through electron-nuclear interactions (e-n). The protons further transfer polarization to other protons through nuclear spin diffusion (nSD), eventually reaching the nuclei of interest (X) via cross polarization (CP). (b) The composition of a DNP sample, in which the solid catalyst is infused

with solution of paramagnetic centers in a solvent that freezes at 90 K. (c) A typical paramagnetic center (TEKPOL) and solvent (1,1,2,2-tetrachloroethane, TCE) used in DNP characterization of heterogeneous catalysts.

1.4 Probing paramagnetic sites in solid catalysts

When the catalytic cycle involves paramagnetic sites directly, the geometric and electronic structures of these sites can be investigated using EPR techniques. The method can also provide insight into their interaction with the local environment, dynamic processes, and spatial proximities.[4,7] The role of EPR in the characterization of solid catalysts and surfaces has been long recognized, however, its scope has been greatly expanded by the development of pulsed methods and *operando* techniques.[7,49] The advantages of EPR include its high sensitivity, the ability to investigate longer distance interactions (from 5 to 20 Å via continuous wave (CW) EPR, and up to 80 Å via pulsed EPR), and information about the spatial distribution of paramagnetic species. Isolated and clustered sites show distinct EPR signatures, making it an attractive technique to investigate solid catalysts with paramagnetic centers.[50]

As in NMR, a static magnetic field B_0 splits the energy levels of the electron spin (Zeeman splitting). In CW-EPR, a weak oscillating magnetic field with a frequency in the microwave range is also applied. It induces transitions between electron spin energy levels. Thus, EPR provides information on the interaction of the electron spin with the external magnetic field, with nuclear spins associated with the electron spin (hyperfine interactions) as well as with other electron spins (isotropic exchange, dipole-dipole interaction, anisotropic and antisymmetric exchange). Most of these interactions (except for the isotropic exchange

interaction) are anisotropic, and depend on the electronic structure, molecular structure, and bonding of the paramagnetic center. Employing MAS (as is routinely done in solid-state NMR) is not an effective strategy, because the strength of the anisotropic interactions in EPR is significantly higher than currently achievable sample spinning frequencies.

In spite of the lower spectral resolution relative to NMR, EPR spectra are highly informative. Although anisotropic interactions are averaged in the solution-state, solid-state EPR spectra of powders and single crystals (and even frozen solutions) are much more complex, and consequently richer in information. For example, randomly oriented microcrystals in solid materials result in a powder-averaged spectrum, which reflects the molecular symmetry of the paramagnetic center. Thus, for a magnetically dilute sample with an unpaired electron not interacting with other nearby spins, the symmetry of the molecule is manifested in the EPR spectrum. Hyperfine interactions between nuclear and electron spins result in multiple resonance lines, depending on the nuclear spin, molecular symmetry, electron-nuclear distance and local dynamics. Moreover, electron spins that are nearby one another experience spin-spin interactions. The resulting spectral broadening can provide direct evidence of clustering in the system.

To gain more precise information on electron-electron and electron-nuclear distances, many pulsed EPR experiments (similar to RF pulse sequences in NMR) have been designed. Microwave pulses with specific phases and inter-pulse delays to induce oscillations in signal intensities as a function of experimental parameters (total evolution time or delay or pulse length) can provide precise hyperfine or dipole-dipole coupling information. Such experiments are powerful tools for studying solid catalysts, yielding information on

paramagnetic sites and their interactions with the framework, as well as their evolution under reaction conditions.[51,52]

1.5 Objectives

This thesis aims to use magnetic resonance spectroscopies to develop a deeper fundamental understanding of silicas and siliceous zeolites. The purpose is to acquire molecular-level information to describe the spatial distribution of surface silanols as well as to identify the precise nature of the active sites due to P-modification of siliceous zeolites. To achieve these goals, experiments were designed to take advantage of the broad scope of information available from magnetic resonance spectroscopic techniques, using a combination of advanced capabilities coupled with existing and novel pulse sequences.

In Chapter 2, we probe the distribution of silanols on silica by grafting paramagnetic VCl_4 and probing its interaction with the silica using EPR and NMR in combination with other characterization techniques. EPR signals are absent at room temperature, but show a distinct Lorentzian lineshape at temperatures less than 20 K characteristic of spin-spin coupling. Addition of a coordinating base regenerates the EPR signals at room temperature by increasing the relaxation time. Based on the behavior of the EPR signals, and supported by NMR experiments, we infer that silanol pairs exist. Spin dilution distinguishes the EPR signatures of spin-spin coupled and isolated centers, leading to an estimate of the silanol cluster size (~ 10).

In Chapter 3, we probe the P-site distribution in P-modified zeosils, using solid-state ^{31}P NMR with frequency-selective detection, DNP enhanced ^{29}Si-filtered ^{31}P detection and ^{31}P-^{31}P correlation experiments. The spectra reveal a previously unappreciated diversity of P-

sites, including evidence for surface-bound oligomers. The dry P-zeosil consists of P-sites that are anchored to the solid phase, including mononuclear sites and dinuclear sites containing the [Si-O-P-O-P-O-Si] motif. These P-sites evolve rapidly when exposed to humidity, even at room temperature, through hydrolysis of P-O-Si and ultimately P-O-P bonds.

In Chapter 4, we elucidate the effect of the framework zeosil on the P-site distribution in P-modified zeosils, using solid-state ^{31}P and ultrafast ^{1}H MAS NMR. The stability of the P-sites is higher in P-BEA than in P-SPP, as seen in the evolution of the P-sites as a function of moisture content using ^{1}H and ^{31}P MAS NMR. POH sites in P-SPP are in fast exchange with water, suggesting that they are readily water-accessible. In contrast, the majority of POH sites in P-BEA exchange slowly with water, making the P-sites more stable to hydrolysis.

In Chapter 5, we investigate the P-site evolution under reaction conditions, i.e., at elevated temperatures and in the presence of a reactant, using ^{31}P and ^{13}C variable temperature and *operando* MAS NMR. The dehydration of ^{13}C-labelled 2-propanol at 140 °C was investigated while monitoring changes in the ^{31}P and ^{13}C MAS NMR spectra, which suggest the formation of phosphate esters.

1.6 References

(1) Pelletier, J. D. A.; Basset, J.-M. Catalysis by Design: Well-Defined Single-Site Heterogeneous Catalysts. *Acc. Chem. Res.* **2016**, *49* (4), 664–677. https://doi.org/10.1021/acs.accounts.5b00518.

(2) Zheng, A.; Li, S.; Liu, S.-B.; Deng, F. Acidic Properties and Structure–Activity Correlations of Solid Acid Catalysts Revealed by Solid-State NMR Spectroscopy. *Acc. Chem. Res.* **2016**, *49* (4), 655–663. https://doi.org/10.1021/acs.accounts.6b00007.

(3) Xu, J.; Wang, Q.; Deng, F. Metal Active Sites and Their Catalytic Functions in Zeolites: Insights from Solid-State NMR Spectroscopy. *Acc. Chem. Res.* **2019**, *52* (8), 2179–2189. https://doi.org/10.1021/acs.accounts.9b00125.

(4) Doorslaer, S. Van; Murphy, D. M. EPR Spectroscopy in Catalysis. *Top. Curr. Chem.* **2011**, *321*, 1–39. https://doi.org/10.1007/128_2011_237.

(5) Kobayashi, T.; Perras, F. A.; Slowing, I. I.; Sadow, A. D.; Pruski, M. Dynamic Nuclear Polarization Solid-State NMR in Heterogeneous Catalysis Research. *ACS Catal.* **2015**, *5* (12), 7055–7062. https://doi.org/10.1021/acscatal.5b02039.

(6) Jaegers, N. R.; Mueller, K. T.; Wang, Y.; Hu, J. Z. Variable Temperature and Pressure Operando MAS NMR for Catalysis Science and Related Materials. *Acc. Chem. Res.* **2020**, *53* (3), 611–619. https://doi.org/10.1021/acs.accounts.9b00557.

(7) A. Brückner. Monitoring Transition Metal Ions (TMI) in Oxide Catalysts during (Re)Action: The Power of Operando EPR. *Phys. Chem. Chem. Phys.* **2003**, *5* (20), 4461–4472. https://doi.org/10.1039/B305884K.

(8) Hlatky*, G. G. Heterogeneous Single-Site Catalysts for Olefin Polymerization. *Chem. Rev.* **2000**, *100* (4), 1347–1376. https://doi.org/10.1021/CR9902401.

(9) Iler, R. K. *The Chemistry of Silica: Solubility, Polymerization, Colloid and Surface Properties and Biochemistry of Silica*; Wiley: New York, 1979.

(10) Zhuravlev, L. T. The Surface Chemistry of Amorphous Silica. Zhuravlev Model. *Colloids Surfaces A Physicochem. Eng. Asp.* **2000**, *173*.

(11) Sheldon, R. A. Selective Catalytic Synthesis of Fine Chemicals: Opportunities and Trends. *J. Mol. Catal. A Chem.* **1996**, *107* (1–3), 75–83. https://doi.org/10.1016/1381-1169(95)00229-4.

(12) Sheldon, R. A. Catalysis: The Key to Waste Minimization. *J. Chem. Tech. Biotechnol* **1997**, *68*, 381–388. https://doi.org/10.1002/(SICI)1097-4660(199704)68:4.

(13) Basset, J. M.; Lefebvre, F.; Santini, C. Surface Organometallic Chemistry: Some Fundamental Features Including the Coordination Effects of the Support. *Coord. Chem. Rev.* **1998**, *178–180*, 1703–1723. https://doi.org/10.1016/S0010-8545(98)00159-3.

(14) Zhdanov, S. P.; Kosheleva, L. S.; Titova, T. I. IR Study of Hydroxylated Silica. *Langmuir* **2002**, *3* (6), 960–967. https://doi.org/10.1021//la00078a014.

(15) Roosmalen, A. J. Van; Mol, J. C. An Infrared Study of the Silica Gel Surface. 2. Hydration and Dehydration. *J. Phys. Chem.* **2002**, *83* (19), 2485–2488. https://doi.org/10.1021/j100482a013.

(16) Morrow, B. A.; McFarlan, A. J. Infrared and Gravimetric Study of an Aerosil and a Precipitated Silica Using Chemical and Hydrogen/Deuterium Exchange Probes. *Langmuir* **2002**, *7* (8), 1695–1701. https://doi.org/10.1021/la00056a022.

(17) Bronnimann, C. E.; Zeigler, R. C.; Maciel, G. E. Proton NMR Study of Dehydration of the Silica Gel Surface. *J. Am. Chem. Soc.* **1988**, *110* (7), 2023–2026. https://doi.org/10.1021/ja00215a001.

(18) Liu, C. C.; Maciel, G. E. The Fumed Silica Surface: A Study by NMR. *J. Am. Chem. Soc.* **1996**, *118* (21), 5103–5119. https://doi.org/10.1021/ja954120w.

(19) Sindorf, D. W.; Maciel, G. E. Silicon-29 NMR Study of Dehydrated/Rehydrated Silica Gel Using Cross Polarization and Magic-Angle Spinning. *J. Am. Chem. Soc.* **1983**, *105* (6), 1487–1493. https://doi.org/10.1021/ja00344a012.

(20) Taha, Z. A.; Deguns, E. W.; Swarup Chattopadhyay, A.; Susannah L. Scott. Formation of Digallium Sites in the Reaction of Trimethylgallium with Silica. *Organometallics*

2006, *25* (8), 1891–1899. https://doi.org/10.1021/om051034o.

(21) Fleischman, S. D.; Scott, S. L. Evidence for the Pairwise Disposition of Grafting Sites on Highly Dehydroxylated Silicas via Their Reactions with Ga(CH3)3. *J. Am. Chem. Soc.* **2011**, *133* (13), 4847–4855. https://doi.org/10.1021/ja108905p.

(22) Peri, J. B.; Hensley, A. L. The Surface Structure of Silica Gel. *J. Phys. Chem.* **1968**, *72* (8), 2926–2933. https://doi.org/10.1021/j100854a041.

(23) Schrader, A. M.; Monroe, J. I.; Sheil, R.; Dobbs, H. A.; Keller, T. J.; Li, Y.; Jain, S.; Shell, M. S.; Israelachvili, J. N.; Han, S. Surface Chemical Heterogeneity Modulates Silica Surface Hydration. *Proc. Natl. Acad. Sci.* **2018**, *115* (12), 2890–2895. https://doi.org/10.1073/pnas.1722263115.

(24) Chien, J. C. W. Study of Surface Structures of Submicron Metal Oxides by Vanadium Tetrachloride as a Paramagnetic Probe. *J. Am. Chem. Soc.* **2002**, *93* (19), 4675–4684. https://doi.org/10.1021/ja00748a005.

(25) Gajan, D.; Copéret, C. Silica-Supported Single-Site Catalysts: To Be or Not to Be? A Conjecture on Silica Surfaces. *New J. Chem.* **2011**, *35* (11), 2403–2408. https://doi.org/10.1039/c1nj20506d.

(26) Copéret, C.; Comas-Vives, A.; Conley, M. P.; Estes, D. P.; Fedorov, A.; Mougel, V.; Nagae, H.; Núñez-Zarur, F.; Zhizhko, P. A. Surface Organometallic and Coordination Chemistry toward Single-Site Heterogeneous Catalysts: Strategies, Methods, Structures, and Activities. *Chem. Rev.* **2016**, *116* (2), 323–421. https://doi.org/10.1021/acs.chemrev.5b00373.

(27) Copéret, C.; Fedorov, A.; Zhizhko, P. A. Surface Organometallic Chemistry: Paving the Way Beyond Well-Defined Supported Organometallics and Single-Site Catalysis.

Catal. Lett. 2017 1479 **2017**, *147* (9), 2247–2259. https://doi.org/10.1007/s10562-017-2107-4.

(28) Fernando Rascón; Raphael Wischert; Christophe Copéret. Molecular Nature of Support Effects in Single-Site Heterogeneous Catalysts : Silica vs. Alumina. *Chem. Sci.* **2011**, *2* (8), 1449–1456. https://doi.org/10.1039/c1sc00073j.

(29) Zhang, J.; Yan, Y.; Chu, Q.; Feng, J. Solid Phosphoric Acid Catalyst for Propene Oligomerization: Effect of Silicon Phosphate Composition. *Fuel Process. Technol.* **2015**, *135*, 2–5. https://doi.org/10.1016/j.fuproc.2014.09.007.

(30) Cavani, F.; Girotti, G.; Terzoni, G. Effect of Water in the Performance of the "Solid Phosphoric Acid" Catalyst for Alkylation of Benzene to Cumene and for Oligomerization of Propene. *Appl. Catal. A Gen.* **1993**, *97* (2), 177–196. https://doi.org/10.1016/0926-860X(93)80083-3.

(31) Prinsloo, N. M. Solid Phosphoric Acid Oligomerisation: Manipulating Diesel Selectivity by Controlling Catalyst Hydration. *Fuel Process. Technol.* **2006**, *87* (5), 437–442. https://doi.org/10.1016/j.fuproc.2005.11.005.

(32) Thomas R. Krawietz; Ping Lin; Karen E. Lotterhos; Paul D. Torres; Dewey H. Barich; Abraham Clearfield, A.; Haw, J. F. Solid Phosphoric Acid Catalyst: A Multinuclear NMR and Theoretical Study. *J. Am. Chem. Soc.* **1998**, *120* (33), 8502–8511. https://doi.org/10.1021/ja9813461.

(33) Cho, H. J.; Ren, L.; Vattipalli, V.; Yeh, Y.-H.; Gould, N.; Xu, B.; Gorte, R. J.; Lobo, R.; Dauenhauer, P. J.; Tsapatsis, M.; Fan, W. Renewable P-Xylene from 2,5-Dimethylfuran and Ethylene Using Phosphorus-Containing Zeolite Catalysts. *ChemCatChem* **2017**, *9* (3), 398–402. https://doi.org/10.1002/cctc.201601294.

(34) Abdelrahman, O. A.; Park, D. S.; Vinter, K. P.; Spanjers, C. S.; Ren, L.; Cho, H. J.; Vlachos, D. G.; Fan, W.; Tsapatsis, M.; Dauenhauer, P. J. Biomass-Derived Butadiene by Dehydra-Decyclization of Tetrahydrofuran. *ACS Sustain. Chem. Eng.* **2017**, *5* (5), 3732–3736. https://doi.org/10.1021/acssuschemeng.7b00745.

(35) Corma, A.; Mengual, J.; Miguel, P. J. Steam Catalytic Cracking of Naphtha over ZSM-5 Zeolite for Production of Propene and Ethene: Micro and Macroscopic Implications of the Presence of Steam. *Appl. Catal. A Gen.* **2012**, *417–418*, 220–235. https://doi.org/10.1016/j.apcata.2011.12.044.

(36) H. Yang; J. Coolman, R.; P. Karanjkar; H. Wang; Z. Xu; H. Chen; J. Moutziaris, T.; W. Huber, G. The Effect of Steam on the Catalytic Fast Pyrolysis of Cellulose. *Green Chem.* **2015**, *17* (5), 2912–2923. https://doi.org/10.1039/c5gc00026b.

(37) Zapata, P. A.; Faria, J.; Ruiz, M. P.; Jentoft, R. E.; Resasco, D. E. Hydrophobic Zeolites for Biofuel Upgrading Reactions at the Liquid–Liquid Interface in Water/Oil Emulsions. *J. Am. Chem. Soc.* **2012**, *134* (20), 8570–8578. https://doi.org/10.1021/ja3015082.

(38) Zhang, L.; Chen, K.; Chen, B.; White, J. L.; Resasco, D. E. Factors That Determine Zeolite Stability in Hot Liquid Water. *J. Am. Chem. Soc.* **2015**, *137* (36), 11810–11819. https://doi.org/10.1021/jacs.5b07398.

(39) Jain, S.; Bjerring, M.; Nielsen, N. C. Efficient and Robust Heteronuclear Cross-Polarization for High-Speed-Spinning Biological Solid-State NMR Spectroscopy. *J. Phys. Chem. Lett.* **2012**, *3* (6), 703–708. https://doi.org/10.1021/jz3000905.

(40) Zhi Hu, J.; A. Sears, J.; S. Mehta, H.; J. Ford, J.; Hun Kwak, J.; Kake Zhu; Yong Wang; Jun Liu; W. Hoyt, D.; F. Peden, C. H. A Large Sample Volume Magic Angle Spinning

Nuclear Magnetic Resonance Probe for in Situ Investigations with Constant Flow of Reactants. *Phys. Chem. Chem. Phys.* **2012**, *14* (7), 2137–2143. https://doi.org/10.1039/c1cp22692d.

(41) Surface, J. A.; Skemer, P.; Hayes, S. E.; Conradi, M. S. In Situ Measurement of Magnesium Carbonate Formation from CO2 Using Static High-Pressure and -Temperature 13C NMR. *Environ. Sci. Technol.* **2012**, *47* (1), 119–125. https://doi.org/es301287n.

(42) Oliver, F. G.; Munson, E. J.; Haw, J. F. High-Temperature in Situ Magic Angle Spinning NMR Studies of Chemical Reactions on Catalysts. *J-Phys. Chem* **1992**, *96*, 8106–8111. https://doi.org/10.1021/j100199a052.

(43) Foley, D. A.; Bez, E.; Codina, A.; Colson, K. L.; Fey, M.; Krull, R.; Piroli, D.; Zell, M. T.; Marquez, B. L. NMR Flow Tube for Online NMR Reaction Monitoring. *Anal. Chem.* **2014**, *86* (24), 12008–12013. https://doi.org/10.1021/ac502300q.

(44) Qi, L.; Alamillo, R.; Elliott, W. A.; Andersen, A.; Hoyt, D. W.; Walter, E. D.; Han, K. S.; Washton, N. M.; Rioux, R. M.; Dumesic, J. A.; Scott, S. L. Operando Solid-State NMR Observation of Solvent-Mediated Adsorption-Reaction of Carbohydrates in Zeolites. *ACS Catal.* **2017**, *7* (5), 3489–3500. https://doi.org/10.1021/acscatal.7b01045.

(45) Walter, E. D.; Qi, L.; Chamas, A.; Mehta, H. S.; Sears, J. A.; Scott, S. L.; Hoyt, D. W. Operando MAS NMR Reaction Studies at High Temperatures and Pressures. *J. Phys. Chem. C* **2018**, *122* (15), 8209–8215. https://doi.org/10.1021/acs.jpcc.7b11442.

(46) Zhao, Z.; Shi, H.; Wan, C.; Hu, M. Y.; Liu, Y.; Mei, D.; Camaioni, D. M.; Hu, J. Z.; Lercher, J. A. Mechanism of Phenol Alkylation in Zeolite H-BEA Using In Situ Solid-

State NMR Spectroscopy. *J. Am. Chem. Soc.* **2017**, *139* (27), 9178–9185. https://doi.org/10.1021/jacs.7b02153.

(47) Vjunov, A.; Hu, M. Y.; Feng, J.; Camaioni, D. M.; Mei, D.; Hu, J. Z.; Zhao, C.; Lercher, J. A. Following Solid-Acid-Catalyzed Reactions by MAS NMR Spectroscopy in Liquid Phase—Zeolite-Catalyzed Conversion of Cyclohexanol in Water. *Angew. Chemie Int. Ed.* **2014**, *53* (2), 479–482. https://doi.org/10.1002/anie.201306673.

(48) Zhi Hu, J.; Y. Hu, M.; Zhenchao Zhao; Suochang Xu; Aleksei Vjunov; Hui Shi; M. Camaioni, D.; F. Peden, C. H.; A. Lercher, J. Sealed Rotors for in Situ High Temperature High Pressure MAS NMR. *Chem. Commun.* **2015**, *51* (70), 13458–13461. https://doi.org/10.1039/c5cc03910j.

(49) Morra, E.; Giamello, E.; Chiesa, M. EPR Approaches to Heterogeneous Catalysis. The Chemistry of Titanium in Heterogeneous Catalysts and Photocatalysts. *J. Magn. Reson.* **2017**, *280*, 89–102. https://doi.org/10.1016/j.jmr.2017.02.008.

(50) Dyrek, K.; Che, M. EPR as a Tool To Investigate the Transition Metal Chemistry on Oxide Surfaces. *Chem. Rev.* **1997**, *97* (1), 305–331. https://doi.org/10.1021/cr950259d.

(51) Morra, E.; Maurelli, S.; Chiesa, M.; Giamello, E. Rational Design of Engineered Multifunctional Heterogeneous Catalysts. The Role of Advanced EPR Techniques. *Top. Catal. 2015 5812* **2015**, *58* (12), 783–795. https://doi.org/10.1007/s11244-015-0418-5.

(52) Morra, E.; Signorile, M.; Salvadori, E.; Bordiga, S.; Giamello, E.; Chiesa, M. Nature and Topology of Metal–Oxygen Binding Sites in Zeolite Materials: 17O High-Resolution EPR Spectroscopy of Metal-Loaded ZSM-5. *Angew. Chemie* **2019**, *131* (36), 12528–12533. https://doi.org/10.1002/ange.201906488.

Chapter 2: EPR Evidence for Silanol Clustering on Silica Surfaces

2.1 Introduction

The tunable properties of silica, SiO_2, including its surface area, pore volume, pore size and particle size make it suitable for its broad use as support in heterogeneous catalysis.[1,2] Silica is also widely used for other applications as dielectric materials in microelectronic devices,[3] stationary phase packing material in liquid-liquid and size exclusion chromatography to perform separations,[4] intravenous drug delivery vectors,[5] and as enzyme immobilization carriers to facilitate glucose biosensors.[6] In all of these applications, the Brønsted acid sites i.e. hydroxyls on its surface known as surface silanols, tune the silica surface property and/or act as points of attachment for further chemical tailoring of the surface to generate sites that in turn determine its activity.[7] There are three types of silanols on the SiO_2 surface: isolated, vicinal and geminal. Heterogeneous catalysts are commonly prepared by immobilizing metal complexes on the surface of SiO_2 via a protonolysis reaction (Figure 2.1a). Spatially dispersed isolated hydroxyl sites are thought to generate well-defined and stable active sites.[8,9] The spatial isolation of these surface-immobilized metal sites is key to the activity and enhanced selectivity of the catalyst, e.g. to prevent deactivation reactions by unwanted reactions such as oligomerization as of the grafted sites, as well as for the rational design and computational modeling of catalysts.[10–12] Hence, generating spatially isolated hydroxyl groups is a prerequisite for well-defined silica-based functionalized surfaces.

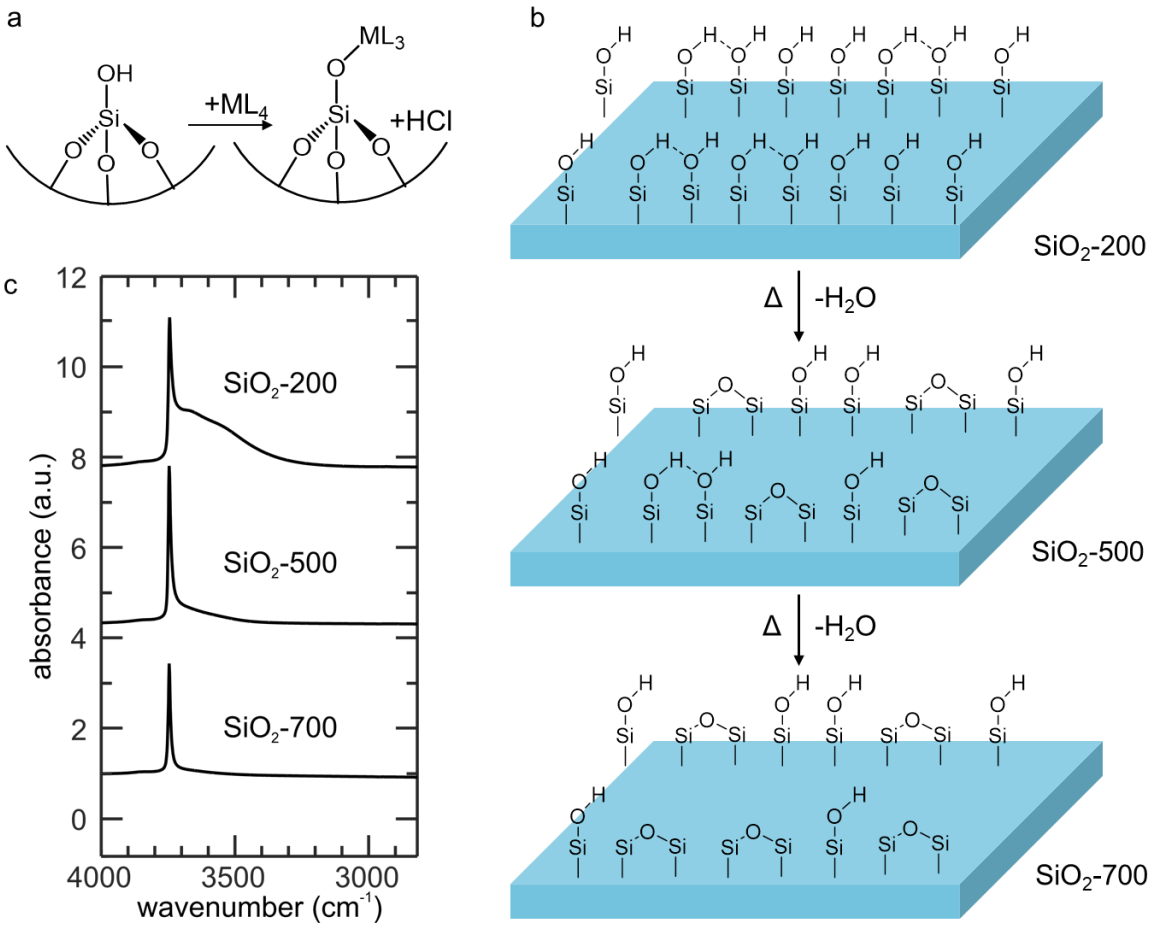

Figure 2.1 The surface of silica and its surface hydroxyls. a) The grafting of a metallic precursor, ML_4 via a protonolysis reaction with the surface hydroxyls. b) The commonly accepted model of a silica surface, in which heating drives the condensation of hydrogen-bonded vicinal species, releasing water, and forming spatially dispersed silanol groups as the silica is treated at 200, 500 and 700 ^{o}C (SiO_2-200, SiO_2-500, SiO_2-700). c) In situ transmission IR spectra of a self-supporting disk of silica after partial dehydroxylation corresponding to

SiO_2-200, SiO_2-500, SiO_2-700. Spectra are normalized to the intensity of the silica lattice overtone at 1863 cm^{-1} and are offset vertically for clarity.

The density of silanols continually decreases with increasing thermal treatment temperature of SiO_2, and is presumed to be accompanied by an increase in the ratio of isolated silanols.[7,13,14] Heating fully hydroxylated SiO_2 to temperatures above 150 °C results in the elimination of water via condensation of hydrogen-bonded vicinal silanols to form siloxane bridges (Figure 2.1b). When the temperature of the thermal treatment of SiO_2 exceeds 450 °C, predominantly isolated hydroxyls are thought to remain, a prerequisite to achieve site isolation in supported catalysts.[8,9,15]

Experimentally, changes in infra-red (IR) spectra are commonly used as evidence for the exclusive presence of isolated hydroxyls.[16–18] SiO_2 heated at 200 °C shows a broad IR signal centered at 3660 cm^{-1} and a narrow, sharp one at 3747 cm^{-1}, assigned to ν(O-H) modes for hydroxyls that are vicinal and unperturbed by hydrogen bonding, respectively (Figure 2.1c). As the SiO_2 is heated to higher temperatures (such as 500 and 700 °C), the broad signal disappears and the narrow one at 3747 cm^{-1} becomes increasingly more pronounced such that the latter dominates at 700 °C. Furthermore, characteristic ^{1}H and ^{29}Si NMR signals are used to differentiate between hydrogen-bonded vicinal and isolated silanols. For instance, the ^{1}H NMR peak at 3.5 ppm is assigned to hydrogen-bonded silanols that has been found to disappear when SiO_2 is pre-treated above 500 °C, while the peak at 1.8 ppm, assigned to isolated silanols, persists.[19,20] These IR and 1D NMR spectral signatures are widely used as evidence for the dominance of isolated silanols on thermally treated SiO_2. While these spectroscopic techniques can differentiate between hydrogen-bonded and non-hydrogen

bonded silanols, neither of these strategies are sensitive to spatial proximity of two or more silanols or silanol-grafted functional groups, and hence cannot differentiate whether non-hydrogen bonded silanols can still be spatially proximal. This differentiation matters when co-located silanols lead to spatially proximal, i.e. non-isolated, silanol-grafted functional groups.

In fact, studies in the literature on metallic precursors grafted onto SiO_2 suggest the presence of a much more complex spatial topology for sianols than is generally presumed for silica subjected to thermal treatment. Stoichiometric studies of reactive halides grafted onto SiO_2 gel by Peri et al suggested that a significant fraction of the surface hydroxyl groups exist pair-wise on SiO_2 that has been thermally treated under vacuum at 600 °C.[21] More recently, the reaction of $Ga(CH_3)_3$ with amorphous and mesoporous SiO_2 treated at 500 °C[22] and 800 °C[23] was characterized by Ga K-edge EXAFS, and a prominent Ga-Ga scattering path at ~3 Å was observed that proves the existence of bridged digallium species. In that study, two thirds of the hydroxyl species was consumed by the reaction of $Ga(CH_3)_3$ requiring two adjacent silanol groups spaced ~3 Å apart. This demonstrates that even after thermal treatment of SiO_2 at 800 °C that is thought to be sufficient to generate spatially isolated silanols, they instead contain predominantly proximal silanols. Another systematic study of surface water diffusivity on SiO_2 nanoparticles revealed a sharp transition in surface water diffusivity around an intermediate silanol density regime achieved with a pre-treatment temperatures between 700 to 800 °C, suggesting that silanols on the SiO_2 surface are spatially clustered.[24] An earlier study noted that the functionalization of Cabosil SiO_2 annealed at 700 °C and reacted with paramagnetic VCl_4 yields a broad EPR signal, which was attributed to exchange-coupled VCl_4 species, again arising from silanol clusters.[25] All of these studies identified non-

isolated silanols on the surface of thermally treated SiO_2 at temperatures where isolated silanols are presumed to dominate, illustrating that the spatial distribution of the surface hydroxyls of SiO_2 is *still* a matter of current debate. Furthermore, the observation that digallium species form across proximal silanols does not rule out the presence of clusters (>2) of silanols, as suggested in previous studies. Elucidation of the number of silanols that form a cluster, whether it is a random distribution, as well as the relative fraction of the silica surface that is unoccupied by the clusters, is important in understanding the reactivity of metallic precursors on silica.

To answer this question, a technique that is sensitive to longer range spatial proximity than a few Å is required. Electron paramagnetic resonance (EPR) affords the characterization of the entire ensemble property of grafted paramagnetic species on silanols, regardless of structural disorder, thereby allowing us to extrapolate these findings to the overall topology of the silica surface of silica. EPR offers direct insight into the spatial distribution of grafted paramagnetic species, since isolated and clustered sites have distinct spectroscopic signatures due to their spin-spin interactions, provided the relaxation times of the paramagnetic centers are sufficiently long to be detectable by EPR. EPR is sensitive to longer distance regimes (from 5 to 20 Å via continuous wave EPR and up to 80 Å via pulsed EPR) than EXAFS (only sensitive up to 5 Å), permitting a longer-range perspective of the spatial distribution of silanols. The goal of this study is therefore to determine whether the surface silanols are spatially proximal, and if so, whether these surface silanols exist in clusters larger than pairs, relying on EPR lineshape analysis that is also insensitive to disorder.

In this study, EPR characterization of paramagnetic VCl_4 grafted onto SiO_2 was performed, aimed at distinguishing between isolated and clustered species. The spatial

interactions between silanol-tethered paramagnetic V(IV) centers and their spin dynamics properties were investigated by varying the sample temperature and adding a coordinating base. EPR line broadening of silanol-tethered paramagnetic V(IV) with systematic spin dilution was used to calculate an approximate value of a silanol cluster size. The findings are harmonized from data derived from EPR measurements, elemental analysis, IR spectroscopy, as well as EXAFS to explore whether a bridging structure of the grafted species exists. This study seeks an understanding of the spatial distribution of surface silanols on SiO_2, and challenges well-accepted strategies to generate isolated catalyst sites on amorphous silica surfaces.

2.2 Results and Discussion

2.2.1 CW EPR spectroscopy investigation of grafted VCl_4

To investigate the spatial distribution of silanols on SiO_2, the surface was functionalized with a paramagnetic probe molecule, VCl_4. Three silicas were investigated: a non-porous, fumed silica (Aerosil-380, A380 383 m^2/g) and two types of mesoporous precipitated silicas (Sylopol 952, S952, 300 m^2/g and Santa Barbara Amorphous type 15, SBA-15, > 550 m^2/g). The $3d^1$ valence electron configuration of V(IV) ions is responsible for a net electron spin S = 1/2. Interaction of the unpaired electron with the ^{51}V nucleus (I = 7/2, natural abundance 99.5 %) is expected to give a distinctive eight-line spectrum, in which the lineshape reflects both the molecular symmetry and interactions with nearby paramagnetic species. However, the tetrahedral symmetry of VCl_4, as well as its Jahn-Teller distortion, result in a small ligand field splitting. The resulting energy separation between the ground and excited states is small,

leading to a short spin-lattice relaxation time (T_1). Consequently, dilute VCl_4 is EPR-silent above 9 K.[26]

Interaction of VCl_4 with an oxide surface should lower the symmetry at V, resulting in a longer T_1 and an observable EPR signal above 9 K.[27] Indeed, deposition of excess VCl_4 onto the surface of γ-Al_2O_3 (followed by the desorption of volatiles) that had been thermally treated at 500 °C (IR spectrum shown in Figure A2.1) gives a material with 2.2 wt % V displaying a high-intensity continuous wave (CW) EPR signal at room temperature (Figure 2.2a). In contrast, when excess VCl_4 is deposited onto silica A380, also pre-treated at 500 °C, with approximately twice the surface area yielding 4.2 wt% V, no EPR signal was detected (Figure 2.2b). Similarly, the EPR spectrum of VCl_4 deposited onto silica A380 treated at 700 °C (Figure 2.2c) and mesoporous silicas SBA-15 and S952 treated at 500 °C (Figure 2.2d and 2.2e) also do not show significant signals relative to VCl_4 on γ-Al_2O_3.

We considered whether the unexpected lack of signal for the V(IV)-modified silica could be a consequence of unintended conversion of V(IV) to an EPR-inactive oxidation state, for example, via oxidation of V(IV) to V(V), or disproportionation of V(IV) to V(III) and V(V). Grafted V(V) sites should be observable via their ^{51}V NMR signals. In the ^{51}V MAS NMR spectrum of VCl_4-modified A380 SiO_2 (treated at 500 °C) (4.2 wt % V), a signal was detected at -297 ppm (Figure A2.2) corresponding to ≡$SiOVOCl_2$ sites.[28] The ^{51}V NMR signal was quantified by comparing the area of the peak with that of an external standard (prepared by grafting $VOCl_3$ onto the same A380 SiO_2 (treated at 500 °C). The V(V) fraction in VCl_4 modified-SiO_2 was estimated to be just 10 % of total V. The NMR signal presumably arises due to contamination of commercial VCl_4 by $VOCl_3$, and/or adventitious oxidation of VCl_4 during sample preparation or during the NMR measurement itself. We further note that the

fraction of V(V) sites in VCl_4-modified SiO_2 could be underestimated if the presence of nearby paramagnetic sites broadens and/or shifts their NMR signals. Precise quantification of paramagnetic effects on the nuclear spins near a transition metal center requires information on *g*-anisotropy, spin-orbit coupling, electron spin-spin coupling and hyperfine interactions, and is beyond the scope of this study. However, since we observe neither shifted V(V) peaks nor broadened components in the NMR spectrum, we assume that paramagnetic effects do not influence the NMR signal appreciably.

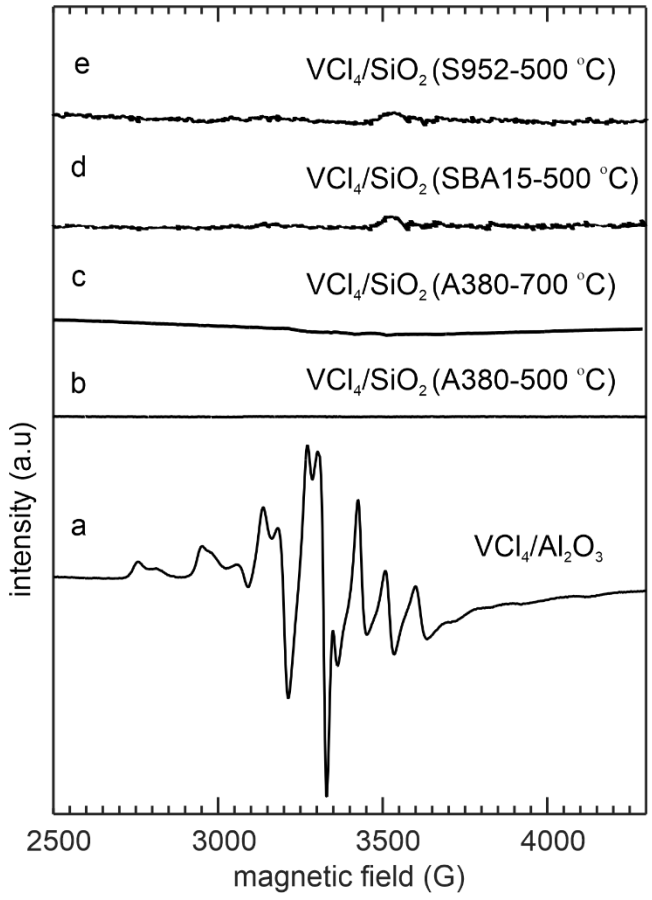

Figure 2.2 CW X-band EPR spectra of VCl_4 modified (a) γ-Al_2O_3 (2.2 wt % V), (b) A380 SiO_2 (4.2 wt% V) dehydroxylated at 500 °C, (c) A380 SiO_2 dehydroxylated at 700 °C, (d) SBA15 SiO_2 dehydroxylated at 500 °C, (e) S952 SiO_2 dehydroxylated at 500 °C. All spectra

were collected at room temperature using the same parameters (time constant = 40.96 ms, receiver gain = 1 x 10^4, attenuation = 20 dB, modulation frequency = 100 kHz, modulation amplitude = 5.45 G) and are reported on the same intensity scale.

2.2.2 Reactions of surface silanols.

The VCl_4 treated SiO_2 was further probed by IR. The sharp band at 3747 cm^{-1} in the IR spectrum of Aerosil-380 SiO_2 pretreated at 500 °C (Figure 2.3a) corresponds to the O-H stretch of non-hydrogen-bonded silanols,[17–19] which are often described as isolated.[9,31] Upon exposure to excess VCl_4 vapor at room temperature, the band almost completely disappears, leaving only a weak, broad band representing inaccessible silanols (Figure 2.3b).[32] This result demonstrates that non-hydrogen-bonded silanols readily react with VCl_4.

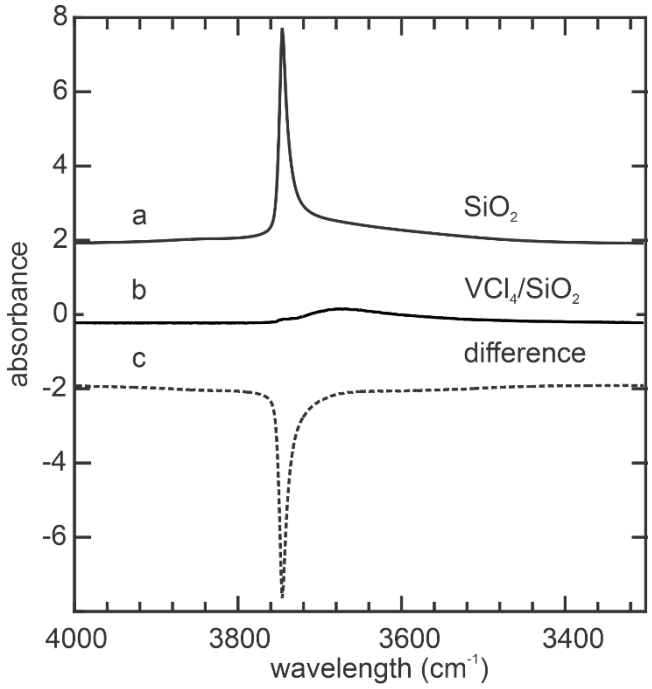

Figure 2.3 *In situ* transmission IR spectra of a self-supporting disk of silica: (a) after partial dehydroxylation *in vacuo* at 500 °C, and (b) after reaction with excess VCl_4 vapor at room

temperature, followed by desorption of volatiles at the same temperature. The difference spectrum is shown in (c). Spectra are offset vertically for clarity.

Scheme 2.1 shows several possible reactions of VCl_4 with surface silanols. The reaction between an isolated silanol and VCl_4 to form site **A** is represented in Scheme 2.1a. Reactions between VCl_4 and nearby silanols were also considered, shown in Scheme 2.1b. Site **B** represents reaction of VCl_4 with a vicinal silanol pair that will yield a visible EPR signal. In sites **C** and **D**, two VCl_4 molecules react with a vicinal silanol pair and interact via a bridging ligand (chloride or silanolate). In site **E**, there is no bridging ligand but the V(IV) centers are nevertheless in close proximity.

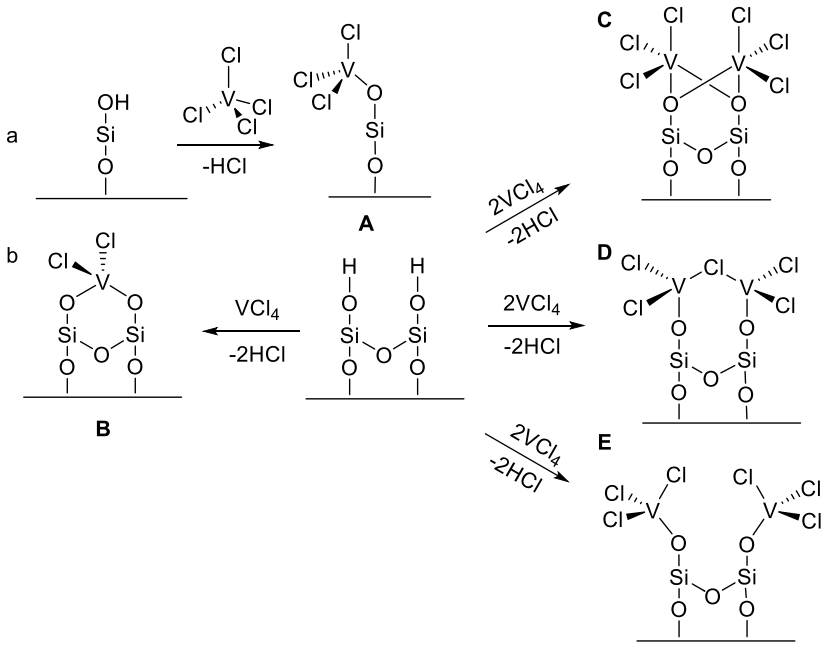

Scheme 2.1 Possible reactions of VCl_4 with (a) an isolated silanol, and (b) vicinal silanols.

According to elemental analysis, the V-modified Aerosil-380 SiO_2 contains (4.2 ± 0.2) wt% V, or 1.3 V/nm^2. Since thermal treatment of the silica at 500 °C results in a surface silanol density of 1.2 OH/nm^2 as reported in previous studies,[33] the V uptake corresponds to a molar ratio V:≡SiOH = 1.1. This reaction stoichiometry is shown in eq 2.1:

$$\equiv SiOH + VCl_4 \rightarrow \text{“}\equiv SiOVCl_3\text{”} + HCl \qquad (2.1)$$

The reaction stoichiometry of Eq. 2.1 is consistent with the formation of any of sites shown in **A**, **C**, **D**, and **E** in Scheme 2.1. Of these, site **A** in Scheme 1 that represents an isolated site is inconsistent with the absence of an EPR signal at room temperature. Eq 1 is not consistent with site **B** (furthermore, site **B** is also inconsistent with the absence of an EPR signal).

The proximity of grafted V sites was assessed by acquiring the V K-edge EXAFS of “≡$SiOVCl_3$”. The prominent feature at ca. 1.8 Å in *R*-space, shown in Figure 2.4, reflects scattering by Cl and O atoms directly bonded to V. The curvefit obtained using a model for “≡$SiOVCl_3$” returned V-O and V-Cl distances of 1.75 and 2.15 Å, respectively (Table 2.1), which are consistent with those of $VOCl_3$, vanadyl silanolates and vanadyl chlorides.[34] The EXAFS, in conjunction with the IR and elemental analysis, is consistent with site **A** as the principal outcome of the reaction between VCl_4 and SiO_2, despite the absence of EPR signals. There is no evidence for coherent V-V scattering (expected at ca. 2.6 Å in *R*-space), ruling out a significant contribution from ligand-bridged sites such as **C** and **D** in Scheme 2.1.

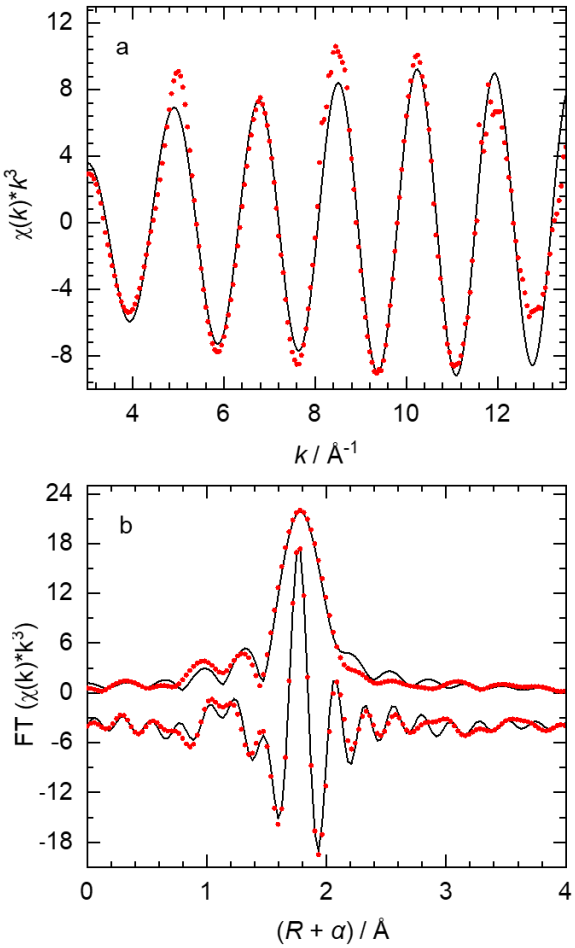

Figure 2.4 V K-edge EXAFS for VCl_4-modified silica, in (a) k^3-weighted k-space, and (b) non-phase-corrected R-space (bottom: imaginary component; and top: FT magnitude). Data is shown as red points; the curvefit is represented by the black lines. Fit parameters are given in Table 1.

Table 2.1 Curvefit parameters[a] for V K-edge EXAFS of VCl_4/SiO_2

Path	N	R / Å	σ^2 / Å^2	d / Å
V-O	1[b]	1.76(2)	0.002(1)	1.745 [c]
V-Cl	3[b]	2.15(1)	0.002(1)	2.145 [d]

[a] Global fit parameters: $S_0^2 = 0.83(9)$, $\Delta E_0 = 1(1)$ eV. Data ranges: $3.0 \leq k \leq 13.5$ Å^{-1}, $1.0 \leq R \leq 3.0$ Å. The total number of variable parameters used in the fit is 5, out of a total of 13 independent data points. [b] Fixed at integer values. [c]Distance for V-O path is from the crystal structure of $V(O)(OSiPh_3)_3$[35]. [d] Distance for V-Cl path is from Material project computed VCl_4 structure (ID 1205372).[f] The R-factor for this fit is 0.025.

Thermodynamic stabilities of different structures for the grafted vanadium sites were also calculated using DFT (see SI for details on the modeling of the silica surface). The free energy of sites **A**-**E** were calculated. In site **E**, without bridging atoms, the V-V distance is long, 4.9 Å. In site **D** the vanadium atoms are linked via a chloride bridge at a V-V distance of 4.1 Å. Site **E** is 278.3 kJ/mol more stable than **D**. Furthermore, **D** is 7.1 kJ/mol more stable than that of the initial SiO_2 and 13.0 kJ/mol more stable than **A** (where V:≡SiOH = 2). Therefore, the most stable site that arises from the reaction between VCl_4 and SiO_2 is **E**.

None of the sites **A**-**D** are fully consistent with the experimental observations, therefore we return to site **E** as a viable and plausible candidate. Although the EXAFS provides no positive evidence for site pairing, the absence of a coherent V-V scattering path does not preclude spatial proximity between the V sites. Since **E** consists of a pair of V(IV) sites that are spatially close but not linked via a bridging ligand, it would not be expected to show a V-V scattering path in the EXAFS. Strong spin-spin interactions between grafted V(IV) sites as schematically shown in **E** may result in extensive EPR line broadening, making the signal difficult to detect at room temperature. In a previous report, a similar suppression of the EPR signal was attributed to the reaction of two VCl_4 with geminal silanols.[36,37] However, the fraction of geminal silanols on silica-500 is expected to be minimal (~ 1-6 %

according to reports on MCM-41 and silica gel with a surface area of 466 m^2/g).[37,38] For isolated silanols, a surface density of 1.2 OH/nm^2 would result in a mean interhydroxyl distance of ca. 9 Å.[16] Considering this distance, and in the absence of exchange coupling (occurring at less than 3 Å) dipolar interactions between between unpaired electrons of the V(IV) centers equals only 25 G (700 MHz), and would be manifested on the V(IV) EPR spectrum in form of splittings of the spectral features. The interactions between unpaired electrons of V(IV) centers at 9 Å is insufficient for broadening beyond detection. The remaining possibility is that silanols are predominantly vicinal. On amorphous silica, vicinal grafted sites such as **E** should exhibit a range of through-space V-V distances, and this structural disorder would lead to destructive interference in (therefore, absence of) the EXAFS signal. In contrast, a distribution of V(IV)-V(IV) distances would manifest itself in broadened EPR lines. The analysis of the temperature dependence of the spin-spin coupling as manifested in the EPR linewidth can provide insight about spatial proximity of V(IV) sites. If V(IV) sites form a coupled network, i.e., multiple V(IV) sites are spatially proximal, a homogeneously broadened EPR line because of the dominance of spin-spin coupling is observed. Thus, a homogenous EPR line indicates clustered nature of the silanols. An inhomogeneously broadened lineshape, is dominated by contributions from static anisotropic interactions, making it difficult to assess whether the broadening is arising from V(IV) grafted onto silanols that are clustered.

2.2.3 Temperature dependence of the EPR spectrum

Spin-spin coupling between V(IV) sites can shorten the electron spin relaxation times and broaden the EPR line widths. Such EPR characteristics therefore are indicative of the

presence of proximal V(IV) centers.[38–40] When the EPR signals of coupled V(IV) sites are not visible at room temperature, their spectra may still be detected at lower temperatures where relaxation times should be increased, resulting in narrower linewidths.[41,42] To test this hypothesis, EPR spectra of VCl_4-modified SiO_2 were collected at temperatures between 293 to 4 K, Figure 2.5. The material remains "EPR-silent" at temperatures between 293 K and down to 100 K, but an observable EPR signal begins to emerge at 60 K and below (albeit with low signal-to-noise ratio). Decreasing the temperature further from 60 to 4 K resulted in higher overall signal intensity as expected due to a greater population of ground-state spin energy levels at low temperature (Figure 2.5b). As the temperature is lowered from 60 to 4 K, the estimated peak-to-peak EPR linewidth also decreased from 64 to 22 mT. This systematic and gradual narrowing of the EPR lines with the decreasing temperature further supports the hypothesis that the EPR line is homogeneously broadened due to spin-spin coupling between the V(IV) sites. In contrast, static anisotropic interactions should broaden EPR lines at low temperatures. To quantitatively characterize whether the EPR line is homogeneously or inhomogeneously broadened, the following Tsallian function Y shown in eq 2.2, was used. It describes the shape of the integrated EPR spectrum as a function of the q parameter (a measure of the Lorentzian/Gaussian characteristics of the EPR lineshape):[42]

$$Y = Y_{max}\left[1 + \left(2^{q-1}-1\right)\left(\frac{B-x_r}{\Gamma}\right)^2\right]^{\frac{-1}{q-1}} \qquad (2.2)$$

where B is the strength of the applied magnetic field, x_r is the central resonance position while Γ is the linewidth (full-width half maximum). A q parameter of 1 represents a Gaussian EPR lineshape indicating inhomogeneous line broadening. A q parameter of 2 represents a Lorentzian EPR lineshape that is characteristic of homogeneous line broadening dominated by spin-spin coupling.

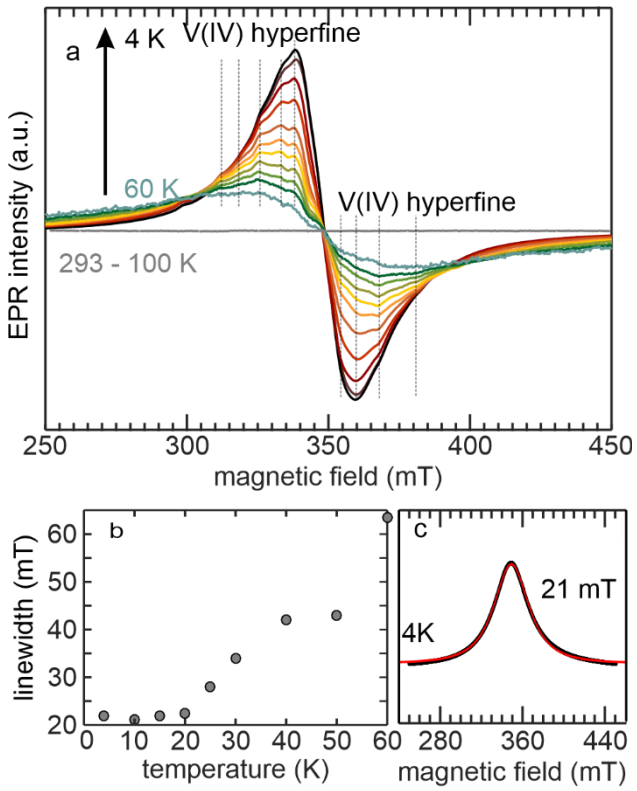

Figure 2.5 Low temperature X-band CW EPR spectra of VCl_4/SiO_2: (a) spectra recorded as the temperature was lowered from 60 to 4 K. All spectra were collected using the same parameters (time constant = 40.96 ms, receiver gain = 1 x 10^4, modulation frequency = 100 kHz, modulation amplitude = 4 G, attenuation = 20 dB) and normalized to the Q (quality) factor of the resonator (see Methods for details). Visible hyperfine features are marked by the dotted lines (b) Changes in the estimated peak-to-peak linewidth as a function of temperature. (c) Integrated EPR spectra acquired at 4 K (black) and its curvefit modelled using a Tsallian function (eq 2.2). The fitted q parameter is 1.7, and the linewidth from the curvefit is also indicated.

Incomplete detection of the EPR spectrum due to the broad linewidth can introduce error into the assessment of the EPR lineshape. Therefore, EPR spectra acquired at lower temperatures (< 20 K) with narrower linewidths (Figure 2.5b, Figure A2.4) are better suited for lineshape analysis. At these temperatures, the value of the q parameter is 1.7 ± 0.05, indicating a predominantly Lorentzian lineshape and therefore confirming that the EPR line is homogeneously broadened by strong spin-spin coupling between proximal V(IV) centers. The remaining Gaussian contribution is attributed to inhomogeneous broadening due to g-anisotropy and hyperfine interactions. This is supported by the observation that below 50 K, hyperfine features superimposed to the broad signal, originating from coupling of the electron spin to ^{51}V, become increasingly resolved. Thus spin-spin coupling between proximal V(IV) centers results in fast relaxation and broadening of the EPR signals that evade detection at room temperature. However, the signals may be regenerated at room temperature if the spin-spin coupling interactions are reduced.

2.2.4 Regeneration of signals at room temperature with a base

Lineshape analysis at low temperature showed that the EPR line is homogeneously broadened. To further establish that the EPR lineshape is dominated by spin-spin interaction due to V(IV) coupling, the coordination environment of the V(IV) center was changed and its lineshape evaluated. This strategy is effective when electron spin relaxation leads to line broadening, and was implemented by adding a coordinating base, CH_3CN to the VCl_4 grafted on SiO_2 which results in a signal at room temperature (Figure 2.6). This indicates that the electron spin relaxation is increased due to the addition of the base through a change in the coordination environment. The unresolved signal, similar to that observed at low

temperatures, was modelled using the Tsallian function in Eq 2.2 to obtain a Lorentzian lineshape having a q parameter of 1.6 (Figure A2.6). Its linewidth is narrow (32 mT) and thus detectable at room temperature.

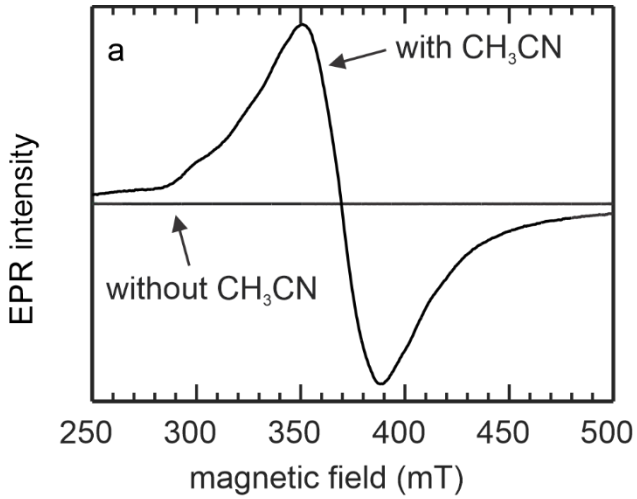

Figure 2.6 CW EPR spectra of VCl_4 on SiO_2 and its changes due to the addition of dry CH_3CN. The spectrum was collected at room temperature with the following parameters: time constant = 40.96 ms, receiver gain = 1 x 10^4, attenuation = 20 dB, modulation frequency = 100 kHz, modulation amplitude = 5.45 G).

When CH_3CN coordinates to the paramagnetic center, an increase in the ligand field splitting likely regenerates EPR signals, allowing the observation of the EPR signals at room temperature. Direct confirmation of the coordination of the CH_3CN to the V(IV) center was sought using pulsed EPR, specifically two-dimensional hyperfine sublevel correlation (HYSCORE) spectroscopy, a technique that provides correlations between nuclear frequencies of different spin manifolds that interact with the unpaired electron.[43,44] This technique relies on electron-nuclear interactions between directly interacting paramagnetic

centers and nearby nuclei (see SI, Figure A2.7) and shows that the CH_3CN is directly interacting with the V(IV) center. Thus, the EPR line, which was invisible at room temperature, reappears due to a change in the coordination environment of the V(IV) center, which reduces the electron-relaxation time, but still is homogeneously broadened. The results so far show that there are V(IV)-V(IV) interactions, suggesting the presence of a significant population of closely associated silanols. Next, the proximity of silanols on the surface of silica was directly investigated by solid-state ^{1}H MAS NMR.

2.2.5 Spatial proximity of surface silanols

The resolution of solid-state ^{1}H MAS NMR spectra can be lowered by strong dipolar broadening between proximal ^{1}H nuclear spins. To increase resolution, a 1D ^{1}H MAS spectrum of SiO_2, partially dehydroxylated at 500 °C, was acquired using fast MAS spinning (50 kHz) at a high magnetic field (18.8 T). Fast MAS and high magnetic fields enable the detection of ^{1}H NMR peaks which may have been obscured due to incompletely averaging of anisotropic interactions in previous studies that relied on slower MAS speeds in the range of 2 – 7 kHz.[20,45,46] The spectrum in Figure 2.7a shows a peak at 1.7 ppm assigned to protons of the non-H-bonded silanols, and a broad peak centered at 3.5 ppm assigned to hydrogen-bonded silanols.[20,45] The upfield peaks at 1.1 and 0.8 ppm were previously observed in silicas using high magnetic field (18.8 T) and 30 kHz,[47] and assigned to non-hydrogen-bonded silanols that are inaccessible to fluorination and deuteration at room temperature. Faster spinning speeds of 62.5 kHz have also revealed that these silanols are inaccessible to water at room temperature (unpublished work).

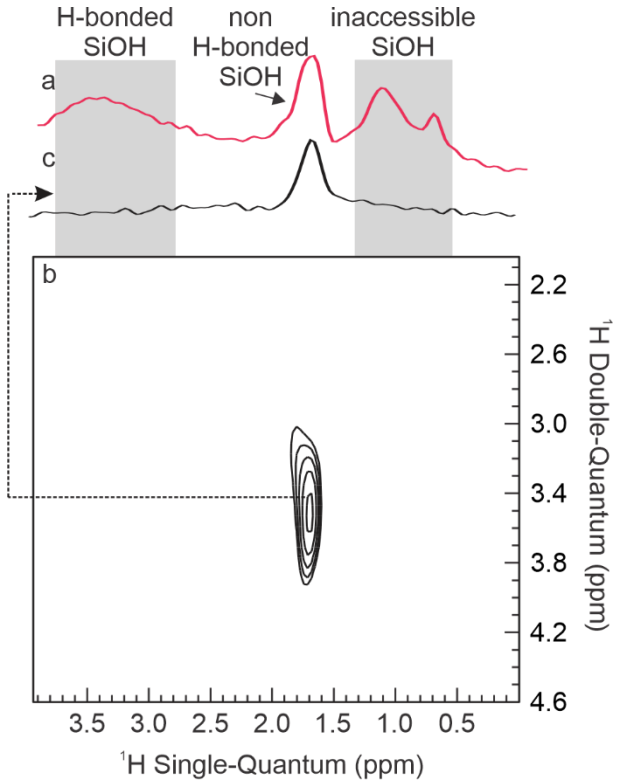

Figure 2.7 ^{1}H MAS NMR spectrum of SiO_2 pretreated at 500 °C: (a) 1D ^{1}H NMR spectrum, acquired using a DEPTH pulse sequence[48] to suppress background signals from the probe; (b) ^{1}H–^{1}H DQ-SQ spectrum, showing an autocorrelation peak assigned to silanol pairs; (c) 1D slice, extracted from the DQ-SQ spectrum, corresponding to the peak at 3.4 ppm in the indirect (DQ) dimension. All data were acquired at 18.8 T, using 50 kHz MAS spinning frequency.

The spatial proximity of silanols in non-porous SiO_2 pretreated at 500 °C was investigated using ^{1}H-^{1}H Double Quantum-Single Quantum (DQ-SQ) MAS NMR spectroscopy. This technique uses dipolar interactions to reveal proximity between nuclei which have similar or even identical chemical shifts. Signals from pairs of nuclei with similar chemical shifts δ appear on the diagonal at (δ, 2δ), where δ and 2δ correspond to the SQ (direct) and DQ (indirect) dimensions. The SQ frequencies are filtered and only the DQ

frequencies, resulting from sites that are nearby one another interacting through dipolar-coupling, are observed in the 2D spectrum. The ^{1}H-^{1}H DQ-SQ MAS NMR spectrum of SiO_2 is shown in Figure 2.7b. The peak at (1.7, 3.4) ppm is a DQ resonance which demonstrates that non-H-bonded, accessible silanols are present at ^{1}H-^{1}H distances of 5 Å or less which are associated with one another.[49] Interestingly, the inaccessible silanols are not nearby one another.

To approximately quantify the fraction of non-hydrogen bonded silanols in pairs, a 1D ^{1}H slice (Figure 2.7c) was extracted from the peak in the 2D ^{1}H-^{1}H DQ-SQ spectrum (Figure 2.7b), which is representative of the non-hydrogen bonded silanols in proximity with one another. Its peak area was compared with that of the 1D ^{1}H NMR spectrum, obtained via direct detection (Figure 2.7a). Comparison of the two peak areas shows that 30 % of the non-hydrogen bonded silanols in the 1D ^{1}H NMR spectrum appear in the slice from the 2D NMR spectrum, which is the fraction of silanols that exist in pairs. Since the efficiency of the pulse sequence used for acquiring the DQ-SQ spectrum is typically only 50 %,[49] at least 60 % of the non-hydrogen bonded silanols thus exist in pairs.

This semi-quantitative assessment of the silanol distribution on the surface of SiO_2 by ^{1}H DQ-SQ NMR demonstrates that a large fraction of non-H-bonded silanols exist in pairs at distances $\leq$ 5 Å. This finding agrees with a previous study of the reaction of $Ga(CH_3)_3$ with SiO_2 thermally treated at 500 °C, which concluded that two-thirds of the resulting grafted $[Ga(CH_3)_2(\mu\text{-}OSi\equiv)]_2$ sites are formed predominantly by reaction of $Ga(CH_3)_3$ with vicinal surface silanols.[24] Mesoporous MCM-41 silica, pretreated at 350 °C (and therefore with a much higher overall silanol density than the non-porous silica in this study) showed separate DQ contributions from hydrogen-bonded OH groups *and* pairs of non-H-bonded SiOH,

however quantification was not attempted.[50] In a recent ^{1}H DQ-SQ MAS NMR study of a non-porous amorphous SiO_2, partially dehydroxylated at 550 °C, a much weaker DQ coherence was observed relative to that of a zeotype-silicate prepared by the delamination of a borosilicate precursor followed by B^{3+} removal to form silanol defects. Based on these measurements, these authors concluded that the silanols in non-porous amorphous silica are randomly distributed on the silica surface.[51] While the silanol of such a surface may be less proximal than in crystalline delaminated zeotype-silicate, the latter is known to have a higher silanol density due to the removal of B^{3+}. Thus, the origin of V(IV) spin-spin coupling arises from surface silanols that are nearby one another. However, these measurements do not show presence of clusters of silanols (i.e. greater than pairs). To investigate the presence of clusters of silanols, strong spin-spin coupling was reduced by decreasing the V(IV) loading and their EPR spectra were recorded.

2.2.6 Dilution of the V(IV) sites to assess silanol cluster sizes

The silica modified with an excess amount of VCl_4 shows a homogeneously broadened lineshape, arising from spin-spin coupled V(IV) centers grafted onto closely associated silanols. To explore the effect of spin-spin coupling of V(IV) on the EPR signal, and determine the silanol cluster sizes, the silica sample was exposed to a reduced and known, as opposed to excess, amounts of VCl_4 vapor (see Methods). One of the resulting modified silicas has a V content of 0.2 wt% (0.04 mmol/g), corresponding to a V/≡SiOH ratio of 0.06. Its room temperature EPR spectrum shows a resolved eight-line hyperfine signal typical of coupling to isolated V(IV) sites (Figure A2.5). Again, and as expected, the signal intensity further increased when the sample was cooled to 100 K (Figure 2.8a). Lowering the temperature also

revealed a broad signal superposed on the resolved eight-line EPR signal that was broadened beyond detection at room temperature. The observation of a broad signal that appears at 100 K suggests that a significant fraction of the V(IV) sites remain clustered.

The EPR spectrum of this sample was deconvoluted into its two broad and narrow components (Figure 2.8). The narrow component, which represents approx. 55 % of the EPR signal at 100 K, was simulated using a spin Hamiltonian corresponding to a single $3d^1$ electron, and is shown in Figure 2.8, in a dark red shade. Isolated ≡SiOVCl_3 sites are expected to have C_{3v} (i.e., axial) symmetry. Simulation of this narrow EPR line was achieved with an axially symmetric g-tensor, yielding $g_{\|} = g_{zz}$ =1.945 and $g_{\perp} = g_{xx} = g_{yy}$ = 1.925, as well as an axially symmetric hyperfine (A) tensor, yielding $A_{\|} = A_{zz}$ = 90 MHz and $A_{\perp} = A_{xx} = A_{yy.}$ = 410 MHz. These values are larger than those reported for neat VCl_4 ($g_{\|}$ = 1.920, $g_{\perp}$ = 1.899, $A_{\|}$ = 72, and $A_{\perp}$ = 120 MHz), which also has axial symmetry due to Jahn-Teller distortion.[27] The larger g and A values are due to the substitution of the -Cl ligand with the -OSi≡. An increase in the g and A parameters was observed for $V(NeMe_2)_4$ when it was grafted onto SiO_2, Al_2O_3 and TiO_2 through protonolysis reactions.[52] The remaining 45 % of the signal detected is broad thus showing that V(IV) remains clustered even at this low V loading.

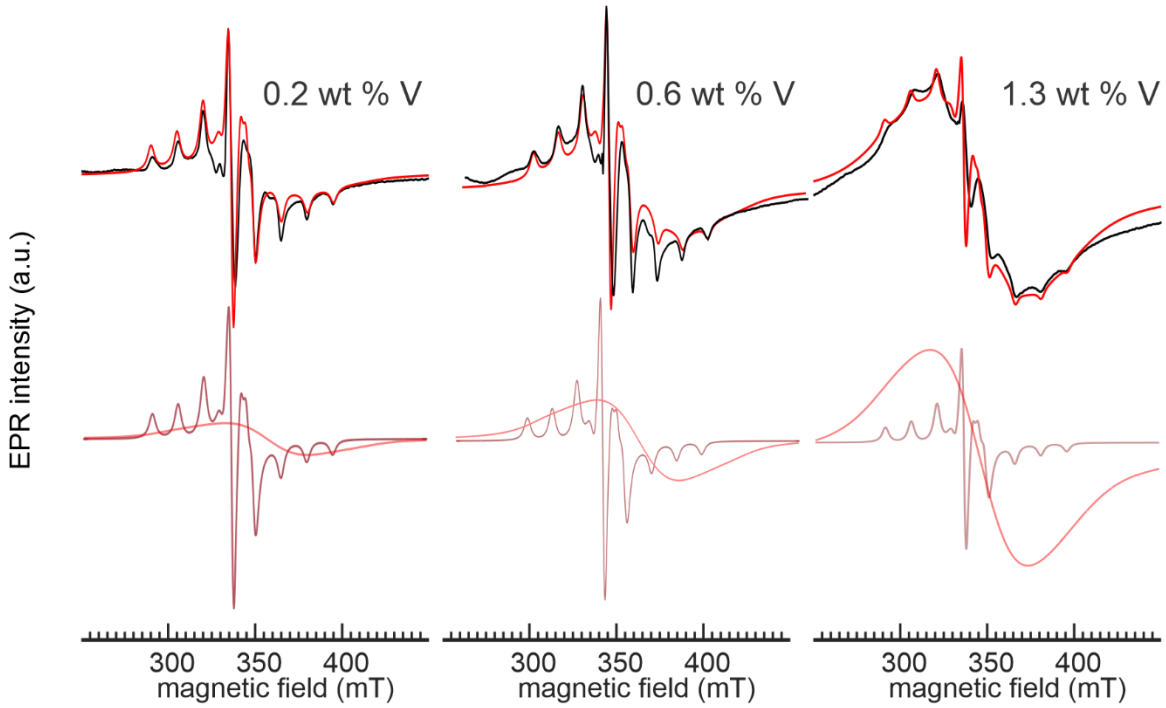

Figure 2.8 CW EPR spectra of VCl_4-modified SiO_2 with increasing V loading, corresponding to reaction of 8, 15 and 34 % of the silanols. All spectra were recorded at 100 K using the same parameters (time constant = 40.96 ms, receiver gain = 1 x 10^4, modulation frequency = 100 kHz, modulation amplitude = 5.45 G, attenuation = 15 dB). Experimental spectra are shown in black, and their simulations in red. The deconvoluted components of the spectra are also shown in different shades of red.

Considering the scenario in which *all* silanols exist in pairs, the EPR spectrum would not show any narrow component. However, the appearance of the narrow component indicates the presence of V(IV) centers that do not experience spin-spin coupling. This suggests that approximately half of the VCl_4 preferentially reacts with silanols that are nearby one another even though there are unreacted silanols remaining on the silica surface. The remaining half do not experience spin-spin coupling. If there are indeed clusters containing *m* silanols, and if

the VCl_4 reacts randomly with them, we investigated whether changing the V(IV) loading on silica and the corresponding contributions from the broad and narrow components could be used to obtain information on the sizes of the silanol clusters.

Other samples were prepared at a range of low to moderate V(IV) loadings corresponding to V:≡SiOH of 0.16, 0.35, and 0.54 (Figure 2.8, Table 2.2). The values of V content in wt % and mmol/g are also provided in Table 2.2. Their EPR spectra were acquired at 100 K and simulated using an isolated and broad component as done for the silica with V:≡SiOH of 0.06. The EPR parameters of the isolated component were constrained and only the relative contributions from each component were varied. Increasing the V(IV) loading results in an increased contribution of the broad component. At 15 % V(IV) loading of the original silanol content, the broad signal comprises 80 % of the EPR spectrum, and increases to 95 and 98 % as the V(IV) content is increased, indicating that spin-spin coupling interactions become stronger.

Table 2.2 Approximate silanol coverage of the V sites on silica and the corresponding contributions of the narrow and the broad components.

approx. silanol reacted (%)	V (wt %)	V (mmol/g)	V:≡SiOH	broad component contribution (%) [a]
5	0.2	0.04	0.06	55
15	0.6	0.12	0.16	88
35	1.3	0.26	0.35	95
50	2.1	0.41	0.54	98
100	4.2	0.82	1.1	N/A

[a] The ratio of the narrow and broad components were obtained from the EPR spectra shown in Figure 2.8.

The distribution of silanols in clusters of different sizes and their reaction with VCl_4 was modeled using the contribution from the broad and narrow components in Table 2.2, to estimate the population of silanol clusters of different sizes. f_m is defined as the fraction of silanols in clusters of size *m*. For example, if 10% of the total silanols occur in clusters of size 5, then f_5=0.1. It was further assumed that silanols react randomly with VCl_4. Hence, if a limiting amount of VCl_4 is used and *x* out of *n* total silanols react to give [≡$SiOVCl_3$], then a silanol chosen at random will have a probability of *p*=*x*/*n* of reacting. Alternatively, 1-*p* will be the probability of it not reacting. Accordingly, the number of clusters of size *m* with exactly *o* (*o*<*m*) V atoms using the binomial distribution was calculated as

$$N_{m,o}=\frac{nf_m}{m}\binom{m}{o}p^o(1-p)^{m-o} \qquad (2.3)$$

Here, $\binom{m}{o}$ accounts for the different ways of choosing *o* reacted silanols out of a total of *m* silanols in the cluster and $p^o(1-p)^{m-o}$ accounts for the probability that exactly *o* silanols react.

A statistical model to calculate the fraction of EPR active V atoms as a function of V loading. Two V atoms are EPR silent if they are separated by a distance less than 5 Å. For our model we define this distance as *l*. To calculate the fraction of EPR active V atoms, the fraction of V atoms with no other V atom closer than *l* was calculated. It was assumed that all clusters with two or more V atoms are EPR silent. This assumption may not be valid for large clusters, where the distance between two V atoms can be more than *l*. With this assumption, only

clusters with one V atom can be potentially EPR active. The total population of single V clusters can be calculated using eq. 2.3 as

$$N_{m,1}=\frac{nf_i}{i}p(1-p)^{i-1}. \qquad (2.4)$$

Furthermore, only those single V clusters will be EPR active which have no other V atoms closer than *l*. Such clusters are defined as isolated V atoms from now on. A few more simplifying assumptions to obtain an analytical expression for the fraction of isolated V atoms were made. First, it was assumed that all silanol clusters are point particles, randomly distributed on a 2D plane. Furthermore, clusters were classified into different categories characterized by the cluster size (*m*) and the number of reacted silanols (*o*). Henceforth, we refer to these categories using a tuple as (*m*, *o*).

With these assumptions, Poisson statistics can be used to calculate the fraction of isolated V atoms. For randomly distributed points on a 2D plane, the probability of finding *q* points inside a circle of radius *l* centered on a randomly chosen point is given by the Poisson distribution as

$$P(q)=\exp(-\lambda)\left(\frac{\lambda^q}{q!}\right) \qquad (2.5)$$

Here, $\lambda=\pi l^2\sigma$, and σ is the number density of points per unit area. The probability that there are no points within a distance *l* is given by

$$P(0)=\exp\left(-\pi l^2\sigma\right) \qquad (2.6)$$

P(0) for each (*m*, *o*) can be calculated using eq 2.6. For this, the number density (number per unit area) of each (*m*,*o*) is required. The surface density of clusters of size *m* with exactly *o* reacted silanols can be expressed in terms of the total silanol density as

$$\sigma_{m,o}=\frac{f_m}{m}\binom{m}{o}p^o(1-p)^{m-o}\sigma_s \qquad (2.7)$$

Here, $\sigma_{m,o}$ is the density of clusters of size m with exactly o reacted silanols and σ_s is the total surface density of silanols (number of silanols per unit area). Accordingly, the probability that there are no clusters with one or more V atoms at a distance less than l from a randomly chosen point is given by

$$\mathbf{P}(0,l) = \prod_{j=1}^{N} \prod_{i=1}^{j} \exp\left[-\pi l^2 \sigma_{j,i}\right] \qquad (2.8)$$

The outer product iterates over clusters of size 1 to N and the inner product iterates over number of reacted silanols for a given cluster size. Finally, we can calculate the fraction of EPR active V atoms by summing over isolated V atoms that have no V atoms closer than l as follows:

$$\text{fraction of EPR active V} = \left[\sum_{i=1}^{N} \frac{f_i}{i} p(1-p)^{i-1}\right] \mathbf{P}(0,l) \qquad (2.9)$$

Here, the first term is the total number of clusters with only one V atom (eq. 4) and the second term is the probability that no V atoms are closer than l from these clusters (eq. 8). When eq. 9 is fit to the experimental data in Table 2, the population of different silanol clusters (f_i) is obtained. The fits are shown in Figure 2.9.

The blue line shows a scenario where all silanols occur in cluster sizes of 1. This curve has no fitting parameters. Clearly, this scenario cannot explain the data point with maximum Vanadium loading (case where all silanols react). It predicts that ca. 33% V are EPR active at maximum loading. But experimental measurements estimate that all V are EPR silent at maximum loading. Hence, we can rule out the scenario where all silanols occur in cluster sizes of 1.

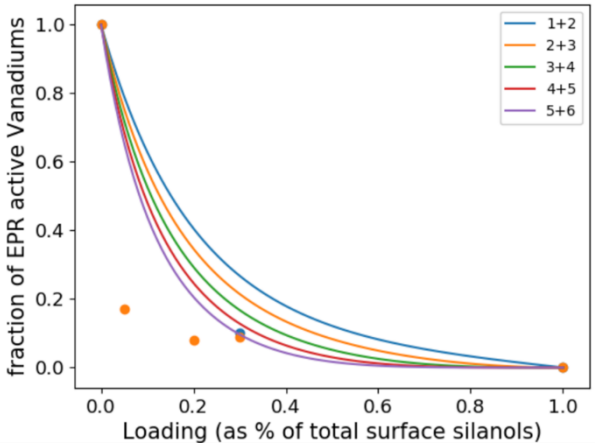

Figure 2.9 The statistical model with different cluster sizes fit to experimental data from Table 2.2.

Since there are only 5 data points, it is not possible to fit more than 5 parameters. Therefore, models with just two cluster sizes were fit at a time. For example, the 1+2 curve indicates a scenario where silanols only occur in cluster sizes of 1 and 2. The plot also shows fits with cluster sizes of 2 and 3, 3 and 4, 4 and 5, and 5 and 6. The populations of different cluster sizes cannot be conclusively determined because of the uncertainty in the experimental measurements and the small number of data points. Nevertheless, large cluster sizes are required to explain the experimental measurements. The fits indicate that the surface of silica has silanols clustered in patches of at least more than 7 silanols.

2.3 Conclusions

Dehydroxylation of non-porous Aerosil silica at 500 ^{o}C results in surface hydroxyl groups that are closely associated with one another. When VCl_4 is reacted with these hydroxyls, spatially coupled $\equiv SiOVCl_3$ sites are formed. These spatial interactions lead to an increased rate of relaxation of the electrons, which can be decreased by reducing the

temperature and confirming that the lineshape is predominantly Lorentzian. Dilution of the paramagnetic center also regenerates the signals, however, it shows that even at low loadings of V (0.2 wt % V), approximately 50 % of the EPR spectrum arises from a broad component, indicating clustered V(IV) sites. Increasing the loading further increases the contribution from the clustered V(IV) sites. Using Poisson statistics, it was determined that the surface of silica has silanols clustered in patches of at least more than 7 silanols.

Consequently, the hydroxyl groups on this silica cannot be described as well-isolated under these treatment conditions. The spatial proximity of the surface silanols was also confirmed by ^{1}H-^{1}H DQ-SQ correlations. The absence of the EPR signals is observed for silica treated at 700 °C, as well as other mesoporous silicas such as Sylopol and SBA-15. These findings bring into attention that widely-accepted site isolation strategies used for silica simply may not suffice to generate species that are unperturbed by one another. Furthermore, they also underscore the complexity of the surface of silica.

2.4 Experimental

2.4.1 Sample Preparation

Aerosil-380, a nonporous, fumed silica, was obtained from Evonik. Sylopol 952, a nonordered mesoporous silica gel, was obtained from Grace-Davison. γ-Al_2O_3 was obtained from Strem. The silicas were thermally treated at 500 °C or 700 °C for at least 12 h under dynamic vacuum (<10^{-4} Torr) to give partially dehydroxylated SiO_2. The Al_2O_3 was calcined in air at 500 °C for 4 h, followed by evacuation (<10^{-4} Torr) at 500 °C for 12 h. VCl_4 (Acros Organics, 99.9 %+), $VOCl_3$ (Sigma-Aldrich, 99.9 %), CH_3CN (Acros Organics, 99.9 %, Extra Dry over Molecular Sieves, AcroSeal™) were stored under vacuum in glass reactors sealed

with high-vacuum Teflon stopcocks (Chemglass). All reagents were degassed by three freeze−pump−thaw cycles prior to use. Silica-supported VCl_4 and $VOCl_3$ were prepared by condensing an excess of the appropriate volatile metal complex as vapor via a high-vacuum manifold into a Pyrex reactor containing the partially dehydroxylated silica, immersed in a liquid N_2 bath. After warming to room temperature, the reaction was allowed to proceed for 30 min. Where indicated, smaller amounts of VCl_4 were transferred by measuring the change in the length of reactors attached with capillaries (2 mm OD). Volatiles were desorbed at room temperature for 1 h by condensing into a liquid N_2 trap. The silica-supported vanadium complexes were transferred to glass ampules in a N_2-filled glovebox and sealed for storage under an inert atmosphere. The ampules were broken and small amounts were removed for further characterization.

2.4.2 Infrared Spectroscopy

IR experiments were performed in a Pyrex in situ IR cell equipped with a quartz bottom and sealed with a high-vacuum ground-glass stopcock greased with Krytox (Varian). Polished KCl windows (32 × 2 mm, International Crystal Laboratories) were affixed to the cell with TorrSeal (Varian). Approximately 30 mg silica was pressed into a self-supporting disk of diameter 1.6 cm and mounted in a quartz sample holder. The silica was heated at 500 °C and $<10^{-4}$ Torr for at least 12 h. VCl_4 vapor was transferred onto the silica disk from a liquid reservoir, using a liquid N_2 bath. The reactor was allowed to warm to room temperature over a period of 30 min. Transmission IR spectra were recorded on a Shimadzu Prestige IR spectrometer equipped with a DTGS detector and purged with CO_2-free dry air. Background and sample spectra were recorded by adding 36 scans at 4 cm^{-1} resolution.

2.4.3 Vanadium Analysis

Vanadium was extracted from the silica or alumina at the end of each experiment. Each sample was weighed in air and stirred in 1.0 M H_2SO_4 to which 3.5% aqueous H_2O_2 (0.03 mL/mL sample solution). The solution was filtered before recording its UV-vis spectrum in a 1-cm square quartz cuvette, using a H_2SO_4/ H_2O_2 solution containing the same concentration of H_2O_2 as the reference. The orange peroxovanadium complex has a well-resolved peak at λ_{max} = 453 nm. A calibration curve was prepared using standard solutions of ammonium metavanadate.

2.4.4 Solid-state NMR Spectroscopy

Silica-supported vanadium materials were packed and sealed in 3.2-mm zirconia rotors inside a N_2-filled glovebox. The rotors were then sealed in glass ampules and transferred to the spectrometer. MAS (magic-angle spinning) NMR spectra were recorded on a Bruker AVANCE III Ultrashield Plus 800 MHz (18.8 T) spectrometer. The ^{51}V NMR spectra (frequency 210.458 MHz) were collected using a solid-echo pulse sequence with a $\pi/2$ pulse (90.91 kHz) of duration 2.75 μs, and an inter-pulse delay corresponding to one rotor period. The relaxation delay was 0.25 s. The samples were spun at 19 kHz using liquid N_2 boiloff. The spinning rate was varied to identify spinning side bands. The amount of NMR-active V was quantified by comparing the absolute integral of the NMR signal with that of the standard, neat liquid $VOCl_3$. The direct ^1H NMR spectrum (frequency 800.130) was collected using a $\pi/2$ pulse (125 kHz) of duration 2 μs, with a relaxation delay of 3 s and a DEPTH pulse sequence using a $\pi/2$ pulse (125 kHz) of duration 2 μs, followed by two π pulses (62.5 kHz)

of duration 4 μs with a relaxation delay of 3 s. The sample was spun at 50 kHz using N_2 boiloff.

2.4.5 Electron Paramagnetic Resonance Spectroscopy

Continuous wave (CW) EPR spectra were recorded on a Bruker EMXplus Spectrometer, operating at microwave frequencies of 9.0-9.8 GHz and equipped with a liquid Helium cryostat (Oxford Inc.) Spectra were recorded at 1 mW microwave power, 100 kHz modulation frequency, and 0.5-0.7 mT modulation amplitude. Spectra were simulated using the Easyspin package in MATLAB.[50]

Pulsed EPR experiments were conducted on a Bruker E580 FT/CW spectrometer at 10 K. Hyperfine Sublevel Correlation (HYSCORE) experiments were carried out using the pulse sequence $\pi/2 - \tau - \pi/2 - t_1 - \pi - t_2 - \pi/2 - \tau -$ echo, with microwave pulse lengths $tp_{\pi/2}$ = 16 ns and tp_{π} = 32 ns. The time intervals t_1 and t_2 were varied in steps of 20 ns, with a sequence repetition delay rate of 1 kHz. An eight-step phase cycle was used to eliminate unwanted echoes. The time traces of the HYSCORE spectra were baseline-corrected with a third-order polynomial, apodized with a Hamming window, zero-filled, and Fourier transformed. HYSCORE spectra were also simulated using the Easyspin package in MATLAB.

2.4.6 X-Ray Absorption Spectroscopy

Spectra were recorded at the V K-edge (5,465 eV) on beamline 4-3 of the Stanford Synchrotron Radiation Lightsource (SSRL), which operates at 3.0 GeV with a ring current of 500 mA. Data were acquired in fluorescence mode, using a PIPS detector. For energy calibration, a vanadium foil was placed after the second ionization chamber following the

incident beam direction. The energy of the first maximum in the first derivative of its XANES was defined to be 5,465 eV.

XAS data were processed and analyzed using the Demeter software package.[51] A linear function was subtracted from the pre-edge region, then the edge jump was normalized using Athena software. The $\chi(k)$ data were isolated by subtracting a smooth, third-order polynomial approximating the absorption background of an isolated atom. The k^3-weighted $\chi(k)$ data were Fourier-transformed after applying a Hanning window function. The amplitude reduction factor (S_0^2), coordination numbers (N_i), distances to the scattering atoms (R_i), and mean-squared displacements (σ_i^2) were obtained by nonlinear fitting, with least-squares refinement, of the EXAFS equation to the Fourier-transformed data in *R*-space, using Artemis software. EXAFS spectra of individual paths were simulated using FEFF6, using imported crystallographic information files of model compounds.

Acknowledgement of contribution: I thank Dr Li Li for collecting and analyzing the EXAFS data, Professor Baron Peters and Dr Salman A. Khan for the DFT and cluster size calculations, and Professor Wanling Shen for helping me set up the ^{1}H MAS DQ-SQ NMR.

2.5 References

(1) Hlatky, G. G. Heterogeneous Single-Site Catalysts for Olefin Polymerization. *Chem. Rev.* **2000**, *100* (4), 1347–1376. https://doi.org/10.1021/cr9902401.

(2) Iler, R. K. *The Chemistry of Silica: Solubility, Polymerization, Colloid and Surface Properties and Biochemistry of Silica*; Wiley: New York, 1979.

(3) Green, M. L.; Gusev, E. P.; Degraeve, R.; Garfunkel, E. L. Ultrathin (<4 Nm) SiO2 and

Si–O–N Gate Dielectric Layers for Silicon Microelectronics: Understanding the Processing, Structure, and Physical and Electrical Limits. *J. Appl. Phys.* **2001**, *90* (5), 2057. https://doi.org/10.1063/1.1385803.

(4) Qiu, H.; Liang, X.; Sun, M.; Jiang, S. Development of Silica-Based Stationary Phases for High-Performance Liquid Chromatography. *Anal. Bioanal. Chem. 2011 39910* **2011**, *399* (10), 3307–3322. https://doi.org/10.1007/S00216-010-4611-X.

(5) Yagüe, C.; Moros, M.; Grazú, V.; Arruebo, M.; Santamaría, J. Synthesis and Stealthing Study of Bare and PEGylated Silica Micro- and Nanoparticles as Potential Drug-Delivery Vectors. *Chem. Eng. J.* **2008**, *137* (1), 45–53. https://doi.org/10.1016/j.cej.2007.07.088.

(6) Yang, H.; Zhu, Y. Size Dependence of SiO2 Particles Enhanced Glucose Biosensor. *Talanta* **2006**, *68* (3), 569–574. https://doi.org/10.1016/j.talanta.2005.04.057.

(7) Zhuravlev, L. T. Characterization of Amorphous Silica Surface. *React. Kinet. Catal. Lett.* **1993**, *50* (2), 15–25. https://doi.org/10.1007/BF02062184.

(8) Fernando Rascón; Raphael Wischert; Christophe Copéret. Molecular Nature of Support Effects in Single-Site Heterogeneous Catalysts : Silica vs. Alumina. *Chem. Sci.* **2011**, *2* (8), 1449–1456. https://doi.org/10.1039/c1sc00073j.

(9) Copéret, C.; Comas-Vives, A.; Conley, M. P.; Estes, D. P.; Fedorov, A.; Mougel, V.; Nagae, H.; Núñez-Zarur, F.; Zhizhko, P. A. Surface Organometallic and Coordination Chemistry toward Single-Site Heterogeneous Catalysts: Strategies, Methods, Structures, and Activities. *Chem. Rev.* **2016**, *116* (2), 323–421. https://doi.org/10.1021/acs.chemrev.5b00373.

(10) Pelletier, J. D. A.; Basset, J.-M. Catalysis by Design: Well-Defined Single-Site

Heterogeneous Catalysts. *Acc. Chem. Res.* **2016**, *49* (4), 664–677. https://doi.org/10.1021/acs.accounts.5b00518.

(11) Basset, J. M.; Lefebvre, F.; Santini, C. Surface Organometallic Chemistry: Some Fundamental Features Including the Coordination Effects of the Support. *Coord. Chem. Rev.* **1998**, *178–180*, 1703–1723. https://doi.org/10.1016/S0010-8545(98)00159-3.

(12) Sheldon, R. A. Catalysis: The Key to Waste Minimization. *J. Chem. Tech. Biotechnol* **1997**, *68*, 381–388. https://doi.org/10.1002/(SICI)1097-4660(199704)68:4.

(13) Sheldon, R. A. Selective Catalytic Synthesis of Fine Chemicals: Opportunities and Trends. *J. Mol. Catal. A Chem.* **1996**, *107* (1–3), 75–83. https://doi.org/10.1016/1381-1169(95)00229-4.

(14) Bahri-Laleh, N.; Hanifpour, A.; Mirmohammadi, S. A.; Poater, A.; Nekoomanesh-Haghighi, M.; Talarico, G.; Cavallo, L. Computational Modeling of Heterogeneous Ziegler-Natta Catalysts for Olefins Polymerization. *Prog. Polym. Sci.* **2018**, *84*, 89–114. https://doi.org/10.1016/j.progpolymsci.2018.06.005.

(15) Zhuravlev, L. T. Concentration of Hydroxyl Groups on the Surface of Amorphous Silicas. *Langmuir* **1987**, *3*, 316–318. https://doi.org/10.1021/la00075a004.

(16) Zhuravlev, L. T. The Surface Chemistry of Amorphous Silica. Zhuravlev Model. *Colloids Surfaces A Physicochem. Eng. Asp.* **2000**, *173*, 1–38. https://doi.org/10.1016/S0927-7757(00)00556-2.

(17) Roosmalen, A. J. Van; Mol, J. C. An Infrared Study of the Silica Gel Surface. 2. Hydration and Dehydration. *J. Phys. Chem.* **2002**, *83* (19), 2485–2488. https://doi.org/10.1021/j100482a013.

(18) Morrow, B. A.; McFarlan, A. J. Infrared and Gravimetric Study of an Aerosil and a

Precipitated Silica Using Chemical and Hydrogen/Deuterium Exchange Probes. *Langmuir* **2002**, *7* (8), 1695–1701. https://doi.org/10.1021/la00056a022.

(19) Zhdanov, S. P.; Kosheleva, L. S.; Titova, T. I. IR Study of Hydroxylated Silica. *Langmuir* **2002**, *3* (6), 960–967. https://doi.org/10.1021//la00078a014.

(20) Bronnimann, C. E.; Zeigler, R. C.; Maciel, G. E. Proton NMR Study of Dehydration of the Silica Gel Surface. *J. Am. Chem. Soc.* **1988**, *110* (7), 2023–2026. https://doi.org/10.1021/ja00215a001.

(21) Liu, C. C.; Maciel, G. E. The Fumed Silica Surface: A Study by NMR. *J. Am. Chem. Soc.* **1996**, *118* (21), 5103–5119. https://doi.org/10.1021/ja954120w.

(22) Peri, J. B.; Hensley, A. L. The Surface Structure of Silica Gel. *J. Phys. Chem.* **1968**, *72* (8), 2926–2933. https://doi.org/10.1021/j100854a041.

(23) Taha, Z. A.; Deguns, E. W.; Swarup Chattopadhyay, A.; Susannah L. Scott. Formation of Digallium Sites in the Reaction of Trimethylgallium with Silica. *Organometallics* **2006**, *25* (8), 1891–1899. https://doi.org/10.1021/om051034o.

(24) Fleischman, S. D.; Scott, S. L. Evidence for the Pairwise Disposition of Grafting Sites on Highly Dehydroxylated Silicas via Their Reactions with Ga(CH3)3. *J. Am. Chem. Soc.* **2011**, *133* (13), 4847–4855. https://doi.org/10.1021/ja108905p.

(25) Schrader, A. M.; Monroe, J. I.; Sheil, R.; Dobbs, H. A.; Keller, T. J.; Li, Y.; Jain, S.; Shell, M. S.; Israelachvili, J. N.; Han, S. Surface Chemical Heterogeneity Modulates Silica Surface Hydration. *Proc. Natl. Acad. Sci.* **2018**, *115* (12), 2890–2895. https://doi.org/10.1073/pnas.1722263115.

(26) Chien, J. C. W. Study of Surface Structures of Submicron Metal Oxides by Vanadium Tetrachloride as a Paramagnetic Probe. *J. Am. Chem. Soc.* **2002**, *93* (19), 4675–4684.

https://doi.org/10.1021/ja00748a005.

(27) Johannesen, R. B.; Candela, G. A.; Tsang, T. Jahn–Teller Distortion: Magnetic Studies of Vanadium Tetrachloride. *J. Chem. Phys.* **2003**, *48* (12), 5544. https://doi.org/10.1063/1.1668254.

(28) Chien, J. C. W.; Boss, C. R. Electron Spin Resonance of Vanadium and Titanium Compounds Electron Spin Resonance of Some Vanadium and Titanium Compounds. **1961**, *20*.

(29) Rice, G. L.; Scott, S. L. Characterization of Silica-Supported Vanadium(V) Complexes Derived from Molecular Precursors and Their Ligand Exchange Reactions. *Langmuir* **1997**, *13* (6), 1545–1551. https://doi.org/10.1021/la960679d.

(30) Ooms, K.; Polenova, T.; Shough, A.-M.; Doren, D. J.; Nash, M. J.; Lobo, R. F. Identification of Mixed Valence Vanadium in ETS-10 Using Electron Paramagnetic Resonance, 51 V Solid-State Nuclear Magnetic Resonance, and Density Functional Theory Studies. https://doi.org/10.1021/jp902275f.

(31) Gajan, D.; Copéret, C. Silica-Supported Single-Site Catalysts: To Be or Not to Be? A Conjecture on Silica Surfaces. *New J. Chem.* **2011**, *35* (11), 2403–2408. https://doi.org/10.1039/c1nj20506d.

(32) Gallas, J.-P.; Goupil, J.-M.; Vimont, A.; Lavalley, J.-C.; Gil, B.; Gilson, J.-P.; Miserque, O. Quantification of Water and Silanol Species on Various Silicas by Coupling IR Spectroscopy and In-Situ Thermogravimetry. *Langmuir* **2009**, *25* (10), 5825–5834. https://doi.org/10.1021/la802688w.

(33) Morrow, B. A. Chapter 3 Surface Groups on Oxides. *Stud. Surf. Sci. Catal.* **1990**, *57* (PA), A161–A224. https://doi.org/10.1016/S0167-2991(08)63996-8.

(34) Deguns, E. W.; Taha, Z.; Meitzner, G. D.; Scott, S. L. An X-Ray Absorption Study of Two VOCl3-Modified Silicas: Evidence for Chloride−Silica Interactions. *J. Phys. Chem. B* **2005**, *109* (11), 5005–5011. https://doi.org/10.1021/jp045886y.

(35) Huang, M.; Dekock, C. W. Triphenylsiloxy Complexes. A Novel Compound Containing a Mo(VI)-P Bond: MoOzCOSiPhsMPPha). *Inorg. Chem* **1993**, *32*, 2287–2291.

(36) Chuang, I.-S.; Kinney, D. R.; Maciel, G. E. Interior Hydroxyls of the Silica Gel System as Studied by 29Si CP-MAS NMR Spectroscopy. *J. Am. Chem. Soc* **1993**, *115*, 8695–8705. https://doi.org/10.1021/ja00072a024.

(37) Luhmer, M.; D'Espinose, J. B.; Hommel, H.; Legrand, A. P. High-Resolution 29Si Solid-State NMR Study of Silicon Functionality Distribution on the Surface of Silicas. *Magn. Reson. Imaging* **1996**, *14* (7–8), 911–913. https://doi.org/10.1016/S0730-725X(96)00180-4.

(38) Augustyniak-Jablokow, M. A.; Borshch, S. A.; Daniel, C.; Hartl, H.; Yablokov, Y. V. EPR Study of the Magnetic States of a Mixed-Valence VIV4VV2 Alkoxypolyoxovanadium Cluster. *New J. Chem.* **2005**, *29* (8), 1064–1071. https://doi.org/10.1039/b412427h.

(39) Magon, C. J.; Lima, J. F.; Donoso, J. P.; Lavayen, V.; Benavente, E.; Navas, D.; Gonzalez, G. Deconvolution of the EPR Spectra of Vanadium Oxide Nanotubes. *J. Magn. Reson.* **2012**, *222*, 26–33. https://doi.org/10.1016/j.jmr.2012.06.004.

(40) Takahashi, H.; Shiotani, M.; Kobayashi, H.; Sohma, J. ESR Study of V2O5 Catalyst on Carriers. *J. Catal.* **1969**, *14* (2), 134–141. https://doi.org/10.1016/0021-9517(69)90418-7.

(41) Doorslaer, S. Van; Murphy, D. M. EPR Spectroscopy in Catalysis. *Top. Curr. Chem.* **2011**, *321*, 1–39. https://doi.org/10.1007/128_2011_237.

(42) Weil, J. A.; Bolton, J. R. *Electron Paramagnetic Resonance: Elementary Theory and Practical Applications*; Wiley Online Books, 2007. https://doi.org/10.1002/0470084987.

(43) Höfer, P.; Grupp, A.; Nebenführ, H.; Mehring, M. Hyperfine Sublevel Correlation (Hyscore) Spectroscopy: A 2D ESR Investigation of the Squaric Acid Radical. *Chem. Phys. Lett.* **1986**, *132* (3), 279–282. https://doi.org/10.1016/0009-2614(86)80124-5.

(44) Silakov, A.; Wenk, B.; Reijerse, E.; Lubitz, W. 14N HYSCORE Investigation of the H-Cluster of [FeFe] Hydrogenase: Evidence for a Nitrogen in the Dithiol Bridge. *Phys. Chem. Chem. Phys.* **2009**, *11* (31), 6592–6599. https://doi.org/10.1039/b905841a.

(45) and, C. C. L.; Maciel*, G. E. The Fumed Silica Surface: A Study by NMR. *J. Am. Chem. Soc.* **1996**, *118* (21), 5103–5119. https://doi.org/10.1021/JA954120W.

(46) and, I.-S. C.; Maciel*, G. E. Probing Hydrogen Bonding and the Local Environment of Silanols on Silica Surfaces via Nuclear Spin Cross Polarization Dynamics. *J. Am. Chem. Soc.* **1996**, *118* (2), 401–406. https://doi.org/10.1021/JA951550D.

(47) Hartmeyer, G.; Marichal, C.; Lebeau, B.; Rigolet, S.; Philippe, C.; Hernandez, J. Speciation of Silanol Groups in Precipitated Silica Nanoparticles by 1H MAS NMR Spectroscopy. *J. Phys. Chem. C* **2007**, *111* (26), 9066–9071. https://doi.org/10.1021/jp071490l.

(48) Odedra, S.; Wimperis, S. Improved Background Suppression in 1H MAS NMR Using Composite Pulses. *J. Magn. Reson.* **2012**, *221*, 41–50. https://doi.org/10.1016/j.jmr.2012.05.010.

(49) Feike, M.; Demco, D. E.; Graf, R.; Gottwald, J.; Hafner, S.; Spiess, H. W. Broadband Multiple-Quantum NMR Spectroscopy. *J. Magn. Reson. Ser. A* **1996**, *122* (2), 214–221. https://doi.org/10.1006/JMRA.1996.0197.

(50) Trébosc, J.; Wiench, J. W.; Huh, S.; Lin, V. S.-Y.; Pruski, M. Solid-State NMR Study of MCM-41-Type Mesoporous Silica Nanoparticles. *J. Am. Chem. Soc.* **2005**, *127* (9), 3057–3068. https://doi.org/10.1021/ja043567e.

(51) Schroeder, C.; Mück-Lichtenfeld, C.; Xu, L.; Grosso-Giordano, N. A.; Okrut, A.; Chen, C.-Y.; Zones, S. I.; Katz, A.; Hansen, M. R.; Koller, H. A Stable Silanol Triad in the Zeolite Catalyst SSZ-70. *Angew. Chemie Int. Ed.* **2020**, *59* (27), 10939–10943. https://doi.org/10.1002/ANIE.202001364.

(52) Grasser, S.; Haeßner, C.; Köhler, K.; Lefebvre, F.; Basset, J.-M. Structures of Paramagnetic VIV Amido Complexes Grafted onto Metal Oxide Surfaces: Model Systems for Heterogeneous Vanadium Catalysts. *Phys. Chem. Chem. Phys.* **2003**, *5* (9), 1906–1911. https://doi.org/10.1039/b301205k.

(53) Stoll, S.; Schweiger, A. EasySpin, a Comprehensive Software Package for Spectral Simulation and Analysis in EPR. *J. Magn. Reson.* **2006**, *178* (1), 42–55. https://doi.org/10.1016/j.jmr.2005.08.013.

(54) Ravel, B.; Newville, M.; IUCr. ATHENA, ARTEMIS, HEPHAESTUS: Data Analysis for X-Ray Absorption Spectroscopy Using IFEFFIT. *urn:issn:0909-0495* **2005**, *12* (4), 537–541. https://doi.org/10.1107/S0909049505012719.

2.6 Appendix

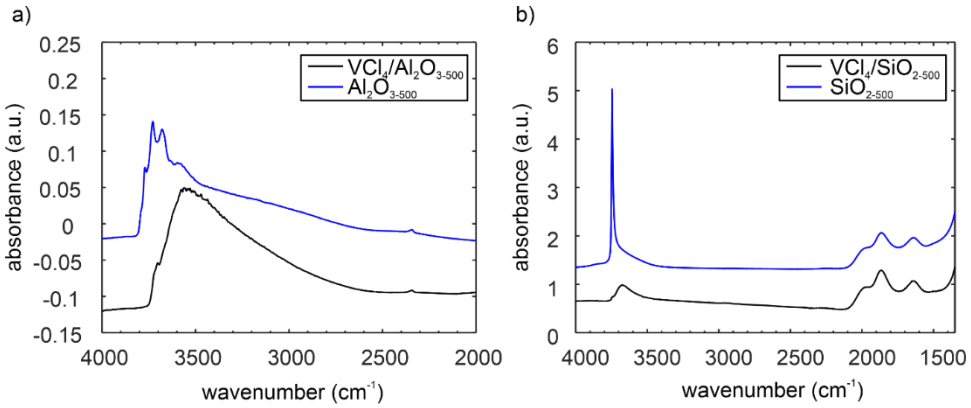

Figure A2.1 IR spectra of self-supporting disk of a) Al_2O_3 and b) SiO_2 after partial dehydroxylation *in vacuo* at 500 °C (blue), and after reaction with excess VCl_4 vapor at room temperature (black), followed by desorption of volatiles at the same temperature.

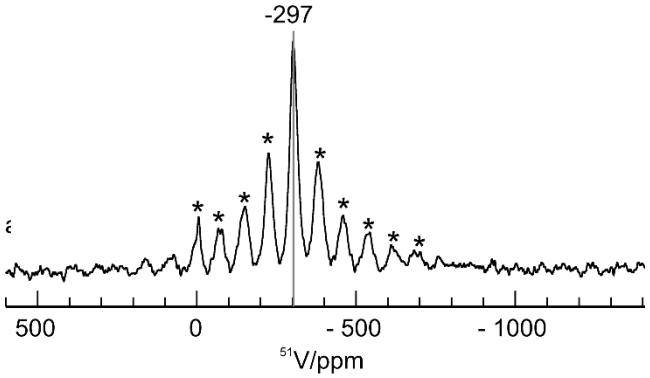

Figure A2.2 Investigation of presence of V(V) in VCl_4/SiO_2 using solid-state ^{51}V MAS NMR spectrum, showing an isotropic peak at -297 ppm (single-pulse spectrum acquired with a pulse length of 2.75 μs and a delay of 2.5 s, at 18.8 T with a spinning speed of 19 kHz).

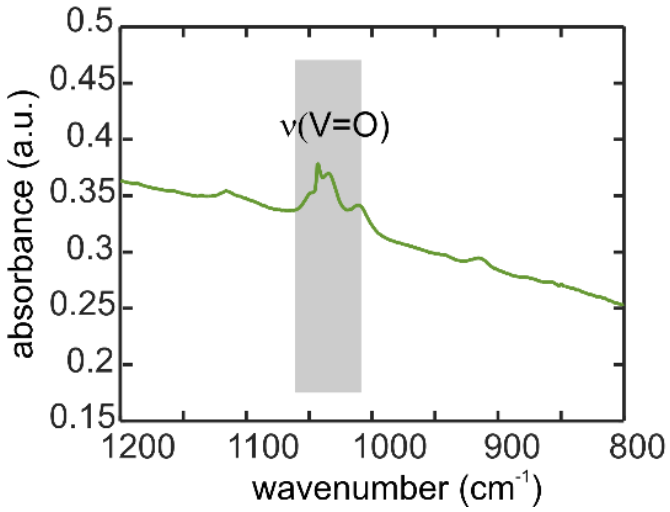

Figure A2.3 The gas-phase IR spectrum of neat VCl_4, zoomed in to show the band corresponding to ν(V=O).

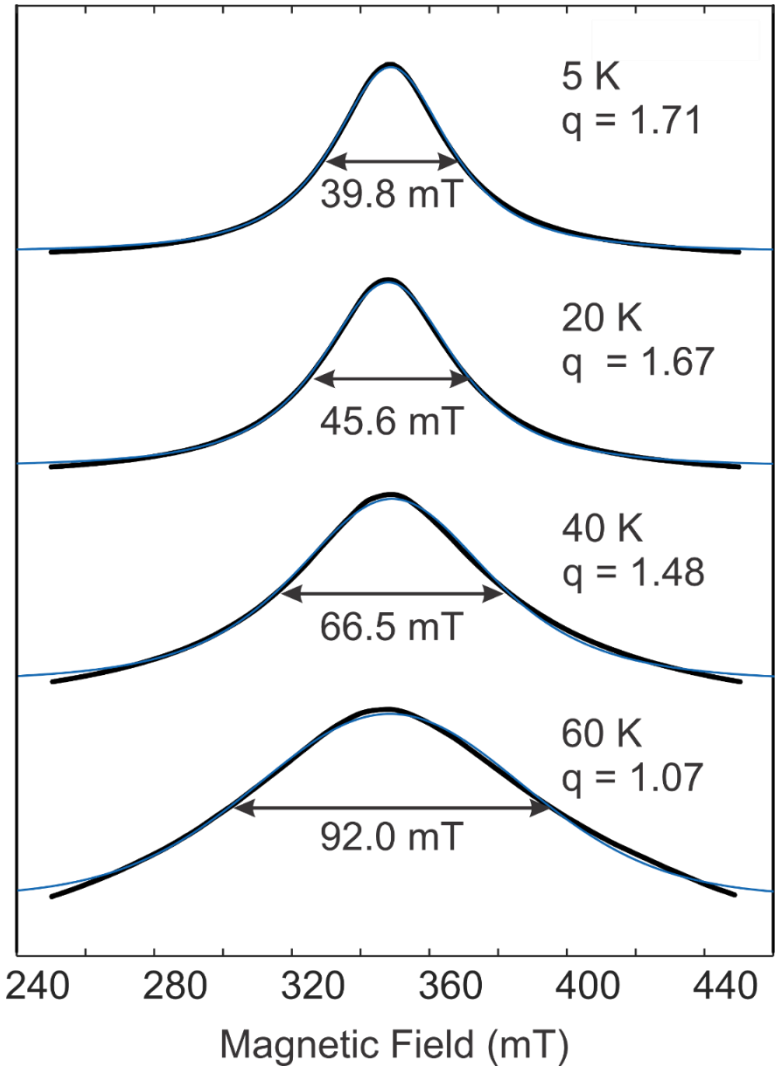

Figure A2.4 Representative CW EPR spectra of VCl_4 modified SiO_2 showing the experimental spectra (black) acquired at 4, 20, 40 and 60 K, and their simulated spectra (blue) using the Tsallian function in equation 2 of the main text.

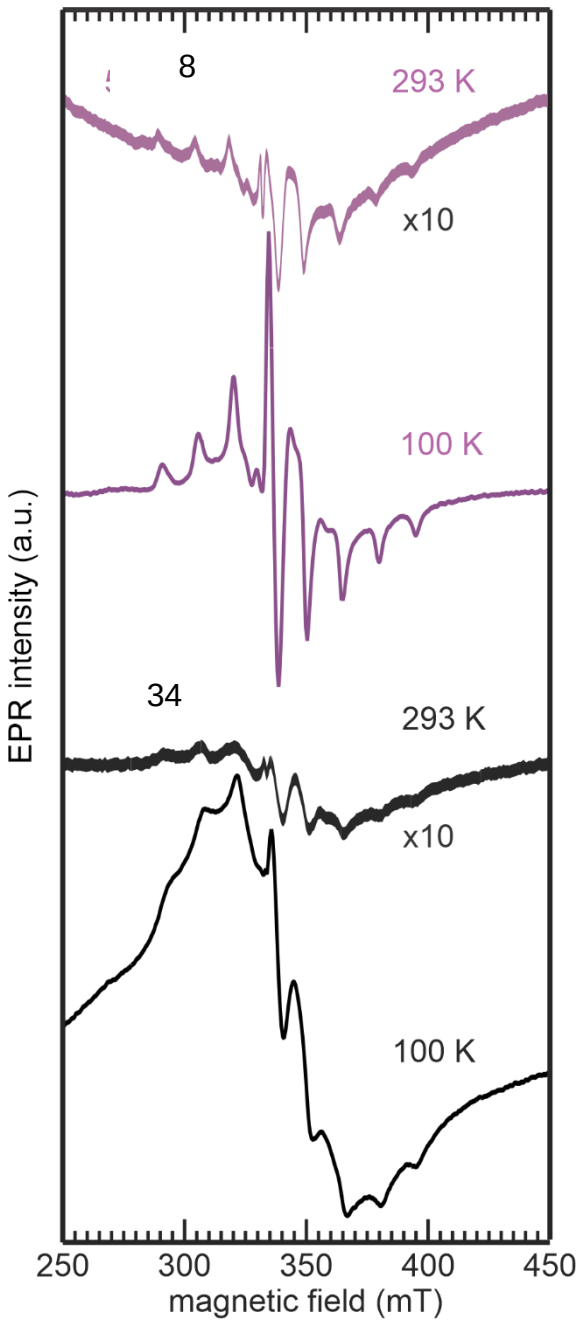

Figure A2.5 CW EPR spectra of VCl_4-modified SiO_2 with increasing V loading, corresponding to reaction of 8 and 34 % of the silanols. All spectra were recorded at 293 and 100 K, as indicated, using the same parameters (time constant = 40.96 ms, receiver gain = 1 x 10^4, modulation frequency = 100 kHz, modulation amplitude = 5.45 G, attenuation = 15

dB). Experimental spectra are shown in black, and their simulations in red. The deconvoluted components of the spectra are also shown in different shades of red.

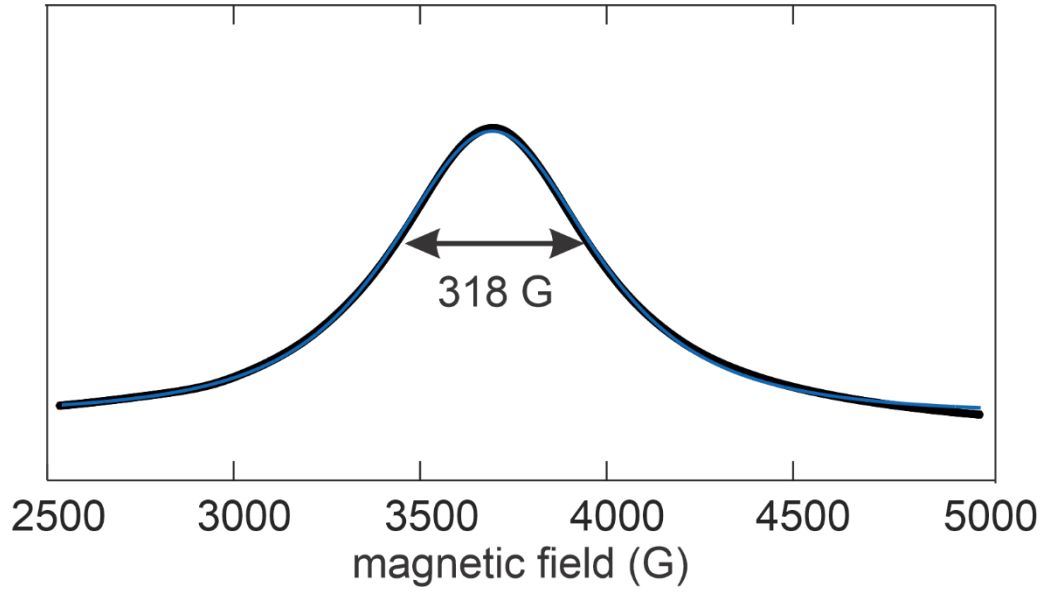

Figure A2.6 CW EPR spectrum of VCl_4 modified SiO_2 exposed to CH_3CN (black) and its simulated fit (blue) using the Tsallian function in equation 2 of the main text.

Table A2.1 Parameters obtained from modelling of the EPR lineshapes of VCl_4 modified SiO_2 acquired at different temperatures. [a]

Temperature (K)	Y_{max}	l	q	x_r
4	0.99	20.9	1.7	349
10	0.99	19.5	1.7	349
15	0.99	21.0	1.7	348
20	0.99	22.8	1.7	348

25	0.98	25.6	1.6	348
30	0.98	28.1	1.6	349
35	0.98	30.5	1.5	349
40	0.98	33.2	1.5	349
45	0.97	36.8	1.4	349
50	0.97	40.1	1.3	349
60	0.98	46.0	1.1	348

[a] The Tsallian function $Y = Y_{max}\left[1 + \left(2^{q-1}-1\right)\left(\frac{B-x_r}{\Gamma}\right)^2\right]^{\frac{-1}{q-1}}$ was used to model the lineshape using the Curve Fitting Toolbox of MATLAB, with 95 % confidence bounds.

DFT calculations. The silica surface was modeled using a vicinal silanol pair with parallel silanols (O-Si-Si-O dihedral angle = 0 °) according to a previously described procedure.XX The Si atoms are capped by peripheral hydroxyl groups (transparent in Figure A2.7) whose positions were fixed in all calculations to mimic the rigidity of the silica support and to prevent unintended hydrogen-bonding interactions. However, one of the reactive silanols in the vicinal pair is allowed to engage in a hydrogen bond to the other reactive silanol. The O-H bond of the former stretches very slightly (from 0.956 to 0.960 Å), suggesting that this interaction is weak.

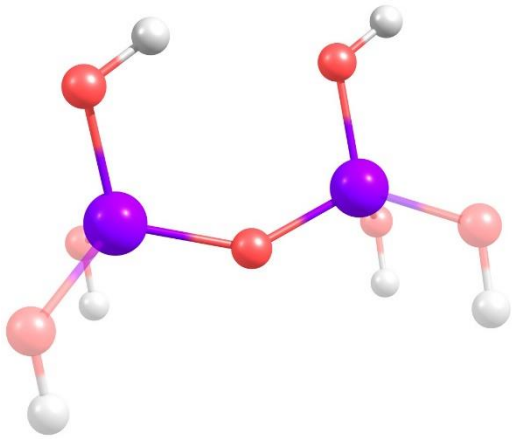

Figure A2.7 Optimized vicinal silanol cluster with parallel reactive hydroxyls (O-Si-Si-O dihedral angle = 0 °) and fixed peripheral hydroxyls (transparent). Color scheme: O (red), H (white), Si (purple).

^{14}N HYSCORE Spectroscopy. To directly probe the coordination between the V(IV) center and the CH_3CN, ^{14}N HYSCORE spectroscopy was used. This technique relies on electron-nuclear interactions and thus V(IV) centers directly coordinating with ^{14}N nuclei in CH_3CN result in cross-peaks at (-7.6, 3.3) and (-3.3, 7.6) on the HYSCORE spectrum in the strong coupling regime i.e. left (+ -) quadrant on the EPR spectrum which correspond to DQ transitions ($\Delta m_I = \pm 2$). In VCl_4 grafted on SiO_2 modified with CH_3CN, intense peaks are observed are in the strong coupling regime. The diagonal ridge is due to artifacts that can occur when the spins have not had sufficient time to relax between each cycle of the pulse sequence, often an issue with ^{14}N due because of its quadrupolar nature.

The experimental ^{14}N HYSCORE spectra were simulated using the MATLAB Easyspin package with the "saffron" function. The experimental parameters, such as magnetic field, excitation frequency, number of points, dwell time, pulse width, and pulse delay, were taken

directly from the HYSCORE experiments. The positions and intensities of the DQ transitions were used to simulate the general features of the spectrum and extract the hyperfine coupling parameters (isotropic hyperfine coupling A_{iso} and dipolar coupling T) and the quadrupolar coupling constant Q. Simulations of the spectra were iteratively done until a set of parameters was obtained that could reproduce the general features of the experimental spectra. The fit was performed using one type of ^{14}N species, where each of the three parameters (A_{iso}, T, Q) were varied until a reasonable fit was observed. A Q value of 2.5 MHz was found, close to the expected values for the quadrupolar coupling constant of ^{14}N in CH_3CN. A_{iso} was determined to be 5 MHz while the T was 0.25 MHz. The observations from HYSCORE confirm that the CH_3CN is coordinating with the V(IV) center, and increasing the relaxation time, making the EPR spectrum visible at room temperature.

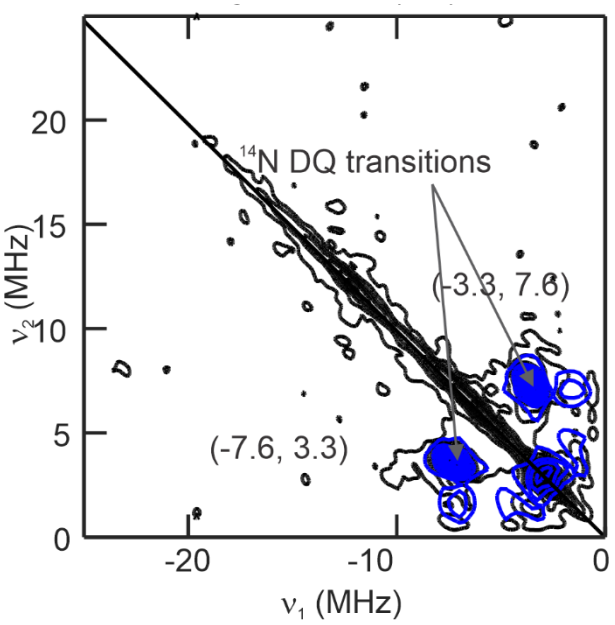

Figure A2.8. The effect of the addition of CH_3CN. 2D pulsed EPR, ^{14}N HYSCORE spectra showing the (+,+) and (+,-) quadrants, obtained at B_0 = 3340 G magnetic field position using the parameters described in Methods. Experimental data is shown in black while the simulation in blue.

Chapter 3: P-site Structural Diversity and Evolution in a Zeosil Catalyst

Reproduced with permission from S.K. Jain, T. Tabassum, L. Li, L. Ren, W. Fan, M. Tsapatsis, S. Caratzoulas, S. Han, and S.L. Scott. "P-site Structural Diversity and Evolution in a Zeosil Catalyst". *J. Am. Chem. Soc.* 2021, *143*, 1968-1983. DOI: doi/10.1021/jacs.0c11768.

3.1 Introduction

Robust catalysts that can transform lignocellulose into fuels and chemicals will be needed to shift chemical manufacturing towards the use of biomass as a source of renewable carbon. Aluminosilicate zeolites are already well-established as catalysts for the conversion of fossil carbon due to their high acidity and stability, and they are poised to play similar roles for biomass-derived carbon.[1,2] However, these zeolites are rapidly deactivated by side-products formed in unselective reactions of biomass intermediates. One approach to improve the selectivity of these catalysts, and thereby enhance their stability, is to attenuate their strong acidity. Moderate Brønsted acidity can be installed in siliceous zeolites by infusing them with orthophosphoric acid (H_3PO_4). Confinement of the acid in these microporous materials may also confer shape-selectivity.[3] The resulting P-zeosils are related compositionally to amorphous H_3PO_4-modified silicas, known as "solid phosphoric acids" (SPAs). The SPAs have been used commercially since the 1930s in large-scale catalytic processes such as propene oligomerization and benzene alkylation.[4–6] Recently, an SPA was also reported to steer the fast pyrolysis of cellulose toward levoglucosenone.[7,8] The active sites in SPAs are suggested to be free phosphoric acid oligomers, whose proximity to the silica surface shifts

the oligomerization equilibria and alters the catalytic activity. Introducing phosphorus also changes the acidity of crystalline aluminosilicates,[9–12] and is widely used to improve zeolite stability under hydrothermal reaction conditions.[13] Yet despite decades of study, it is still unclear whether the catalytic activity of P-modified silicas and zeolites is due to free H_3PO_4, various polyphosphoric acid oligomers, or P-sites covalently bonded to the solid phase.

Recently, a self-pillared pentasil (SPP) and a dealuminated Beta (BEA) zeolite, both modified with phosphorus, were reported to catalyze two noteworthy reactions: the Diels-Alder coupling of carbohydrate-derived 2,5-dimethylfuran with ethylene to give *p*-xylene, and the tandem dehydration-ring opening of tetrahydrofuran to give 1,3-butadiene.[14,15] Both zeosils are all-silica materials (i.e., containing no aluminum) and, in the absence of phosphorus, show no activity for either reaction. Their enhanced activity and selectivity relative to H_3PO_4 was attributed to surface-bound P-sites,[14] although the existence of such sites was not established. Surface and/or pore confinement in a siliceous material could promote H_3PO_4 condensation with itself and/or the silica framework, leading to formation of P-O-P and/or P-O-Si linkages.[16] Describing the environment-dependent speciation of these P-sites is a necessary first step towards establishing structure-activity relationships for P-based solid acid catalysts.

X-ray diffraction (XRD) cannot be used to study structures of P-sites in amorphous materials, or the disordered phases of semi-crystalline materials like P-modified aluminum (hydro)oxides and P-zeosils. However, total X-ray scattering has recently been applied to the structural analysis of adsorbed (poly)phosphates, through analysis of the differential pair-distribution function. The findings suggest the formation of surface-bound complexes, although the ability to resolve structural information when multiple sites are present is low.[17–

[19] The sites in P-containing silica glasses, aluminophosphate and aluminosilicate molecular sieves, as well as silicophosphates, have been probed using a variety of spectroscopic techniques.[20] In principle, the presence of P-O-Si and P-O-P linkages can be confirmed by their characteristic IR[21–23] and Raman vibrations,[24,25] but here too precise assignments are elusive in the presence of multiple types of P and Si species. Linear combination analysis of the P K-edge XANES suggested the formation of various adsorbed (poly)phosphates on γ-Al_2O_3.[26] Shifts in the P $L_{2,3}$-edge XANES were correlated with polyphosphate chain length in SiO_2-P_2O_5 and Na_2O-SiO_2-P_2O_5 glasses,[27] but the presence of P-O-Si linkages could not be confirmed. Various computational studies reached inconsistent conclusions regarding the thermodynamic stabilities of such linkages in different materials.[28,29] To-date, there are no comparable studies on P-zeosils.

Solid-state NMR spectroscopy is a powerful way to probe the nature of P-sites directly, and can be used to study both crystalline and amorphous materials. In particular, ^{31}P Magic-Angle Spinning NMR (MAS-NMR) has been used extensively to investigate silicophosphate gels/glasses,[30–32] SPA catalysts,[33] phosphates adsorbed on aluminum (hydr)oxides,[17,26] and partially dealuminated P-modified aluminosilicate zeolites.[13] Replacement of H by Si gives rise to surface-bound P-sites with structures described as $O=P(OH)_2(OSi)$, $O=P(OH)(OSi)_2$, and $O=P(OSi)_3$. The last member of the series, $P(OSi)_4$, is observed in crystalline silicophosphate phases. Adopting a nomenclature conventionally used for ^{29}Si NMR signals, the anchored P-sites are labeled Q^n, where *n* denotes the number of Si next-nearest neighbors (i.e., P-O-Si linkages).

In aqueous solution, H_3PO_4 exists in concentration-dependent equilibria with several linear and cyclic oligomers, including pyrophosphoric acid ($H_4P_2O_7$), acyclic

tripolyphosphoric acid ($H_5P_3O_{10}$), and cyclic metaphosphoric acid ($H_3P_3O_9$).[34,35] Acyclic oligomers with the general formula $H_{m+2}P_mO_{3m+1}$ dominate the distribution.[34–36] They have been identified in the literature using a P^m nomenclature,[37] where *m* denotes the degree of oligomerization. The characteristic ^{31}P NMR signals for H_3PO_4 (P^1) and $H_4P_2O_7$ (P^2) appear at 0 and -12 ppm, respectively.[33] Trimetaphosphoric acid (P^3) has a single type of P-site with a chemical shift of -22 ppm,[38] while tripolyphosphoric acid has one internal and two terminal P-sites, with chemical shifts similar to those of trimetaphosphoric and pyrophosphoric acids, respectively.[33] Solid, fully condensed P_4O_{10} (phosphoric anhydride, P^4) gives rise to a signal at -46 ppm.[39]

Scheme 3.1 depicts the overlap of the ^{31}P NMR chemical shift ranges for Q^n sites with those of the corresponding P^{n+1} sites.[30,31] For amorphous siliceous materials, assignments are further complicated by the low ^{31}P NMR spectral resolution. These materials generally show fast nuclear spin relaxation arising from inhomogeneity in the local magnetic fields of the ^{31}P nuclei, dipolar interactions, and large ^{31}P chemical shift anisotropies (CSAs). The size of the CSAs relative to the MAS frequency also results in strong spinning sidebands that make the crowded ^{31}P NMR spectra more difficult to analyze. For sites with the same total number of Y substituents (Y = P or Si), but different chemical identities for Y (e.g., $O{=}P(OH)_2(OSi)$, Q^1, vs. $H_4P_2O_7$, P^2), it is usually impossible to assign a signal to a particular P-site based on its chemical shift alone. Precise identification of oligomers with P-O-P linkages, or surface-anchored sites with Si-O-P linkages, or mixed sites that contain both types of linkages,[40] remains an unsolved problem. Indeed, framework-anchored sites in siliceous materials have yet to be observed experimentally. Yet the ability to distinguish them is necessary to describe, model, and eventually tune the catalytic activity of P-modified materials.

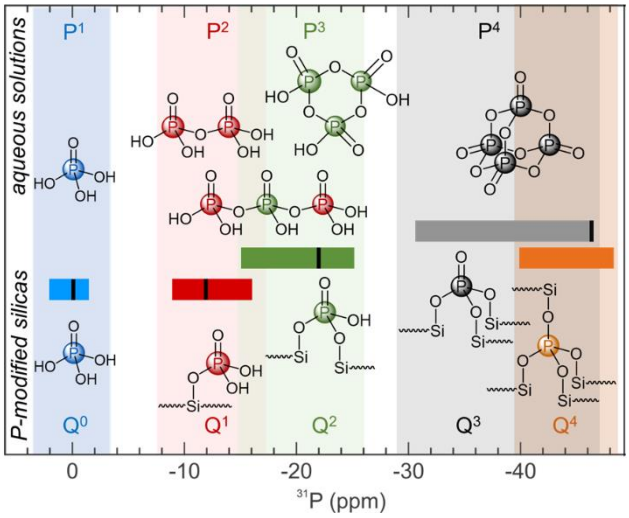

Scheme 3.1 Structures of typical Q^n sites and their reported chemical shift ranges[14,31,40–48] (colored horizontal bars), as well as P^m sites and their discrete chemical shifts[33,38,39] (black vertical bars within each chemical shift range). The labels follow the principal naming conventions found in the literature for solid phases (Q^n) and aqueous solutions (P^m).

For crystalline siliceous materials, the presence and relative abundance of P-O-P and P-O-Si linkages can be established using multi-dimensional NMR experiments. For example, P-O-Si linkages in crystalline silicophosphates were observed using *J*-coupling-based 2D ^{29}Si-^{31}P NMR correlation spectroscopy.[32,49] Interactions *between* P-sites were assessed by ^{31}P-^{31}P correlation experiments, which probe through-bond (*J*-) or through-space (*D*-) coupling.[50–53] Unfortunately, *J*-coupling based approaches are not readily applied to the characterization of disordered P-sites in P-zeosils, due to the rapid relaxation of the ^{31}P and ^{29}Si nuclear spin coherence. Instead, the nature of the linkages in such materials must be demonstrated using techniques based on *D*-coupling. Such multi-dimensional experiments involving ^{31}P or ^{29}Si

are very challenging for dilute P-zeosils, due to the inherently low NMR sensitivity and low receptivity of ^{29}Si (4.7% natural abundance, with a gyromagnetic ratio only 20 % that of ^{1}H).

Recent advances in NMR that overcome its inherently low sensitivity are generating new opportunities for characterizing connectivities between ^{31}P and ^{29}Si nuclear spins. In particular, Dynamic Nuclear Polarization (DNP) can boost the sensitivity of MAS-NMR by several orders of magnitude,[54] making it possible to conduct multi-dimensional solid-state NMR studies of siliceous materials even with natural abundance ^{29}Si. Specifically, ^{29}Si-^{31}P and ^{31}P-^{31}P correlation experiments can be performed using DNP-enhanced MAS NMR with reasonable experimental times (a few hours). In this study, DNP-enhanced MAS-NMR spectroscopy was combined with advanced NMR pulse sequences to identify the P-sites present in a P-zeosil.

P-modified SPP, with an atomic ratio Si/P of 27, is a meso/microporous Mobil Five (MFI)-type zeolite. Consisting of orthogonally-intergrown single unit-cell MFI nanosheets (Scheme 3.2), it is hydrothermally stable at moderate temperatures.[55–57] Its framework encompasses both conventional MFI micropores located within the 2 nm-thick nanosheets, as well as mesopores formed between the intergrown nanosheets and defined by the external surfaces of the MFI nanosheets, which are mostly terminated by (010) planes. The material shows a rich P-speciation, which depends strongly on the extent of hydration. We aim to identify the surface-bound and near-surface phosphoric acid oligomers and monomers, including those in which P-O-P and P-O-Si linkages are present simultaneously in the same P-sites.

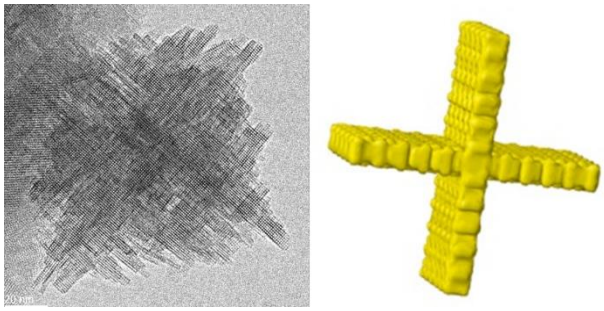

Scheme 3.2 Transmission electron microscopy image of a typical Self-Pillared Pentasil (SPP) particle (left), consisting of orthogonally-intergrown MFI nanosheets of single-unit-cell (2 nm) thickness, and a schematic of the basic unit, showing two 2 nm-thick intergrown MFI nanosheets (right).

3.2 Results and discussion

3.2.1 Describing the P-sites in dry P-SPP

To explore the P-sites present in the absence of water, P-SPP (Si/P = 27) was dried *in vacuo* at 450 °C. Its 1D ^{31}P MAS NMR spectrum was recorded without exposure of the dry material to air, using direct excitation at 18.8 T (Figure 3.1a). The spectrum consists predominantly of an isotropic peak at -44 ppm and its spinning sideband at 21 ppm, confirmed by comparison to the simulation in Figure 3.1a. According to Scheme 3.1, it is either a P^4 or a Q^3 signal. From this point forward, we will use only the Q^n-nomenclature for simplicity.

The chemical shift anisotropy (CSA), also obtained from the simulation of the ^{31}P MAS NMR spectrum, is (-205 ±29) ppm (i.e., 66 ± 9 kHz at 18.8 T, Table A3.1). The linewidth, ca. 3.5 kHz at ν_r = 20 kHz, suggests that it is dominated by isotropic chemical shift dispersion, arising from the superposition of multiple, structurally heterogeneous P-sites with distinct isotropic chemical shifts. Such sites may include surface-bound $O{=}P(OSi)_3$, non-surface-bound P_4O_{10}, and components of more complex mixed sites. Although the broad Q^3

signal and its spinning sidebands are the dominant spectral features, minor Q^n signals ($n \neq 3$) may also be present, and could account for the additional signal intensity not predicted by the simulated spinning sidebands of the Q^3 signal. However, the poor spectral resolution and low signal-to-noise ratio (SNR) preclude more definitive characterization of the material on the basis of this spectrum alone.

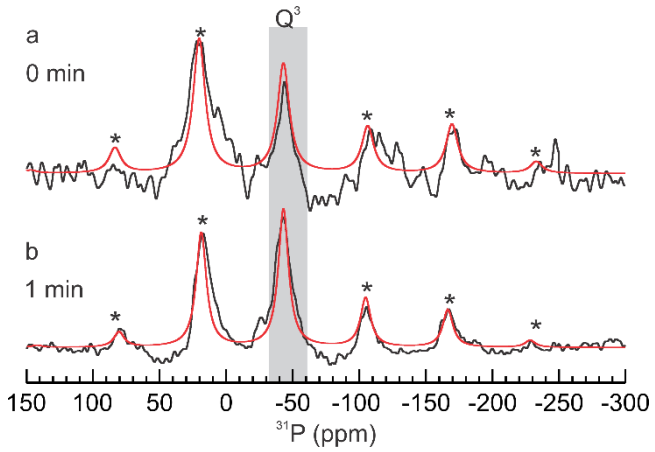

Figure 3.1 ^{31}P MAS-NMR spectra (black) of P-SPP (Si/P = 27), in (a) its fully dry state (i.e., 0 min ambient exposure), and (b) after 1 min exposure to the laboratory ambient. Both spectra were recorded at room temperature and 18.8 T, with 20 kHz MAS and a 5s repetition delay. The number of scans for the dry and 1 min air-exposed samples was 1024 and 256, respectively. Asterisks indicate spinning sidebands. Simulations (red) were performed using the CSA model in Topspin 4.0.6.

Many catalytic reactions involving biomass are conducted in the presence of water, and/or generate water as a by-product. Since previous studies of SPA[4,36,58] and P-modified zeolites[59] show that both P-speciation and/or activity are very sensitive to the hydration state,

we investigated the effect of water on the P-site distribution in the P-zeosil. The ^{31}P NMR spectrum of dry P-SPP was recorded again after removing the rotor cap to effect a brief (ca. 1 min) air exposure at room temperature in the laboratory ambient (we will refer to this operation as "ambient exposure" throughout the rest of the paper). Although the chemical shift of the major isotropic peak at -44 ppm did not change, another small, isotropic peak became clearly apparent at -25 ppm (Figure 3.2). Its chemical shift is typical of a Q^2 signal. At the same time, the absolute area of the NMR spectrum increased by a factor of 10 and the SNR increased 12-fold, resulting in a better-resolved sideband pattern. The higher NMR sensitivity in this minimally hydrolyzed state reflects a reduced CSA, (-160 ± 9) ppm, compared to (-205 ± 29) ppm for the dry material. This change leads to increased efficiency of the RF excitation.

Since the CSA values are larger than the RF amplitude (~35 kHz) used for the excitation pulse, the appearance of the spinning sideband manifold may be distorted by the non-uniform excitation, increasing the uncertainties in the CSA parameters (see Table A3.1). Nevertheless, the changes in the overall spectral intensity and sideband patterns confirm a reduction in CSA after just 1 min ambient exposure (see Figure A3.1). The reduction in CSA occurs concurrently with a decrease in linewidth of the isotropic Q^3 peak, from 3.5 to 3.0 kHz. This indicates that the isotropic chemical shift dispersion is also lower in ambient air-exposed P-SPP. These observations are consistent with an increase in average mobility and/or a reduced structural heterogeneity of the P-sites relative to the fully dry state.

3.2.2 Gradual changes in P speciation upon exposure to moisture

The extent of P-zeosil hydration was increased by prolonging the ambient exposure (by removing the NMR rotor cap for longer times). The resulting changes in P speciation were

observed by ^{31}P NMR (Figure 3.2a). After 4 min ambient exposure, the peak at -25 ppm became more intense and a new peak appeared at -11 ppm. These signals correspond to chemical shifts in the Q^2 and Q^1 ranges, respectively. Thus, exposure to a very small amount of water vapor for even a brief duration (4 min) is sufficient to convert some of the P-sites with signals in the Q^3 region to new P-sites. After further ambient exposure (9 min), four distinct groups of signals are present (Q^n, where n = 0-3), including a new peak at 0 ppm (Q^0) assigned to H_3PO_4. A second isotropic Q^3 peak at -38 ppm emerges, distinct from spinning sidebands. The spinning sidebands become successively less intense and all peaks narrow as the extent of hydration increases, presumably due to higher mobility and/or greater homogeneity in the remaining P-site structures.

Trends in the various Q^n peak areas with ambient exposure time (Figure 3.2b) reflect on the relative hydrolytic stabilities of each group of P-sites (spectra for all ambient exposure times are shown in Figure A3.2). The Q^3 signals, which dominate the spectrum of the dry material, decrease gradually in intensity, disappearing completely after ca. 25 min. Over the same time period, the Q^2 signal intensity first increases and then decreases, suggesting that hydrolysis of some P-sites, initially responsible for Q^3 signals gives new sites with Q^2 signals. The intensities of the Q^1 and Q^0 signals increase monotonically, but only after an induction period (which is shorter for Q^1 than for Q^0). The P-sites responsible for these two groups of signals must therefore be mostly secondary hydrolysis products, formed from P-sites associated with the Q^2 signals (although some could be formed directly by hydrolysis of the more stable sites associated with Q^3 signals). A ^{31}P NMR spectrum recorded after many days of ambient exposure (Figure A3.3) shows that most P-sites are eventually converted to H_3PO_4 (responsible for the Q^0 signal), while only a small residual Q^1 signal remains. Thus, the

sensitivity to hydrolysis of the various groups of P-sites follows the general (and expected) order $Q^3 > Q^2 > Q^1$.

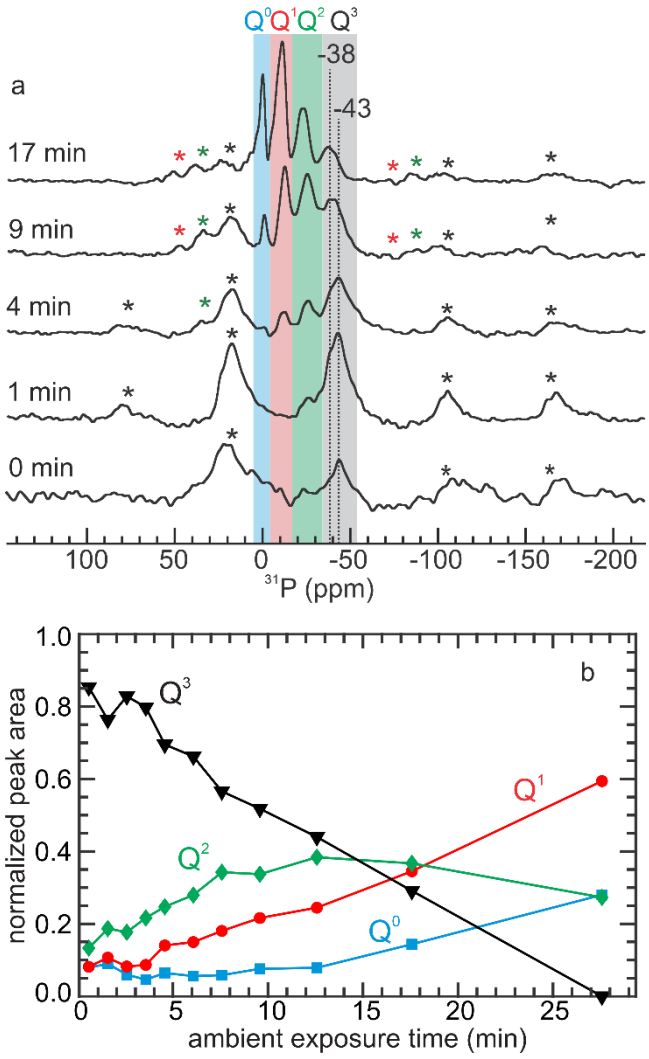

Figure 3.2 The effect of ambient exposure time (correlated approximately with the amount of adsorbed water) at room temperature, on the P speciation in P-SPP: (a) ^{31}P MAS NMR spectra recorded after each ambient exposure time, as noted. All spectra were recorded at room temperature in an 18.8 T magnet using 20 kHz MAS. Spinning sidebands for Q^1, Q^2, and Q^3 signals are indicated by * in red, green, and black, respectively. (b) Approximate time profile of the integrated peak intensities (including spinning sidebands) for each group of Q^n signals.

Overall, NMR measurements in the presence of variable water content reveal that multiple types of P-sites, with different sensitivities to water, coexist in partly hydrolyzed P-SPP. Under reaction conditions, P-SPP is neither completely dry nor fully hydrolysed, hence a distribution of P-sites with different Q^n signals will be present. More insightful methods are needed to assess the nature of these P-sites, in particular, the identities of the sites responsible for the different Q^3 signals, and whether any of the sites are surface-bound (via P-O-Si linkages).

3.2.3 Resolving P-speciation using DNP-enhanced MAS NMR

In principle, overlapping signals arising due to P-sites with either P-O-P or P-O-Si linkages can be distinguished via their ^{31}P-^{31}P and ^{31}P-^{29}Si correlations. However, conventional 1D ^{31}P MAS-NMR spectra such as those shown in Figure 3.1 already require tens of minutes of acquisition times (78 min for the fully dry material, and 22 min after 1-min ambient exposure). Hence, several days would be required to conduct the corresponding 2D measurements. Dynamic Nuclear Polarization (DNP) enhances NMR sensitivity dramatically by transferring electron spin polarization from a paramagnetic polarizing agent such as the TEKPOL biradical to solvent protons, and then (by cross-polarization) to ^{31}P nuclei. The resulting signal enhancements shorten the times required for ^{31}P-^{29}Si and ^{31}P-^{31}P correlation experiments significantly, and also facilitate the selective 1D detection of the various Q^n signals.

The DNP-enhanced ^{1}H-^{31}P CP-MAS spectrum of nearly-dry P-SPP shown in Figure 3.3a (recorded after ambient exposure time of ca. 2 min) could be acquired in less than 1 min using a ramped-CP pulse sequence (see Methods). The spectrum has a much higher SNR than a spectrum of the same material recorded for 22 min without DNP (i.e., with the microwave source turned off, see Figure A3.4 for comparison). The DNP-enhanced spectrum exhibits two major isotropic peaks, at -42 and -25 ppm, both with intense spinning sidebands. Based on their chemical shifts, these isotropic peaks correspond to P-sites with Q^3 and Q^2 signals, respectively. In contrast to the ^{31}P MAS-NMR spectrum in Figure 3.2a, the intensities of both signals are similar. ^{1}H-^{31}P CP detection is expected to enhance the Q^2 signal intensity relative to Q^3, since the abundance of nearby ^{1}H should be higher for sites that give rise to Q^2 signals (Scheme 3.1). The spinning sidebands are also stronger in Figure 3.3a compared to Figure 3.2a. This is a consequence of the slower MAS rate in the DNP experiment (7 kHz, vs. 20 kHz in the absence of DNP). The direct ^{31}P spectra recorded at 9.4 T with DNP, and 18.8 T without DNP, are compared in Figure A3.5. Unfortunately, the intense spinning sidebands resulting from the slower MAS rate preclude the observation of any Q^1 or Q^0 signals in the ^{1}H-^{31}P ramped-CP-MAS spectrum.

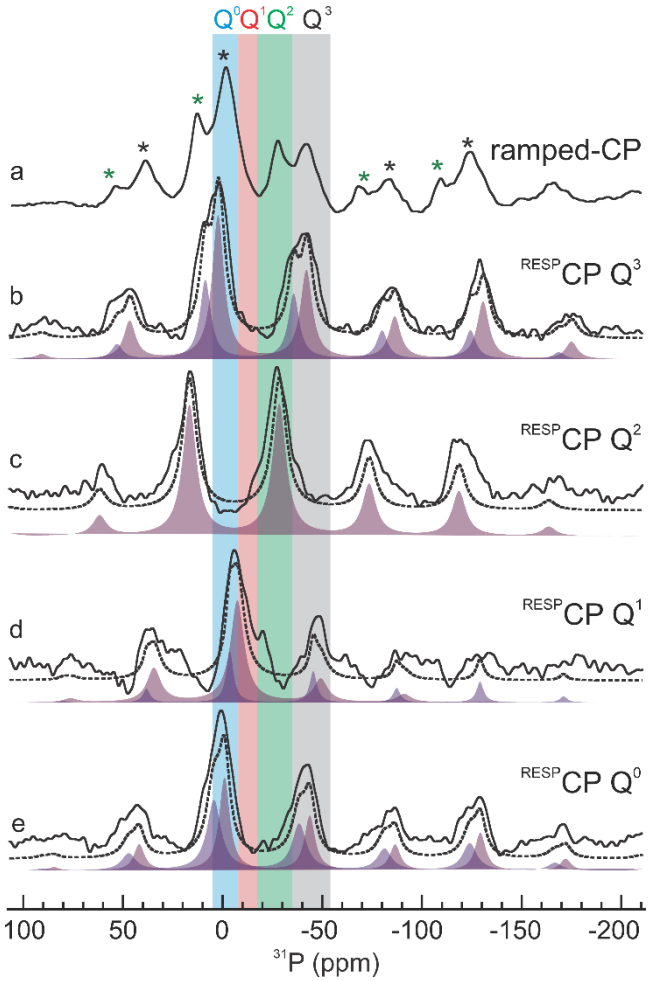

Figure 3.3 DNP-enhanced ^{1}H-^{31}P CP/MAS spectra (solid black lines) of nearly-dry P-SPP (after 2 min ambient-exposure), recorded using (a) ramped CP, and (b-e) ^{RESPIRATION}CP. In the ^{RESP}CP experiments, the RF frequency was set to (b) -42 ppm, (c) -25 ppm, (d) -11 ppm, or (e) 0 ppm. All spectra were acquired at 9.4 T, 7 kHz MAS, and 95 K. Spinning sidebands for Q^2 and Q^3 signals are indicated by * in green and black, respectively. Simulated spectra (sum: dotted black lines) were obtained with a CSA model, using either a single component (a, c; filled purple spectrum), or two-components (b, d, e; filled spectra in two shades of purple). See Methods section for details. Fit parameters are given in Table 3.1

To better resolve the Q^1 and Q^0 signals, we performed frequency-selective CP detection using the $^{\text{RESPIRATION}}$CP pulse sequence.[60] This approach reveals the distinct sideband pattern of each region. The RF offset frequency was centered sequentially in each of the four Q^n regions ($0 \leq n \leq 3$). The series of DNP-enhanced $^{\text{RESPIRATION}}$CP spectra recorded in this way are shown in Figure .

Setting the RF offset frequency in the Q^3 region (-42 ppm) enhances the Q^3 signals, while suppressing others. In the $^{\text{RESPIRATION}}$CP spectrum, the main isotropic peak has a shoulder (Figure 3.3b), reflecting a second P-site with a chemical shift in this region. The corresponding simulation requires two isotropic signals in the Q^3 region, with chemical shifts C_{iso} of -43 and -36 ppm (Table 3.1). This result is consistent with the observation of two isotropic Q^3 signals at -43 and -38 ppm by direct ^{31}P MAS NMR at 18.8 T (Figure 3.2). Their CSA values of (-147 ± 9) and (-135 ± 30) ppm, respectively), are significantly lower than that reported for P_4O_{10}, -300 ppm.[39] We infer from this comparison that both Q^3 signals arise from P-sites linked to the zeosil framework by P-O-Si linkages. However, unambiguous confirmation of such linkages requires ^{29}Si-^{31}P correlation experiments (see below).

To observe signals in the Q^2 region, a second $^{\text{RESPIRATION}}$CP spectrum was recorded with the RF offset frequency set at -25 ppm. The resulting spectrum contains a single isotropic signal with C_{iso} of (-28 ± 1) ppm, Figure 3.3c, and a CSA of (-127 ± 9) ppm (Table 3.1). A third $^{\text{RESPIRATION}}$CP spectrum was recorded with an RF offset frequency set at -11 ppm, in the Q^1 region. The spectrum in Figure 3.3d contains two peaks within 2 kHz of the RF frequency (i.e., both in the $^{\text{RESPIRATION}}$CP range). According to the simulated spectrum, the major peak is a spinning sideband of the Q^3 signal at (-46 ± 2) ppm, while the minor peak is an isotropic Q^1 signal at (-8 ± 1) ppm with a relatively small CSA, (-78 ± 14) ppm. For comparison, the

isotropic Q^1 signals are completely obscured by spinning sidebands in the ramped-CP spectrum (Figure 3.3a). Finally, setting the RF frequency to 0 ppm revealed no new isotropic signals, Figure 3.3e. In this region, Q^0 signals overlap directly with Q^3 spinning sidebands. The spectrum is well-simulated using only CSA parameters for the Q^3 signals (Table 3.1). All four $^{\text{RESPIRATION}}$CP experiments were repeated at a different MAS frequency (5 kHz) to confirm the positions of the isotropic peaks (Figure A3.7).

Table 3.1 CSA parameters for nearly-dry P-SPP, obtained by fitting a simulated spectrum to its $^{\text{RESPIRATION}}$CP data

RF offset [a]	**CS_{iso}** [b,c]	**CSA**[c]	η	**LB**
ppm	**ppm**	**ppm**		**kHz**
-42 (Q^3)	-43 ± 1 (Q^3)	-147 ± 9	0.1	1.2
	-36 ± 2 (Q^3)	-135 ± 30	0.1	1.1
-25 (Q^2)	-28 ± 1 (Q^2)	-127 ± 9	0.1	1.3
-11 (Q^1)	-8 ± 1 (Q^1)	-78 ± 14	0.0	1.4
	-46 ± 2 (Q^3)	-140 ± 45	0.1	0.7
0 (Q^0)	-44 ± 1 (Q^3)	-149 ± 16	0.1	0.9
	-39 ± 1 (Q^3)	-142 ± 15	0.1	1.1

[a] Spectra were recorded at 9.4 T with 7 kHz MAS, using a radiofrequency (RF) offset frequency (in ppm) corresponding in turn to each Q^n region (shown in parentheses). [b] Isotropic chemical shift (in ppm) derived from simulation of the experimental NMR spectrum. The corresponding Q^n region is shown in parentheses. [c] The CS_{iso} and CSA uncertainties represent

the variation in each parameter that causes a 1 % decrease in fit quality, defined as the overlap between the simulated and experimental spectra (see Methods section for details).

Overall, the frequency-selective ^{RESPIRATION}CP spectra show that nearly-dry P-SPP contains predominantly P-sites with chemical shifts in the Q^3 and Q^2 regions, with a minor contribution from P-sites with chemical shifts in the Q^1 region. There is no evidence for a significant Q^0 signal in the nearly-dry state. Furthermore, although there are at least two distinct types of P-sites with chemical shifts in the Q^3 region, the observed CSA values suggest that neither corresponds to P_4O_{10}. To be sure that they are covalently bound to the zeosil, the existence of P-O-Si connectivity must be established by direct experiments.

3.2.4 Introducing a more precise nomenclature for P-speciation

The appearance of multiple types of sites with signals in the same Q^n category suggests the need for a more descriptive notation. Here we introduce a more precise nomenclature for P-species using the label Q^n_m, where the upper index (n) represents the total number of P-O-Y bonds. Y can either be Si or P (note that this definition differs from the original definition of n used in Scheme 3.1). The lower index (m) indicates the number of P-O-Si bonds. Thus, the signal for the surface-bound site $(SiO)_3P{=}O$ is denoted Q^3_3. This notation enables us to distinguish between signals for exclusively surface-bound P-sites (m = n), free (poly)phosphoric acid oligomers (m = 0) and surface-bound polyphosphoric acid species (0 < m < n). It is especially useful for describing "mixed" sites in which a surface-bound P-site is also part of a polyphosphoric acid oligomer. For example, Q^3_2 precisely identifies the Q^3 signal corresponding to the surface-bound P-site (underlined) in $(SiO)_2\underline{P}(O)OP(O)(OX)_2$, where X

denotes H or Y (Si or P). Moreover, this notation is readily adapted to describe multinuclear sites. For example, a dinuclear site with two P-sites connected via a P-O-P linkage could be represented by Q_2^3-Q_2^3. Similarly, a trinuclear site could be denoted Q_2^3-Q_0^2-Q_2^3. The Q_m^n notation identifies signals with different n values that have distinct chemical shifts, regardless of m. A corollary is that Q_m^n signals with different m values have similar chemical shifts if they have the same n. Therefore, the simpler Q^n designation includes all signals for distinct P-sites with $m \leq n$, i.e., with the same number of P-O-H bonds. Q_0^0 is, of course, synonymous with Q^0, because only m = 0 is possible. Some of the possible structures for P-sites belonging to the same Q^n categories are shown in Scheme 3.3.

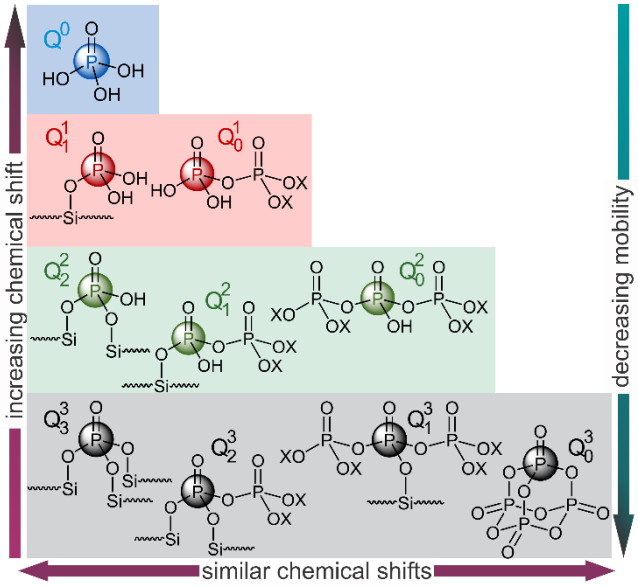

Scheme 3.3 Some of the P-sites possible in P-SPP, including surface-bound sites, free polyphosphoric acid oligomers, and mixed sites.[a] The sites (indicated with colored circles) are grouped horizontally according to chemical shift, and ranked vertically in order of their mobility. [a] X denotes H, Si or P.

3.2.5 Impact of hydrolysis on Brønsted acidity in P-SPP

Before attempting to identify P-sites spectroscopically, we explored local P-site structure variations and their potential impact on the Brønsted acidity of P-SPP. Experimental investigations of acidity differences via titration and/or probe reactions are convoluted with changes in site distribution, therefore we undertook an assessment of the relative acidities of a subset of individual P-sites using gas phase electronic structure calculations instead. Due to the complexity of the SPP structure (Scheme 3.2), we constructed simple cluster models of mono-, di- and trinuclear sites capped with silyl groups ($-SiH_3$). For example the mononuclear P-sites in P-SPP are represented by Q^3_3, Q^2_2, Q^1_1 and Q^0 cluster models, i.e., the series corresponding to progressive hydrolysis of a Q^3_3 cluster model, according to Scheme 3.3.

In general, even proton transfers involve the nuclear motion of several atoms. We simplified the problem by limiting our preliminary analysis to a comparison of electronic structures, using a frontier orbital approach. In Mulliken's charge transfer theory, proton transfer starts with formation of a hydrogen-bond between a Brønsted acid (H-bond donor, D) and a base (H-bond acceptor, A), in an acid-base adduct [DH···A].[61–64] In the process, electron density is transferred from a non-bonding pair on the base to an antibonding orbital on the acid. The wavefunction of the acid-base adduct is a superposition of several contributions, including ionic ($D^{-}\cdots HA^{+}$) and polar ($D^{-}\cdots H^{+}\cdots A$) resonance forms.[65–69] The polar resonance structure is particularly important when the transferring H-in-flight is stabilized electrostatically by the donor and acceptor, especially when there is no activation barrier for proton transfer.[70,71] The D-H heterolytic bond strength (i.e., the deprotonation energy) is therefore a potential descriptor of acidity. However, Keeffe et al.[72] demonstrated that these bond strengths correlate poorly when the reaction has an activation barrier. In such cases, ab

initio calculations confirm the importance of the ionic form to charge transfer between the H-bond donor and acceptor, and the constancy of partial charge on the H-in-flight (0.3-0.5 e, depending on the charge localization method).[61,63–65]

For the series of P-acids represented by cluster models here, each interacting with the same base, the relevant antibonding orbital is the lowest unoccupied molecular orbital (LUMO), shown in Figures A3.14-A3.17 and the geometric coordinates are given in Table S2. Its energy determines the HOMO-LUMO gap, where a smaller gap corresponds to a more acidic proton. A corollary is that the LUMO energies reflect the relative abilities of each acid site to accept electron density, and relinquish a proton, even without explicit reference to a specific base. For sites with more than one acidic proton, the LUMO of the geometry-optimized structure is delocalized over all chemically equivalent OH groups.

The LUMO energies are given in Figure 3.4 and Table A3.3. Of the mononuclear P-site models, the Q_2^2 model is the least acidic, while the Q_1^1 and Q^0 models have similar acidities. Initial hydrolysis of a P-O-Si linkage therefore results in increased acidity. We note that when the P-sites are embedded in the zeosil, some of their POH groups may engage in H-bonding with silanol groups of nearby defect sites. Such interactions will alter the shape of the LUMO and its relative energy, resulting in increased acidity of the remaining (i.e., non-H-bonded) POH groups. For example, a Q_1^1 site might become less acidic than a Q_2^2 site, if one of the OH groups of Q_1^1 is H-bonded.

The impact of H-bonding on acidity is clearly evident in the dinuclear P-site models Q_m^n-$Q_{m'}^{n'}$ (all with a single P-O-P linkage), shown in Figure A3.15. For each optimized geometry, the number of H-bonds in maximized, and the LUMO is delocalized over the protons that do not participate in H-bonds. The regions of LUMO delocalization correspond

to areas of more positive electrostatic potential, where a base would bind more strongly. For example, in the dinuclear Q_0^1-Q_0^1 model cluster with four acidic hydroxyl groups, the minimum energy structure has two hydroxyls H-bonded to O=P groups and two that are free from H-bonding (one on each of the two P-sites). The minimum energy structures for the Q_1^2-Q_0^1 and Q_2^3-Q_0^1 models each have a single non-H-bonded OH, located on the Q_0^1 P-site. In the Q_1^2-Q_1^2 and Q_2^3-Q_1^2 models, all OH groups are engaged in H-bonds in the lowest energy structures.

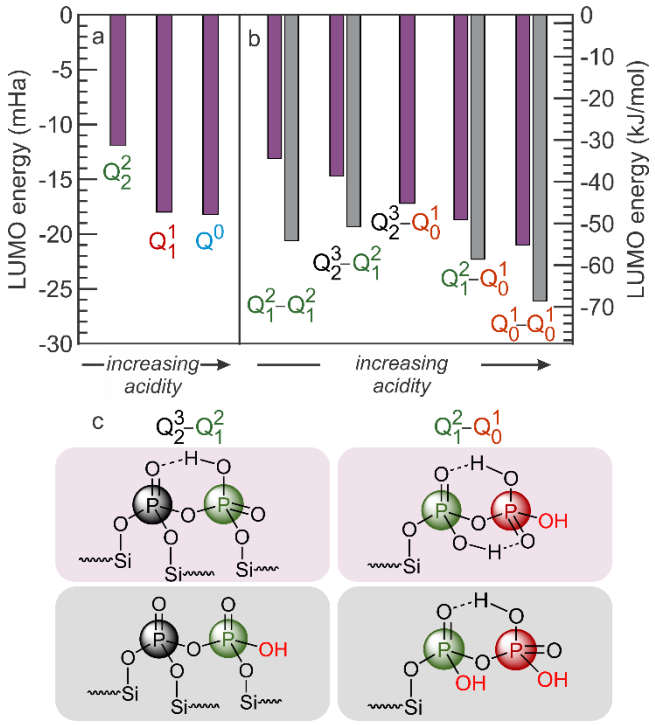

Figure 3.4 Comparison of calculated energies for the lowest unoccupied molecular orbital (LUMO) in model clusters, for representative P-sites which are (a) mononuclear, and (b) dinuclear. Purple bars represent energies for minimum-energy geometries; gray bars represent higher energy structures with fewer H-bonds. (c) Comparison of structures depict geometries with different numbers of H-bonds, for two of the dinuclear models.

Similar to the mononuclear models, the overall pattern that emerges for many of the dinuclear models is enhanced acidity as the P-O-Si linkages are progressively hydrolysed, in the order Q_2^3-Q_1^2 < Q_2^3-Q_0^1 < Q_1^2-Q_0^1 < Q_0^1-Q_0^1, (Figure 3.4b and Scheme A3.1). The predicted acidity of the Q_1^2-Q_1^2 model is anomalously low, likely because it has no hydroxyl groups free of H-bonding in the minimum-energy geometry. The prediction for the Q_2^3-Q_0^1 model may be affected by partly delocalization of its LUMO over a silyl H atom, increasing the acidity of its free OH.

We investigated the impact of H-bonding on acidity in the dinuclear models. Conformations close to the global minimum-energy geometry, but with fewer intramolecular H-bonds, are shown in the gray bars in Figure 3.4b; some structures are compared in Figure 3.4c. For example, the Q_0^1-Q_0^1 conformer with one H-bond has a higher total energy (by 11.5 kJ/mol), and a lower LUMO energy (indicating stronger acidity), compared to the global minimum structure with two H-bonds. Disrupting one H-bond in each of the Q_1^2-Q_0^1 and Q_2^3-Q_1^2 models likewise increases the conformer energies, while lowering the corresponding LUMO energies, hence increasing their acidity. We note that the predicted differences in acidity caused by such changes in conformation are similar in magnitude to differences between minimum energy conformers for the dinuclear structures. For example, the higher energy Q_1^2-Q_0^1 conformer is noticeably more acidic than the minimum-energy Q_2^3-Q_0^1 conformer (for the latter, no higher energy structure without the H-bond was located).

The higher energy dinuclear conformers (computed as gas phase models) all appear to be readily accessible at finite temperatures. For example, at ca. 100 °C, they lie within 3 k_BT of their minimum-energy geometries (k_B is Boltzmann's constant). Although H-bonding with

silanol groups or framework oxygen atoms is possible in the zeolite, causing the minimum-energy geometries of the P-sites to differ from its gas phase geometry, the situation is expected to be similar (with the caveats that confinement may restrict conformational changes, or modulate the time scales over which they occur). The acidity of an individual P-site is, therefore, dynamic, and a more complete assessment require a statistical model to predict the average acidity for a distribution of species and conformations.

A comparison of the dinuclear and mononuclear model energies in Figure 3.4 further reveals that P-O-P hydrolysis generally results in reduced acidity. For example, the OH group of the Q_0^1 side of the Q_1^2-Q_0^1 site is slightly more acidic than Q^0 itself. Similarly, breaking the P-O-P bond in dinuclear Q_0^1-Q_0^1 yields two mononuclear Q^0 sites that are less acidic than the dinuclear site as reported experimentally[73]. Similar trends are seen in the LUMO energies of trinuclear model sites: the acidity of Q_2^3-Q_0^2-Q_0^1 is higher than that of dinuclear Q_2^3-Q_0^1, formed by P-O-P hydrolysis (Table A3.3).

Thus, our calculations predict that the presence of water will change P-site acidity in complex ways. In general, we expect an initial increase due to faster hydrolysis of the P-O-Si linkages, followed by a decrease due to slower hydrolysis of the P-O-P linkages. More sophisticated models capable of predicting the evolution of acidity will require a more precise identification of the P-sites present in the P-zeosil as a function of environmental conditions. As a first step towards such insight, we applied 2D MAS NMR techniques to establish P-O-Si and P-O-P connectivity by resolving Q_m^n signals corresponding to structures with different m values.

3.2.6 Spectroscopic evidence for surface-bound P-sites

P-O-Si linkages have been identified in well-defined, crystalline silicophosphates, via their ^{29}Si and ^{31}P NMR spectroscopic signatures.[32,41,74] For example, the ^{29}Si signal at ca. -210 ppm for six-coordinate Si atoms in crystalline $Si_5O(PO_4)_6$ was associated with a ^{31}P signal at -44 ppm using *J*- and *D*- based 2D correlation spectroscopy.[32] Mixed-phase materials such as silicophosphate gels, consisting of the crystalline phases $Si_5O(PO_4)_6$, $Si(HPO_4)_2$•H_2O and SiP_2O_7 as well as amorphous phases, have also been studied by ^{29}Si and ^{31}P NMR.[30,31,40] While P-O-Si linkages were identified in the crystalline phases, peak assignments for the amorphous phase were ambiguous due to chemical shift overlap for species with P-O-P and/or P-O-Si linkages (Scheme 3.1).

Since we ruled out P_4O_{10} as the origin of Q^3 signals based on comparison of their CSA values, the signals must arise from sites that contain P-O-Si linkages. Candidates include Q_3^3 and $Q_2^3 - Q_2^3$ sites. With DNP-induced signal amplification, it becomes feasible to establish the presence of P-O-Si linkages based on through-space dipolar coupling between ^{29}Si and ^{31}P. Specifically, a Double CP (DCP) pulse sequence[75] can selectively detect ^{31}P NMR signals from sites that are spatially proximal to ^{29}Si. Since the DCP transfer efficiency depends on through-space dipolar coupling from ^{1}H to ^{29}Si to ^{31}P, only ^{31}P sites connected to nearby ^{29}Si sites (e.g., surface-bound P-sites) yield strong intensities, while P-sites that interact weakly with ^{29}Si atoms in the zeosil framework should result in low or no intensity.

DNP-enhanced ^{31}P MAS-NMR spectra recorded for nearly-dry P-SPP, with and without ^{29}Si-filtering, are compared in Figure 3.5a. The strong signal intensities observed for both the Q^3 and Q^2 regions of the ^{29}Si-filtered DCP spectrum suggest that these include P-sites with P-O-Si linkages. Due to the low overall DCP efficiency, the evidence is only qualitative.

Even so, the total intensity of the Q^3 signals (including their spinning sidebands) relative to the Q^2 signals is higher in the ^{29}Si-filtered ^{31}P DCP spectrum compared to the ramped ^{1}H-^{31}P CP spectrum. This finding implies that P-sites with signals in the Q^3 region have, on average, more P-O-Si linkages than P-sites with signals in the Q^2 region. The minor Q^1 signal observed via $^{\text{RESPIRATION}}$CP is not resolved in the CP and DCP spectra, and hence will not be discussed further here.

More quantitative information about the average ^{29}Si-^{31}P coupling strength was sought for each group of P-sites by acquiring buildup curves. Figure 3.5c shows how the peak intensity for each type of Q^n signal in the ^{29}Si-filtered ^{31}P DCP spectra (I_{DCP}) varies relative to its intensity in the ^{31}P CP spectrum (I_{CP}), as a function of the DCP mixing time, τ_{DCP}. A mono-exponential equation, $I_{DCP}/I_{CP} = a(1-\exp(-\tau_{DCP}/T_{DCP}))$, was refined to the data to obtain the buildup time constant T_{DCP}. I_{DCP}/I_{CP} is the ratio of the peak intensities in the DCP and CP spectra for a given value of τ_{DCP}, and the constant a is the asymptotic value of the corresponding ratio. In the absence of nuclear spin relaxation, the latter corresponds to the fraction of ^{31}P sites with at least one P-O-Si linkage, assuming 100 % DCP efficiency. (Since in practice the DCP efficiency is lower, the value of a is difficult to interpret quantitatively, therefore we will not discuss the refined values further.)

For nearly-dry P-SPP, the value of T_{DCP} for the Q^3 signals is (20.0 ± 0.9) s. This is shorter than for the Q^2 signals, (32.8 ± 7.1) s, indicating that the P-sites responsible for the Q^3 signals are more strongly coupled to Si relative to those responsible for the Q^2 signals. This finding is consistent with the relative intensities of the signals in the ^{29}Si-filtered ^{31}P DCP spectra (Figure 3.5a).

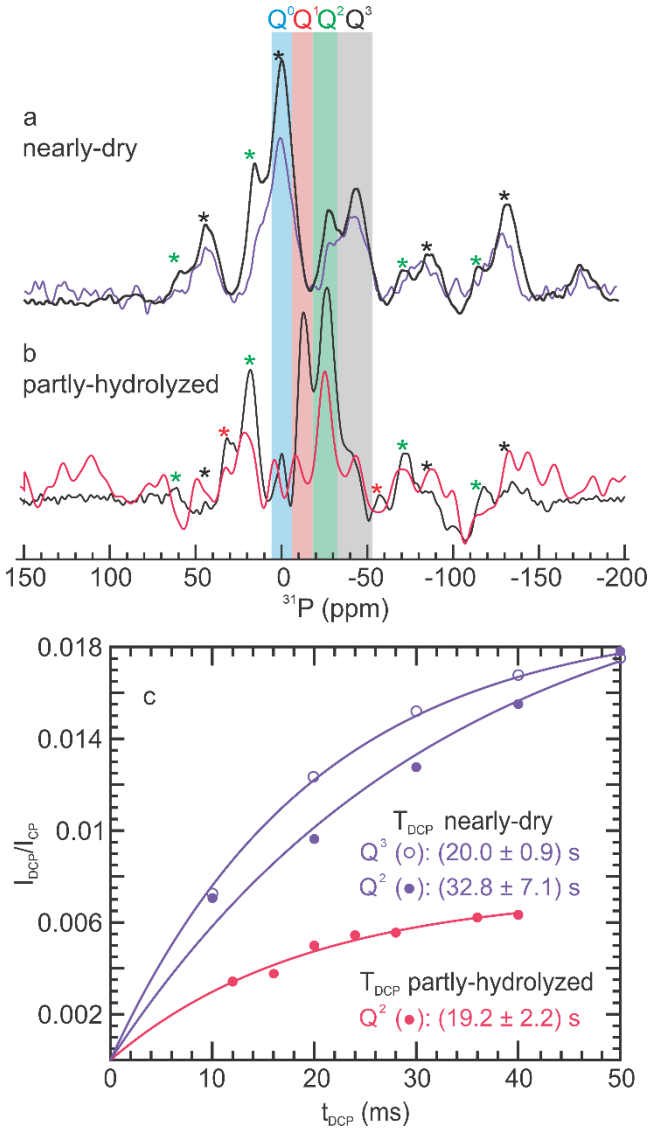

Figure 3.5 Comparison of DNP-enhanced ^{1}H-^{31}P CP and ^{29}Si-filtered ^{31}P DCP MAS-NMR spectra (a,b), and the corresponding DCP buildup curves (c), for nearly-dry and partly-hydrolyzed P-SPP. Both ^{1}H-^{31}P CP spectra (black) were acquired in 16 scans. The DCP spectra (colored) were acquired for (a) nearly-dry material (2048 scans), and (b) partly-hydrolyzed material (768 scans), prepared by exposure of the dry material to air for 2 or 10 min, respectively. Both were recorded with a 40 ms mixing time ($\boldsymbol{\tau}_{DCP}$). Spinning sidebands for Q^1, Q^2, and Q^3 signals are indicated by * in red, green, and black, respectively. (c) ^{31}P DCP peak

intensity relative to CP intensity (both normalized by number of scans), for various signals as a function of mixing time. The solid lines are curvefits obtained using a mono-exponential model (see below). Experimental spectra for all mixing times, and the regions used to obtain the peak areas, are shown in Figure A3.8.

Thus nearly-dry P-SPP contains at least two major P-sites with signals in the Q^3 region (differing in chemical shifts and CSAs), neither of which is P_4O_{10}, and at least one major site with a signal in the Q^2 region. P-sites with signals in the Q^1 region make a minor contribution. P-O-Si linkages are present in all major sites, but are relatively more abundant in those with Q^3 signals. Table 3.2 shows the minimum number of structures required to account for the experimental observations for dry/nearly-dry P-SPP. The slower buildup of the Q^2 signals is consistent with Q_2^3-Q_1^2 sites formed by hydrolysis of Q_2^3-Q_2^3, or with non-surface-bound Q_0^2 sites, possibly as part of more complex, trinuclear P-sites such as Q_2^3-Q_0^2-Q_2^3.

To probe the sensitivity of the P-O-Si linkages to water, P-SPP was partly-hydrolyzed by increasing the ambient exposure time to 10 min. In the ^{1}H-^{31}P CP spectrum (without ^{29}Si-filtering), the signal intensity in the Q^3 region of the partly-hydrolyzed material is much lower (Figure 3.5b) relative to that of the nearly-dry material (dominated by Q^3 signals). The signal intensities in both the Q^2 and Q^1 regions are comparable, and higher than in the Q^3 region. Furthermore, a small Q^0 signal representing H_3PO_4 that was absent in the spectrum of the nearly-dry material becomes visible for the partly-hydrolyzed material. For all τ_{DCP} values tested, the residual Q^3 signal is weak in the ^{29}Si-filtered DCP spectrum of the partly-hydrolyzed material, Figure A3.8b. Given the low peak intensity, the T_{DNP} value could not be

measured. Nevertheless, the persistence of a Q^3 signal suggests that some surface-bound Q^3 P-sites (e.g., Q_3^3 and/or Q_2^3) remain.

Table 3.2. Spectroscopic evidence for proposed structures of major mononuclear and dinuclear P-sites present in P-SPP, in three different hydration states

Label	Structure	Hydration state		
		Nearly dry	Partly hydrolyzed	Fully hydrolyzed
Q_3^3	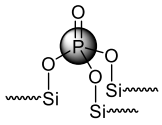	DCP		
Q_2^3-Q_2^3	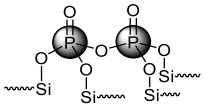	DCP	DCP	
Q_1^2-Q_1^2	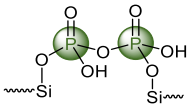	DCP	DCP	
Q_2^2	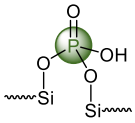		DCP	
Q_0^1-Q_0^1	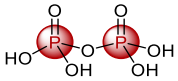		DCP	DCP
Q^0	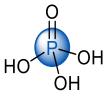			DCP
Q_2^3-Q_1^2	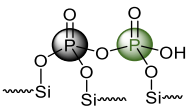	RFDR	RFDR	

Q_1^2-Q_0^1	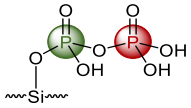	RFDR

The most intense signal, in the Q^2 region, arises from surface-bound P-sites with lower CSA relative to the nearly-dry state (i.e., Q_2^2 and/or Q_1^2). Moreover, the buildup time for this signal, (19.2 ± 2.2 s), is much shorter than for the nearly-dry material (32.8 ± 7.1 s), suggesting that partial hydrolysis leads to a new type of surface-bound P-site in the Q^2 region. The most likely candidate is Q_2^2, arising from hydrolysis of Q_3^3 (Scheme 3.4 and Scheme A3.2). Finally, the suppression of the Q^1 signal in the ^{29}Si-filtered ^{31}P DCP spectrum is consistent with its assignment to Q_0^1, arising from P-sites that are not surface-bound. The poor SNR for signal in the Q^1 region precludes measurement of an accurate buildup time for this signal. Table 3.2 shows the minimum number of structures required to account for the spectra of the P-sites in partly-hydrolyzed P-SPP.

The CP and DCP experiments were repeated after exposure of P-SPP to air for 10 d to generate a fully-hydrolyzed material (Figure A3.8c). Both NMR spectra are dominated by the signal corresponding to H_3PO_4 (Q^0), which remains associated with the zeolite but lacks P-O-Si linkages. The overall SNR of the ^{29}Si-filtered ^{31}P DCP spectrum is significantly lower compared to spectra of the nearly-dry or partly-hydrolyzed material, consistent with cleavage of all P-O-Si linkages. As expected, the DCP buildup time for the Q^0 peak in the fully-hydrolyzed material is very slow, (50 ± 11) s (Figure A3.9), compared to the Q^3 and Q^2 buildup rates in the nearly-dry and partly-hydrolyzed states.

These DCP experiments provide direct evidence for P-O-Si linkages in dry P-SPP, and their hydrolysis with increasing exposure to water. However, a coherent explanation for the

spectroscopic observations requires P-species containing P-O-P as well as P-O-Si linkages. The minimum number of structures required therefore includes the dinuclear P-sites shown in Table 3.2. To verify this hypothesis, we investigated the presence of P-O-P′ linkages in P-SPP using 2D ^{31}P-^{31}P correlation spectroscopy. The results allow us to assess the relationships between sites containing P-O-P linkages and those with P-O-Si linkages, and to evaluate their relative hydrolytic stabilities.

3.2.7 Spectroscopic evidence for P-O-P′ linkages

The existence of oligomers in concentrated phosphoric acid solutions is well-known.[4] To investigate the presence of oligomers containing P-O-P linkages in P-SPP, we acquired homonuclear ^{31}P-^{31}P correlation spectra, using a radio-frequency-driven recoupling (RFDR) pulse sequence.[76] Polarization is transferred from one P-site to a nearby P-site via dipolar (through-space) coupling. For P-sites directly linked via a bridging oxygen (P-O-P), the coupling was reported to be ca. 900 Hz (described as "strongly-correlated").[39] Numerical simulations based on quantum mechanics suggest that an RFDR mixing time (τ_{RFDR}) of ca. 700 μs is optimal to detect strongly-correlated P-sites (Figure A3.10). Adjacent P-sites not connected by P-O-P linkages, i.e., "weakly-correlated" sites with dipolar couplings <900 Hz, require a longer τ_{RFDR} for efficient polarization transfer.

Figure 3.6a shows the 2D homonuclear ^{31}P-^{31}P correlation spectrum for nearly-dry P-SPP, recorded with DNP enhancement. It includes isotropic self-correlations (along the main diagonal) and correlations between each isotropic signal and its sidebands (along the secondary diagonals, parallel to the main diagonal but separated from it by the spinning frequency). The main on-diagonal peaks at (-29, -29), (-43, -43) ppm are self-correlations of

the Q^2 and Q^3 signals, respectively; the self-correlation of a Q^3 spinning sideband is visible at (-1, -1) ppm. Peaks on the secondary diagonals at (-1, -43) and (-43, -1) ppm are self-correlations between the isotropic Q^3 signals and their spinning sidebands.

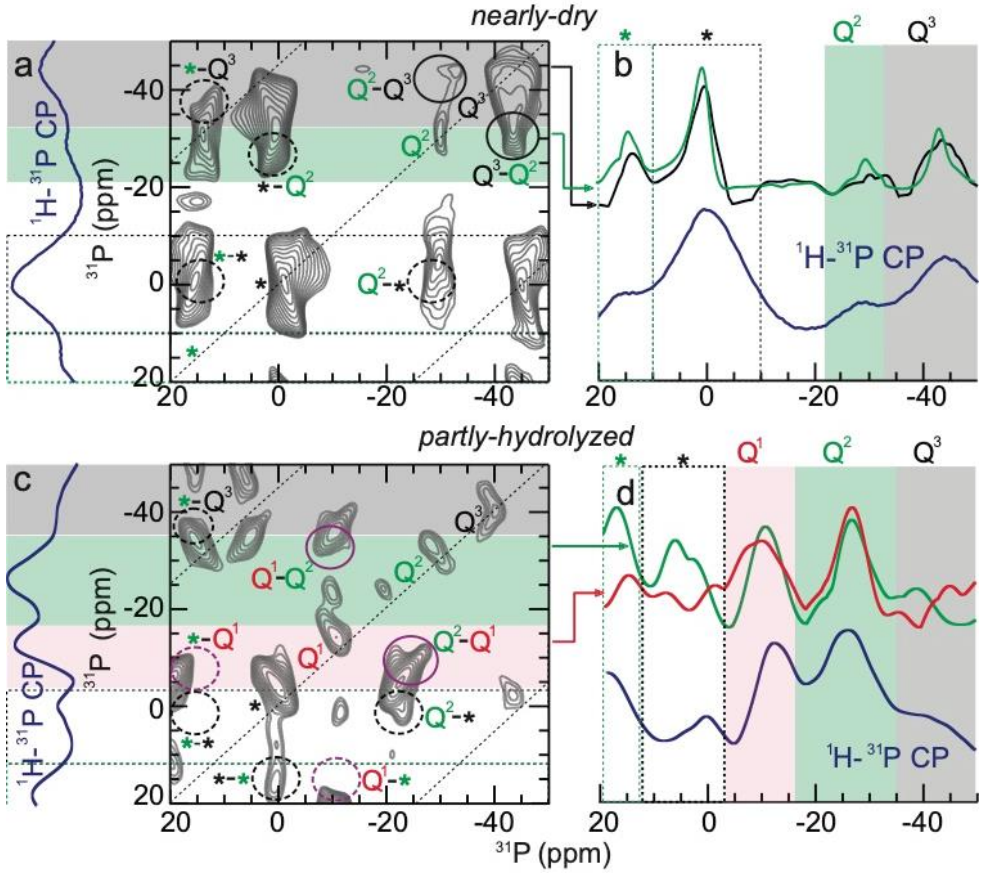

Figure 3.6 DNP-enhanced ^{31}P-^{31}P correlation spectra and their 1D projections for: (a,b) nearly-dry P-SPP, and (c,d) partly-hydrolyzed P-SPP. Both spectra were recorded at 9.4 T and 7 kHz MAS, with an RFDR mixing time of 714 μs. For reference, the corresponding ^{1}H-^{31}P CP spectra are shown to the left of the 2D plots, and below the 1D projections in blue. The gray, green and red shaded stripes highlight the Q^3, Q^2, and Q^1 regions, respectively. The corresponding sideband regions are shown by the dashed (unshaded) stripes (same color codes). Asterisks denote spinning sidebands for Q^3 (gray) and Q^2 (green) signals, respectively.

Solid circles denote Q^3-Q^2 (black) and Q^2-Q^1 (purple) cross-peaks, respectively. Dashed circles indicate cross-peaks involving a spinning sideband.

The key new information in these data is contained in the off-diagonal peaks, or cross-peaks, which indicate proximity between P-sites with different chemical shifts. They reveal proximal P-sites whose Q^n signals correspond to different *n* values (i.e., P-O-P′ linkages). Off-diagonal cross-peaks are located at (0, -30), (-30, 0), (-30, -43) and (-43, -30) ppm. Their chemical shift values indicate a correlation between a Q^3 signal (or its spinning sideband) and a Q^2 signal. These cross-correlations can also be observed in the 1D projections of the regions for different Q^n signals. Figure 3.6b compares these projections for the Q^3 and Q^2 regions with the ^{1}H-^{31}P CP spectrum (blue). The row from the Q^3 region (black) clearly contains the Q^2 signal, while the row from the Q^2 region (green) also clearly contains the Q^3 signal. This result confirms a strong correlation between Q^3 and Q^2 signals, arising from dinuclear P-sites.

Even if present, proximal P-sites whose Q^n signals correspond to the same *n* and *m* values (i.e., identical P-sites linked by P-O-P, such as Q^3_2-Q^3_2), cannot be distinguished from self-correlations in the 2D RFDR spectra. Although cross-peaks for signals with the same *n* value but different *m* values, such as Q^3_2-Q^3_1, are in principle observable, they will appear near the broad on-diagonal peaks and may be difficult to resolve. Double quantum-single quantum (DQ-SQ) NMR experiments[77] could be used to obtain correlations between such sites with similar chemical shifts. However, our attempts to conduct such experiments with P-SPP using the supercycled POST C5 (SPC5) pulse sequence[78] were unsuccessful, most likely due to the large ^{31}P CSA and/or rapid ^{31}P relaxation.

To confirm that the cross-peaks in the RFDR spectra of the nearly-dry material arise due to intramolecular P-O-P′ linkages, rather than intermolecular correlations, the same 2D experiment was repeated with a longer mixing time (Figure A3.11). The optimum mixing time for weakly-coupled P-sites (i.e., those not linked via P-O-P′) should be significantly longer. However, the intensities of the cross-peaks relative to the diagonal peaks did not increase upon doubling τ_{RFDR} from 714 to 1428 μs (see Figures A3.11-A3.13). Thus, the Q^3-Q^2 cross-peaks arise from strongly-correlated (P-O-P′-linked) dinuclear sites. This observation is consistent with the presence of Q_2^3-Q_1^2 sites, as shown in Table 3.2. Their presence in nearly-dry P-SPP was suggested by the ^{RESPIRATION}CP results (Figure 3.3b), which revealed a second type of Q^3 site (in addition to mononuclear Q_3^3). The postulated Q_2^3-Q_2^3 sites should generate Q_2^3-Q_1^2 sites upon hydrolysis. Such a transformation is consistent with the greater susceptibility of the P-O-Si linkage relative to the P-O-P linkage.

The RFDR spectrum of partly-hydrolyzed P-SPP shows on-diagonal peaks for all four Q^n regions (Figure 3.6c). A pair of cross-peaks at (-12, -26) and (-26, -12) ppm correlates Q^1 and Q^2 signals, and hence implies a P-O-P′ relationship between them. A second pair of cross-peaks at (-2, +18) and (+18, -2) ppm correlates Q^3 and Q^2 spinning sidebands. A cross-peak at (-23, -2) ppm relates the isotropic Q^2 signal to a Q^3 spinning sideband, while a cross-peak at (+15, -38 ppm) relates a Q^2 sideband to the isotropic Q^3 signal. These correlations confirm the existence of P-O-P′ linkages in two kinds of dinuclear P-sites, giving rise to Q^2-Q^1 and Q^3-Q^2 signals (Table 3.2). The 1D projections of the corresponding rows in the Q^2 (green) and Q^1 (red) regions show the appropriate cross-peaks (Figure 3.6d). In combination with the ^{29}Si-filtered ^{31}P DCP NMR results, this finding suggests two kinds of dinuclear P-sites in partly-hydrolyzed P-SPP, depicted in Table 3.2 as Q_2^3-Q_1^2 and Q_1^2-Q_0^1.

3.2.8 Origin of the P-site distribution in P-SPP

Based on all the spectroscopic information presented thus far, the P-sites and their hydrolysis pathways are summarized in Scheme 3.4. Due to the low P-loading (Si/P = 27), we consider only mononuclear and dinuclear P-sites in this minimal model. However, the co-existence of larger oligomers in P-SPP cannot be ruled out. Certain trinuclear mixed species, shown in the SI, would also give signals consistent with the experimental observations.

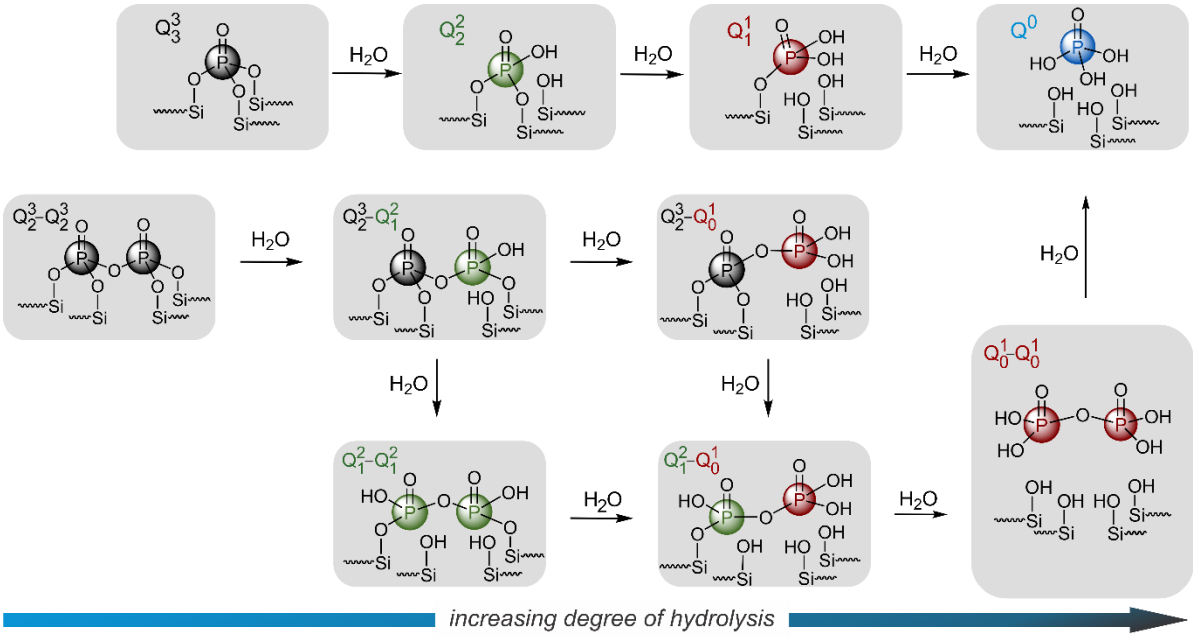

Scheme 3.4 Proposed structures for the major P-sites in P-SPP and their corresponding Q_m^n signal designations, as well as their likely hydrolysis pathways.

In the top row of Scheme 3.4, surface-bound Q_3^3 sites reflect condensation of H_3PO_4 with silanol nest defects in the SPP micropores and/or external (mesopore) silanols. These

sites should be converted by hydrolysis to Q_2^2, Q_1^1, and finally, Q^0 sites. Both Q_3^3 and Q_2^2 signals are present in the spectrum of the partly-hydrolyzed material. However, the NMR signature of surface-bound Q_1^1 was not observed in the ^{29}Si-filtered ^{31}P DCP spectrum of partly-hydrolyzed P-SPP, suggesting that this site is particularly unstable towards hydrolysis, and hence evades detection.

In the second row of Scheme 3.4, dinuclear surface-bound Q_2^3-Q_2^3 sites reflect reactions of $H_4P_2O_7$ with silanol nests. Hydrolysis of one of the P-O-Si bonds would result in formation of Q_2^3-Q_1^2 sites (consistent with the DCP results reported above, and confirmed by RFDR). Further P-O-Si hydrolysis would account for our observations of several mixed P-sites: Q_2^3-Q_0^1, Q_1^2-Q_1^2, and Q_1^2-Q_0^1 as well as free pyrophosphoric acid (Q_0^1-Q_0^1). The intermediate hydrolysis products Q_1^2-Q_1^2 and Q_0^1-Q_0^1, while expected, cannot be observed by RFDR. However, the presence of Q_0^1-Q_0^1 sites can be inferred from the observation of a Q^1 signal in the ^{1}H-^{31}P CP spectrum of partly hydrolyzed P-SPP (Figure 3.5b), combined with the finding that these are not Q_1^1 sites based on analysis of the ^{29}Si-filtered ^{31}P DCP spectrum. Thus we conclude that the Q^1 signals represent Q_0^1-Q_0^1 sites. Eventually, all surface-bound P-sites are converted to Q^0 sites in the fully-hydrolyzed state. However, the persistence of P-O-P linkages and the late appearance of the Q^0 signal, is consistent with the expected greater hydrolytic instability of P-O-Si relative to P-O-P.

3.3 Conclusions

Phosphorus-modified self-pillared pentasil (P-SPP) is highly selective in the formation of biomass-derived commodity chemicals such as *p*-xylene and butadiene.[14,15] The origin of the catalytic activity lies in the structures of its confined P-sites, whose moderate Brønsted acidity (P-OH) promotes selective transformations aided by the shape- and size-constraints of the zeolite micropores. The nature of the P-sites, including how they interact with the zeolite framework and with each other, was explored using DNP-enhanced solid-state NMR spectroscopy, including $^{\text{RESPIRATION}}$CP NMR, ^{29}Si-filtered ^{31}P DCP NMR, and 2D ^{31}P-^{31}P correlation NMR, in combination with DFT calculations. Dry P-SPP contains predominantly two types of fully-condensed P-sites: mononuclear (Q^3_3) and oligomeric (most likely dinuclear, Q^3_2-Q^3_2). Although neither is acidic, the NMR results confirm that both are surface-bound. Their presence was confirmed by ^{29}Si-filtered ^{31}P DCP correlation NMR spectroscopy. The mononuclear site undergoes hydrolysis of a P-O-Si linkage to form a Q^2_2 site, before eventually being converted to H_3PO_4 (Q^0), presumably via an unstable Q^1_1 intermediate.

Frequency-selective detection using $^{\text{RESPIRATION}}$CP suggests the presence of additional dinuclear P-sites with *both* P-O-Si and P-O-P linkages in dry P-SPP. The most likely candidate is surface-bound Q^3_2-Q^3_2. It is rapidly converted to a Q^3_2-Q^2_1 site, detected by 2D ^{31}P-^{31}P correlation NMR, via selective hydrolysis of a P-O-Si linkage when the zeolite is briefly exposed to moisture. Further hydrolysis leads to the formation of other surface-bound dinuclear sites such as a Q^2_1-Q^1_0 site, leading eventually to non-surface-bound $H_4P_2O_7$ (Q^1_0-Q^1_0). The P-O-P linkage is the last to hydrolyze, finally forming H_3PO_4 (Q^0).

This study reveals that the Brønsted acidity in P-SPP arises from a diverse mixture of partly-hydrolyzed surface-bound and non-surface-bound mononuclear and dinuclear sites, even at low P-loadings (P/Si = 27). The presence of trinuclear and higher oligomers cannot be excluded, and are presumably even more important for zeosils with higher P contents. The P-site distribution is determined by the extent of hydrolysis, and has important consequences for the Brønsted acidity. Although the precise identities of the active sites in P-zeosils have yet to be established, and must be under reaction conditions, this work represents a step toward the rational design of supported acid catalysts with improved activity and selectivity.

3.4 Experimental

3.4.1 Sample Preparation

P-modified self-pillared pentasil (P-SPP), with Si/P = 27, was synthesized following a previously described procedure.[19] The material was dried by dehydration at 450 °C and $<10^{-4}$ Torr for 12 h, then packed and sealed in a 3.2-mm zirconia NMR rotor in a N_2-filled glove-box. To obtain partially hydrolyzed materials, the rotor cap was removed manually for a short period of time (timed with a stopwatch), then replaced. Air-exposure times are approximate. The experiments reported in Figure 3.2 were performed on consecutive days, when the relative humidity varied between 74 and 78 % during the measurement time.

3.4.2 Direct excitation solid-state MAS-NMR spectroscopy

^{31}P MAS-NMR measurements were performed at room temperature on a Bruker AVANCE III Ultrashield Plus 18.8 T Spectrometer (corresponding to ^{1}H and ^{31}P frequencies

of 800 and 323.85 MHz, respectively) at a MAS frequency of 20 kHz. The sample was packed in a 3.2 mm zirconia rotor with N_2 gas as both bearing and drive gas to ensure a no exposure to moisture during data acquisition. A single 90 ° excitation pulse of length 7 μs was used on the ^{31}P channel. An aqueous phosphoric acid solution (1 M) provided the chemical shift reference.

3.4.3 DNP-enhanced MAS-NMR spectroscopy

To acquire DNP-enhanced MAS-NMR spectra, 1,1,2,2-tetrachloroethane (TCE, Sigma-Aldrich) was dried using standard procedures[79] and stored over molecular sieves in a Schlenk flask equipped with a Teflon stopcock. The TEKPOL biradical (Cortecnet) was dissolved in TCE under N_2 atmosphere to give a 16 mM solution. In a N_2-filled glove-box, dehydrated P-SPP (30 mg) was mixed with 60 μL of the biradical solution. The resulting paste was packed into 3.2-mm sapphire rotor and sealed in a glass ampule for transfer to the spectrometer. No radical quenching was observed within one week of rotor packing, as judged by the lack of apparent change in the ^{31}P NMR intensities. Experiments were performed on a Bruker 400 MHz MAS-DNP-NMR system at 9.4 T and -178 °C, using as MAS frequency either 5 or 7 kHz. The latter is the maximum spinning rate we can achieve under DNP conditions. Ramped Cross-polarization (ramped-CP), with a ramp on the ^{1}H channel and a rectangular shape on the X (^{31}P or ^{29}Si) channel, was applied to accomplish both ^{1}H-^{31}P and ^{1}H-^{29}Si polarization transfers. The CP efficiency was optimized by varying the RF amplitude (power level) on the X channel while fixing the proton RF amplitude at 68 kHz, with a ramp from 70 to 100 % power. For ^{1}H-^{31}P CP, a contact time of 2 ms was used, with SPINAL-64 decoupling (RF amplitude 110 kHz and 3.8 μs pulse length) during acquisition. Frequency-

selective ^{1}H-^{31}P cross-polarization was achieved using the Rotor Echo Short Pulse Irradiation Cross-Polarization ($^{RESPIRATION}CP$) pulse sequence,[60] with short pulse length of 5 μs. CSA parameter fitting was performed using the Solid Line Shape Analysis (SOLA) toolbox in Topspin-4.0.6 (Bruker), which uses the Haeberlen convention[80] for the chemical shift tensor parameters, $|\delta_{zz} - \delta_{iso}| \geq |\delta_{xx} - \delta_{iso}| \geq |\delta_{yy} - \delta_{iso}|$, where the isotropic CS is defined as $\delta_{iso} = (\delta_{11} + \delta_{22} + \delta_{33})/3$, the CSA is $\Delta\delta = \delta_{zz} - (\delta_{xx} + \delta_{yy})/2$, and the asymmetric parameter is $\eta = (\delta_{yy} - \delta_{xx})/(\delta_{zz} - \delta_{iso})$. The program uses a simplex algorithm to optimize the overlap between simulated and experimental spectra by varying the chemical shift tensor parameters, and line-broadening in each iteration. The uncertainties in the fit parameters were determined by manually varying the CSA and CS_{iso} one by one from the optimum values until the overlap decreased by ±1 %. This change resulted in a visually detectable decrease in fit quality. Reported parameter values are the average of the values in the two error limits.

^{29}Si-filtered ^{31}P DCP spectra were recorded by exciting the ^{29}Si sites using 10 ms of ^{1}H-^{29}Si CP (Figure A3.18) contact time, prior to the DCP block for the ^{29}Si-^{31}P polarization transfer. The ^{1}H-^{29}Si mixing time was optimized to maximize ^{29}Si peak intensities. During DCP, the RF amplitude on the ^{29}Si channel was varied adiabatically using a tangential shape,[81] while a square pulse was used on the ^{31}P channel and SPINAL-64 decoupling (110 kHz RF amplitude and 3.8 μs pulse length) on the ^{1}H channel . The RF amplitudes during the DCP block were optimized by varying the power level on the ^{31}P channel while keeping the ^{29}Si power level fixed. The optimum amplitudes were found to be 39.5 and 31.5 kHz on the ^{29}Si and ^{31}P channels, respectively. Previously, the mixing time τ_{DCP} = 40 ms (used for ^{29}Si-^{31}P polarization transfer via DCP) was shown to be optimal for detecting P-O-Si linkages in previous studies of silicophosphates.[74] To record buildup curves of nearly-dry and hydrolyzed

materials, τ_{DCP} was varied from 10 to 50 ms in steps of 10 ms. For the partly-hydrolyzed material, τ_{DCP} was varied from 10 to 40 ms in steps of 5 ms. Peak intensities for the nearly-dry material were determined by summing the areas under the isotropic peaks in the region -20 to -65 ppm, as well as the areas under the most intense of the corresponding spinning sidebands, i.e., in the region from +30 to -15 ppm. For the partly-hydrolyzed material, only the isotropic peak intensities were considered because the sidebands are much weaker. To obtain I_{DCP}/I_{CP} and plot the buildup curves, the area under each peak and its corresponding sidebands was normalized by the number of scans, then divided by the normalized ^{1}H-^{31}P CP peak area in the same region. The buildup time T_{DCP} was obtained from each buildup curve using a simple mono-exponential model, $I_{DCP}/I_{CP} = a(1-\exp(-\tau_{DCP}/T_{DCP}))$.

^{31}P-^{31}P correlation spectra were recorded using a Radio Frequency Driven Recoupling (RFDR) pulse sequence. DNP-enhanced ^{1}H-^{31}P ramped-CP was used with the aforementioned parameters to increase sensitivity. RFDR was performed using 180 ° pulses of length 5.6 μs on the ^{31}P channel for two mixing times: 714 and 1428 μs, corresponding to 5 and 10 rotor periods, respectively, at 7 kHz MAS. 2D experiments were performed using 160 increments in the indirect dimension, with 8 scans per increment. ^{1}H decoupling was achieved with SPINAL-64 decoupling (110 kHz RF amplitude and 3.8 μs pulse length) during the acquisition and the indirect delay, while CW irradiation (110 kHz amplitude) was used during RFDR mixing period. The 1D projections were calculated in Topspin-4.0.6 by summing the rows of the 2D spectrum in the range -49 to -34 ppm for Q^3, -32 to -21 ppm for Q^2 and -6 to 7 ppm for * (spinning sideband of Q^3). The ratio of the areas of the off-diagonal peaks to the diagonal peaks was used to determine the extent of polarization transfer.

The numerical simulations for determining the optimum RFDR mixing time were performed using SIMPSON-4.0.[82] A spin system was constructed with two ^{31}P spins, corresponding to Q^2 and Q^3 signals with appropriate chemical shift tensor parameters (isotropic chemical shifts of -43 and -29 ppm, and anisotropies of -190 and -125 ppm, respectively). The MAS frequency of 7 kHz and proton frequency of 400 MHz were used in the simulations to mimic the experimental conditions. Buildup curves were simulated for dipolar couplings of 1200, 900, 600, and 300 Hz (Figure A3.10). For a P-P dipolar coupling typical of a P-O-P linkage (ca. 900 Hz), maximum polarization transfer using RFDR was achieved after ca. 700 μs.

3.4.4 Electronic structure calculations

All electronic structure calculations were performed with Gaussian 09[83] at the M062X/aug-cc-pvtz level of theory. The SCF cycle convergence was set at 10^{-8}, and optimized geometries were converged to 0.0003 Ha/Bohr. Stationary points were verified by vibrational frequency analysis (zero imaginary frequencies).

Acknowledgement of contribution: I thank Professor Sheetal K. Jain for designing the NMR measurements, Dr Stavros Caratzoulas for performing the DFT calculations and Dr Limin Ren for synthesizing the materials. I also thank Li Li for initial sample preparation and handling. I acknowledge Professor Michael Tsapatsis and Professor Wei Fan for their insights and collaborative efforts in the characterization of the materials.

3.5 References

(1) Muraza, O.; Galadima, A. Isomerization and Alkylation of Biomass-Derived Compounds in Aqueous Media over Hydrophobic Solid Acid Catalysts: A Mini Review. *Ind. Eng. Chem. Res* **2014**, *53*, 17869–17877.

(2) Qi, L.; Alamillo, R.; Elliott, W. A.; Andersen, A.; Hoyt, D. W.; Walter, E. D.; Han, K. S.; Washton, N. M.; Rioux, R. M.; Dumesic, J. A.; Scott, S. L. Operando Solid-State NMR Observation of Solvent-Mediated Adsorption-Reaction of Carbohydrates in Zeolites. *ACS Catal.* **2017**, *7*, 3489–3500.

(3) Caeiro, G.; Magnoux, P.; Lopes, J. M.; Ribeiro, F. R.; Menezes, S. M. C.; Costa, A. F.; Cerqueira, H. S. Stabilization Effect of Phosphorus on Steamed H-MFI Zeolites. *Appl. Catal., A* **2006**, *314*, 160–171.

(4) Prinsloo, N. M. Solid Phosphoric Acid Oligomerisation: Manipulating Diesel Selectivity by Controlling Catalyst Hydration. *Fuel Process. Technol.* **2006**, *87*, 437–442.

(5) Cavani, F.; Girotti, G.; Terzoni, G. Effect of Water in the Performance of the "Solid Phosphoric Acid" Catalyst for Alkylation of Benzene to Cumene and for Oligomerization of Propene. *Appl. Cata. A-Gen.* **1993**, *97*, 177–196.

(6) Zhang, J.; Yan, Y.; Chu, Q.; Feng, J. Solid Phosphoric Acid Catalyst for Propene Oligomerization: Effect of Silicon Phosphate Composition. *Fuel Process. Technol.* **2015**, *135*, 2–5.

(7) Zhang, Z.; Lu, Q.; Ye, X.; Wang, T.; Wang, X.; Dong, C. Selective Production of Levoglucosenone from Catalytic Fast Pyrolysis of Biomass Mechanically Mixed with Solid Phosphoric Acid Catalysts. *Bioenerg. Res.* **2015**, *8*, 1263–1274.

(8) Santander, J. A.; Alvarez, M.; Gutierrez, V.; Volpe, M. A. Solid Phosphoric Acid Catalysts Based on Mesoporous Silica for Levoglucosenone Production via Cellulose Fast Pyrolysis. *J. Chem. Technol. Biotechnol.* **2019**, *94*, 484–493.

(9) Blasco, T.; Corma, A.; Martínez-Triguero, J. Hydrothermal Stabilization of ZSM-5 Catalytic-Cracking Additives by Phosphorus Addition. *J. Catal.* **2006**, *237*, 267–277.

(10) Rahimi, N.; Karimzadeh, R. Catalytic Cracking of Hydrocarbons over Modified ZSM-5 Zeolites to Produce Light Olefins: A Review. *Appl. Catal., A* **2011**, *398*, 1–17.

(11) Ding, J.; Wang, M.; Peng, L.; Xue, N.; Wang, Y.; He, M.-Y. Combined Desilication and Phosphorus Modification for High-Silica ZSM-5 Zeolite with Related Study of Hydrocarbon Cracking Performance. *Appl. Catal. A: Gen.* **2015**, *503*, 147–155.

(12) Altynkovich, E. O.; Potapenko, O. V.; Sorokina, T. P.; Doronin, V. P.; Gulyaeva, T. I.; Talzi, V. P. Butane–Butylene Fraction Cracking over Modified ZSM-5 Zeolite. *Pet. Chem.* **2017**, *57*, 215–221.

(13) Xue, N.; Chen, X.; Nie, L.; Guo, X.; Ding, W.; Chen, Y.; Gu, M.; Xie, Z. Understanding the Enhancement of Catalytic Performance for Olefin Cracking: Hydrothermally Stable Acids in P/HZSM-5. *J. Catal.* **2007**, *248*, 20–28.

(14) Cho, H. J.; Ren, L.; Vattipalli, V.; Yeh, Y.-H.; Gould, N.; Xu, B.; Gorte, R. J.; Lobo, R.; Dauenhauer, P. J.; Tsapatsis, M.; Fan, W. Renewable *p* -Xylene from 2,5-Dimethylfuran and Ethylene Using Phosphorus-Containing Zeolite Catalysts. *ChemCatChem* **2017**, *9*, 398–402.

(15) Abdelrahman, O. A.; Park, D. S.; Vinter, K. P.; Spanjers, C. S.; Ren, L.; Cho, H. J.; Vlachos, D. G.; Fan, W.; Tsapatsis, M.; Dauenhauer, P. J. Biomass-Derived Butadiene by Dehydra-Decyclization of Tetrahydrofuran. *ACS Sustain. Chem. Eng.* **2017**, *5*, 3732–3736.

(16) Lercher, J. A.; Rumplmayr, G. Controlled Decrease of Acid Strength by Orthophosphoric Acid on ZSM5. *Appl. Catal.* **1986**, *25*, 215–222.

(17) Wang, X.; Li, W.; Harrington, R.; Liu, F.; Parise, J. B.; Feng, X.; Sparks, D. L. Effect of Ferrihydrite Crystallite Size on Phosphate Adsorption Reactivity. *Environ. Sci. Technol.* **2013**, *47*, 10322–10331.

(18) Wang, X.; Hu, Y.; Tang, Y.; Yang, P.; Feng, X.; Xu, W.; Zhu, M. Phosphate and Phytate Adsorption and Precipitation on Ferrihydrite Surfaces. *Environ. Sci. Technol.* **2017**, *4*, 2193–2204.

(19) Wang, X.; Phillips, B. L.; Boily, J.-F.; Hu, Y.; Hu, Z.; Yang, P.; Feng, X.; Xu, W.; Zhu, M. Phosphate Sorption Speciation and Precipitation Mechanisms on Amorphous Aluminum Hydroxide. *Soil Syst.* **2019**, *3*, 20.

(20) van der Bij, H. E.; Weckhuysen, B. M. Phosphorus Promotion and Poisoning in Zeolite-Based Materials: Synthesis, Characterisation and Catalysis. *Chem. Soc. Rev.* **2015**, *44*, 7406–7428.

(21) Busca, G.; Ramis, G.; Lorenzelli, V.; Rossi, P. F.; La Ginestra, A.; Patrono, P. Phosphoric Acid on Oxide Carriers. 1. Characterization of Silica, Alumina, and Titania Impregnated by Phosphoric Acid. *Langmuir* **1989**, *5*, 911–916.

(22) Abdelghany, A. M.; Zeyada, H. M.; ElBatal, H. A.; Fetouh, R. Synthesis and Spectral Properties of Nd_2O_3-Doped Sodium Silicophosphate Glass. *Silicon* **2016**, *8*, 325–330.

(23) Ahsan, M. R.; Uddin, M. A.; Mortuza, M. G. Infrared Study of the Effect of P_2O_5 in the Structure of Lead Silicate Glasses. *Appl. Phys.* **2005**, *43*, 11.

(24) Kosinski, S. G.; Krol, D. M.; Duncan, T. M.; Douglas, D. C.; MacChesney, J. B.; Simpson, J. R. Raman and NMR Spectroscopy of SiO_2 Glasses CO-Doped with Al_2O_3 and P_2O_5. *J. Non. Cryst. Solids* **1988**, *105*, 45–52.

(25) Shibata, N.; Horigudhi, M.; Edahiro, T. Raman Spectra of Binary High-Silica Glasses and Fibers Containing GeO_2, P_2O_5 and B_2O_3. *J. Non. Cryst. Solids* **1981**, *45*, 115–126.

(26) Wan, B.; Huang, R.; Diaz, J. M.; Tang, Y. Polyphosphate Adsorption and Hydrolysis on Aluminum Oxides. *Environ. Sci. Technol.* **2019**, *53*, 9542–9552.

(27) Li, D.; Fleet, M. E.; Bancroft, G. M.; Kasrai, M.; Pan, Y. Local Structure of Si and P in SiO_2–P_2O_5 and Na_2O–SiO_2–P_2O_5 Glasses: A XANES Study. *J. Non. Cryst. Solids* **1995**, *188*, 181–189.

(28) Liu, Z.; Chen, Z.-X.; Ding, W.; Kang, G.-J.; Li, Z. A Density Functional Study of Pentacoordinated Phosphorus Species in ZSM-5 Zeolite. *J Mol. Struc.-theochem* **2010**, *948*, 99–101.

(29) Sastre, G.; Lewis, D. W.; Catlow, C. R. A. Structure and Stability of Silica Species in SAPO Molecular Sieves. *J. Phys. Chem.* **1996**, *100*, 6722–6730.

(30) Aronne, A.; Turco, M.; Bagnasco, G.; Pernice, P.; Di Serio, M.; Clayden, N. J.; Marenna, E.; Fanelli, E. Synthesis of High Surface Area Phosphosilicate Glasses by a Modified Sol−Gel Method. *Chem. Mater.* **2005**, *17*, 2081–2090.

(31) Clayden, N. J.; Esposito, S.; Pernice, P.; Aronne, A. Solid State ^{29}Si and ^{31}P NMR Study of Gel Derived Phosphosilicate Glasses. *J. Mater. Chem.* **2001**, *11*, 936–943.

(32) Coelho, C.; Azais, T.; Bonhomme-Coury, L.; Maquet, J.; Massiot, D.; Bonhomme, C. Application of the MAS-J-HMQC Experiment to a New Pair of Nuclei $\{^{29}Si,^{31}P\}$: $Si_5O(PO_4)_6$ and SiP_2O_7 Polymorphs. *J. Magn. Reson.* **2006**, *179*, 114–119.

(33) Krawietz, T. R.; Lin, P.; Lotterhos, K. E.; Torres, P. D.; Barich, D. H.; Clearfield, A.; Haw, J. F. Solid Phosphoric Acid Catalyst: A Multinuclear NMR and Theoretical Study. *J. Am. Chem. Soc.* **1998**, *120*, 8502–8511.

(34) Huhti, A.-L.; Gartaganis, P. A. The Composition of the Strong Phosphoric Acids. *Can. J. Chem.* **1956**, *34*, 785–797.

(35) Jameson, R. F. The Composition of the "Strong" Phosphoric Acids. *J. Chem. Soc.* **1959**, 752–759.

(36) Prinsloo, N. M. Preparation of a Solid Phosphoric Acid Catalyst from Low-Quality Kieselguhr Parameters Controlling Catalyst Quality and Performance. *Ind. Eng. Chem. Res.* **2007**, *46*, 7838–7843.

(37) de Klerk, A.; Leckel, D. O.; Prinsloo, N. M. Butene Oligomerization by Phosphoric Acid Catalysis: Separating the Effects of Temperature and Catalyst Hydration on Product Selectivity. *Ind. Eng. Chem. Res.* **2006**, *45*, 6127–6136.

(38) Villa, M.; Scagliotti, M.; Chiodelli, G. Short Range Order in the Network of the Borophosphate Glasses: A ^{31}P NMR-MAS (Magic Angle Spinning) Study. *J. Non-Cryst. Solids* **1987**, *94*, 101–121.

(39) Jeschke, G.; Hoffbauer, W.; Jansen, M. Survival of Dipolar Splittings between Equivalent Nuclei in High-Speed MAS-NMR—Interpretation of the ^{31}P Coupling Patterns for Tetraphosphorus Decaoxide. *Chem. - Eur. J.* **1998**, *4*, 1755–1761.

(40) Szu, S.-P.; Klein, L. C.; Greenblatt, M. Effect of Precursors on the Structure of Phosphosilicate Gels: ^{29}Si and ^{31}P MAS-NMR Study. *J. Non-Cryst. Solids* **1992**, *143*, 21–30.

(41) Coelho, C.; Babonneau, F.; Azaïs, T.; Bonhomme-Coury, L.; Maquet, J.; Laurent, G.; Bonhomme, C. Chemical Bonding in Silicophosphate Gels: Contribution of Dipolar and J-Derived Solid State NMR Techniques. *J. Sol-Gel Sci. Technol.* **2006**, *40*, 181–189.

(42) Wang, L.; Samuels, W. D.; Exarhos, G. J.; Lee, B. I.; Cao, Z. ^{31}P and ^{29}Si NMR Study of Sol–Gel-Synthesized Phosphate Ceramics. *J. Mater. Chem.* **1998**, *8*, 165–169.

(43) Mudrakovskii, I. L.; Mastikhin, V. M.; Shmachkova, V. P.; Kotsarenko, N. S. High-Resolution Solid-State ^{29}Si and ^{31}P NMR of Silicon-Phosphorous Compounds Containing Six-Coordinated Silicon. *Chem. Phys. Lett.* **1985**, *120*, 424–426.

(44) García, A.; Colilla, M.; Izquierdo-Barba, I.; Vallet-Regí, M. Incorporation of Phosphorus into Mesostructured Silicas: A Novel Approach to Reduce the SiO_2 Leaching in Water. *Chem. Mater.* **2009**, *21*, 4135–4145.

(45) Das, S. K.; Bhunia, M. K.; Chakraborty, D.; Khuda-Bukhsh, A. R.; Bhaumik, A. Hollow Spherical Mesoporous Phosphosilicate Nanoparticles as a Delivery Vehicle for an Antibiotic Drug. *Chem. Comm.* **2012**, *48*, 2891–2893.

(46) Hartmann, P.; Jana, C.; Vogel, J.; Jäger, C. ^{31}P MAS and 2D Exchange NMR of Crystalline Silicon Phosphates. *Chem. Phys. Lett.* **1996**, *258*, 107–112.

(47) Grimmer, A.-R.; Haubenreisser, U. High-Field Static and MAS ^{31}P NMR: Chemical Shift Tensors of Polycrystalline Potassium Phosphates $P_2O_5 \cdot xK_2O$ ($O \leq x \leq 3$). *Chem. Phys. Lett.* **1983**, *99*, 487–490.

(48) Tropp, J.; Blumenthal, N. C.; Waugh, J. S. Phosphorus NMR Study of Solid Amorphous Calcium Phosphate. *J. Am. Chem. Soc.* **1983**, *105*, 22–26.

(49) Coelho, C.; Azaïs, T.; Bonhomme-Coury, L.; Laurent, G.; Bonhomme, C. Efficiency of the Refocused ^{31}P–^{29}Si MAS-J-INEPT NMR Experiment for the Characterization of Silicophosphate Crystalline Phases and Amorphous Gels. *Inorg. Chem.* **2007**, *46*, 1379–1387.

(50) Fayon, F.; King, I. J.; Harris, R. K.; Evans, J. S. O.; Massiot, D. Application of the Through-Bond Correlation NMR Experiment to the Characterization of Crystalline and Disordered Phosphates. *C. R. Chim.* **2004**, *7*, 351–361.

(51) O'Dell, L. A.; Guerry, P.; Wong, A.; Abou Neel, E. A.; Pham, T. N.; Knowles, J. C.; Brown, S. P.; Smith, M. E. Quantification of Crystalline Phases and Measurement of Phosphate Chain Lengths in a Mixed Phase Sample by ^{31}P Refocused INADEQUATE MAS NMR. *Chem. Phys. Lett.* **2008**, *455*, 178–183.

(52) J. King, I.; Fayon, F.; Massiot, D.; K. Harris, R.; O. Evans, J. S. A Space Group Assignment of ZrP_2O_7 Obtained by ^{31}P Solid State NMR. *Chem. Comm.* **2001**, *0*, 1766–1767.

(53) Helluy, X.; Marichal, C.; Sebald, A. Through-Bond Indirect and Through-Space Direct Dipolar Coupling ^{31} P MAS NMR Constraints for Spectral Assignment in the Cubic 3 × 3 × 3 Superstructure of TiP_2O_7. *J. Phys. Chem. B* **2000**, *104*, 2836–2845.

(54) Lilly Thankamony, A. S.; Wittmann, J. J.; Kaushik, M.; Corzilius, B. Dynamic Nuclear Polarization for Sensitivity Enhancement in Modern Solid-State NMR. *Prog. Nucl. Magn. Reson. Spectrosc.* **2017**, *102–103*, 120–195.

(55) Zhang, X.; Liu, D.; Xu, D.; Asahina, S.; Cychosz, K. A.; Agrawal, K. V.; Wahedi, Y. A.; Bhan, A.; Hashimi, S. A.; Terasaki, O.; Thommes, M.; Tsapatsis, M. Synthesis of Self-Pillared Zeolite Nanosheets by Repetitive Branching. *Science* **2012**, *336*, 1684–1687.

(56) Guefrachi, Y.; Sharma, G.; Xu, D.; Kumar, G.; Vinter, K. P.; Abdelrahman, O. A.; Li, X.; Alhassan, S.; Dauenhauer, P. J.; Navrotsky, A.; Zhang, W.; Tsapatsis, M. Steam-Induced

Coarsening of Single-Unit-Cell MFI Zeolite Nanosheets and Its Effect on External Surface Brønsted Acid Catalysis. *Angew. Chem. Int. Ed.* **2020**, *59*, 9579–9585.

(57) Norton, A. M.; Kim, D.; Zheng, W.; Akter, N.; Xu, Y.; Tenney, S. A.; Vlachos, D. G.; Tsapatsis, M.; Boscoboinik, J. A. Reversible Formation of Silanol Groups in Two-Dimensional Siliceous Nanomaterials under Mild Hydrothermal Conditions. *J. Phys. Chem. C* **2020**, *124*, 18045–18053.

(58) Coetzee, J. H.; Mashapa, T. N.; Prinsloo, N. M.; Rademan, J. D. An Improved Solid Phosphoric Acid Catalyst for Alkene Oligomerization in a Fischer–Tropsch Refinery. *Appl. Catal., A* **2006**, *308*, 204–209.

(59) van der Bij, H. E.; Weckhuysen, B. M. Phosphorus Promotion and Poisoning in Zeolite-Based Materials: Synthesis, Characterisation and Catalysis. *Chem. Soc. Rev.* **2015**, *44*, 7406–7428.

(60) Jain, S.; Bjerring, M.; Nielsen, N. C. Efficient and Robust Heteronuclear Cross-Polarization for High-Speed-Spinning Biological Solid-State NMR Spectroscopy. *J. Phys. Chem. Lett.* **2012**, *3*, 703–708.

(61) Mulliken, R. S. The Interaction of Electron Donors and Acceptors. *J. Chim. Phys.* **1964**, *61*, 20–38.

(62) Reed, A. E.; Curtiss, L. A.; Weinhold, F. Intermolecular Interactions from a Natural Bond Orbital, Donor-Acceptor Viewpoint. *Chem. Rev.* **1988**, *88*, 899–926.

(63) Timoneda, J. I.; Hynes, J. T. Nonequilibrium Free Energy Surfaces for Hydrogen-Bonded Proton-Transfer Complexes in Solution. *J. Phys. Chem.* **1991**, *95*, 10431–10442.

(64) Thompson, W. H.; Hynes, J. T. Model Study of the Acid−Base Proton-Transfer Reaction of the $ClH\cdots OH_2$ Pair in Low-Polarity Solvents. *J. Phys. Chem. A* **2001**, *105*, 2582–2590.

(65) Ratajczak, H. Charge-Transfer Properties of the Hydrogen Bond. I. Theory of the Enhancement of Dipole Moment of Hydrogen-Bonded Systems. *J. Phys. Chem.* **1972**, *76*, 3000–3004.

(66) Warshel, A. Dynamics of Enzymatic Reactions. *Proc. Natl. Acad. Sci. U. S. A.* **1984**, *81*, 444–448.

(67) Warshel, Arieh.; Russell, Stephen. Theoretical Correlation of Structure and Energetics in the Catalytic Reaction of Trypsin. *J. Am. Chem. Soc.* **1986**, *108*, 6569–6579.

(68) Warshel, A.; Weiss, R. M. An Empirical Valence Bond Approach for Comparing Reactions in Solutions and in Enzymes. *J. Am. Chem. Soc.* **1980**, *102*, 6218–6226.

(69) Warshel, A. Dynamics of Reactions in Polar Solvents. Semiclassical Trajectory Studies of Electron-Transfer and Proton-Transfer Reactions. *J. Phys. Chem.* **1982**, *86*, 2218–2224.

(70) Harris, N.; Wei, W.; Saunders, W. H.; Shaik, S. Origins of Nonperfect Synchronization in the Lowest-Energy Path of Identity Proton Transfer Reactions Leading to Delocalized Anions: A VBSCF Study[1]. *J. Am. Chem. Soc.* **2000**, *122*, 6754–6758.

(71) Wu, W.; Shaik, S.; Saunders, W. H. Comparative Study of Identity Proton-Transfer Reactions between Simple Atoms or Groups by VB Methods. *J. Phys. Chem. A* **2002**, *106*, 11616–11622.

(72) Keeffe, J. R.; Gronert, S.; Colvin, M. E.; Tran, N. L. Identity Proton-Transfer Reactions from C−H, N−H, and O−H Acids. An Ab Initio, DFT, and CPCM-B3LYP Aqueous Solvent Model Study. *J. Am. Chem. Soc.* **2003**, *125*, 11730–11745.

(73) Irani, R. R.; Callis, C. F. Metal Complexing by Phosphorus Compounds. IV. Acidity Constants. *J. Phys. Chem.* **1961**, *65*, 934–937.

(74) Lejeune, C.; Coelho, C.; Bonhomme-Coury, L.; Azaïs, T.; Maquet, J.; Bonhomme, C. Studies of Silicophosphate Derivatives by $^{31}P \rightarrow ^{29}Si$ CP MAS NMR. *Solid State Nucl. Magn. Reson.* **2005**, *27*, 242–246.

(75) Schaefer, J.; McKay, R. A.; Stejskal, E. O. Double-Cross-Polarization NMR of Solids. *J. Magn. Reson.* **1979**, *34*, 443–447.

(76) Bennett, A. E.; Rienstra, C. M.; Griffiths, J. M.; Zhen, W.; Lansbury, P. T.; Griffin, R. G. Homonuclear Radio Frequency-Driven Recoupling in Rotating Solids. *J. Chem. Phys.* **1998**, *108*, 9463–9479.

(77) Feike, M.; Jäger, C.; Spiess, H. W. Connectivities of Coordination Polyhedra in Phosphate Glasses from ^{31}P Double-Quantum NMR Spectroscopy. *J. Non-Cryst. Solids* **1998**, *223*, 200–206.

(78) Hohwy, M.; Rienstra, C. M.; Jaroniec, C. P.; Griffin, R. G. Fivefold Symmetric Homonuclear Dipolar Recoupling in Rotating Solids: Application to Double Quantum Spectroscopy. *J. Chem. Phys.* **1999**, *110*, 7983–7992.

(79) Williams, D. B. G.; Lawton, M. Drying of Organic Solvents: Quantitative Evaluation of the Efficiency of Several Desiccants. *J. Org. Chem.* **2010**, *75*, 8351–8354.

(80) Mehring, M. *Principles of High Resolution NMR in Solids*, 2nd ed.; Springer-Verlag: Berlin Heidelberg, 1983.

(81) Hediger, S.; Meier, B. H.; Ernst, R. R. Adiabatic Passage Hartmann-Hahn Cross Polarization in NMR under Magic Angle Sample Spinning. *Chem.Phys. Lett.* **1995**, *240*, 449–456.

(82) Bak, M.; Rasmussen, J. T.; Nielsen, N. C. SIMPSON: A General Simulation Program for Solid-State NMR Spectroscopy. *J. Magn. Reson.* **2011**, *213*, 366–400.

(83) Frisch, M. J.; Trucks, G. W.; Schlegel, H. B.; Scuseria, G. E.; Robb, M. A.; Cheeseman, J. R.; Scalmani, G.; Barone, V.; Mennucci, B.; Petersson, G. A.; Nakatsuji, H.; Caricato, M.; Li, X.; Hratchian, H. P.; Izmaylov, A. F.; Bloino, J.; Zheng, G.; Sonnenberg, J. L.; Hada, M.; Ehara, M.; Toyota, K.; Fukuda, R.; Hasegawa, J.; Ishida, M.; Nakajima, T.; Honda, Y.; Kitao, O.; Nakai, H.; Vreven, T.; Montgomery Jr., J. A.; Peralta, J. E.; Ogliaro, F.; Bearpark, M. J.; Heyd, J.; Brothers, E. N.; Kudin, K. N.; Staroverov, V. N.; Kobayashi, R.; Normand, J.; Raghavachari, K.; Rendell, A. P.; Burant, J. C.; Iyengar, S. S.; Tomasi, J.; Cossi, M.; Rega, N.; Millam, N. J.; Klene, M.; Knox, J. E.; Cross, J. B.; Bakken, V.; Adamo, C.; Jaramillo, J.; Gomperts, R.; Stratmann, R. E.; Yazyev, O.; Austin, A. J.; Cammi, R.; Pomelli, C.; Ochterski, J. W.; Martin, R. L.; Morokuma, K.; Zakrzewski, V. G.; Voth, G. A.; Salvador, P.; Dannenberg, J. J.; Dapprich, S.; Daniels, A. D.; Farkas, Ö.; Foresman, J. B.; Ortiz, J. V; Cioslowski, J.; Fox, D. J. Gaussian 09. Gaussian, Inc.: Wallingford, CT, USA 2009.

3.6 Appendix

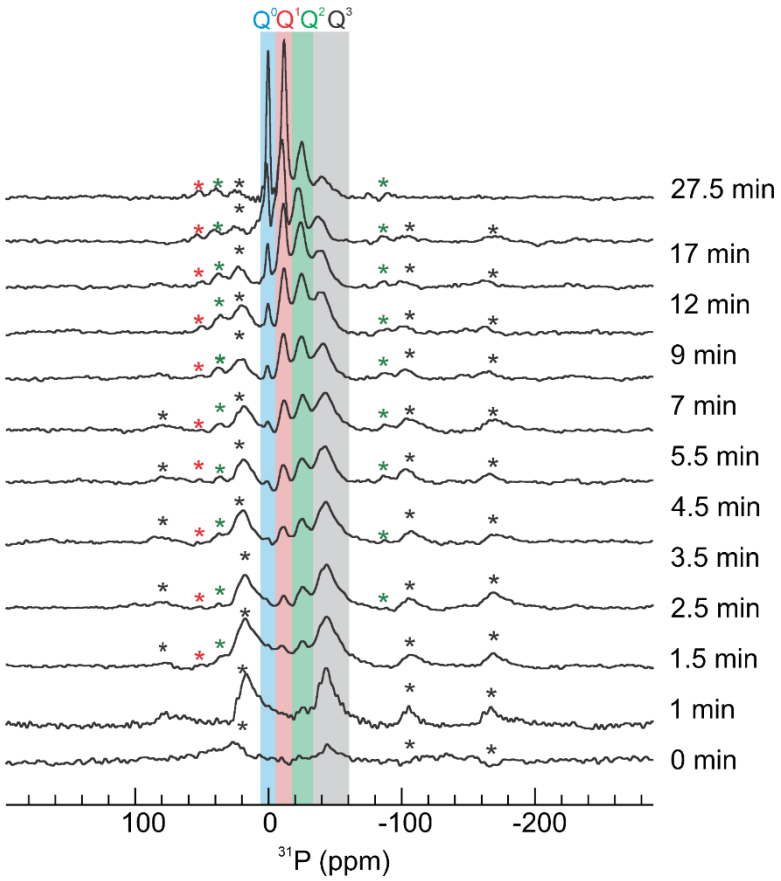

Figure A3.1 The effect of ambient exposure time (correlated with the amount of adsorbed water), on the P speciation in P-SPP at room temperature. ^{31}P MAS NMR spectra were recorded after each air exposure time, as noted. All spectra were recorded at room temperature in an 18.8 T magnet using 20 kHz MAS. Spinning sidebands for Q^1, Q^2, and Q^3 signals are indicated by * in red, green, and black, respectively. Each ^{31}P NMR spectrum corresponds to a data point in Figure 3.2b (main text).

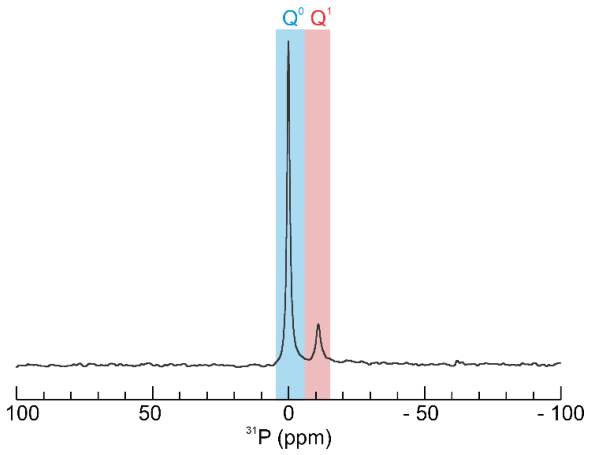

Figure A3.2 ^{31}P MAS NMR spectrum of P-SPP, recorded after extended ambient exposure (several days). The spectrum was recorded at room temperature in an 18.8 T magnet, using 20 kHz MAS.

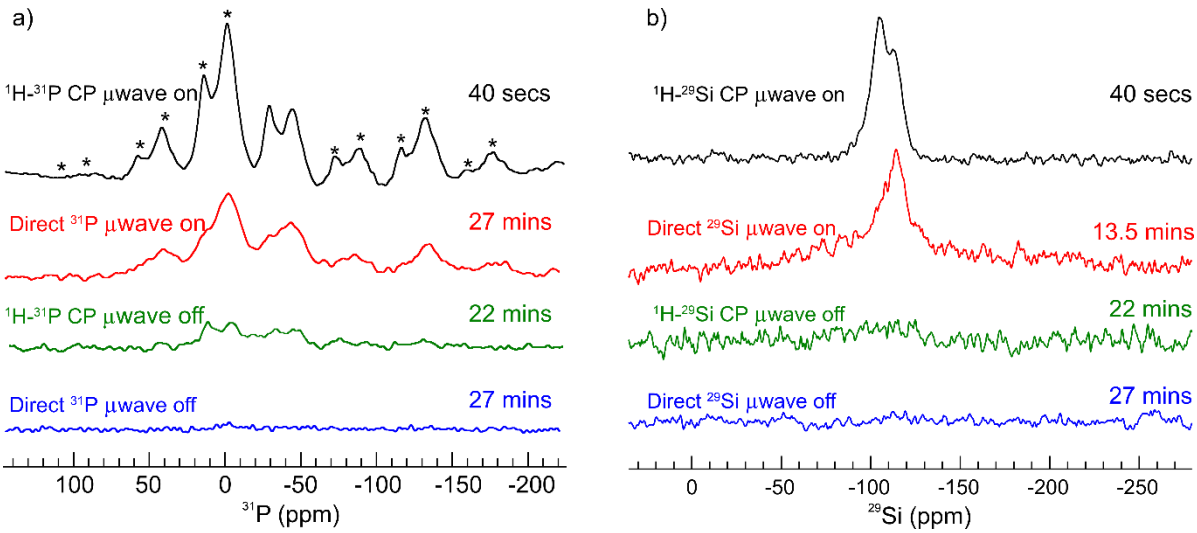

Figure A3.3 Comparison of MAS-NMR spectra (direct and CP) for nearly-dry P-SPP: (a) ^{31}P MAS-NMR, and (b) ^{29}Si MAS-NMR, acquired with (black and red) or without (green and blue) DNP. The spectra were recorded at 9.4 T with MAS frequency 7 kHz and at temperature 95 K (i.e., DNP conditions). The experimental acquisition time for each spectrum is noted in

the legend on the right. The DNP-enhanced CP spectra show a significant sensitivity boost, which is helpful in performing the advanced NMR spectroscopy experiments shown in the main text.

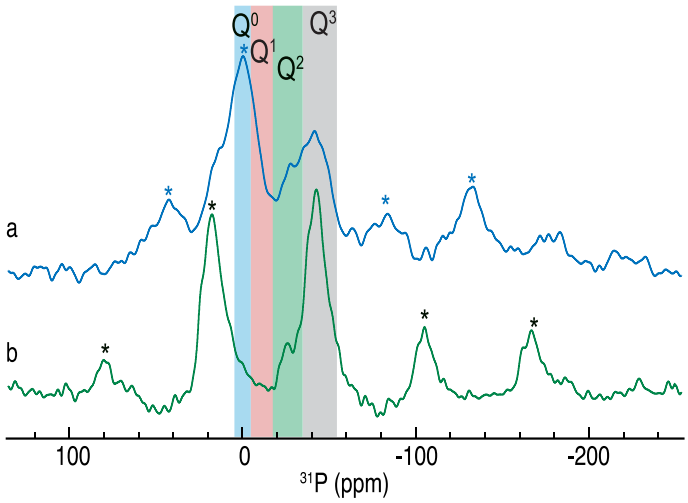

Figure A3.4 A comparison of direct ^{31}P spectra of P-SPP recorded (a) at 9.4 T under DNP conditions, 95 K with 7 kHz MAS, for a nearly-dry (after 2 mins of ambient exposure) sample, and (b) at 18.8 T and room temperature with 20 kHz MAS, for a similarly nearly-dry (after 1 min of ambient exposure) sample. The isotropic peaks are better resolved at 18.8 T, but cannot be directly compared to the spectrum at 9.4 T, given the slightly different state of the sample determined by different experimental conditions.

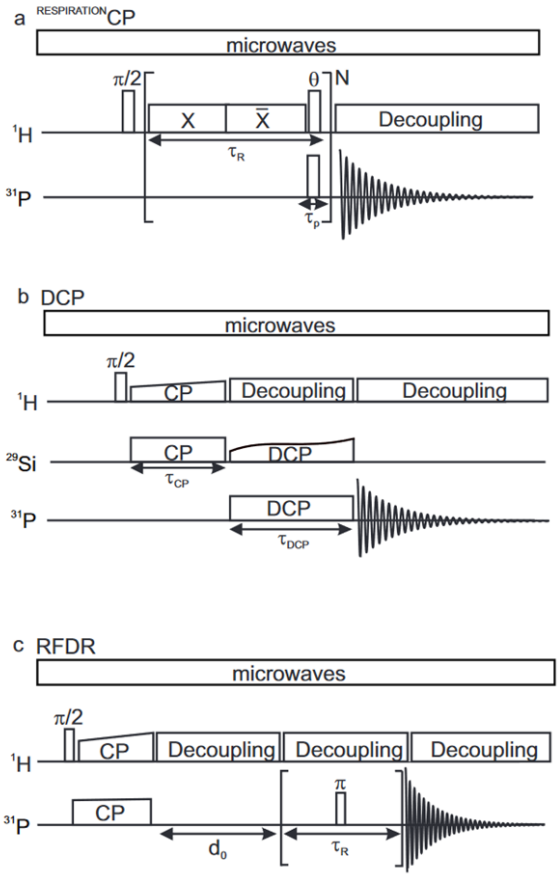

Figure A3.5 Pulse sequences used to record (a) ^{RESPIRATION}CP, (b) DCP and (c) RFDR experiments under DNP conditions.

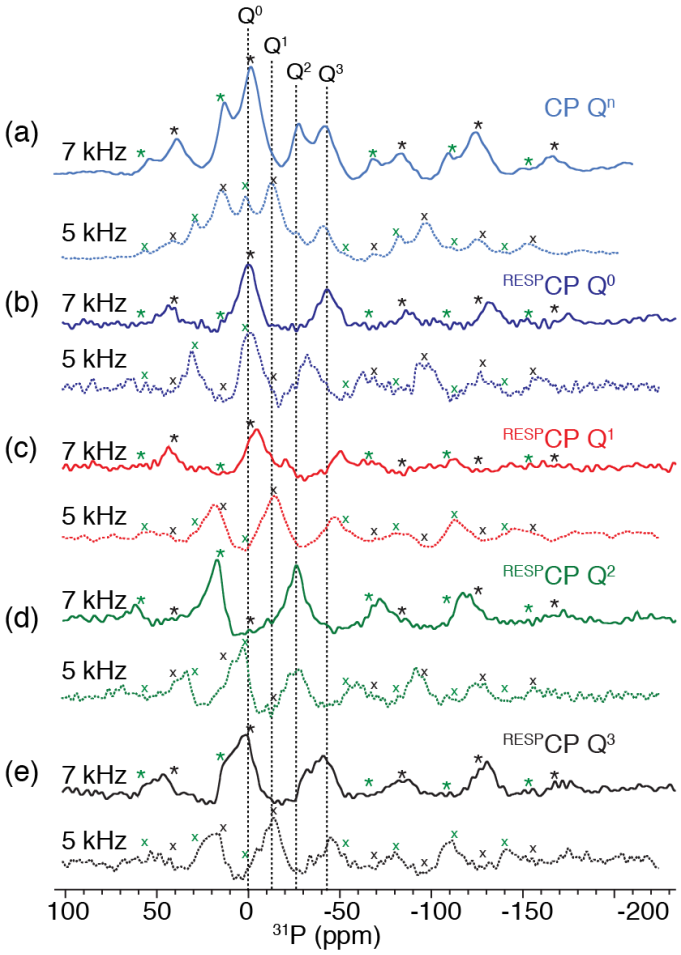

Figure A3.6 Comparison of DNP-enhanced ^{1}H-^{31}P CP-MAS spectra of nearly-dry P-SPP, recorded using (a) ramped CP, and (b-e) ^{RESPIRATION}CP. All spectra were acquired at 9.4 T and 95 K, using either 7 kHz (solid) or 5 kHz (dashed) MAS frequency. (The spectra recorded with 7 kHz MAS are also shown in Figure 3 in the main text.) The isotropic peak positions were confirmed by comparing the spectra at the two MAS frequencies. Spinning sidebands at 7 and 5 kHz are denoted by * and ×, respectively. The RF frequency for ^{RESPIRATION}CP was set at (b) 0 ppm, (c) -11 ppm, (d) -25 ppm, or (e) -42 ppm. The spectra in (b) show evidence for Q^3 signals (with 7 kHz MAS) and for a Q^2 signal (with 5 kHz MAS) because, at their respective MAS frequencies, the spinning sidebands of both signals appear at 0 ppm. In (c), the spectrum recorded with 5 kHz MAS shows a Q^1 signal, but no Q^3 signal is observed unlike

7 kHz MAS. This is expected because at 5 kHz MAS the rotor period to short pulse length of the ^{RESPIRATION}CP becomes longer compared to MAS 7 kHz, which make it more narrow banded such that the Q^3 sideband goes out of the optimum ^{RESPIRATION}CP frequency range. In (d) and (e), isotropic peaks are observed in the Q^2 and Q^3 regions with their spinning sidebands, as expected and discussed in the main text.

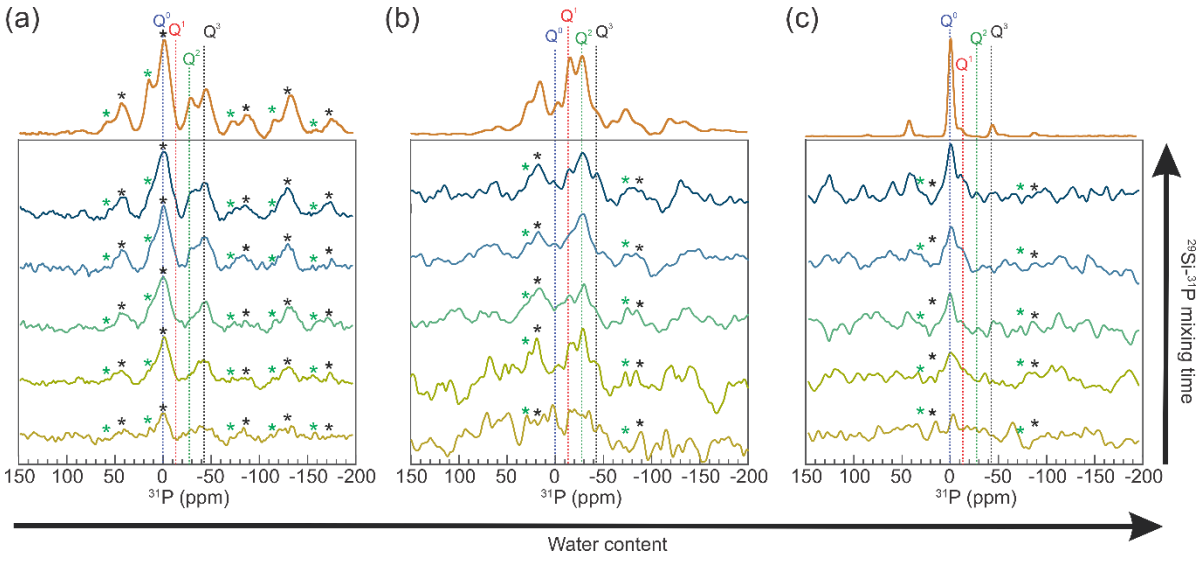

Figure A3.7 DCP spectra for (a) nearly-dry, (b) partly-hydrolyzed, and (c) fully-hydrolyzed P-SPP. All spectra were acquired using DNP at 9.4 T, 7 kHz MAS, and 95 K. The DCP spectra in (a) and (c) were acquired using mixing times of 10, 20, 30, 40 and 50 ms, and in (b) using 8, 16, 24, 32 and 40 ms, increasing from bottom to top. The ^{1}H-^{31}P CP spectra (brown) are shown for reference. The grey, green and red bars indicate regions used for calculating peak areas for Q^3, Q^2 and Q^1 signals. Buildup curves for ^{29}Si to ^{31}P polarization transfer using DCP are shown in Figure 4 of the main text and Figure A3.6. Spinning sidebands are denoted by *.

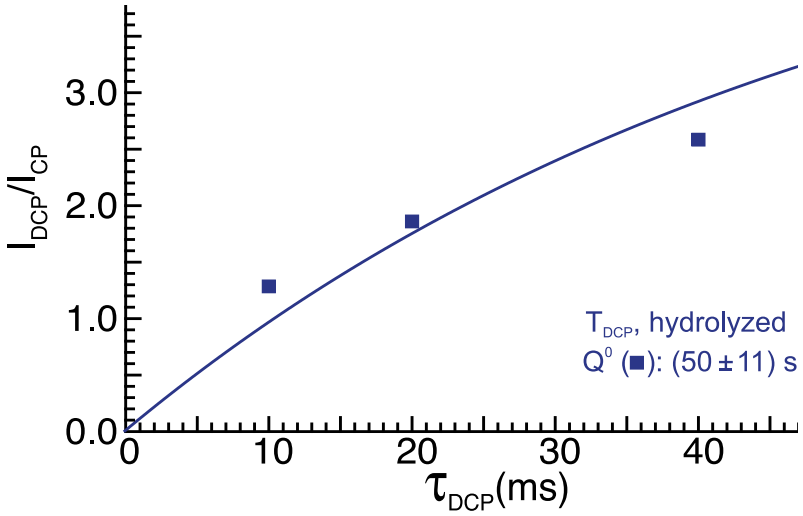

Figure A3.8 The DCP vs. CP buildup curve for the Q^0 signal of hydrolyzed P-SPP, for various mixing times (τ_m). The solid line is the curvefit obtained using a mono-exponential model.

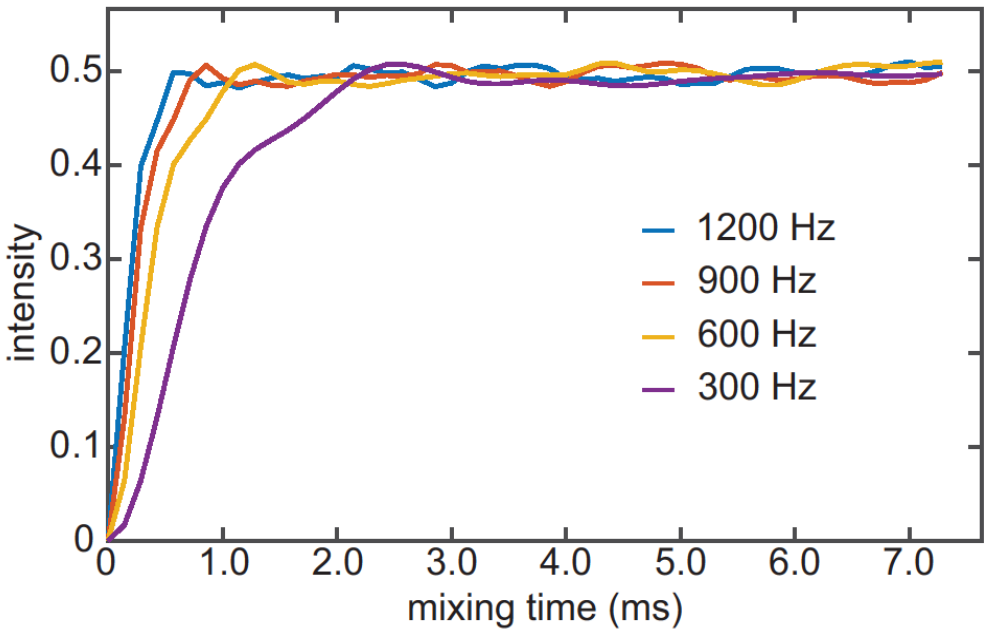

Figure A3.9 Numerical simulations of ^{31}P-^{31}P polarization transfer curves, assuming a two-spin system with chemical shift tensors in the Q^2 and Q^3 regions, shown as function of mixing time, τ_M (ms). The simulations were performed on SIMPSON,[12] a simulation program for solid-state NMR experiments, using 180° pulses of length 7.04 μs. Dipolar couplings with

300, 600, 900 and 1200 Hz ,corresponding to the relative distances of 4.03, 3.20, 2.80 and 2.54 Å between the two ^{31}P spins, were considered.

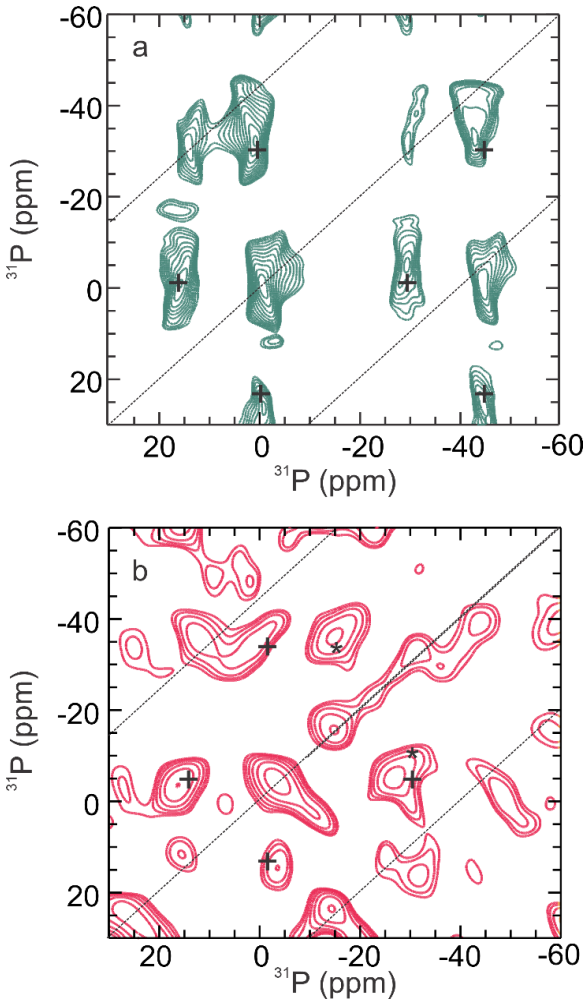

Figure A3.10 DNP-enhanced ^{31}P-^{31}P correlation spectra, probing the existence of P-O-P′ linkages and types of P-site oligomers for: (a) dry P-SPP-27, and (b) partially hydrolyzed P-SPP-27. Both spectra were recorded at 9.4 T and 7 kHz MAS frequency, with a RFDR mixing time of 1428 μs. (RFDR spectra acquired at a mixing time of 714 μs are shown in Figure 3.5 in the main text.) The dashed lines indicate self-correlations of the isotropic peaks and their

spinning sidebands. The "+" symbols indicate cross-peaks for Q^3_m–Q^2_m signals. Asterisks indicate cross-peaks for Q^2–Q^1 signals.

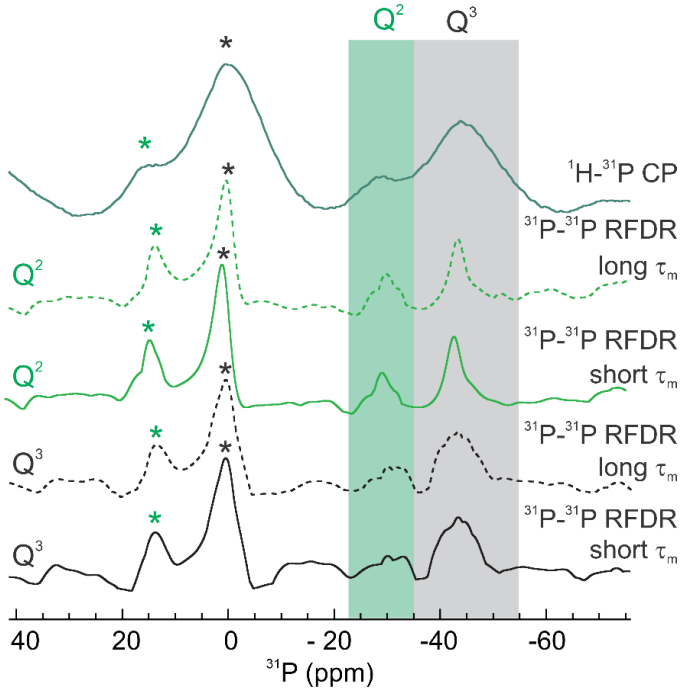

Figure A3.11 Comparison of the ^{1}H-^{31}P CP spectrum (top row) of nearly-dry P-SPP with the 1D projections from RFDR spectral analysis (4 bottom rows). Black and green spectra correspond to Q^3 and Q^2 regions, respectively. The solid lines belong to the 2D RFDR plots in Figure 3.6a of the main text. It was recorded with a short mixing time (τ_M = 0.714 ms). The dashed lines are from the 2D spectra shown in Figure A3.8a, acquired using a long mixing time (τ_M =1.428 ms). The comparable intensities of the Q^2 and Q^3 signals (corresponding to short and long τ_M values, respectively) indicate that the ^{31}P-^{31}P coupling is less than 900 Hz (see simulations in Figure A3.7).

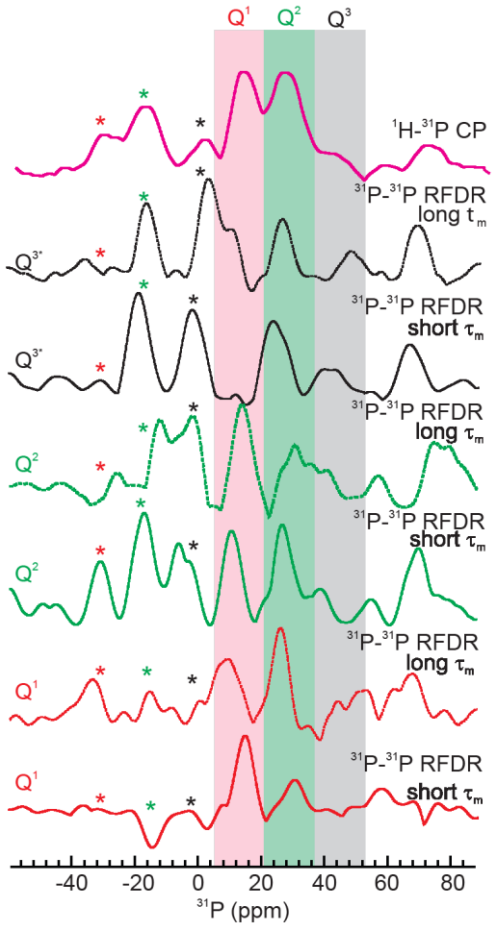

Figure A3.12 Comparison of the ^{1}H-^{31}P CP spectrum (top row) for partly-hydrolyzed P-SPP with the 1D projections from RFDR spectral analysis (6 bottom rows). Black, green and red spectra correspond to Q^3 (black), Q^2 (green) and Q^1 (red) regions. The solid-lines belong to the 2D RFDR plots in Figure 3.6b of the main text. It was recorded with a short mixing time (τ_M = 0.714 ms). The dashed lines are from the 2D spectra shown in Figure A3.8b,a acquired using a long mixing time (τ_M =1.428 ms). The intensities of the Q^2 and Q^3 signals corresponding to short and long τ_M values, respectively, are comparable or lower, indicating that the ^{31}P-^{31}P coupling is less than 900 Hz (see simulations in Figure A3.7).

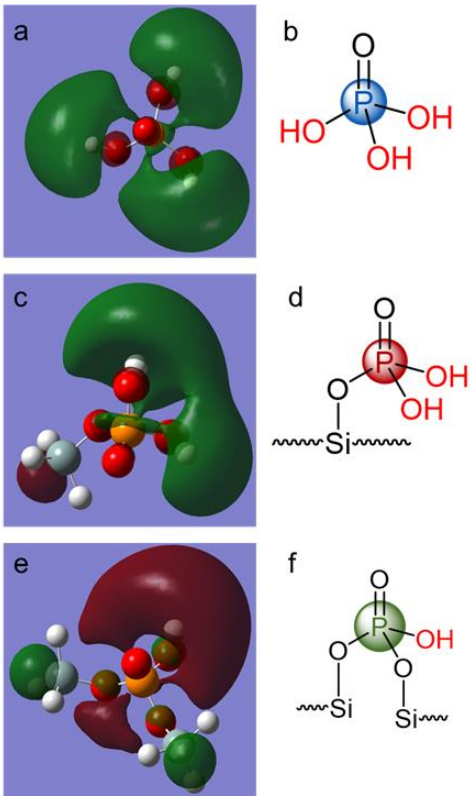

Figure A3.13 DFT-optimized geometries of Q^0, Q_1^1 and Q_2^2 cluster models: (a), (c), and (e) Lowest occupied molecular orbital (LUMO, anti-bonding), showing equal distribution of the amplitude over the three equivalent hydrogen atoms. (Color code: H: white; O: red; P: orange.) Energies are summarized in Table A3.3. (b), (d) and (f) show the chemical structures corresponding to (a), (c) and (e), with acidic hydroxyls shown in red.

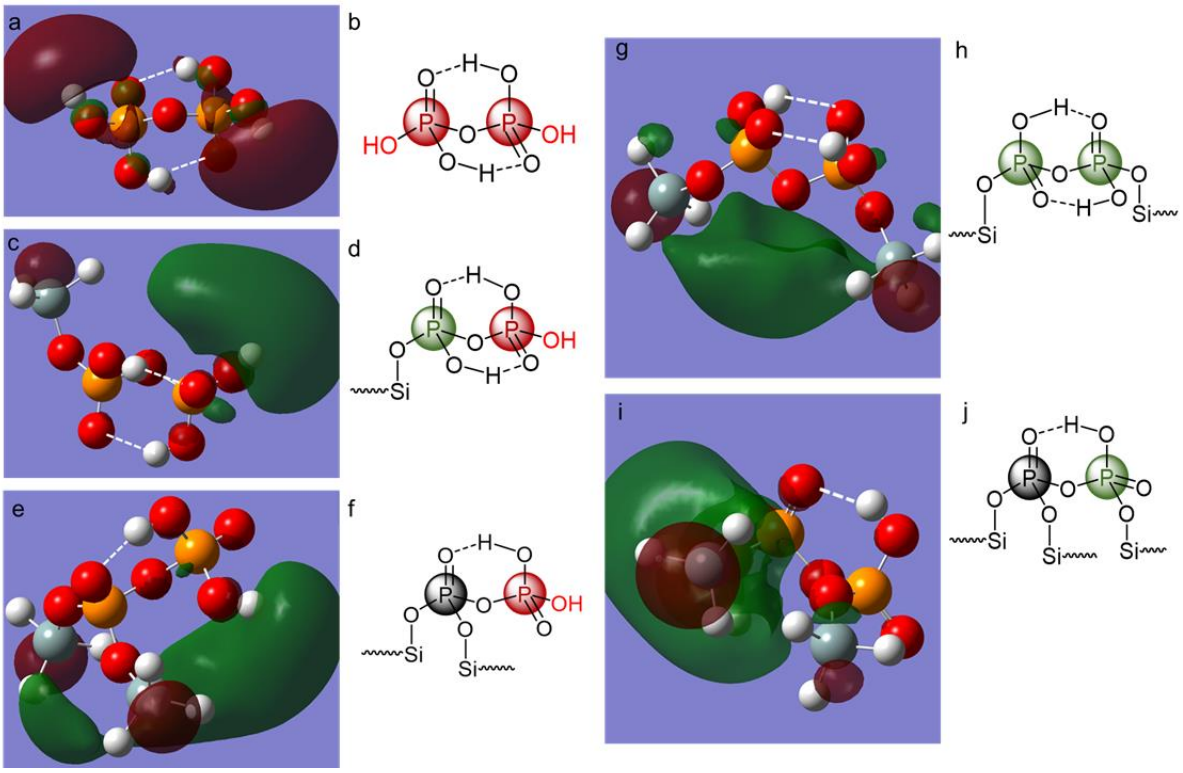

Figure A3.14 DFT-optimized geometries of the dinuclear cluster models Q_0^1-Q_0^1, Q_1^2-Q_0^1, Q_2^3-Q_0^1, Q_1^2-Q_1^2 and Q_1^3-Q_1^2 in their lowest energy structures. (a), (c), (e), (g), and (i) are depictions of the LUMO, showing the distribution of the amplitude over the acidic H atoms. (Color code: H: white; O: red; P: orange; Si: grey.) Energies are summarized in Table A3. (b), (d), (f), (h) and (j) are the chemical structures corresponding to (a), (c), (e), (g), and (i), respectively, with acidic hydroxyls are shown in red.

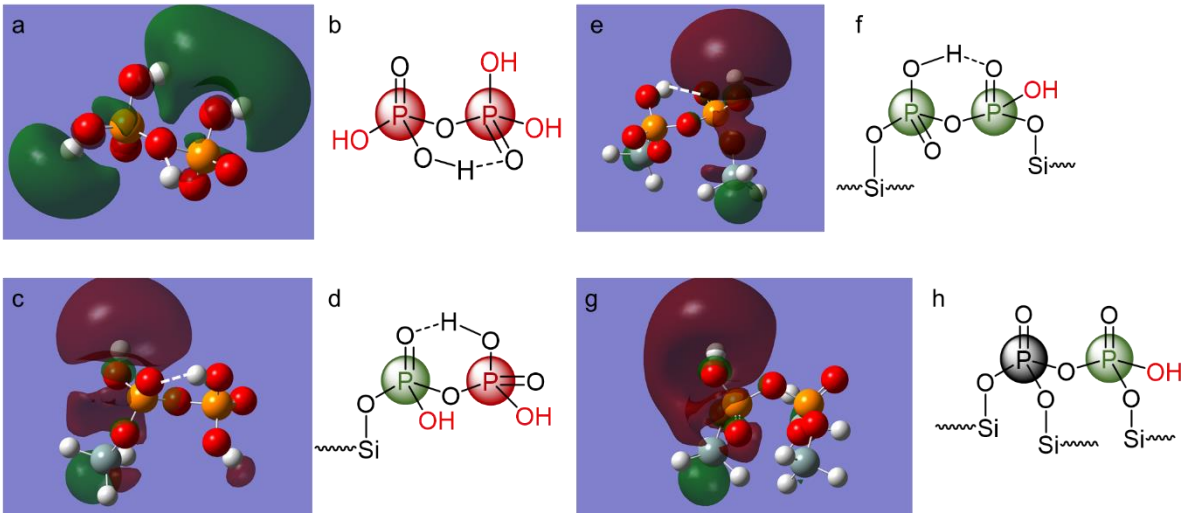

Figure A3.15 DFT-optimized geometries of higher energy conformers for the dinuclear cluster models Q_0^1-Q_0^1, Q_1^2-Q_0^1, Q_1^2-Q_1^2 and Q_1^3-Q_1^2, each with one less intramolecular H-bond compared to the minimum-energy geometries shown in Figure A3.12. (a), c), e) and (g) depict LUMOs, showing the distribution of the amplitude over the acidic H atoms that do not participate in intramolecular hydrogen bonds. (Color code: H: white; O: red; P: orange; Si: grey.) Energies are summarized in Table A3. (b), (d), (f), and (h) are the chemical structures for (a), (c), (e), and (g), respectively, with acidic hydroxyls shown in red.

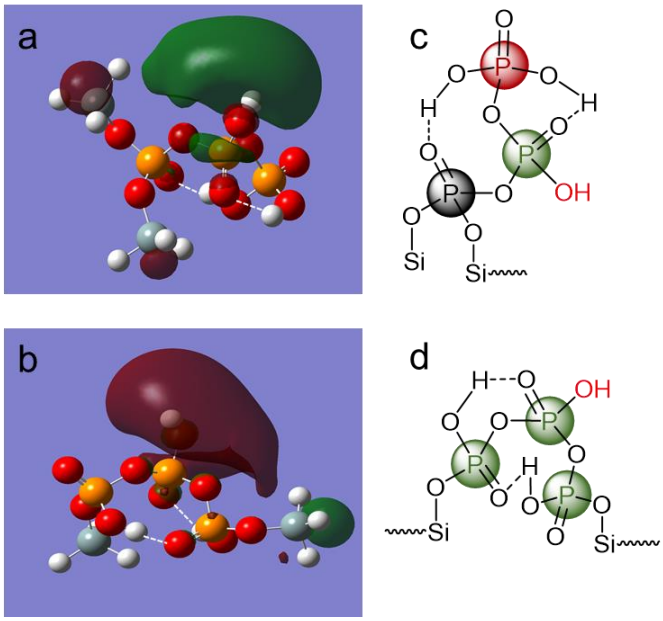

Figure A3.16 DFT-optimized geometries of the trinuclear cluster models Q_2^3-Q_0^2-Q_0^1 and Q_1^2-Q_0^2-Q_1^2. (a) and (b) depict LUMOs, showing the distribution of the amplitude over the acidic H atoms. (Color code: H: white; O: red; P: orange; Si: grey.) Energies are summarized in Table A3.3. (c) and (d) are the chemical structures corresponding to (a) and (b) respectively.

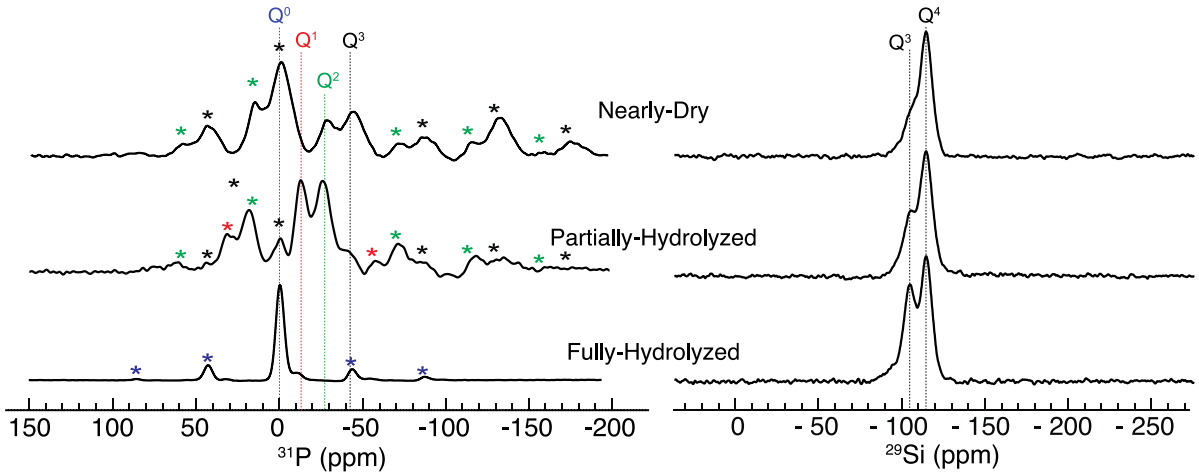

Figure A3.17 DNP-enhanced ^{1}H-^{31}P and ^{1}H-^{29}Si CP-MAS NMR spectra of P-SPP in three hydrolysis states, recorded at 9.4 T and 95 K with 7 kHz MAS.

Table A3.1 Parameters obtained by fitting the simulated spectrum of the CSA model in Topspin to experimental spectra of P-SPP [a]

Air exposure time (min)	CS_{iso} (ppm)	CSA (ppm)	η	LB (kHz)
0	-44 ±2	-205±29	0.1	3.5
1	-44±2	-160±9	0.1	3.0

[a] The spectra were recorded at 18.8 T, using 20 kHz MAS.

Table A3.2 Optimized Geometries

Geometries of optimized models, at the M062X/aug-cc-pvtz theory level.

Q^0 (Electronic energy: -644.21035549 Ha):

P	-0.37284100	0.50212300	0.03518800
O	-1.94859600	0.39462200	-0.12252200
H	-2.40257700	1.18178300	0.19564600
O	0.07632000	1.02594300	-1.39440500
H	0.94118200	1.44849200	-1.37328500
O	0.07617600	-1.01988500	-0.00315100
H	0.18182700	-1.39129000	0.87881200
O	0.10501400	1.28145500	1.18151700

Q_1^1 (Electronic energy: -934.92785612 Ha):

P	-0.36897400	0.70845800	0.23784300
O	-1.94219900	0.81480400	0.06314400
H	-2.30786000	0.24917600	-0.62459200
O	0.22561800	0.94157800	-1.22575700
H	0.63126500	1.81110200	-1.30693100
O	-0.10742400	-0.83034400	0.45026600
O	0.16093700	1.59827100	1.27088200
Si	0.92028200	-1.53836900	1.58052900

H	0.88090200	-2.97660100	1.27284000
H	2.27797000	-0.99706900	1.40352300
H	0.41161100	-1.27219000	2.93477000

Q_2^2 (Electronic energy: -1225.64798458 Ha):

P	-0.21291900	0.65451900	-0.18939900
O	-1.75258100	0.83337000	-0.45229400
O	0.41965400	0.55978700	-1.64505200
H	1.04314000	1.27649800	-1.80046600
O	-0.09754400	-0.81628800	0.35106300
O	0.38767800	1.68562600	0.67184300
Si	0.76718300	-1.34983600	1.68974300
H	0.60307100	-2.81166800	1.68933900
H	2.18350400	-0.97762700	1.53581800
H	0.19326300	-0.75495700	2.90774400
Si	-2.76957000	2.00077900	0.20121200
H	-2.32218000	3.33582300	-0.22848800
H	-4.10058800	1.69143900	-0.34365700
H	-2.76134900	1.88736000	1.66927500

Q_0^1-Q_0^1 (Electronic energy: -1211.99762558 Ha):

P	-1.36945800	0.04902300	-0.00247200
O	0.00000000	0.00000000	0.86169300
O	-2.51038400	0.08733100	1.07596100
H	-2.92388700	0.95489500	1.14613500
O	-1.50817700	-1.39888400	-0.58519400
H	-0.66478200	-1.69843500	-0.97770000
P	1.36945800	-0.04902300	-0.00247200
O	2.51038400	-0.08733300	1.07596100
H	2.92388400	-0.95489800	1.14613500
O	1.50817800	1.39888500	-0.58519200
H	0.66478400	1.69843700	-0.97769900
O	1.31372500	-1.18501800	-0.93803600
O	-1.31372600	1.18501900	-0.93803400

Q_1^2-Q_0^1 (Electronic energy: -1502.71616999 Ha)

P	1.33773600	-0.17173500	0.00784800
O	0.09295600	0.72020300	0.53781500
O	2.38662000	-0.10466600	1.17656200
H	2.46171900	-0.94049100	1.64986300
O	2.00490700	0.71445500	-1.09754200
H	1.32828700	1.06796600	-1.70948900
P	-1.15845000	0.84019300	-0.48907400

O	-2.16475400	1.76573300	0.24228300
O	-1.84528400	-0.58092100	-0.41172800
H	-1.19085000	-1.29373100	-0.54336200
O	-0.67025900	1.28467400	-1.80048600
O	0.85700800	-1.51555500	-0.35634800
Si	-3.29223300	1.48264700	1.46621100
H	-4.46745700	0.82974600	0.87142100
H	-2.66170600	0.62819500	2.48608500
H	-3.62142800	2.81083200	2.00002100

Q_2^3-Q_0^1 (Electronic energy: -1793.43151111 Ha):

P	1.63208900	-0.20886000	-0.42427900
O	0.55303500	0.97550900	-0.15694100
O	0.65259500	-1.42724800	-0.78085900
H	0.81049100	-1.75441700	-1.67329000
O	2.19146800	-0.53879500	0.99842600
H	1.50669400	-0.46861200	1.69904600
P	-0.61187500	0.90660400	0.94322800
O	-1.85456700	0.33584200	0.17660000
O	-0.96231000	2.40081300	1.18146000
O	-0.18800900	0.13599600	2.12283700
O	2.59765000	0.11586800	-1.46248800

Si	-2.47638700	-1.21995000	-0.03382900
H	-3.91259400	-1.11058100	0.26781100
H	-2.27574800	-1.58763500	-1.44395300
H	-1.79594600	-2.14254500	0.88405600
Si	-1.84625000	3.53444700	0.30225300
H	-3.27678200	3.28098200	0.53726800
H	-1.43775400	4.84386200	0.82586400
H	-1.50834200	3.38154900	-1.12258700

Q_1^2-Q_1^2 (Electronic energy: -1793.43489736 Ha)

P	0.69255800	-1.24195400	0.13267500
O	-0.14671800	0.04454700	0.65903200
O	1.46268400	-1.73224700	1.38775300
O	1.82535800	-0.61076200	-0.76856700
H	1.44329700	0.01412100	-1.41647400
P	-1.08078900	0.75716500	-0.46197300
O	-1.73612400	1.94609000	0.29014500
O	-2.27625800	-0.25601400	-0.65709400
H	-1.94045100	-1.16099100	-0.81364300
O	-0.26660500	1.08155800	-1.64017900
O	-0.22560400	-2.19693300	-0.50085600
Si	-3.06270500	2.03396800	1.32977600

H -4.29139900 1.95033900 0.52693600

H -2.97149000 0.92295600 2.29149700

H -2.94013600 3.33740000 1.99652100

Si 2.89516100 -1.21009300 2.11152700

H 2.86996000 0.26035800 2.18043300

H 2.88883600 -1.81439900 3.45071000

H 4.02715400 -1.69126900 1.30634000

Q_2^3-Q_1^2 (Electronic energy: -2084.15131312 Ha):

P 1.65958700 -0.04419300 -0.50049100

O 0.54177700 1.09040900 -0.18555400

O 0.73287900 -1.27799900 -0.87055200

O 2.27966600 -0.37316600 0.90046600

H 1.60084100 -0.39840900 1.60755200

P -0.61271600 0.92041200 0.91586200

O -1.84625500 0.37106400 0.11741300

O -1.00342800 2.38635500 1.24985000

O -0.16325100 0.08964300 2.04285300

O 2.59498100 0.34248200 -1.54743800

Si -2.37693000 -1.16799300 -0.31852800

H -3.83413800 -1.14824700 -0.11771300

H -2.06003800 -1.35983000 -1.74443200

H -1.72150400 -2.17401900 0.52831200

Si	-1.90140500	3.55713700	0.43667600
H	-3.32880000	3.25392000	0.62799700
H	-1.53496400	4.83611500	1.05776400
H	-1.53735400	3.51309100	-0.98927600
Si	0.87682600	-2.26676500	-2.23043900
H	2.25467800	-2.77056500	-2.32317700
H	-0.07681800	-3.36201500	-1.98501500
H	0.49348000	-1.49961400	-3.42643800

Q_1^2-Q_0^2-Q_1^2 (Electronic energy: -2361.21673235 Ha):

P	-1.33068300	0.63491000	0.85770800
O	0.14428700	0.86460300	0.12733800
O	-0.97664300	-0.15505500	2.15275400
H	-0.23364900	-0.81625800	2.11908400
O	-2.02631600	-0.35006000	-0.13541000
P	1.08466000	-0.00182300	-0.77666000
O	2.28876700	-0.44497000	0.19745900
O	1.75639100	1.03641200	-1.73842700
H	1.68841400	1.95772800	-1.46253300
O	0.50537600	-1.18771500	-1.42480200
O	-1.98144700	1.91988500	1.03931200

P	2.18399200	-1.83306000	1.02874700
O	1.03910100	-1.80397000	1.95023600
O	3.57450800	-1.97193000	1.69011100
O	2.17404500	-2.95282900	-0.07826700
H	1.49637100	-2.77252500	-0.75903000
Si	5.08075000	-2.48721300	1.11676100
H	6.05280700	-1.98851700	2.09713400
H	5.06644500	-3.95537100	1.05383800
H	5.28545100	-1.89055000	-0.21332500
Si	-2.21809000	-2.00594800	-0.33824700
H	-3.52590800	-2.35657800	0.24249000
H	-2.20014800	-2.27269900	-1.78126400
H	-1.14059700	-2.71524600	0.37439500

Q_2^3-Q_0^2-Q_0^1 (Electronic energy: -2361.21612668 Ha):

P	-1.02945600	0.31009600	0.57546800
O	0.51723100	0.38833500	-0.04083500
O	-0.88422100	-0.70351300	1.75330200
H	0.01485300	-0.84766700	2.14910200
O	-1.82022500	-0.47590000	-0.54054600
H	-1.44872000	-1.35506600	-0.71584200

P	1.32727100	-0.77491500	-0.72665000
O	2.62819300	-0.94684300	0.19817500
O	1.91566000	-0.14909600	-2.03895900
H	1.98609700	0.81239300	-2.04250500
O	0.59373800	-2.03501100	-0.89707600
O	-1.51847100	1.65379200	0.82572300
P	2.61226600	-1.75583000	1.60398300
O	1.55407400	-1.26965300	2.50209500
O	4.05989000	-1.53888200	2.10932500
O	2.51954500	-3.25130200	1.19409100
Si	5.59300200	-1.62101200	1.41127100
H	6.51654600	-1.90436900	2.51636900
H	5.58114000	-2.70107300	0.41061200
H	5.87163100	-0.31890600	0.78684700
Si	1.22577400	-4.33672400	0.98929000
H	-0.02224900	-3.66572600	1.37452200
H	1.24965600	-4.78612000	-0.40620600
H	1.53598900	-5.45038800	1.90185300

Table A3.3 LUMO energies for various model sites

Model site	LUMO Energy (mHa)	
	Equilibrium geometry	Non-equilibrium geometry[a,b]
Q^0	-18.2	-
Q_1^1	-18.0	-
Q_2^2	-11.9	-
Q_0^1-Q_0^1	-21.0	-26.1 (11.6)
Q_1^2-Q_0^1	-18.7	-22.3 (11.0)
Q_1^2-Q_1^2	-13.1	-20.6 (16.3)
Q_2^3-Q_0^1	-17.2	-17.2 (n/a)[c]
Q_2^3-Q_1^2	-14.7	-19.3 (17.1)
Q_2^3-Q_0^2-Q_0^1	-26.3 (for Q_0^2)	-
Q_1^2-Q_0^2-Q_1^2	-24.6 (for Q_0^2)	-

[a] Low-lying non-equilibrium geometries with broken intramolecular hydrogen bonds were isolated from relaxed scans in the direction of a P-O-P=O torsion and then re-optimized to the nearest local minimum.

[b] Energies of the local minima relative to the equilibrium geometry, in kJ/mol.

[c] Local minimum with fewer intramolecular hydrogen bonds not found.

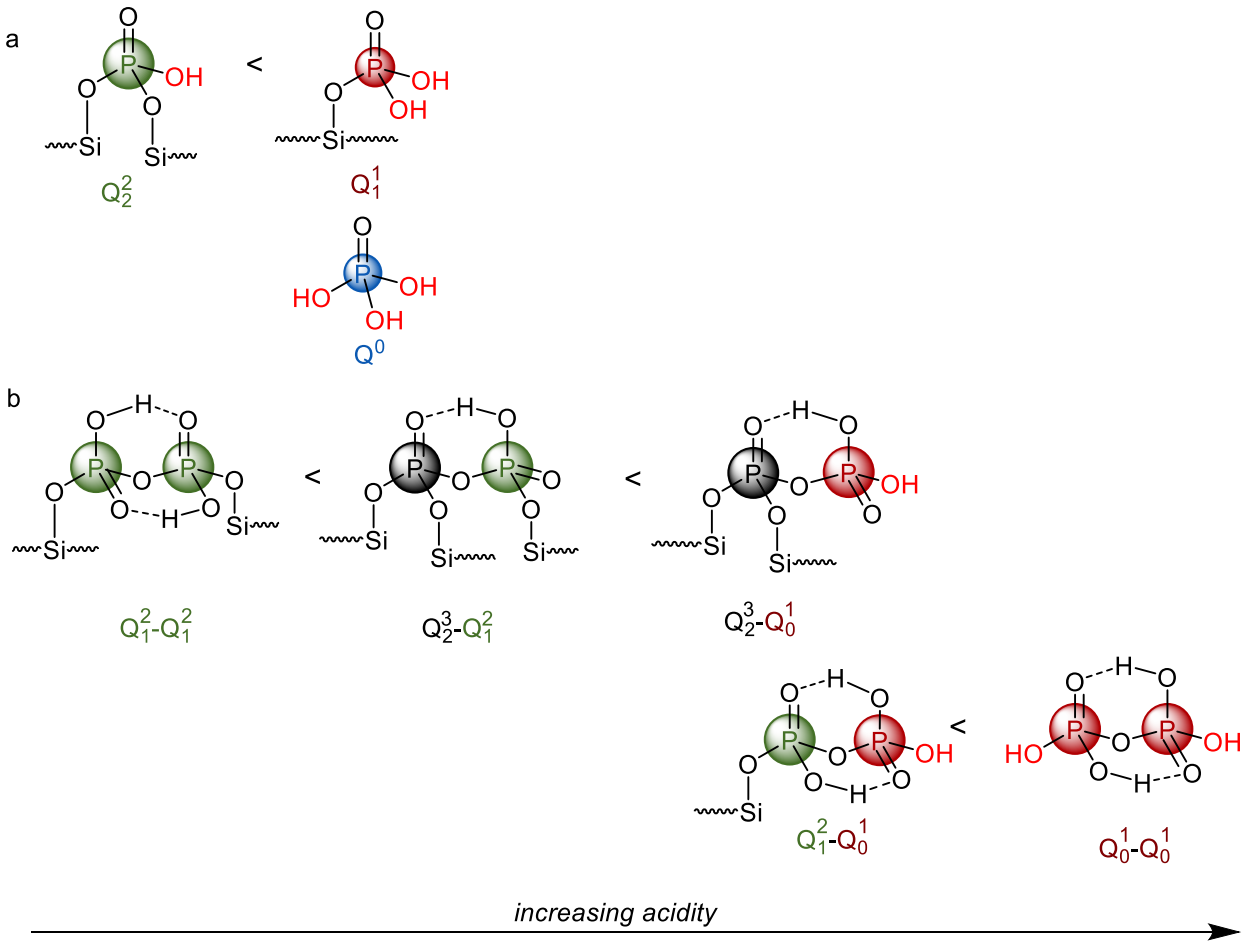

Scheme A3.1 Relative acidities of P-site models, for (a) mononuclear and (b) dinuclear sites, according to DFT calculations of LUMO energies. The acidic hydroxyls are shown in red.

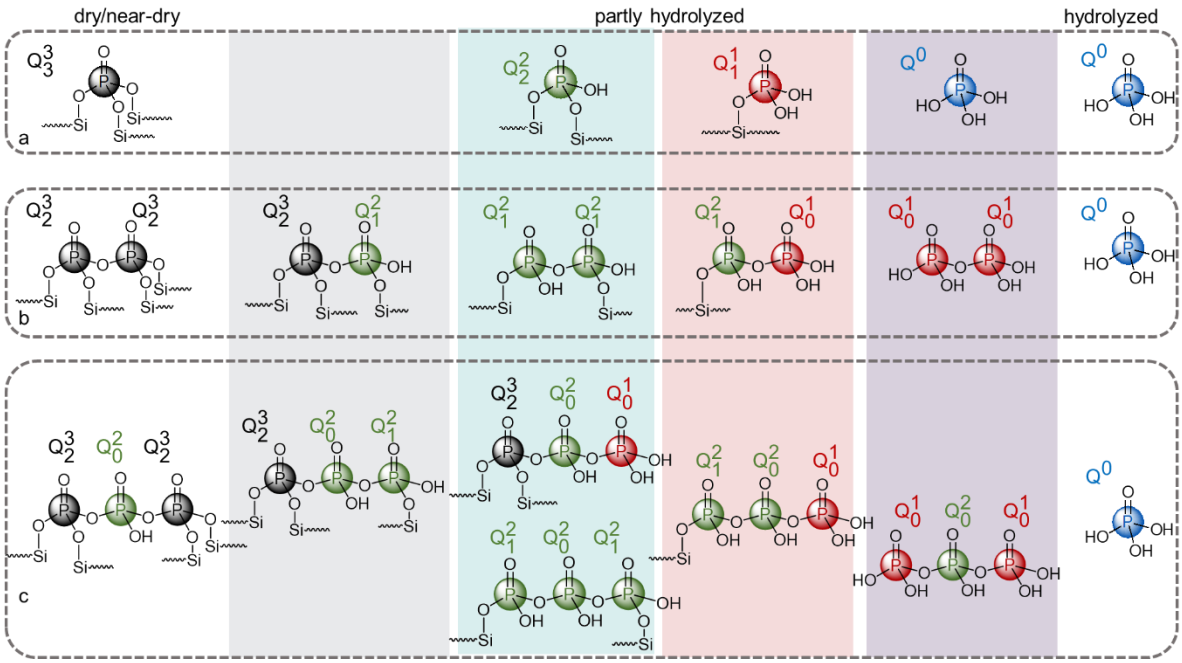

Scheme A3.2 Hydrolysis pathways consistent with NMR observations. Paths **a** and **b** are described and shown in the main text. Path **c** considers the trimeric Q^3_2-Q^2_0-Q^3_2 structure. It is proposed based on the DCP buildup curves, which suggest Q^3 sites are strongly coupled to the ^{29}Si of the P-SPP relative to the Q^2 sites. Hydrolysis of Q^3_2-Q^2_0-Q^3_2 gives rise to multiple possibilities, including Q^2_1-Q^2_0-Q^2_1. Their presence cannot be confirmed by multi-quantum NMR, due to the short relaxation times of the ^{31}P spins in the P-SPP material.

Additional References

(1) Bak, M.; Rasmussen, J. T.; Nielsen, N. C. SIMPSON: A General Simulation Program for Solid-State NMR Spectroscopy. *J. Magn. Reson.* **2011**, *213* (2), 366–400.

(2) Tošner, Z.; Andersen, R.; Stevensson, B.; Edén, M.; Nielsen, N. C.; Vosegaard, T. Computer-Intensive Simulation of Solid-State NMR Experiments Using SIMPSON. *J. Magn. Reson.* **2014**, *246*, 79–93.

Chapter 4: Stabilization of P-sites in P-zeosils by Increased Framework Hydrophobicity

4.1 Introduction

The tunable micropores and acid site densities of zeolites make them powerful as shape-selective catalysts for upgrading biomass-derived molecules to higher value chemicals.[1–6] However, biomass conversion frequently involves reactants that entrain water, and/or dehydration reactions that generate it. This is a concern because zeolites tend to be unstable in hot water, and in the presence of steam.[7] When zeolite frameworks, such as ZSM-5 are exposed to hot water or steam, dealumination and hydrolysis of Si-O-Si and Si-O-Al bonds results in a partially amorphous material, which can lead to deactivation of the catalyst and lower yields of desired products such as H_2, CH_4, and coke precursors.[8–10] Zeolite stability can be enhanced by dealumination, which increases hydrophobicity, and by P-modification.[11–14] Brønsted acidic zeolites functionalized with organosilanes that cap silanol defects also have higher hydrolytic stability compared to their hydrophilic unfunctionalized analogs,[11] and are therefore more stable catalysts for alcohol dehydration and alkylation of 2-propanol and *m*-cresol, respectively.[9]

Al-free zeolites (*aka* zeosils) are more hydrophobic and therefore more stable towards hydrolysis than materials with low Si/Al ratios. P-modification of zeosils installs P-OH sites with moderate Brønsted acidity. These P-zeosils are reported to catalyze the selective conversion of glucose-derived DMF to *p*-xylene,[15] and of furfural-derived THF to 1,3-butadiene.[16] In our recent solid-state NMR investigation of a P-modified self-pillared pentasil (P-SPP), we discovered a diverse group of P-sites, whose relative abundance and acidity

varies as a function of water content due to progressive hydrolysis of first P-O-Si and then P-O-P linkages.[17] Since the local water concentration depends on the hydrophobicity of the zeolite framework, the evolution of the P-site distribution is likewise expected to be vary with the zeolite.

The amount of water near the active site can also affect the outcome of zeolite-catalyzed reactions.[18,19] For instance, water generated by the acid-catalyzed condensation in the methanol-to-olefin (MTO) transformation competes with methanol for adsorption on Brønsted acid sites.[20] Water also catalyzes the formation of formaldehyde, an MTO intermediate responsible for suppressing initiation and termination rates in the hydrocarbon pool mechanism.[21] Water clustering also affects acidity, by converting protons associated with the zeolite framework to $(H_2O)_nH_3O^+$ ions.[22,23] Nevertheless, their confinement in the zeolite micropores confers higher acidity than homogeneous solutions at the same proton density.[24–26] Magic-angle spinning nuclear magnetic resonance (MAS NMR) is a powerful tool to probe water interacting with zeolites.[27,28] In HZSM-5, distinct ^{1}H NMR signals were reported for Brønsted acid sites (BAS) in the micropores, water strongly adsorbed at BAS, and extra-crystalline water.[29] Silane-treatment of the external zeolite surface prevented liquid-phase water from accessing BAS in the micropores.[29]

In this study, solid-state NMR methods are used to probe the P-site distribution and its water-sensitivity in two P-zeosils: hydrophilic SPP and hydrophobic BEA. Differences in the SPP and BEA architectures presumably confer different hydrophobicities: SPP has an open, house-of cards architecture with abundant SiOH defects that are readily accessible to water, while dealuminated BEA has SiOH nests that are buried inside the pores. Since resolution is limited in conventional ^{1}H MAS NMR, ultrafast MAS (in excess of 50 kHz) was used to

investigate the nature and abundance of hydroxyl groups in the two zeosils, before and after P-modification. ^{31}P MAS NMR was used to observe the P-site distribution as a function of water content, and to assess the role of the zeolite framework on P-site accessibility and hydrolytic stability.

4.2 Results and Discussion

4.2.1 Effect of the zeosil framework on the distribution of P-sites in dehydrated zeosils

To observe the impact of the framework on the types of P-sites formed by post-synthetic modification with H_3PO_4, the ^{31}P MAS NMR spectrum of dehydrated P-BEA was acquired (Figure 4.1a). It is compared with the previously reported[17] spectrum of dehydrated P-SPP in Figure 4.1b. The latter shows a broad isotropic peak at -43 ppm. This signal and its strong spinning sidebands were assigned to rigid, surface-bound Q^3-sites which lack POH groups (Scheme 4.1, dotted box). Although signals from other Q^n ($n \neq 3$) sites may be present, their intensities are low enough for the dehydrated zeolite to make their contributions undetectable in this poorly-resolved spectrum. In contrast, the spectrum of dehydrated P-BEA clearly contains signals for multiple Q^n (n = 1, 2, 3) sites. The isotropic peak at -45 ppm corresponds to Q^3 sites, while the peaks at -28 and -10 ppm are assigned to Q^2 and Q^1 sites, respectively. Thus, dehydrated P-BEA has a higher fraction of acidic P-sites (i.e., with POH groups) relative to dehydrated P-SPP.

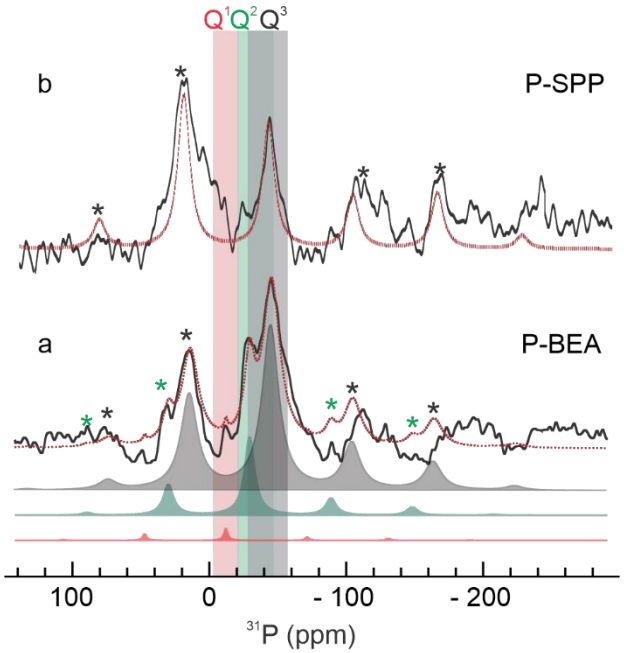

Figure 4.1 ^{31}P MAS NMR spectra (black) of dehydrated P-zeosils: (a) P-BEA, and (b) P-SPP, both with Si/P = 27, and the corresponding simulations (red) that include contributions for each Q^n component. Both materials were handled under strictly inert conditions. Their spectra were recorded at room temperature and 18.8 T, using 20 kHz MAS. Asterisks (*) indicate spinning sidebands. Simulations were performed using the CSA model in Topspin 4.0.6. Deconvolution of the spectrum of P-BEA into its Q^n components is shown in the shaded spectra, which are offset vertically.

The relative proportions of each type of P-site in dehydrated P-BEA were estimated by spectral deconvolution (shaded spectra in Figure 4.1a). Fitting the simulated spectrum to the experimental data (shown in red and black, respectively) yields the results in Table 4.1. Despite the uncertainty due to the low SNR, both visual inspection and deconvolution show that the areas decrease in the order $Q^3 > Q^2 >> Q^1$. The linewidths of the Q^3 and Q^2 signals are broadened by chemical shift heterogeneity, which are not averaged out by MAS. They may

arise from sites that are framework-bound via P-O-Si linkages, oligomeric polyphosphoric acids containing P-O-P linkages, or mixed sites containing both P-O-Si and P-O-P linkages. It is difficult to assess whether this is true for the Q^1 signals, as their contribution to the ^{31}P MAS NMR spectrum is small (4 %).

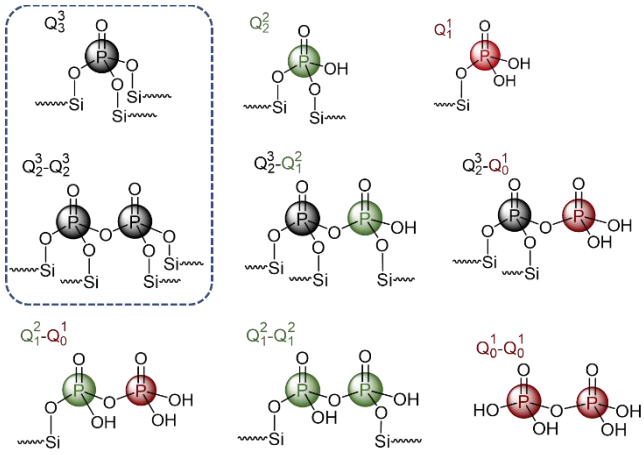

Scheme 4.1 Proposed structures for mononuclear (top row) and dinuclear (middle and bottom rows) P-sites present in the P-zeosils. The two types of Q^3 sites previously proposed[1] to give distinct signals in the ^{31}P MAS NMR spectrum of dehydrated P-SPP are indicated by the dashed box.

Table 4.1 Comparison of chemical shift parameters for dehydrated P-SPP and P-BEA, obtained by fitting simulated spectra to the experimental data [a]

air exposure time (min)	material	region	CS_{iso} (ppm)	CSA [c] (ppm)	fractional contribution [b]
0	P-BEA	Q^3	-45	-130 ± 17	0.65
		Q^2	-28	-100 [d]	0.31

		Q^1	-10	-80 [d]	0.04
	P-SPP	Q^3	-44	-205 ± 29 [c]	-
1	P-BEA	Q^3	-42	-119	0.31
		Q^3	-35	-140	0.31
		Q^2	-25	-124	0.22
		Q^2	-19	-113	0.10
		Q^1	-10	-72	0.05
	P-SPP	Q^3		-160 ± 9	-

[a] Spectra were recorded at 18.8 T using 20 kHz MAS. [b] The fractional contribution is the contribution of each component to the total spectrum intensity. [c] Uncertainties in the fit parameters were determined by varying each CSA value manually in turn from its optimum value, until the spectral overlap of the simulated and experimental data decreased by ±1%. This change resulted in a visually detectable decrease in fit quality. Reported parameter values are the average of the values at the (±) error limits. [d] Error bars for the CSA values of the Q^2 and Q^1 signals could not be determined, due to poor SNR.

Since several structures can give rise to multiple signals in the same Q^n region, we will use the more precise naming convention introduced in our previous work:[17] Q^n_m, in which the upper index (n) represents the total number of P–O–Y bonds (where Y can either be Si or P), while the lower index (m) indicates only the number of P–O–Si bonds. This notation enables us to distinguish signals for exclusively surface-bound P-sites ($m = n$), free (poly)phosphoric acid oligomers ($m = 0$), and surface-bound polyphosphoric acid species ($0 < m < n$). Thus, a Q^2 signal may have contributions corresponding to sites that only contain P-O-Si linkages

(Q_2^2) or mixed dinuclear sites such as $Q_1^2 - Q_0^1$ containing both P-O-Si and P-O-P linkages (Scheme 4.1). Dinuclear $Q_1^2 - Q_0^1$ sites would contribute to the Q^1 signal as well. It is evident that the Q^2 and Q^1 signals observed in dehydrated P-BEA must arise from P-sites that are not present in P-SPP.

Simulation of the spinning sideband pattern yields the chemical shift anisotropy (CSA) for each site, reflecting on their mobility and/or symmetry. CSA values corresponding to each isotropic chemical shift (CS_{iso}) are listed in Table 4.1. Interestingly, the CSA value for the Q^3 site in P-BEA (-130 ppm) is significantly smaller than for the related site in P-SPP (-205 ppm). In our previous study, we observed larger CSAs for more rigid, framework-bound monomeric Q_m^n ($m = n$) sites than for more mobile oligomeric Q_m^n ($m < n$) sites that have the same value of *n* but are not framework-bound. The latter are formed as the framework-bound monomeric sites of P-SPP hydrolyze.[17] We hence suggest that the Q^3 sites with smaller CSA in P-BEA are also more mobile compared to those in P-SPP. Compared to the rigid framework-bound Q^3 sites in P-SPP (Q_3^3 and Q_2^3, Scheme 4.1a), P-BEA framework likely includes more mobile Q^3 sites with P-O-P linkages, e.g., Q_1^3 or Q_0^3. The CSA values for the Q^2 and Q^1 signals in dehydrated P-BEA are comparable to those reported previously for slightly hydrolyzed P-SPP (oligomeric $Q_2^3 - Q_1^2$ and $Q_0^1 - Q_0^1$ sites). Taken together,[17] we can conclude that dehydrated P-BEA contains a greater population of P-O-P linkages while P-SPP contains a greater population of P-O-Si linkages.

Since water is present or is a product of many acid-catalyzed reactions, the stability of the P-zeosils in the presence of water is of interest. According to our previous study, the Q^3 sites in dehydrated P-SPP hydrolyze rapidly upon exposure to ambient moisture, resulting in their conversion to Q^2, Q^1, and eventually Q^0 sites. Furthermore, we have previously

established that P-O-Si linkages hydrolyze faster than P-O-P linkages. Since the P-sites in dehydrated P-BEA have fewer P-O-Si linkages and more P-O-P linkages compared to P-SPP, we expect the hydrolytic stability of P-sites of P-BEA to be greater compared to P-SPP.

4.2.2 Comparative hydrolytic stability of P-sites

Next, the hydrolytic stability of P-BEA was assessed, and compared with P-SPP. A sample of dehydrated P-BEA in an NMR rotor was briefly exposed to the laboratory ambient by opening the rotor cap for short periods of time. ^{31}P NMR spectra were recorded as the extent of zeosil hydration increased.

The ^{31}P NMR spectrum of dehydrated P-BEA changes gradually upon exposure to small amounts of water vapor (Figure 4.2). Air exposure lasting just 1 min resulted in the emergence of a new Q^3 peak at -37 ppm, in addition to the original peak at -45ppm in the Q^3 region. The CSA values of the two types of Q^3 sites are -141 and -129 ppm, respectively, indicating they are both more mobile than Q^3_3 sites (simulated spectrum shown in Figure A4.1). Two distinct Q^3 sites with different CSAs were also observed in P-SPP after 2 min exposure to ambient conditions.[17] Q^3 signals with lower CSAs could arise from $Q^3_2 - Q^2_1$ or $Q^3_2 - Q^1_0$ sites shown in Scheme 4.1. 1 min exposure of P-BEA to air also causes signals in the Q^2 and Q^1 regions to increase in intensity, at the expense of signal intensity in the Q^3 region. Furthermore, the poorly resolved signal at -28 ppm in the Q^2 region is replaced by two signals at -19 and -25 ppm. Thus, the briefly air-exposed material contains multiple types of Q^2 sites (e.g., $Q^3_2 - Q^2_1$, $Q^2_1 - Q^2_1$ and/or $Q^2_1 - Q^1_0$). The CSA values of the two Q^2 signals are -123 ppm (peak at -25 ppm) and -112 ppm (peak at -19 ppm), while that of the Q^1 signals is

estimated to -75 ppm, respectively, consistent with the expected increase in mobility upon partial hydrolysis.

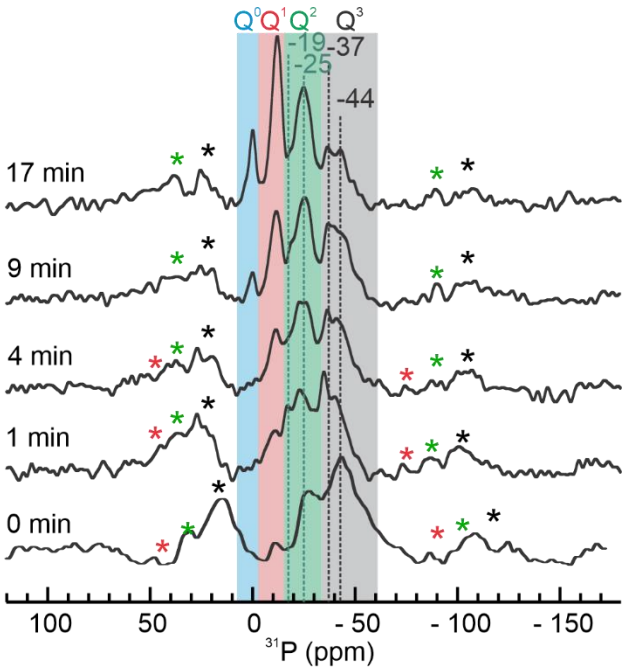

Figure 4.2 The effect of air exposure time (and hence, increasing hydration), on the ^{31}P MAS NMR spectrum of initially dehydrated P-BEA. All spectra were recorded at room temperature in an 18.8 T magnet using 20 kHz MAS. Spinning sidebands for the Q^1, Q^2 and Q^3 signals are indicated by * in red, green, and black, respectively.

After 4 min ambient exposure of P-BEA, peaks in the Q^2 and Q^1 regions become more prominent, while the intensity in the Q^3 region continues to decrease. After 9 min ambient exposure, a Q^0 signal is observed. As hydrolysis proceeds, all Q^n signals become narrower and their spinning sidebands become less intense. These observations indicate increasing mobility, and are qualitatively similar to trends reported for P-SPP.[17]

To assess changes in the Q^n distribution quantitatively, the integrated peak areas were tracked as a function of ambient exposure time, starting from the initial dehydrated state. The results are compared for the two P-zeosils in Figure 4.3 (spectra corresponding to all ambient exposure times are shown in Figure A4.2). Their behaviors are visibly different between P-SPP and P-BEA. As previously reported,[17] the P-sites in P-SPP undergo hydrolysis stepwise, $Q^3 \rightarrow Q^2 \rightarrow Q^1 \rightarrow Q^0$, and the Q^3 signals disappear entirely after approx. 30 min ambient exposure. In contrast, the Q^3 signals in P-BEA these sites decline from 60 % to about 12 % of total P-sites within 30 min, then do not change significantly upon longer exposure (up to 120 min, Figure A4.3). The fraction of Q^2 sites in P-BEA remains largely unchanged, suggesting these sites are stable, while the Q^1 and Q^0 signals increase slowly. In other words, all P-sites in P-BEA are considerably more stable towards hydrolysis than those in P-SPP. The fully hydrolyzed spectrum of both P-BEA and P-SPP show predominantly Q^0 and Q^1 sites (Figure A4.4 and A4.5).

Thus, the differences in the initial distribution, as well as stabilities of P-sites in the two different zeosils are evident. The abundance and stability of P-O-Si and P-O-P linkages in the P-modified zeosils is expected to be a function of both the number and accessibility of the hydroxyl groups that are present in the unmodified zeosil, prior to the introduction of phosphorus. To understand the role of the framework in stabilizing P-sites towards hydrolysis, we investigated the distribution of hydroxyl groups and water in the unmodified zeosils, and compared to that in P-zeosil by ^{1}H NMR spectroscopy.

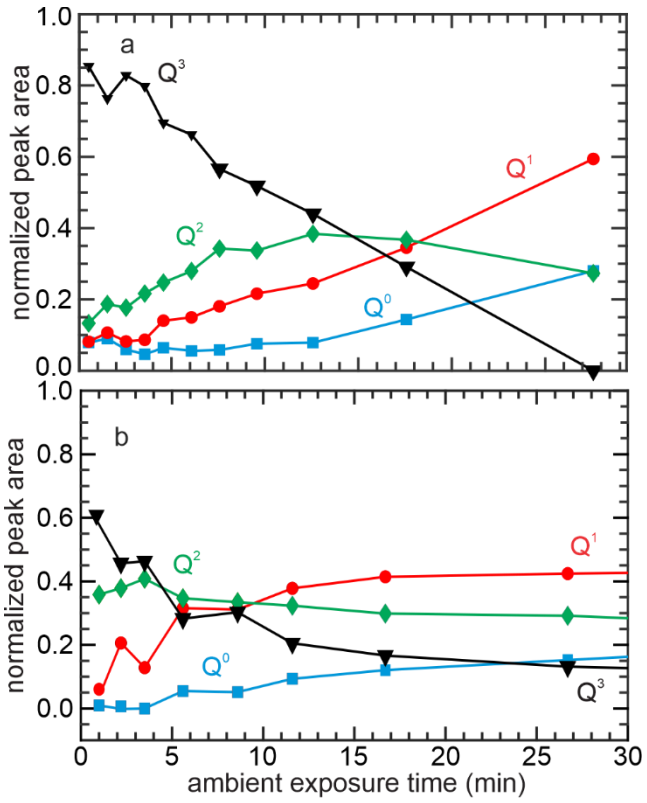

Figure 4.3 Evolution of P-sites quantified by their integrated peak intensities (including spinning sidebands) for different groups of P-sites in (a) P-SPP, and (b) P-BEA, as a function of water content. The areas of the peaks in each Q^n region are normalized to the total peak area at each time point.

4.2.3 Silanol distribution in the unmodified zeosils

Protons associated with hydroxyl groups and water in zeolites experience significant ^1H-^1H dipole coupling, resulting in line broadening and severe spectral overlap. Assessing their distribution by ^1H NMR requires sufficiently high spectral resolution. The spectrum of dehydrated SPP acquired at ν_R =16 kHz consists of a broad peak spanning from 4 to -2 ppm (Figure 4.4a). To increase the resolution, ^1H MAS NMR spectra were acquired using ultrafast MAS (frequency ν_R = 62.5 kHz) to average the dipole-dipole coupling interactions more

effectively.[30] Figure 4.4b shows the considerable improvement in resolution afforded by ultrafast MAS.

In the ^{1}H MAS NMR spectra of dehydrated zeolites, non-H-bonded SiOH groups that arise from crystallite lattice termination typically give rise to peaks in the range 1.8-2.2 ppm.[31,32] In studies of BEA and ZSM zeolites, a peak even further upfield peak (1.2 ppm) has been observed and also assigned to non-H-bonded SiOH groups.[31,32] The broad shoulder extending downfield from 2.2 ppm, as far as 8 ppm in some cases, is assigned in zeosils to H-bonded SiOH groups, as well as water H-bonded to SiOH.[33–35] The exact locations and linewidths of the broad signals depend on the extent of H-bonding, rate of chemical exchange, and relative amounts of water and SiOH present. We will refer to them simply as exchange-averaged SiOH/H_2O resonances.

The ^{1}H NMR spectrum of dehydrated SPP, recorded using ultrafast MAS, was integrated (see Experimental for details). The total OH content, (6.9 ± 1.1) mmol/g, determined from the same material measured twice, is considerably larger than values reported for silicalite, 0.2-0.4 mmol/g depending on crystallite size.[36] The increase is due to the house-of-cards architecture of SPP (Figure A4.6), which results in a much larger number of SiOH defects. The spectrum of dehydrated SPP reveals resonances for non-H-bonded SiOH groups at 0.8, 1.2, and 1.8 ppm. According to the spectral deconvolution, they are superposed on a very broad peak, centered at 1.8 ppm. Since this broad feature spans a chemical shift range of ca. 2.5 ppm, it represents SiOH groups with considerable chemical shift heterogeneity. Broad signals are often observed in disordered systems such as amorphous silicas. The peak, which represents the majority of silanols (59 %), is also likely broadened

due to H-bonding interactions. The fractional contributions of all the silanol signals are summarized in Table 4.2.

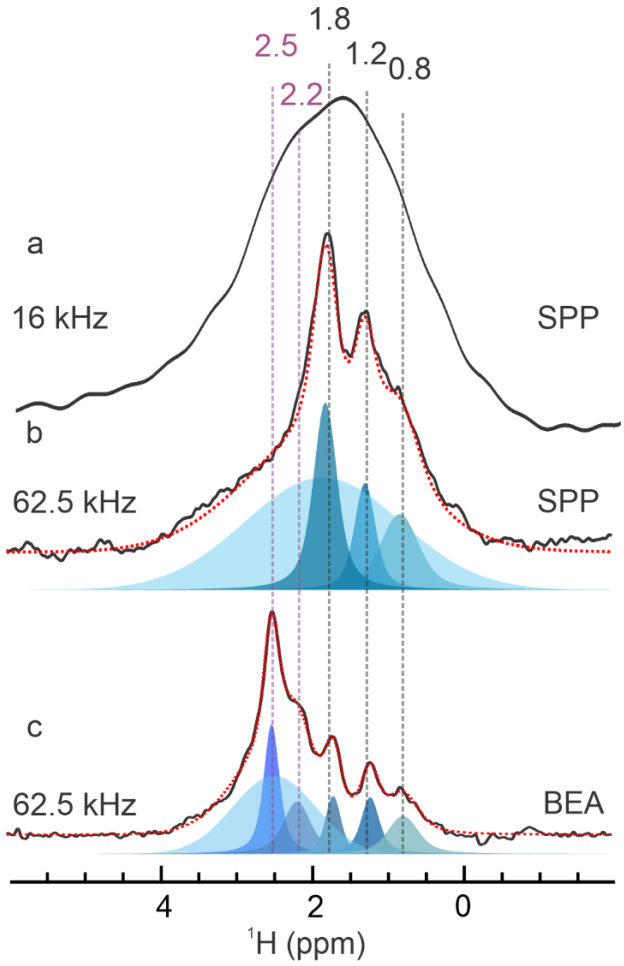

Figure 4.4 ^{1}H MAS NMR spectra (black solid line) of two zeosils in their dehydrated forms: (a), (b) SPP and (c) dealuminated BEA (both handled under a strictly inert atmosphere). The spectra were recorded at room temperature and 18.8 T with spinning frequencies (ν_R) of (a) 16 kHz, and (b), (c) 62.5 kHz. Dry N_2 was used as both bearing and spinning gases. Samples were packed under N_2 in 3.2-mm (16 kHz MAS) and 1.3-mm (62.5 kHz) rotors, and therefore represent different zeosil masses. The peak heights in (a) and (b) are normalized to highlight the improvement in resolution. Spectra were simulated (sum: red dotted line) using the

Gaussian/Lorentzian model in TopSpin 4.0.6. The deconvoluted contributions are shown as shaded spectra. Peaks shared by the two zeosils are labeled in black; peaks unique to BEA are labeled in purple.

Table 4.2 Types and relative amounts of silanols present in dehydrated SPP and BEA, classified according to their peak widths

^{1}H (ppm)		**SPP**		**BEA**	
Narrow	**Broad**	**FWHM (Hz)**	**Fraction**	**FWHM (Hz)**	**Fraction**
0.8		580	0.12	470	0.10
1.2		315	0.09	280	0.09
1.8		360	0.19	235	0.07
	1.8	1950	0.59		
2.2				430	0.13
2.5				240	0.18
	2.5			1030	0.43

The ultrafast ^{1}H MAS NMR spectrum of dehydrated, dealuminated BEA zeolite is shown in Figure 4.4c. Its total hydroxyl content, (2.7 ± 1.5) mmol/g, is about half that of SPP. This finding is consistent with the expectation that BEA is more crystalline and more hydrophobic. ^{1}H NMR resonances associated with non-H-bonded SiOH groups appear at 1.8, 1.2 and 0.8 ppm, similar to the peaks observed for SPP. In addition, there are two sharp peaks at 2.2 and 2.5 ppm. Narrow ^{1}H signals at or above 2.2 ppm are typically assigned to bridging

hydroxyls associated with extra-framework alumina, Al(OH)Al.[37] However, the Al content determined by ICP analysis is negligible (Al content = 0.0145 μmol/g, Si/Al ~1600), consistent with the very weak signals in the ^{27}Al NMR (Figure A4.7). Furthermore, there are no ^{1}H NMR peaks corresponding to either Si(OH)Al sites (3.8 - 5.2 ppm) or terminal AlOH groups (-0.2 ppm).[32,37–39] Consequently, the narrow resonances above 2 ppm are assigned to non-H-bonded SiOH groups present in BEA, but not SPP. They may be associated with SiOH nests created by dealumination. The broad peak centered at 2.5 ppm is assigned to silanols in an amorphous phase and/or H-bonded silanols. It represents the largest fraction of silanols in BEA (43 %, Table 4.2). Notably, all ^{1}H resonances in BEA, both broad and narrow, have smaller FWHMs compared to those in SPP, consistent with crystalline BEA having more uniform silanol sites than disordered SPP.

To compare accessibility of the silanol sites to water in the two zeosil frameworks, each was exposed to the laboratory ambient by briefly opening the NMR rotor. For SPP, a few minutes of ambient exposure resulted in no significant differences in its ^{1}H NMR spectrum. However, after 20 min, the total ^{1}H content of the zeosil increased, corresponding to the adsorption of ~2 mmol H_2O/g (Figure 4.5a). The intensities of the narrow ^{1}H NMR peaks at 0.8 and 1.2 ppm changed little (Figure A4.9, Table A4.2), suggesting that they represent SiOH groups not readily accessible to water. A similar attribution was made for silanols associated with amorphous silica nanoparticles, where ^{1}H resonances in this chemical shift range were unaffected by exposure to aqueous NH_4F, or liquid D_2O (1 d at room temperature).[40] In contrast, the narrow silanol peak at 1.8 ppm in the spectrum of SPP decreased slightly in intensity upon exposure to water and a new peak appeared at 2.9 ppm, indicating silanols undergoing exchange-averaging with H_2O. A much longer (~15 h) ambient

exposure resulted in a tripling of the adsorbed water content, to ~6 mmol/g, and the disappearance of the narrow peak centered at 1.8 ppm (Figure A4.9, Table A4.3). The exchange-averaged shifted further downfield to 4.2 ppm, approaching the expected chemical shift of bulk water (4.8 ppm).[41] There is a shoulder at 4.3 ppm on the main water peak indicating water in a different location, perhaps in zeolite pores of a different size where it does not exchange readily with silanols and the main population of water. The peaks at 0.8 and 1.1 ppm persist, and thus remain water-inaccessible. A broad signal is also present, which is slightly upfield shifted at 1.4 ppm, the origin of which is unknown.

Brief (20 min) ambient exposure of dehydrated BEA resulted in adsorption of 2 mmol H_2O/g zeosil (Figure 4.5b). The non-H-bonded SiOH peaks at 0.7 and 1.1 ppm remain visible, confirming that these SiOH groups are largely water-inaccessible (Figure A4.9, Table A4.5). The intensities of the downfield peaks (above 2 ppm) decreased, and a new, intense peak at 3.1 ppm with a shoulder at 3.6 was observed. The downfield shifted peak is due to exchange-averaging between accessible SiOH sites and adsorbed H_2O. A further shift to 3.9 ppm, in the direction of the chemical shift of bulk water (4.8 ppm), was observed upon longer ambient exposure (~15 h). The water peak has shoulders at 3.3 and 4.5 ppm (Figure A4.9, Table A4.6), presumably caused by adsorption of water into pores not in fast exchange with the main water peak. The areas of the ^{1}H NMR peaks for exchanged-averaged SiOH/H_2O increase as a function of water content, while the water-inaccessible SiOH signals are largely unaltered (Figure A4.9). The broad signal at 2.5 ppm appears to move upfield, eventually stabilizing at 1.8 ppm.

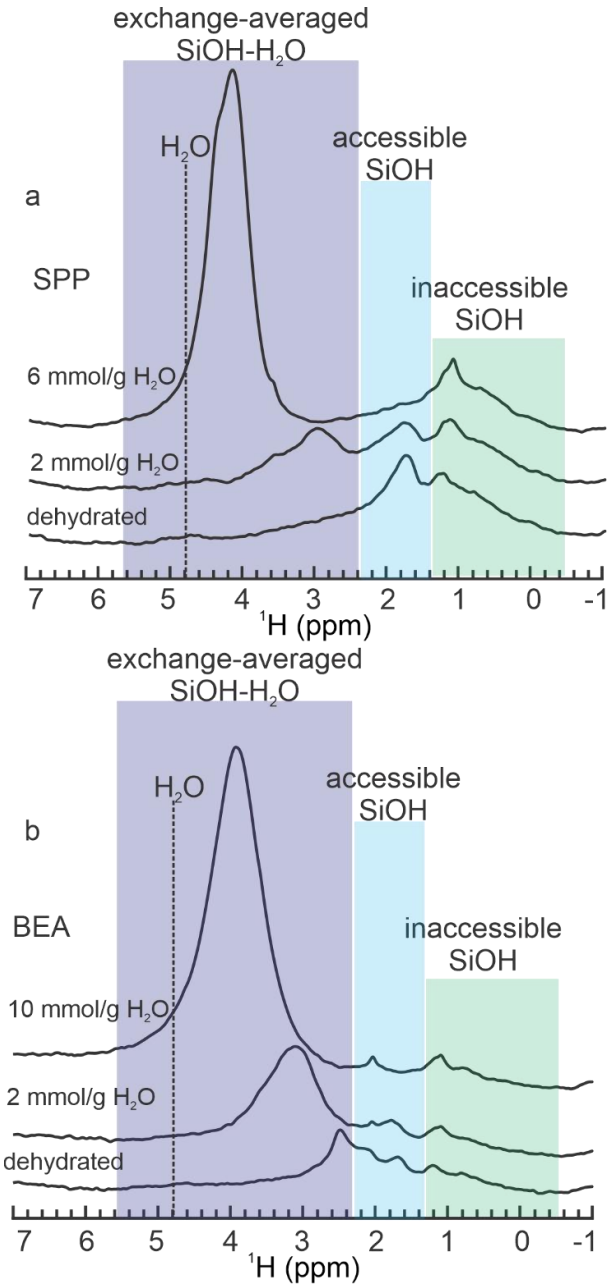

Figure 4.5. ^{1}H MAS NMR spectra of (a) SPP, and (b) dealuminated BEA, showing the evolution of as a function of adsorbed water content (introduced by ambient exposure of the dehydrated zeolite). The amount of adsorbed H_2O was quantified using an external spin-counting reference. All spectra were recorded at room temperature and 18.8 T, using 62.5 kHz MAS. The expected position of the bulk H_2O signal is indicated with a dashed line.

4.2.4 Effect of P-modification on zeosil silanols

H_3PO_4 was incorporated into the zeosils by wetness impregnation at room temperature, followed by calcination in flowing air at 600 °C.[15] According to the ^{1}H MAS-NMR spectrum of fully dehydrated P-SPP (Si/P = 27), P-modification resulted in suppression of the original SiOH signals (both water-accessible and -inaccessible), Figure 4.6a. After calcination, only a small peak at 1.7 ppm with a shoulder at ~2 ppm remains. Thus, H_3PO_4 reacts with all types of SiOH in SPP, including those which are inaccessible to water upon brief exposure to the laboratory ambient, to form P-O-Si linkages to the zeolite framework. Considering that the initial SiOH content of SPP is 6.9 mmol/g, and the P-content in the material is 0.57 mmol/g (because of Si/P = 27), SiOH/P = 12, which is much higher than the expected value of 3 (for a material containing predominantly Q^3 sites). This means that the decrease in the SiOH content by 95 % cannot only be explained by the formation of P-O-Si linkages, and likely is due to condensation of H-bonded SiOH to form ≡SiOSi≡. Similarly, P-modification of BEA also resulted in dramatic changes in the ^{1}H NMR spectrum, Figure 4.6b. The signals for all types of SiOH are attenuated by 92 %, however, the value of SiOH/P (=5) is higher than expected in this case too, suggesting that condensation of H-bonded SiOH occurs. Variability in amount of P added to the materials also results in differences in the consumption of surface SiOH.

Qualitatively, combining insights from ^{1}H and ^{31}P NMR, the predominantly framework-bound nature of P-sites in dehydrated P-SPP is consistent with the higher SiOH density in the SPP framework, which allows the formation of more P-O-Si linkages. In contrast, the lower SiOH density in BEA, as well as the structural differences between BEA

and SPP, likely contributes towards more sites with mixed P-O-Si and P-O-P linkages, Scheme 4.2.

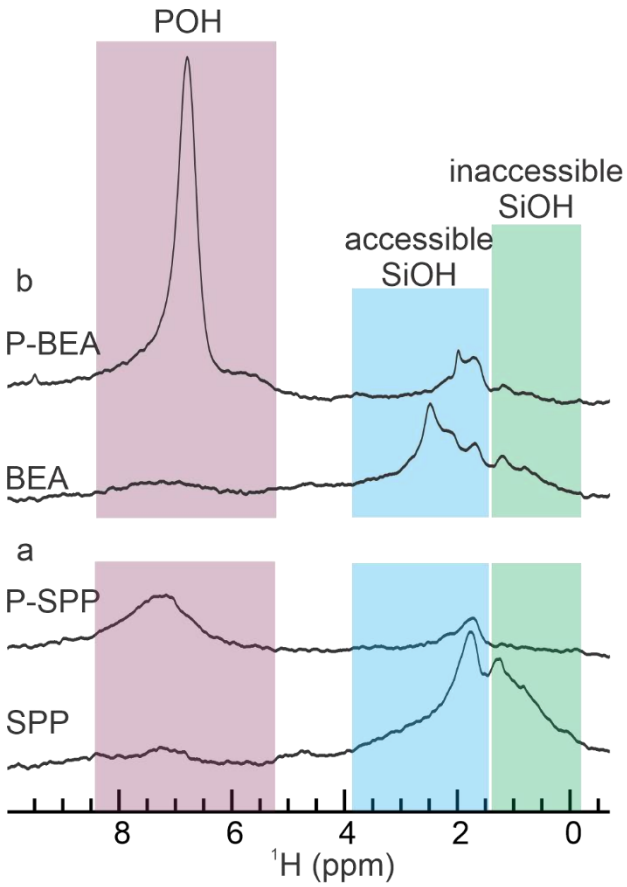

Figure 4.6 Comparison of ^{1}H MAS NMR spectra for dehydrated SPP and BEA zeolites, with and without P-modification (Si/P = 27). The intensities are normalized to the number of scans to allow with direct comparison of the intensities. All spectra were recorded at room temperature at 18.8 T, using 62.5 kHz MAS. Liquid N_2 boiloff was used as both bearing and spinning gases.

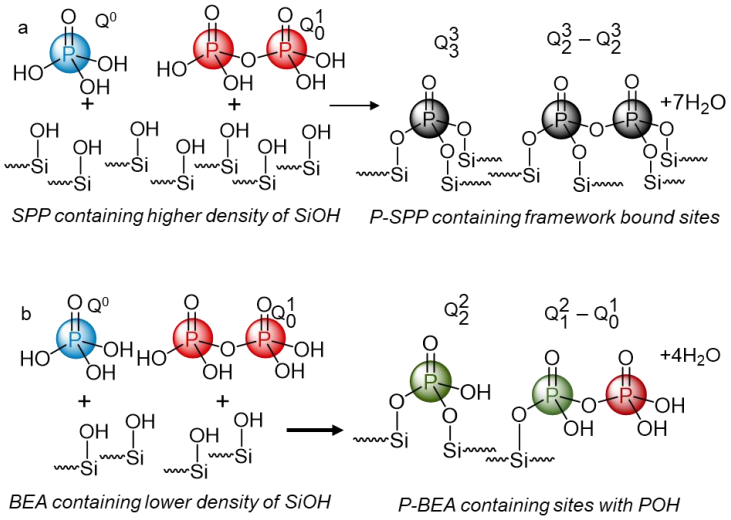

Scheme 4.2 Formation of P-sites in the zeosils: (a) SPP, and (b) BEA, by condensation of H_3PO_4 and $H_4P_2O_7$ with SiOH groups.

In addition to residual unreacted SiOH signals, the ^{1}H NMR spectra of dehydrated P-zeosils also contain new signals at ca. 7 ppm (Figure 4.6). We assign them to POH groups. In silicophosphate glasses and phosphates, their ^{1}H chemical shifts appear over a large range, from 15.8 to 6.6 ppm depending on the synthesis procedure and thermal treatment.[42,43] The intensity of the peak in the two P-zeosils should depend on the number of POH groups present. In addition, the position and intensity may depend on the presence of residual water in exchange with POH. The POH ^{1}H signal in this material is far more intense in P-BEA than in P-SPP, however we have observed that it is dependent on the synthesis procedure which can lead to different amounts of P in the material, thus impacting the amount of POH sites (Figure A4.10).

In dehydrated P-SPP, the POH peak appears at 7.2 ppm. The signal is broad (FWHM ~1000 Hz) even when acquired under conditions of ultrafast MAS. There is presumably an inhomogeneous distribution of rigid POH groups, arising from the chemical shift dispersion

in the SPP framework that renders the local environment of POH heterogeneous. The POH signal in dehydrated P-BEA is significantly narrower (FWHM 270 Hz), and appears slightly upfield, at 6.8 ppm. The narrower linewidth in P-BEA is likely due to the lower structural heterogeneity in the BEA framework, which is also reflected in the relatively narrower ^{1}H MAS NMR resonances of the SiOH groups (Figure 4.4b and Table 4.2). The differences in the zeosil P-site distribution observed by both ^{1}H and ^{31}P MAS NMR are expected to impact their stability in the presence of water, as discussed in the next section.

4.2.5 Assessment of hydrolytic stability

To compare the stability of P-sites in the two zeosils towards hydrolysis, ^{1}H MAS NMR spectra were recorded after the introduction of small amounts of water, by timed exposure of the dehydrated samples to the laboratory ambient. In P-SPP, several brief (few min) exposures caused the peak at 7.2 ppm assigned to POH to increase in intensity and to move gradually upfield towards the chemical shift of bulk water at 4.8 ppm (Figure 4.7a). These changes are consistent with bulk water accessing the P-OH and moving the chemical shift towards it (Scheme 4.3).

After a long ambient exposure (~18 h) of P-SPP, the position of the POH peak stabilizes at approx. 5.9 ppm. It has two shoulders, at approx. 6.3 and 5.4 ppm. They may arise from differences in the pore filling mechanisms of the zeosil cages. Mesoporous silicas such as MCM-41 and SBA-15, with pore diameters of 3 and 8 Å, respectively, show differences in the ^{1}H NMR chemical shifts as the amount of adsorbed water increases, due to their different pore filling mechanisms.[44] For MCM-41, the chemical shifts show a bimodal distribution for the adsorbed water layer in fast exchange with surface SiOH groups, and absorbed water in

the pores. In contrast, water in SBA-15 shows a single ^{1}H NMR peak with a continuously varying chemical shift. It is hence plausible that water absorbed to different pores in P-SPP can give rise to the shoulders, as a consequence of the different pore filling mechanisms.

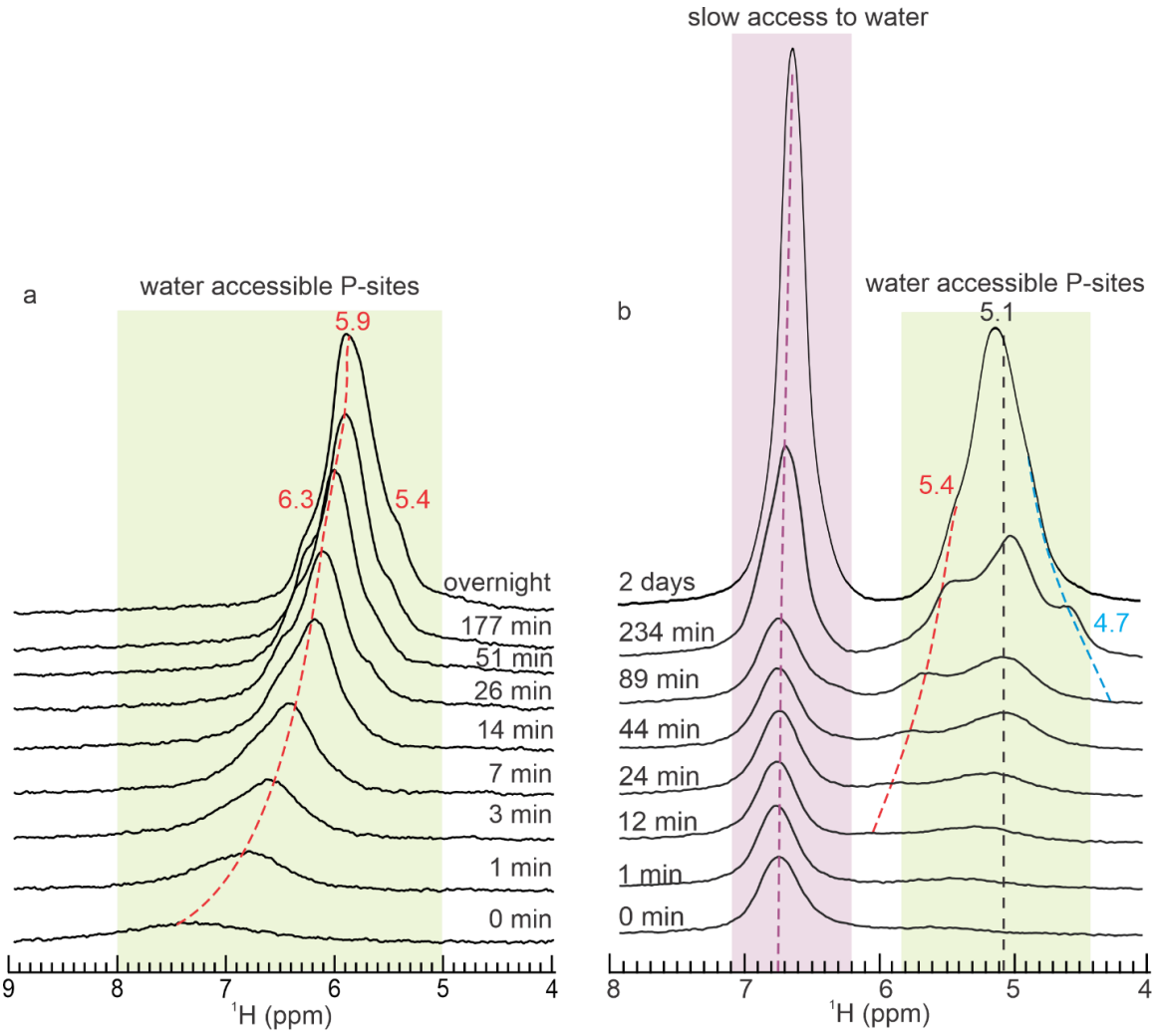

Figure 4.7 The effect of increasing room temperature ambient exposure, and hence water content, on the ^{1}H MAS NMR spectra of (a) P-SPP, and (b) P-BEA. The zeosils were initially dehydrated under vacuum at 450 °C. Spectra were recorded at room temperature and 18.8 T, using 62.5 kHz MAS.

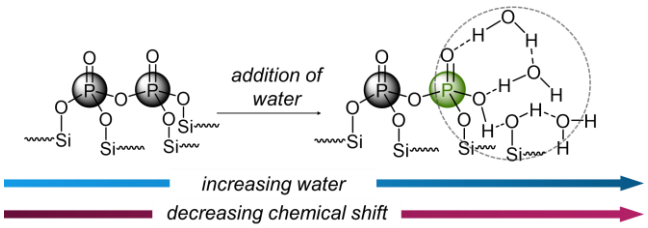

Scheme 4.3 Simplified schematic of a Q_2^3-Q_2^3 site undergoing hydrolysis to form a Q_2^3-Q_1^2 site. The ^{1}H NMR signal is composed of contributions from protons in POH, SiOH and H_2O (dotted grey circle) all hydrogen-bonded to one another and in fast chemical exchange. With the addition of more water that can access the P-sites, the chemical shift further decreases.

The hydrolysis behavior of P-BEA differs dramatically from that of P-SPP. According to the ^{1}H MAS NMR spectrum, ambient exposure does not cause the initial intensity of the POH peak at 6.8 ppm to change at all for the first 89 min, even though water is clearly visible in the spectrum, as a broad peak at 5.5 ppm, after just 1 min exposure (Figure 4.7b). After 12 min, its position stabilizes at 5.2 ppm, but it continues to increase in intensity. After 12 min, a second broad peak appears at 6.2 ppm, then shifts to 5.4 ppm as it increases in intensity upon further ambient exposure. Much later (after 234 min), a third broad signal appears at 4.5 ppm. It shifts to 4.7 ppm and increases in intensity upon further ambient exposure. Upon ambient exposure over even longer times (~2 days), all three peaks begin to coalesce at 5.1 ppm, suggesting that the fast exchange limit is finally reached. Similar to P-SPP, the resolved water signals are suggested to arise from H_2O in different pore locations (i.e., pore types) within the zeosil.

The majority of the P-sites in P-BEA, reflected in the POH peak at 6.8 ppm, therefore appear to resist hydrolysis despite increasing water content for ~ 90 min. This finding is consistent with the ^{31}P MAS NMR observations on the greater stability of the P-site

distribution in P-BEA relative to P-SPP, Figure 4.3b. After 234 min exposure, the POH peak begins to increase in intensity, but its chemical shift still does not change significantly, in sharp contrast to the behavior observed for P-SPP (Figure 4.7a). Thus, adsorbed H_2O to P-BEA does not interact with the P-sites or exchange protons with POH groups. Eventually (after ~2 days), the POH peak intensity increases significantly, presumably due to P-O-P and/or P-O-Si hydrolysis. However, there is no apparent accompanying shift in the peak position, and therefore no exchange with the protons of free water or nearby SiOH, and thus we speculate that the peak intensity increases due to P-O-P hydrolysis. The peak areas of the two regions have been plotted as a function of ambient exposure in Figure A4.15. Similar overall behavior was observed for a separately prepared batch of the two materials, however the hydrolysis occurred at a faster timescale, likely due to the higher relative humidity and the variability in P-content (Figure A4.11 and A4.12).

These results suggest that most of the P-sites in P-BEA are difficult for water to access (Scheme 4.4a). The hydrophobic zeosil may also contain some hydrophilic domains where POH groups are in fast exchange with H_2O, indicated by the small fraction of sites that are moving towards the chemical shift of water i.e. water-accessible. In contrast, the more open architecture in P-SPP results in most regions being readily accessible to water (Scheme 4.4b) since exchange is evident in the gradually shifting ^1H chemical signal. Eventually, all P-sites in both P-SPP and P-BEA hydrolyze to become Q^0 and Q^1 sites. When water is present in large excess, the ^1H MAS NMR spectra of both P-zeosils show a single peak at approx. 5.2 ppm (Figure A4.9). For P-BEA, the ^1H NMR peak appears to be unsymmetrical and broader, suggesting that the zeosil has different types of well-defined pores. The chemical shift is slightly different from that expected for water in zeolites (5.1 ppm).[29]

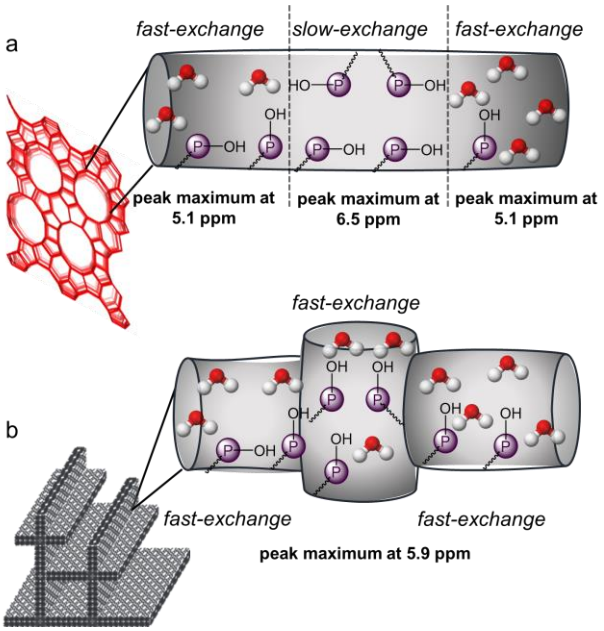

Scheme 4.4 Proposed distribution of P-sites in (a) P-BEA, and (b) P-SPP, and the consequences for the appearance of the ^{1}H MAS NMR signals.

These experiments show that P-site accessibility differs significantly in the two P-zeosils, likely due to architectural differences between SPP and BEA. Although the initial proton content in dehydrated P-BEA is larger than in P-SPP, BEA appears to have domains that are not readily accessible to water. This difference, as well as the greater abundance of hydrolytically robust P-O-P linkages, results in higher hydrolytic stability of the P-sites in P-BEA relative to P-SPP where the linkages are dominated by hydrolytically sensitive P-O-Si and the open framework which allows ready access to water.

4.3 Conclusions

P-modified self-pillared pentasil (P-SPP) and dealuminated zeolite BEA (P-BEA) having different hydroxyl contents were investigated. Upon P-modification, dehydrated P-BEA has less framework-bound sites, on average, with more POH groups (such as $Q_2^3 - Q_1^3$, $Q_1^2 - Q_0^1$ and $Q_0^1 - Q_0^1$) and are thus acidic, in contrast to the Q_3^3 and $Q_2^3 - Q_2^3$ sites which are the majority of P-sites in dehydrated P-SPP (which do not contain POH).

The impact of water on the two frameworks and their P-site distribution was compared using ^{31}P and ultra-fast ^{1}H MAS NMR. P-sites in P-BEA are more resistant to hydrolysis and persist over longer timescales compared to those in P-SPP. Quantification of the hydroxyl content confirms that SPP contains more SiOH groups. Ultra-fast ^{1}H MAS NMR affords improved resolution, which shows a distribution of different types of SiOH groups present in the two zeosils. The accessibility of the P-sites to water differs. The BEA framework results in a population of P-sites which are in slow exchange with water. On the other hand, the open architecture of the SPP framework results in more water-accessible P-sites. Additionally, P-BEA contains a greater fraction of sites with P-O-P linkages that undergo slower hydrolysis compared with P-O-Si linkages that are predominant in P-SPP, as a consequence of the different architectures of the two frameworks. Thus, the framework plays a role in the accessibility of H_2O to P-sites, which in turn is likely to influence the stability of the active P-sites in the catalytic conversion of oxygenated species from biomass.

4.4 Experimental

4.4.1 Sample Preparation

All-silica self-pillared pentasil (SPP), dealuminated zeolite BEA, and their P-modified analogs (P-SPP and P-BEA, each with a Si/P ratio of 27), were synthesized following previously described procedures.[15,45] Each material was dried at 450 °C under dynamic vacuum (<10^{-4} Torr) for 12 h before use. NMR samples were packed and sealed in either a 1.3- or 3.2-mm zirconia rotors inside a N_2-filled glove-box. The rotors were flame-sealed in glass ampoules for transfer to the spectrometer. To minimize ambient exposure, the ampoules were opened immediately prior to insertion of the rotor into the probe. Liquid N_2 boiloff was used as both bearing and drive gas, to ensure that samples were protected from exposure to moisture during data acquisition.

To obtain partially hydrolyzed materials, the rotor cap was removed manually for a short period of time (timed with a stopwatch), then replaced. Air-exposure times are approximate, due to human error. These experiments were conducted on days during which the relative humidity was 74-78 % for P-SPP, and 71-73 % for P-BEA (for the ^{31}P experiments), and 52-56 % (for the ^{1}H experiments) unless otherwise indicated.

4.4.2 Direct excitation solid-state MAS-NMR spectroscopy

^{1}H, ^{27}Al and ^{31}P MAS-NMR measurements were performed at room temperature on a Bruker AVANCE III Ultrashield Plus 18.8 T Spectrometer (corresponding to ^{1}H, ^{27}Al and ^{31}P frequencies of 800.130, 208.489 and 323.85 MHz, respectively) at MAS frequencies of 20 kHz or 62.5 kHz, as indicated. ^{31}P NMR measurements were made in 3.2-mm rotors using a single $\pi/2$ excitation pulse of length 7 μs on the ^{31}P channel. An aqueous phosphoric acid

solution (1 M) provided the chemical shift reference. ^{27}Al NMR measurements were made in 3.2-mm rotors using a single π/2 excitation pulse of length 1.9 μs on the ^{27}Al channel. An aqueous $Al(NO_3)_3$ solution (1 M) provided the chemical shift reference. ^{1}H NMR measurements were made in 1.3-mm rotors using a single π/2 excitation pulse of length 1.9 μs on the 1H channel. Adamantane was used as the chemical shift reference.

4.4.3 Quantitative analysis of ^{1}H NMR spectra

A precisely weighed amount of tetrakis(trimethylsilyl)silane (TKS, 1.5 mg) was loaded into a 1.3-mm rotor inside a N_2-filled glovebox and used as an external standard. The areas of the peaks of the zeosils (unmodified and P-modifed) were obtained from spectral deconvolutions using the Gaussian/Lorentzian model in TopSpin 4.0.6. These were compared with that of the external TKS standard. The amount of H_2O introduced by ambient exposure of each sample was determined from the subsequent increase in total peak area.

Acknowledgement of contribution: I thank Professor Sheetal Jain for his help in the NMR measurements. I am grateful to Professor Michael Tsapatsis and Professor Wei Fan for our collaboration on this project and their students Jacky Lu and Jason Gulbinski for synthesis of the materials.

4.5 References

(1) Zhang, L.; Pham, T. N.; Faria, J.; Resasco, D. E. Improving the Selectivity to C4 Products in the Aldol Condensation of Acetaldehyde in Ethanol over Faujasite Zeolites.

Appl. Catal. A Gen. **2015**, *504*, 119–129. https://doi.org/10.1016/j.apcata.2014.11.018.

(2) Zhu, X.; Lobban, L. L.; Mallinson, R. G.; Resasco, D. E. Bifunctional Transalkylation and Hydrodeoxygenation of Anisole over a Pt/HBeta Catalyst. *J. Catal.* **2011**, *281* (1), 21–29. https://doi.org/10.1016/j.jcat.2011.03.030.

(3) Ausavasukhi, A.; Huang, Y.; To, A. T.; Sooknoi, T.; Resasco, D. E. Hydrodeoxygenation of M-Cresol over Gallium-Modified Beta Zeolite Catalysts. *J. Catal.* **2012**, *290*, 90–100. https://doi.org/10.1016/j.jcat.2012.03.003.

(4) Sooknoi, T.; Danuthai, T.; Lobban, L. L.; Mallinson, R. G.; Resasco, D. E. Deoxygenation of Methylesters over CsNaX. *J. Catal.* **2008**, *258* (1), 199–209. https://doi.org/10.1016/j.jcat.2008.06.012.

(5) Caratzoulas, S.; Davis, M. E.; Gorte, R. J.; Gounder, R.; Lobo, R. F.; Nikolakis, V.; Sandler, S. I.; Snyder, M. A.; Tsapatsis, M.; Vlachos, D. G. Challenges of and Insights into Acid-Catalyzed Transformations of Sugars. *J. Phys. Chem. C* **2014**, *118* (40), 22815–22833. https://doi.org/10.1021/jp504358d.

(6) Cheng, Y.-T.; Jae, J.; Shi, J.; Fan, W.; Huber, G. W. Production of Renewable Aromatic Compounds by Catalytic Fast Pyrolysis of Lignocellulosic Biomass with Bifunctional Ga/ZSM-5 Catalysts. *Angew. Chemie* **2012**, *124* (6), 1416–1419. https://doi.org/10.1002/ange.201107390.

(7) Sievers, C.; Scott, S. L.; Noda, Y.; Qi, L.; Albuquerque, E. M.; Rioux, R. M. Phenomena Affecting Catalytic Reactions at Solid−Liquid Interfaces. *ACS Catal.* **2016**, *6* (12). https://doi.org/10.1021/acscatal.6b02532.

(8) Ravenelle, R. M.; Schübler, F.; Damico, A.; Danilina, N.; Van Bokhoven, J. A.; Lercher, J. A.; Jones, C. W.; Sievers, C. Stability of Zeolites in Hot Liquid Water. *J.*

Phys. Chem. C **2010**, *114* (46), 19582–19595. https://doi.org/10.1021/jp104639e.

(9) Corma, A.; Mengual, J.; Miguel, P. J. Steam Catalytic Cracking of Naphtha over ZSM-5 Zeolite for Production of Propene and Ethene: Micro and Macroscopic Implications of the Presence of Steam. *Appl. Catal. A Gen.* **2012**, *417–418*, 220–235. https://doi.org/10.1016/j.apcata.2011.12.044.

(10) Yang, H.; Coolman, R. J.; Karanjkar, P.; Wang, H.; Xu, Z.; Chen, H.; Moutziaris, T. J.; Huber, G. W. The Effect of Steam on the Catalytic Fast Pyrolysis of Cellulose. *Green Chem.* **2015**, *17* (5), 2912–2923. https://doi.org/10.1039/c5gc00026b.

(11) Zhang, L.; Chen, K.; Chen, B.; White, J. L.; Resasco, D. E. Factors That Determine Zeolite Stability in Hot Liquid Water. *J. Am. Chem. Soc.* **2015**, *137* (36), 11810–11819. https://doi.org/10.1021/jacs.5b07398.

(12) Zapata, P. A.; Faria, J.; Ruiz, M. P.; Jentoft, R. E.; Resasco, D. E. Hydrophobic Zeolites for Biofuel Upgrading Reactions at the Liquid-Liquid Interface in Water/Oil Emulsions. *J. Am. Chem. Soc.* **2012**, *134* (20), 8570–8578. https://doi.org/10.1021/ja3015082.

(13) Blasco, T.; Corma, A.; Martínez-Triguero, J. Hydrothermal Stabilization of ZSM-5 Catalytic-Cracking Additives by Phosphorus Addition. *J. Catal.* **2006**, *237* (2), 267–277. https://doi.org/10.1016/j.jcat.2005.11.011.

(14) Van Der Bij, H. E.; Weckhuysen, B. M. Phosphorus Promotion and Poisoning in Zeolite-Based Materials: Synthesis, Characterisation and Catalysis. *Chem. Soc. Rev.* **2015**, *44* (20), 7406–7428. https://doi.org/10.1039/c5cs00109a.

(15) Cho, H. J.; Ren, L.; Vattipalli, V.; Yeh, Y.-H.; Gould, N.; Xu, B.; Gorte, R. J.; Lobo, R.; Dauenhauer, P. J.; Tsapatsis, M.; Fan, W. Renewable *p* -Xylene from 2,5-

Dimethylfuran and Ethylene Using Phosphorus-Containing Zeolite Catalysts. *ChemCatChem* **2017**, *9* (3), 398–402. https://doi.org/10.1002/cctc.201601294.

(16) Abdelrahman, O. A.; Park, D. S.; Vinter, K. P.; Spanjers, C. S.; Ren, L.; Cho, H. J.; Vlachos, D. G.; Fan, W.; Tsapatsis, M.; Dauenhauer, P. J. Biomass-Derived Butadiene by Dehydra-Decyclization of Tetrahydrofuran. *ACS Sustain. Chem. Eng.* **2017**, *5* (5), 3732–3736. https://doi.org/10.1021/acssuschemeng.7b00745.

(17) Jain, S. K.; Tabassum, T.; Li, L.; Ren, L.; Fan, W.; Tsapatsis, M.; Caratzoulas, S.; Han, S.; Scott, S. L. P-Site Structural Diversity and Evolution in a Zeosil Catalyst. *J. Am. Chem. Soc.* **2021**, *143* (4), 1968–1983. https://doi.org/10.1021/jacs.0c11768.

(18) Chen, K.; Damron, J.; Pearson, C.; Resasco, D.; Zhang, L.; White, J. L. Zeolite Catalysis: Water Can Dramatically Increase or Suppress Alkane C-H Bond Activation. *ACS Catal.* **2014**, *4* (9), 3039–3044. https://doi.org/10.1021/cs500858d.

(19) Wang, H.; Hou, Y.; Sun, W.; Hu, Q.; Xiong, H.; Wang, T.; Yan, B.; Qian, W. Insight into the Effects of Water on the Ethene to Aromatics Reaction with HZSM-5. *ACS Catal.* **2020**, *10* (9), 5288–5298. https://doi.org/10.1021/acscatal.9b05552.

(20) De Wispelaere, K.; Hemelsoet, K.; Waroquier, M.; Van Speybroeck, V. Complete Low-Barrier Side-Chain Route for Olefin Formation during Methanol Conversion in H-SAPO-34. *J. Catal.* **2013**, *305*, 76–80. https://doi.org/10.1016/j.jcat.2013.04.015.

(21) Bollini, P.; Chen, T. T.; Neurock, M.; Bhan, A. Mechanistic Role of Water in HSSZ-13 Catalyzed Methanol-to-Olefins Conversion. *Catal. Sci. Technol.* **2019**, *9* (16), 4374–4383. https://doi.org/10.1039/c9cy01015g.

(22) Vener, M. V; Rozanskay, X.; Sauer, J. Protonation of Water Clusters in the Cavities of Acidic Zeolites: (H 2 O) n ÁH-Chabazite, n = 1-4w. *Phys. Chem. Chem. Phys.* **2009**,

11 (11), 1702–1712. https://doi.org/10.1039/b817905k.

(23) Wang, M.; Jaegers, N. R.; Lee, M. S.; Wan, C.; Hu, J. Z.; Shi, H.; Mei, D.; Burton, S. D.; Camaioni, D. M.; Gutiérrez, O. Y.; Glezakou, V. A.; Rousseau, R.; Wang, Y.; Lercher, J. A. Genesis and Stability of Hydronium Ions in Zeolite Channels. *J. Am. Chem. Soc.* **2019**, *141* (8), 3444–3455. https://doi.org/10.1021/jacs.8b07969.

(24) Shi, H.; Eckstein, S.; Vjunov, A.; Camaioni, D. M.; Lercher, J. A. Tailoring Nanoscopic Confines to Maximize Catalytic Activity of Hydronium Ions. *Nat. Commun.* **2017**, *8* (1), 1–7. https://doi.org/10.1038/ncomms15442.

(25) Eckstein, S.; Hintermeier, P. H.; Zhao, R.; Baráth, E.; Shi, H.; Liu, Y.; Lercher, J. A. Influence of Hydronium Ions in Zeolites on Sorption. *Angew. Chemie - Int. Ed.* **2019**, *58* (11), 3450–3455. https://doi.org/10.1002/anie.201812184.

(26) Liu, Y.; Vjunov, A.; Shi, H.; Eckstein, S.; Camaioni, D. M.; Mei, D.; Baráth, E.; Lercher, J. A. Enhancing the Catalytic Activity of Hydronium Ions through Constrained Environments. *Nat. Commun.* **2017**, *8* (1), 1–8. https://doi.org/10.1038/ncomms14113.

(27) Kasai, P. H.; Jones, P. M. MAS-NMR Spectroscopic Study of Water in Zeolites. *J. Mol. Catal.* **1984**, *27* (1–2), 81–93. https://doi.org/10.1016/0304-5102(84)85072-5.

(28) Gabuda, S. P.; Kolesnikov, A. S.; Kozlova, S. G.; Lundin, A. G.; Moroz, N. K. H NMR Study of Zeolite Water Structure and Broensted Acid Centers in Chabazite. *Appl. Magn. Reson.* **2011**, *41* (2–4), 439–447. https://doi.org/10.1007/s00723-011-0279-4.

(29) Chen, K.; Kelsey, J.; White, J. L.; Zhang, L.; Resasco, D. Water Interactions in Zeolite Catalysts and Their Hydrophobically Modified Analogues. *ACS Catal.* **2015**, *5* (12), 7480–7487. https://doi.org/10.1021/acscatal.5b02040.

(30) Zhang, R.; Mroue, K. H.; Ramamoorthy, A. Proton-Based Ultrafast Magic Angle

Spinning Solid-State NMR Spectroscopy. *Acc. Chem. Res.* **2017**, *50* (4), 1105–1113. https://doi.org/10.1021/acs.accounts.7b00082.

(31) Hunger, M. Multinuclear Solid-State NMR Studies of Acidic and Non-Acidic Hydroxyl Protons in Zeolites. *Solid State Nuclear Magnetic Resonance*. Elsevier February 1, 1996, pp 1–29. https://doi.org/10.1016/0926-2040(95)01201-X.

(32) Hunger, M.; Ernst, S.; Steuernagel, S.; Weitkamp, J. High-Field 1H MAS NMR Investigations of Acidic and Non-Acidic Hydroxyl Groups in Zeolites H-Beta, H-ZSM-5, H-ZSM-58 and H-MCM-22. *Microporous Mater.* **1996**, *6* (5–6), 349–353. https://doi.org/10.1016/0927-6513(96)00043-0.

(33) Bronnimann, C. E.; Chuang, I. ssuer; Hawkins, B. L.; Maciel, G. E. Dehydration of Silica—Aluminas Monitored by High-Resolution Solid-State Proton NMR. *J. Am. Chem. Soc.* **1987**, *109* (5), 1562–1564. https://doi.org/10.1021/ja00239a043.

(34) Liu, C. C.; Maciel, G. E. The Fumed Silica Surface: A Study by NMR. *J. Am. Chem. Soc.* **1996**, *118* (21), 5103–5119. https://doi.org/10.1021/ja954120w.

(35) Schroeder, C.; Siozios, V.; Hunger, M.; Hansen, M. R.; Koller, H. Disentangling Brønsted Acid Sites and Hydrogen-Bonded Silanol Groups in High-Silica Zeolite H-ZSM-5. *J. Phys. Chem. C* **2020**, *124* (42), 23380–23386. https://doi.org/10.1021/acs.jpcc.0c06113.

(36) Vidoni, A.; Ravikovitch, P. I.; Afeworki, M.; Calabro, D.; Deckman, H.; Ruthven, D. Adsorption of CO2 on High Silica MFI and DDR Zeolites: Structural Defects and Differences between Adsorbent Samples. *Microporous Mesoporous Mater.* **2020**, *294*, 1–10. https://doi.org/10.1016/j.micromeso.2019.109818.

(37) Lohse, U.; Löffler, E.; Hunger, M.; Stöckner, J.; Patzelová, V. Hydroxyl Groups of the

Non-Framework Aluminium Species in Dealuminated Y Zeolites. *Zeolites* **1987**, *7* (1), 11–13. https://doi.org/10.1016/0144-2449(87)90111-4.

(38) Chen, K.; Abdolrhamani, M.; Sheets, E.; Freeman, J.; Ward, G.; White, J. L. Direct Detection of Multiple Acidic Proton Sites in Zeolite HZSM-5. *J. Am. Chem. Soc.* **2017**, *139* (51), 18698–18704. https://doi.org/10.1021/jacs.7b10940.

(39) Piedra, G.; Fitzgerald, J. J.; Dando, N.; Dec, S. F.; Maciel, G. E. Solid-State 1 H NMR Studies of Aluminum Oxide Hydroxides and Hydroxides. *Inorg. Chem.* **1996**, *35* (12), 3474–3478.

(40) Hartmeyer, G.; Marichal, C.; Lebeau, B.; Rigolet, S.; Caullet, P.; Hernandez, J. Speciation of Silanol Groups in Precipitated Silica Nanoparticles by 1H MAS NMR Spectroscopy. *J. Phys. Chem. C* **2007**, *111* (26), 9066–9071. https://doi.org/10.1021/jp071490l.

(41) Sebastiani, D.; Parrinello, M. Ab-Initio Study of NMR Chemical Shifts of Water under Normal and Supercritical Conditions. *ChemPhysChem* **2002**, *3* (8), 675–679. https://doi.org/10.1002/1439-7641(20020816)3:8<675::AID-CPHC675>3.0.CO;2-O.

(42) Wenslow, R. M.; Mueller, K. T. Structural Details of Aqueous Attack on a Phosphate Glass by 1H/31P Cross-Polarization NMR. *J. Phys. Chem. B* **1998**, *102* (45), 9033–9038. https://doi.org/10.1021/jp9824252.

(43) Clayden, N. J.; Esposito, S.; Pernice, P.; Aronne, A. Solid State 1H NMR Study, Humidity Sensitivity and Protonic Conduction of Gel Derived Phosphosilicate Glasses. *J. Mater. Chem.* **2002**, *12* (12), 3746–3753. https://doi.org/10.1039/b205950a.

(44) Grünberg, B.; Emmler, T.; Gedat, E.; Shenderovich, I.; Findenegg, G. H.; Limbach, H. H.; Buntkowsky, G. Hydrogen Bonding of Water Confined in Mesoporous Silica

MCM-41 and SBA-15 Studied by 1H Solid-State NMR. *Chem. - A Eur. J.* **2004**, *10* (22), 5689–5696. https://doi.org/10.1002/CHEM.200400351.

(45) Zhang, X.; Liu, D.; Xu, D.; Asahina, S.; Cychosz, K. A.; Agrawal, K. V.; Wahedi, Y. Al; Bhan, A.; Hashimi, S. Al; Terasaki, O.; Thommes, M.; Tsapatsis, M. Synthesis of Self-Pillared Zeolite Nanosheets by Repetitive Branching. *Science (80-.).* **2012**, *336* (6089), 1684–1687. https://doi.org/10.1126/science.1221111.

4.6 Appendix

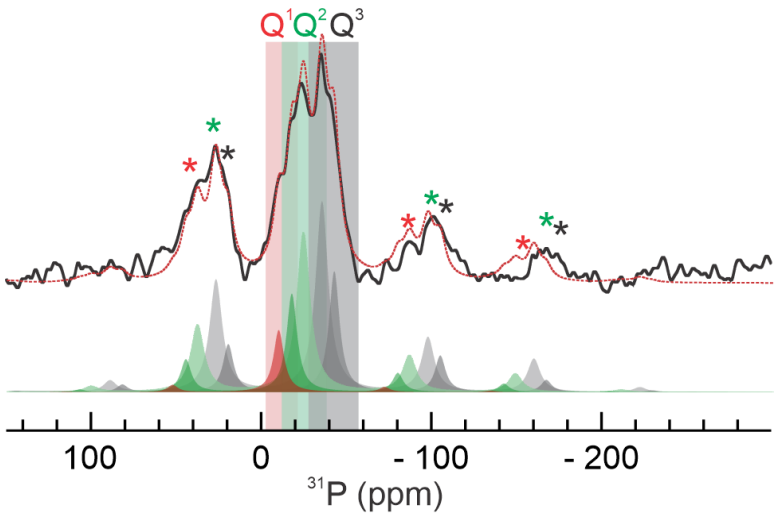

Figure A4.1 ^{31}P MAS NMR spectra (black) of dehydrated P-BEA with Si/P = 27, and the corresponding simulation (red) that includes contributions for each Q^n component after 1 min of ambient exposure. The spectrum was recorded at room temperature and 18.8 T, using 20 kHz MAS. Asterisks (*) indicate spinning sidebands. Simulations were performed using the CSA model in Topspin 4.0.6. Deconvolution of the spectrum of P-BEA into its Q^n components is shown in the shaded spectra.

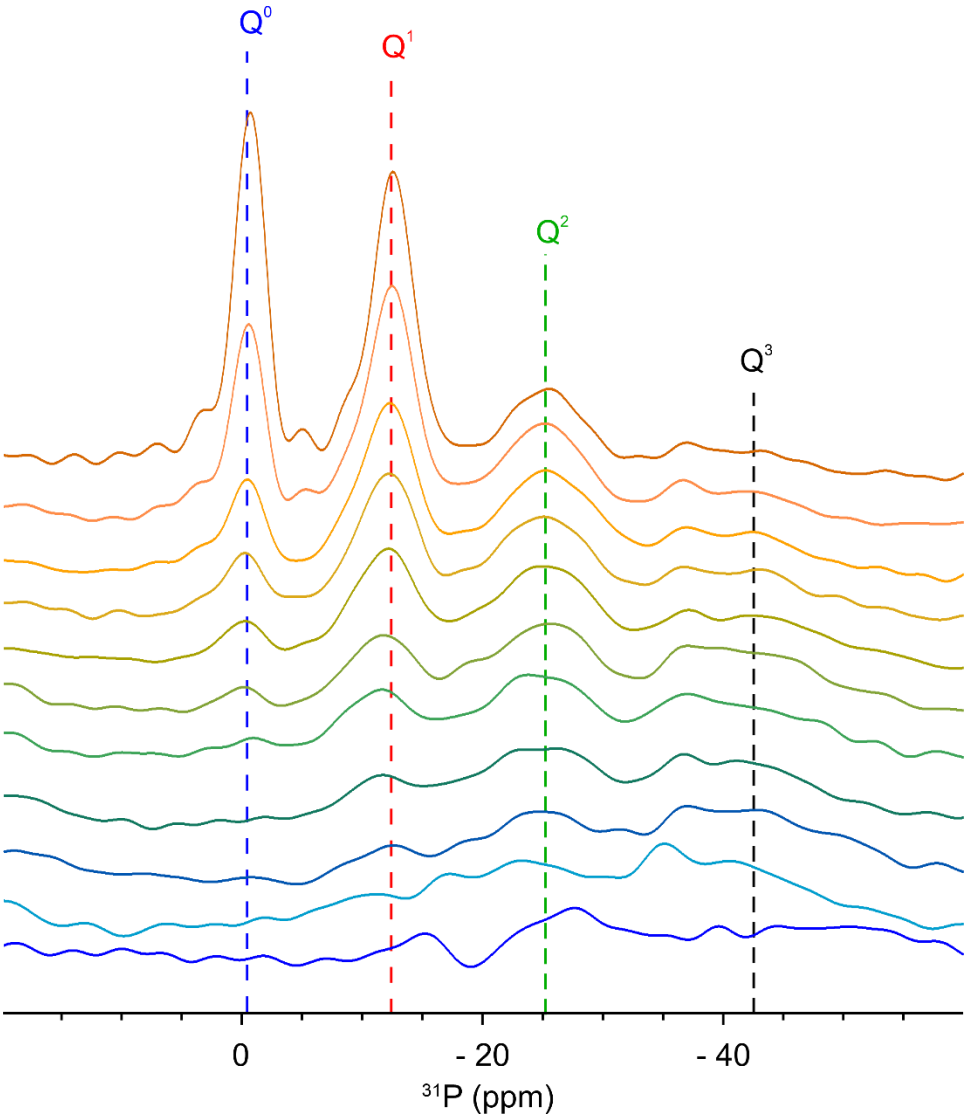

Figure A4.2 The effect of ambient exposure time (correlated with the amount of adsorbed water), on the P speciation in P-BEA (Si/P) at room temperature. ^{31}P MAS NMR spectra were recorded after each air exposure time, as noted. All spectra were recorded at room temperature in an 18.8 T magnet using 20 kHz MAS. Each ^{31}P NMR spectrum corresponds to a data point in Figure 4.3b (main text).

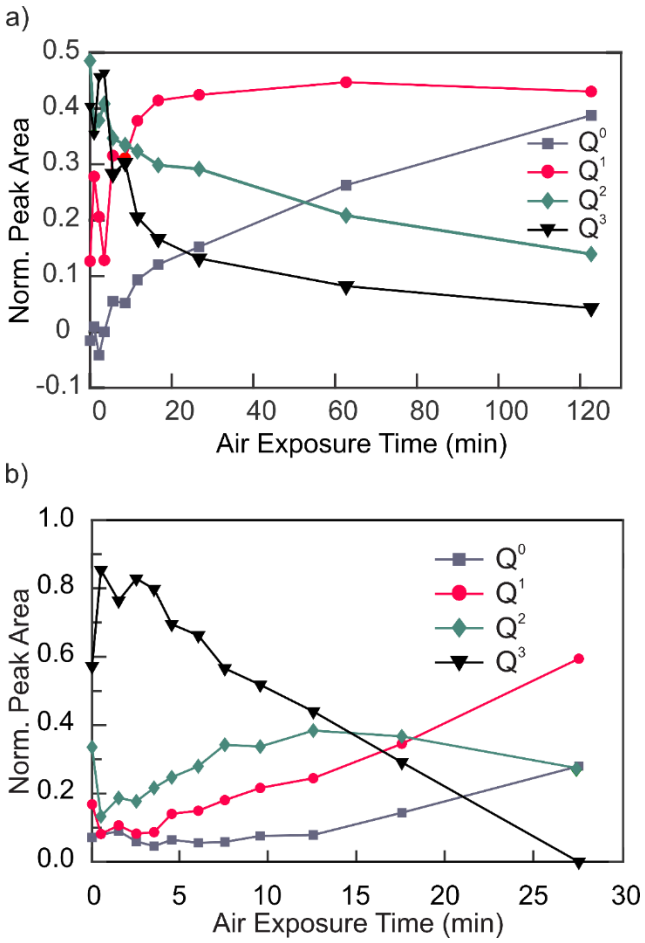

Figure A4.3 Evolution of P-sites quantified by their integrated peak intensities (including spinning sidebands) for different groups of P-sites in (a) P-SPP, and (b) P-BEA, as a function of water content. The areas of the peaks in each Q^n region are normalized to the total peak area at each time point.

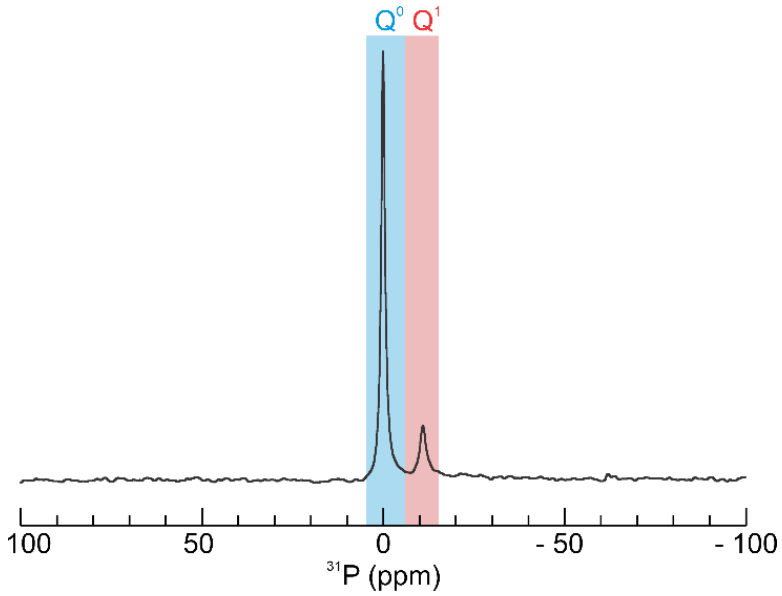

Figure A4.4 ^{31}P MAS NMR spectrum of P-SPP, recorded after extended ambient exposure (several days). The spectrum was recorded at room temperature in an 18.8 T magnet, using 20 kHz MAS.

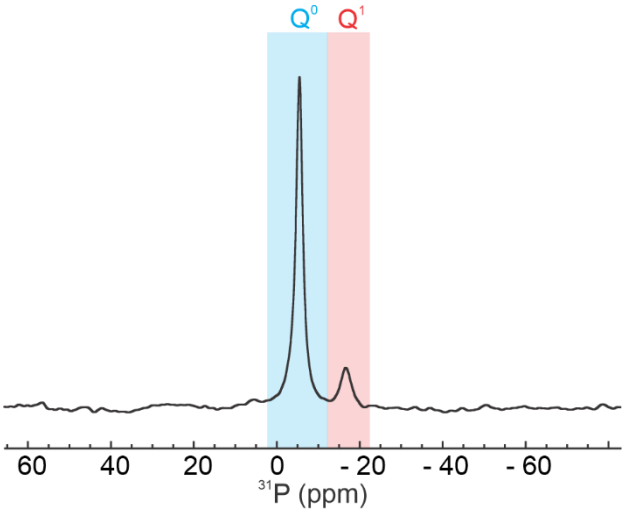

Figure A4.5 ^{31}P MAS NMR spectrum of P-BEA, recorded after extended ambient exposure (several days). The spectrum was recorded at room temperature in an 18.8 T magnet, using 20 kHz MAS.

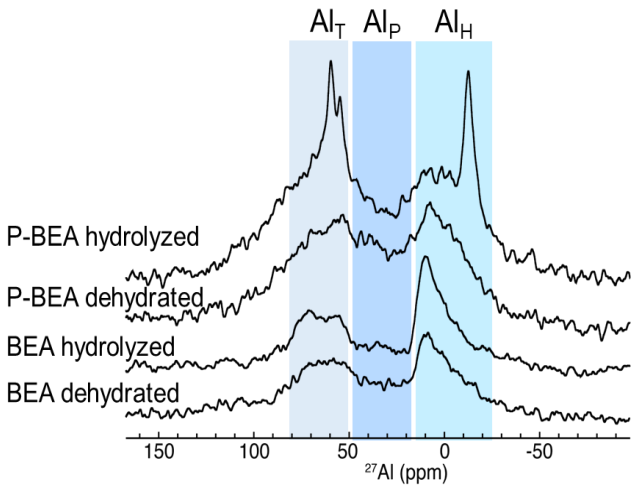

Figure A4.6 Comparison of ^{27}Al MAS NMR spectra of dehydrated and hydrolyzed BEA and P-BEA (Si/P = 27). All spectra were recorded at room temperature on 18.8 T spectrometer, using 20 kHz MAS. Spectra of the dehydrated materials were recorded while using N_2 as both bearing and spinning gases.

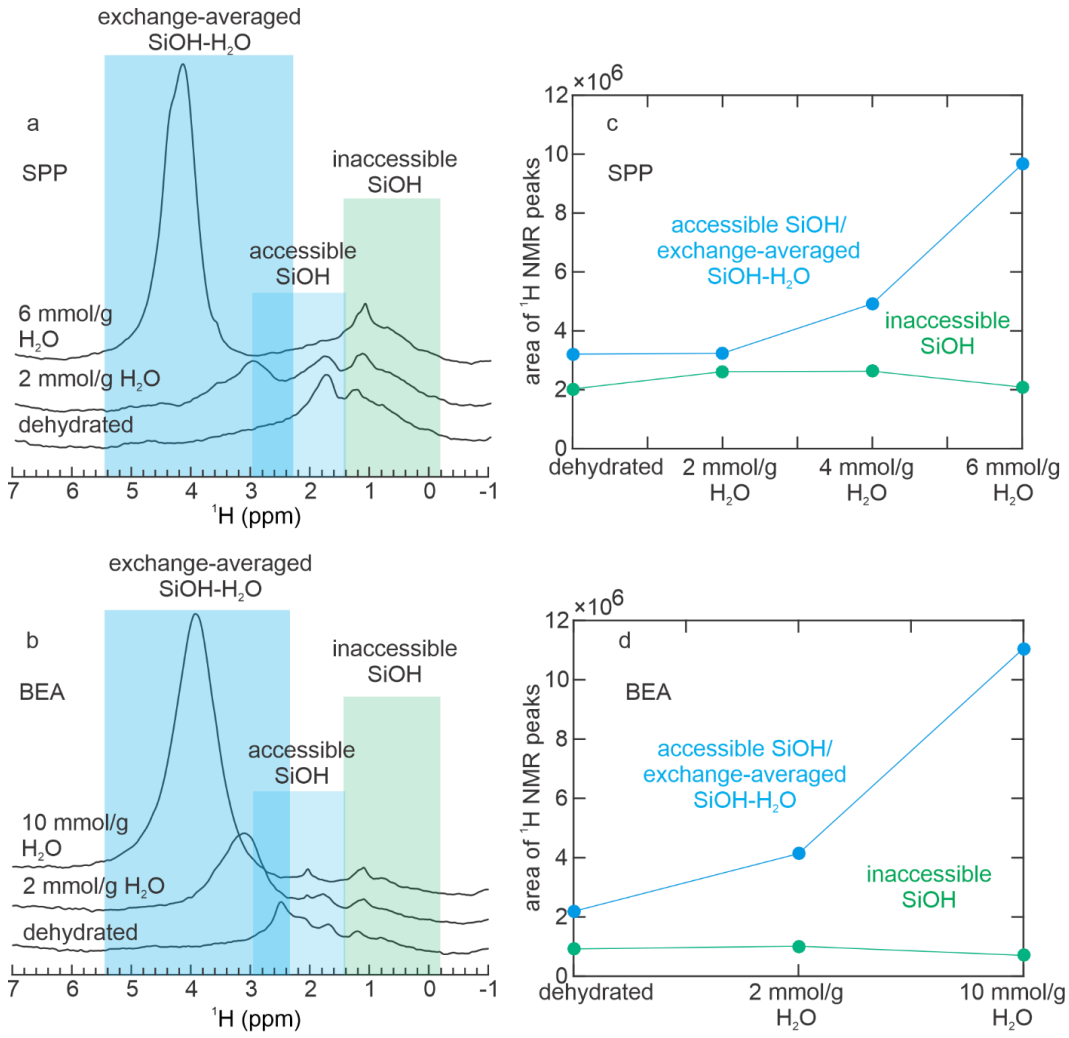

Figure A4.7 ^{1}H MAS NMR spectra of (a) SPP and (b) dealuminated BEA zeosil, showing the evolution of the spectra as a function of water content (introduced by ambient exposure of the dehydrated zeolite). The amounts of absorbed H_2O were determined using an external reference. All spectra were recorded at room temperature and 18.8 T, using 62.5 kHz MAS. Spectra of the dry materials were recorded under N_2, while using N_2 as both bearing and spinning gases. Estimated ^{1}H peak areas showing the evolution of the spectra as a function of the inaccessible and the exchanged-averaged SiOH/accessible SiOH peaks of c) SPP and d) BEA.

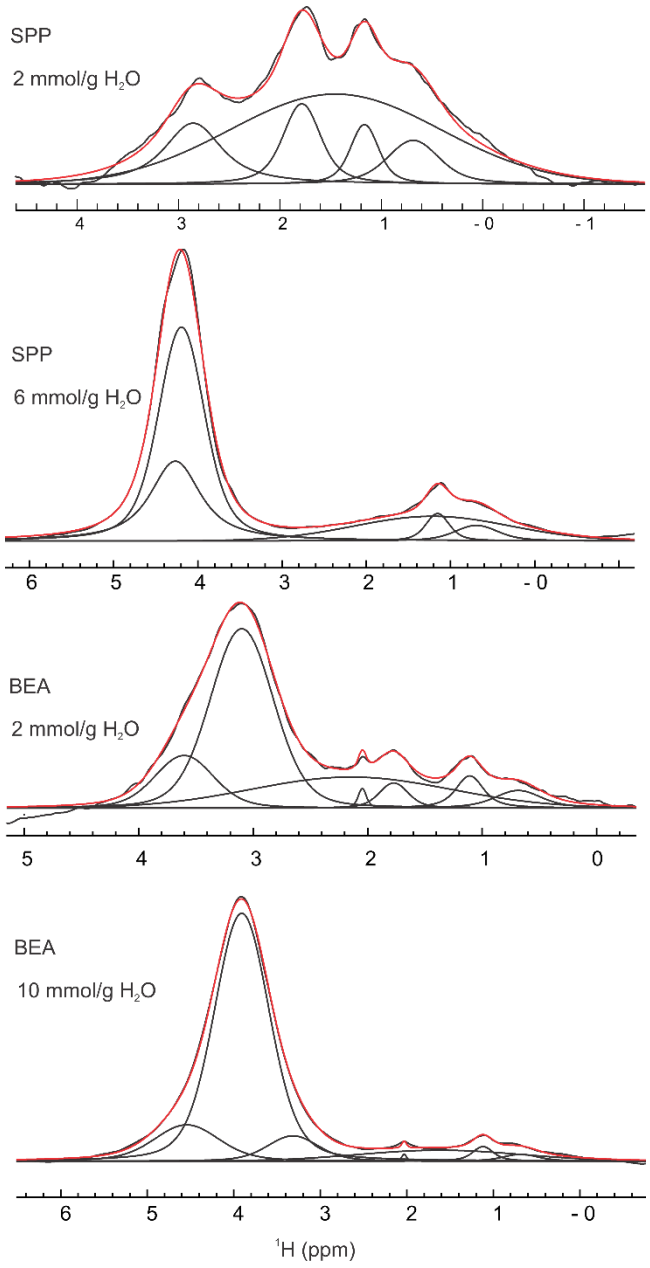

Figure A4.8 ^{1}H MAS NMR spectra of SPP and dealuminated BEA zeosil (black) and their spectral deconvolutions (red) containing different water content as indicated. All spectra were recorded at room temperature and 18.8 T, using 62.5 kHz MAS. Spectra of the dry materials were recorded under N_2, while using N_2 as both bearing and spinning gases.

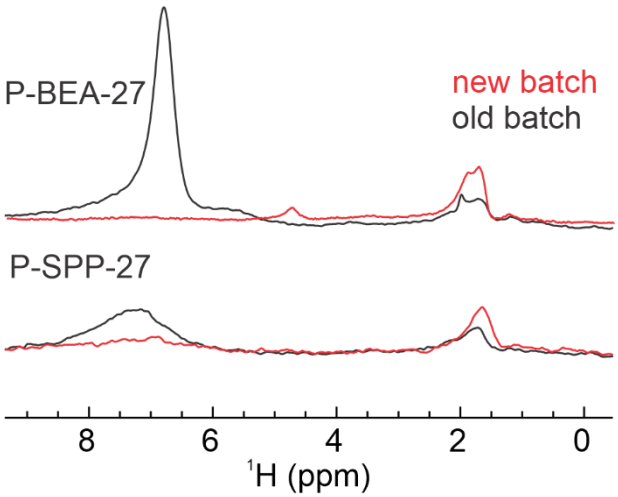

Figure A4.9 ^{1}H MAS NMR spectra of dehydrated P-SPP and P-BEA showing differences in POH signal intensities due to variability in the P-content. All spectra with directly comparable intensities were recorded at room temperature at 18.8 T, using 62.5 kHz MAS. Liquid N_2 boiloff was used as both bearing and spinning gases.

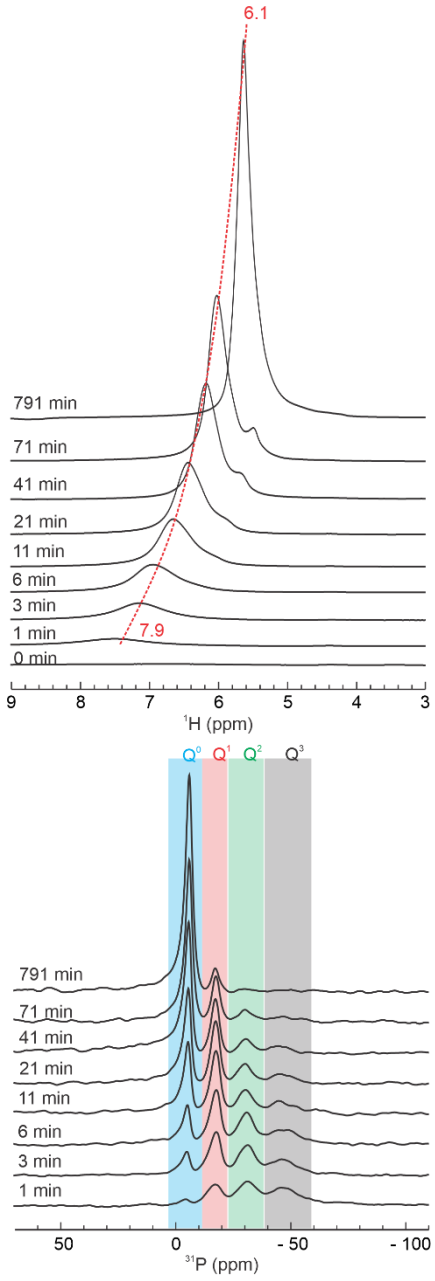

Figure A4.10 The effect of increasing room temperature ambient exposure, and hence water content, on the (a) ^{1}H and (b) ^{31}P MAS NMR spectra of a different batch of P-SPP recorded at a relative humidity of 76 %. The zeosil was initially dehydrated under vacuum at 450 °C. Spectra were recorded at room temperature and 18.8 T, using 62.5 kHz MAS.

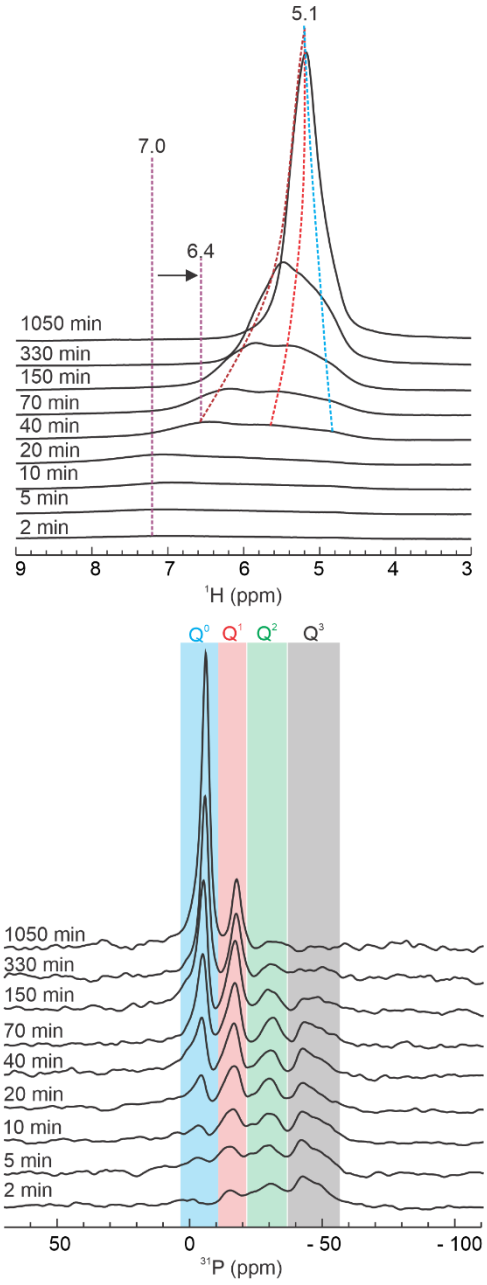

Figure A4.11 The effect of increasing room temperature ambient exposure, and hence water content, on the (a) ^{1}H and (b) ^{31}P MAS NMR spectra of a different batch of P-BEA recorded at a relative humidity of 76 %. The zeosil was initially dehydrated under vacuum at 450 °C. Spectra were recorded at room temperature and 18.8 T, using 62.5 kHz MAS.

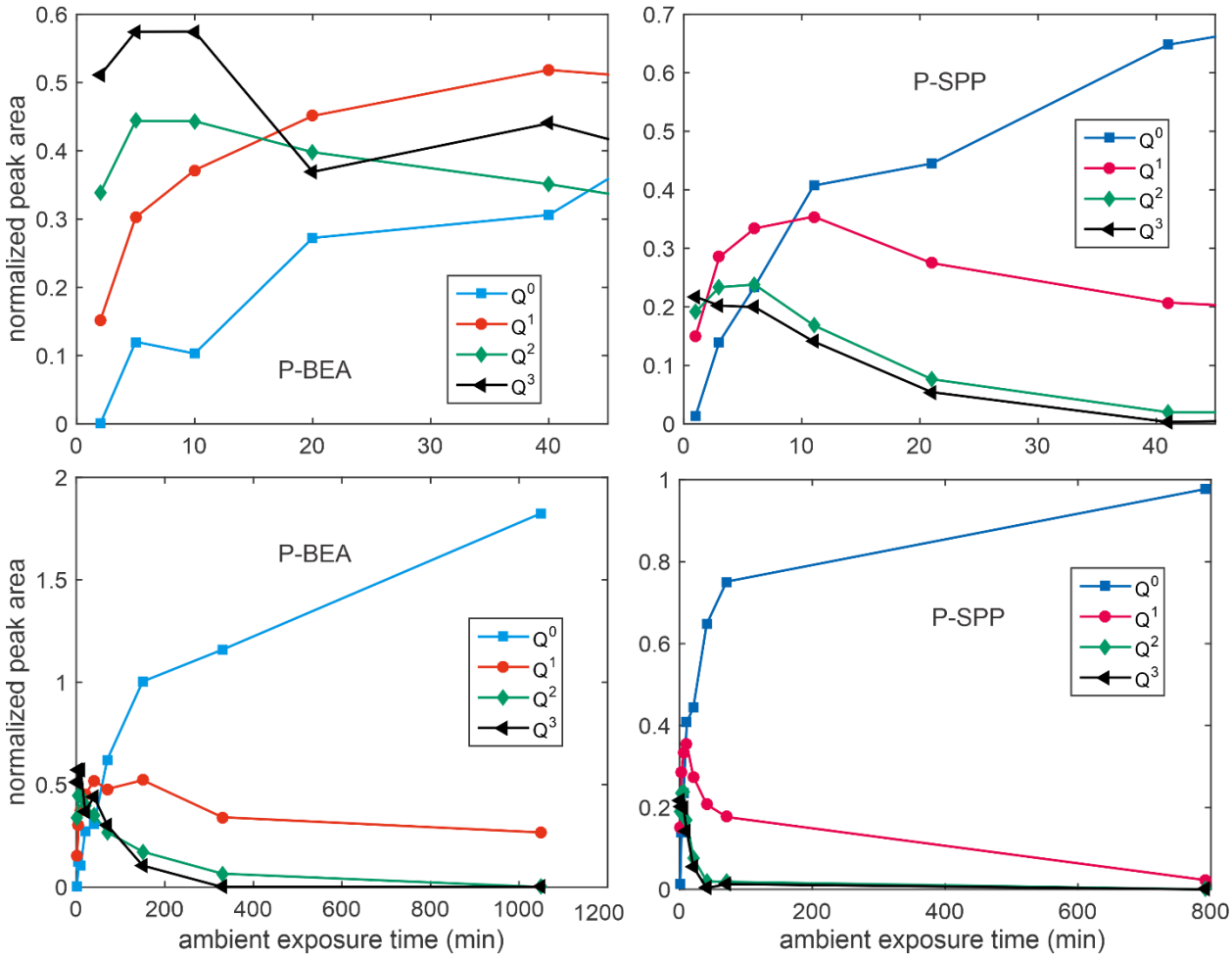

Figure A4.12 Evolution of P-sites quantified by their integrated peak intensities for different groups of P-sites in another batch of P-SPP (right), and P-BEA (left), as a function of water content when the relative humidity was 76 %. The spectra were acquired using ultrafast ^{31}P MAS at 62.5 kHz under an 18.8 T magnetic field, and are shown in Figures S10 and S11. The areas of the peaks in each Q^n region are normalized to the total peak area in the final hydrolyzed state. The top panels show the evolution for a period of 45 min, and the bottom panels show evolution upon longer exposure.

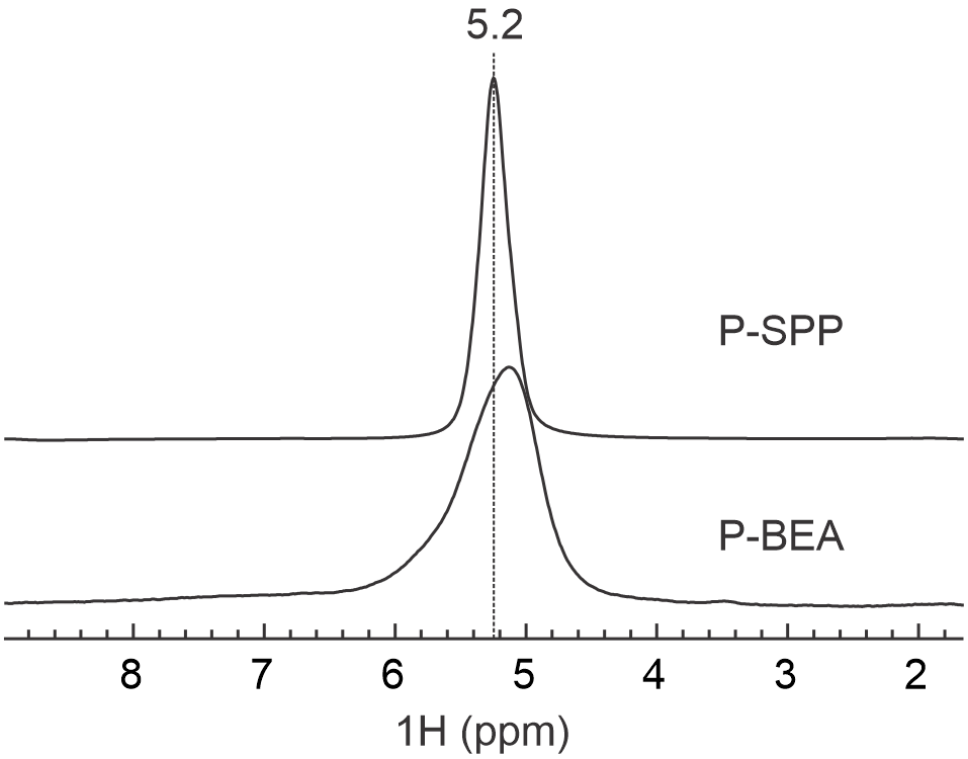

Figure A4.13 ^{1}H MAS NMR spectra of hydrolyzed P-SPP and P-BEA. All spectra with directly comparable intensities were recorded at room temperature at 18.8 T, using 62.5 kHz MAS. Liquid N_2 boiloff was used as both bearing and spinning gases.

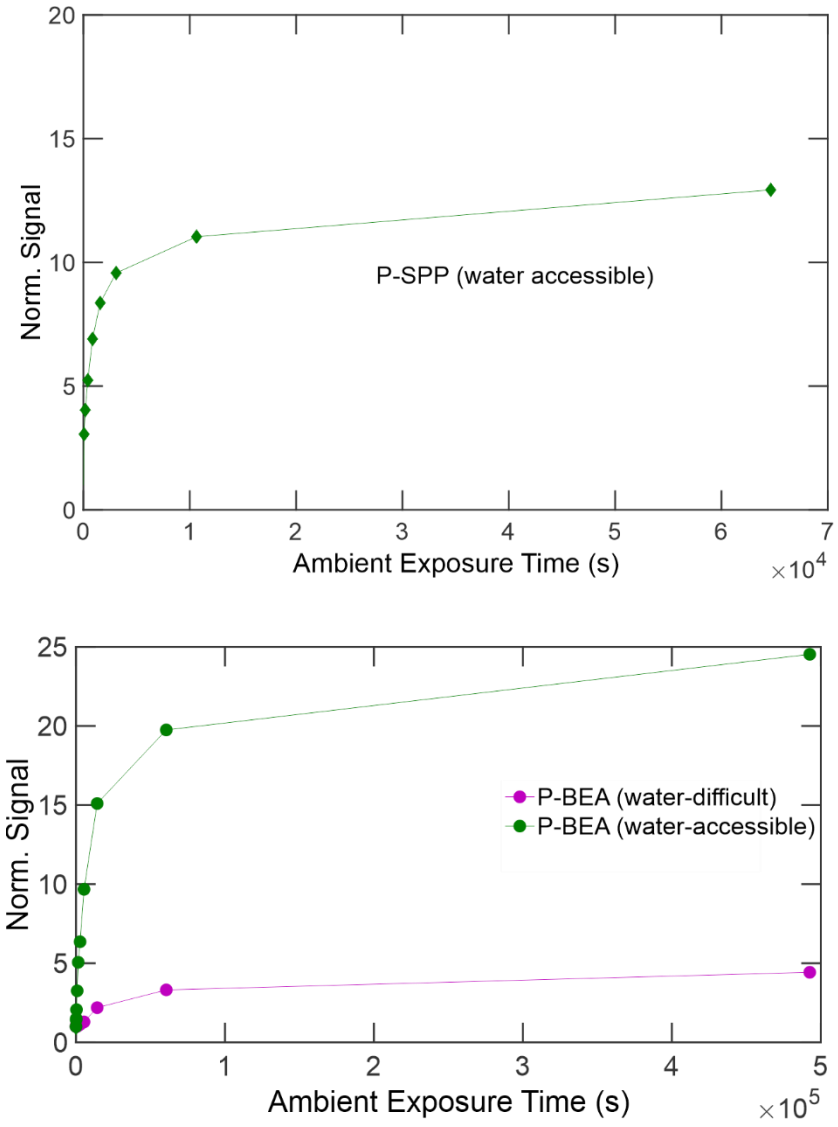

Figure A4.14 ^{1}H MAS NMR peak areas of the water accessible and water difficult regions of the of P-SPP (a) and P-BEA (b). The areas of each data point were normalized to the peak area of the first spectrum of P-SPP and P-BEA, respectively.

Table A4.1 Silanols present in dehydrated SPP, according to their peak widths, and their relative contributions, normalized to the total peak area in SPP containing 6 mmol/g H_2O.

Narrow	Broad	FWHM (Hz)	Fraction
0.8		580	0.04
1.2		315	0.03
1.8		360	0.06
	1.8	1950	0.18

Table A4.2 Silanols present in SPP after 20 min of ambient exposure, according to their peak widths, and their relative contributions, normalized to the total peak area in SPP containing 6 mmol/g H_2O.

Narrow	Broad	FWHM (Hz)	Fraction
0.8		580	0.04
1.2		315	0.03
1.8		410	0.05
	1.5	1960	0.16
	2.9	700	0.08

Table A4.3 Silanols present in SPP after 15 h of ambient exposure, according to their peak widths, and their relative contributions, normalized to the total peak area in SPP containing 6 mmol/g H_2O.

Narrow	Broad	FWHM (Hz)	Fraction
0.8		580	0.03
1.2		315	0.04
1.8		x	x
	1.4	1650	0.16
4.2		500	0.51
4.3		475	0.25

Table A4.4 Silanols present in dehydrated BEA, according to their peak widths, and their relative contributions, normalized to the total peak area in BEA containing 10 mmol/g H_2O.

Narrow	Broad	FWHM (Hz)	Fraction
0.8		470	0.02
1.2		280	0.02
1.8		235	0.01
2.2		430	0.02
2.5		240	0.03
	2.5	1030	0.08

Table A4.5 Silanols present in BEA after 20 min of ambient exposure, according to their peak widths, and their relative contributions, normalized to the total peak area in BEA containing 10 mmol/g H_2O.

Narrow	Broad	FWHM (Hz)	Fraction
0.8		470	0.02
1.2		280	0.02
1.8		280	0.01
2.1		80	0.01
	2.1	1640	0.10
3.1		570	0.20
3.6		560	0.05

Table A4.6 Silanols present in BEA after 15 h of ambient exposure, according to their peak widths, and their relative contributions, normalized to the total peak area in BEA containing 10 mmol/g H_2O.

Narrow	Broad	FWHM (Hz)	Fraction
0.8		470	0.02
1.2		280	0.02
	1.8	1780	0.10
2.1		60	0.01
3.3		640	0.07
3.9		665	0.80
4.5		810	0.14

Table A4.7 Estimated hydroxyl contents (mmol/g) in the dry zeosils, with and without P-modification[a]

	water-inaccessible SiOH	**water-accessible SiOH**	**POH**
SPP	1.0	3.6	0
P-SPP	0	0.3	1.5
BEA	0.4	1.8	0
P-BEA	0.2	0.2	3

[a] Hydroxyl contents were determined by deconvolution of the ^{1}H NMR spectrum using Topspin, and comparison of the deconvoluted peak areas to an external standard (see Methods).

Chapter 5: Dehydration of 2-propanol on a P-modified Zeosil: An Investigation by *Operando* NMR

5.1 Introduction

Chemical transformations of lignocellulosic biomass derivatives into fuels and chemicals requires stable, active and selective catalysts with optimal acidities.[1–7] Orthophosphoric acid (H_3PO_4) modified siliceous zeolites (P-zeosils) have moderate Bronsted acidities, optimal for the selective catalysis of two noteworthy reactions: the Diels-Alder coupling of carbohydrate-derived 2,5-dimethylfuran with ethylene to give *p*-xylene, and the tandem dehydration-ring opening of tetrahydrofuran to give 1,3-butadiene.[8,9] The enhanced activity and selectivity of the P-zeosils compared to H_3PO_4 was attributed to surface-bound P-sites. However, our study on a P-modified self-pillared pentasil zeosil (P-SPP) using solid-state NMR revealed the diverse nature of the P-sites and how they interact with the zeolite framework and one another.[10] Dehydrated P-SPP contains predominantly two types of fully-condensed P-sites: mononuclear and oligomeric, which are both surface-bound. In the presence of water, both sites undergo hydrolysis through the breakage of P-O-Si and ultimately P-O-P linkages to ultimately result in predominantly H_3PO_4. This study shows that the Brønsted acidity in P-SPP arises from a diverse mixture of partly-hydrolyzed surface-bound and non-surface-bound mononuclear and dinuclear sites, even at low P-loadings (P/Si = 27). The P-site distribution is determined by the extent of hydrolysis, and has important consequences for the Brønsted acidity.

The water released in the reaction as a by-product may impact the P-site distribution. Water is known to destabilize the zeolite framework, and consequently also the catalytic

reactions that it participates in.[11–14] A strategy to mitigate water induced instability of the zeolite framework is to hydrophobize the framework.[15,16] Thus, the effect of the zeosil framework on the stability of P-sites was also explored. A dealuminated BEA zeolite framework, containing fewer surface hydroxyls than SPP, impacts the P-site distribution in its dehydrated state, resulting in more oligomeric sites. Upon exposure to water, the SPP framework, which has a more open architecture, allows facile accessibility, resulting in rapid hydrolysis of the P-sites. On the other hand, the BEA framework results in P-sites that are less accessible to water, and therefore, slower hydrolysis of P-sites relative to those in SPP. The BEA framework also generates more oligomeric sites containing P-O-P linkages, that hydrolyze slower than P-O-Si. Thus, controlling the hydrophobicity of the framework may be a strategy to control P-site distribution, and consequently, the acidity of the P-sites under reaction conditions. However, investigating structure-property relationships of P-zeosils and reaction mechanisms in dehydration reactions requires characterization tools with molecular level precision, combined with the ability of studying the catalysts under reaction conditions, i.e. at elevated temperatures and pressures.

NMR spectroscopy is well suited for *in-situ* analysis, since it does not require separation of molecules in complex mixtures,[17,18] while being sensitive to the chemical environment of the nuclei in the reaction system.[19,20] Solid-state magic angle spinning (MAS) NMR has the additional advantage of being able to study heterogeneous systems comprising of solids, liquids and gases, in which interactions between molecules and solid catalysts can be elucidated. However, observing multiphase systems, at elevated temperatures and pressures, is challenging for designing solid-state MAS NMR experiments, in which samples spin at several thousands of Hz in a strong magnetic field. The development of operando MAS

NMR technology has enabled probing catalytic systems over a wide range of pressures, temperatures and chemical environments.[21–23] Time-resolved interactions between molecules and active sites can be used to reveal the nature of the active site under catalytic conditions.[24–26] This also enables monitoring chemical transformations if/when side products, such as water, are generated.

In this study, we investigated P-site speciation of a P-zeosil using ^{31}P and ^{13}C variable temperature and operando MAS NMR at high temperatures and in the presence of a reactant. P-site distribution in P-modified dealuminated zeolite BEA (P-BEA) with Si/P = 27 was explored from room temperature to 200 °C. To explore the catalysts under reaction conditions, P-BEA with a higher Si/P ratio (Si/P = 3) was chosen, which has relatively higher catalytic activity. The dehydration of ^{13}C labelled 2-propanol at 140 °C, used as a probe reaction, was investigated *in operando* by monitoring changes in the ^{31}P and ^{13}C MAS NMR spectra. The insights from this study demonstrate that P-site distribution is dependent on both temperature as well as the reactant, thus taking a step towards identification of the active sites in the P-zeosils.

5.2 Results and Discussion

5.2.1 Effect of temperature on the distribution of P-sites

Prior to investigating the P-site distribution under reaction conditions, the evolution of P-sites at elevated temperatures was explored. The ^{31}P MAS NMR spectrum of hydrolyzed P-BEA (Si/P = 27) predominantly shows signals at 0 ppm and a minor fraction of signals at –11 ppm (Figure 1a) at room temperature. Ortho- (H_3PO_4) and pyro-phosphoric ($H_4P_2O_7$) acid sites are referred to as Q^0 and Q^1 and they typically show signals at 0 and -12 ppm,

respectively,[27] and, as established in our previous studies, are predominant in the hydrolyzed state of the P-zeosil. When the temperature is increased to 100 °C, the intensity of the Q^0 sites decreases, while that of the Q^1 sites slightly increases. Their chemical shifts move slightly upfield. Further increasing the temperatures to 125, 150, 175 and 200 °C results in a consistent decrease of the peak intensity in the Q^0 and Q^1 regions. Analysis of the peak areas of the signals shows that Q^1 site formation plateaus off after 100 °C (Figure 2a, S1 and Table A5.1).

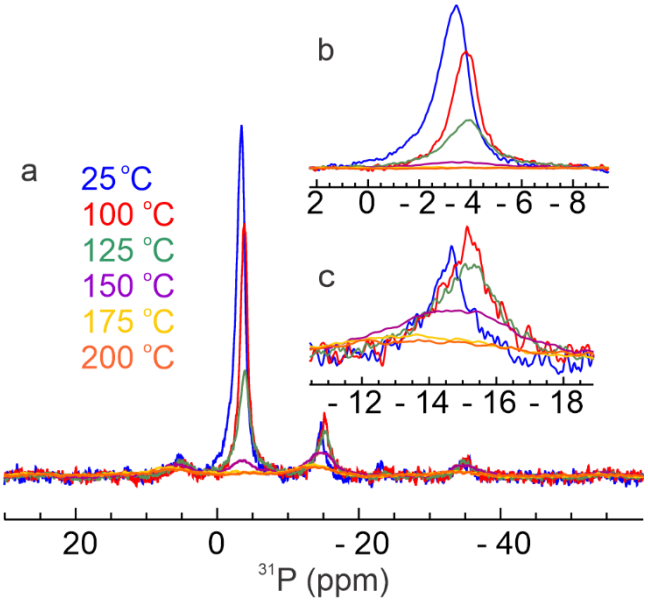

Figure 5.1 ^{31}P MAS NMR spectra of hydrolyzed P-BEA (Si/P = 27) (a) acquired at variable temperatures as indicated. (b) and (c) show the peaks corresponding to Q^0 and Q^1 sites, respectively. The spectra were recorded at 11.75 T under 4 kHz MAS.

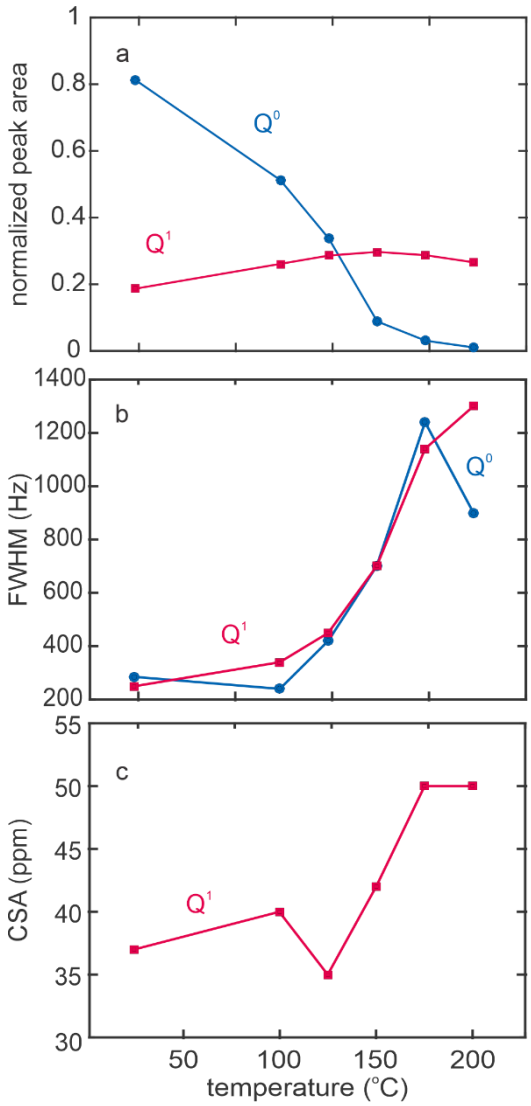

Figure 5.2 Evolution of the (a) peak area (normalized to that of the spectrum acquired at 293 K), (b) chemical shift anisotropy and (c) linewidths (full-width half maximum) of signals corresponding to Q^0 (blue) and Q^1 (red) sites in P-BEA-27 as a function of temperature. The CSA model in the SOLA program in TopSpin 4.0.6 was used to obtain simulated spectra and the corresponding parameters (normalized peak areas, chemical shift anisotropy and linewidths) at each temperature.

The conversion of Q^0 to oligomeric Q^1 sites occurs through the condensation between two Q^0 sites containing POH, or to framework-bound Q^1 sites by the condensation of POH with framework SiOH, releasing H_2O (Scheme 5.1). A POH in H_3PO_4 can condense with nearby SiOH to form $O=P(OH)_2(OSi)$, which also gives rise to a signal in the same region as $H_4P_2O_7$. Further condensation (presumably at temperatures above 200 °C) results in $O=P(OH)(OSi)_2$ and $O=P(OSi)_3$ which results in signals in the Q^2 and Q^3 regions. However, it should be noted that several structures (oligomeric and "mixed") result in multiple signals in the same Q^n region. H_2O is released through condensation, which is known to affect the P-site distribution by hydrolyzing P-O-Si and P-O-P linkages at room temperature. For instance, H_2O can hydrolyze the P-O-P or P-O-Si linkages in Q^1 sites to generate Q^0. Thus, the increase in Q^1 sites at elevated temperatures suggest that condensation is preferred over hydrolysis at these temperatures.

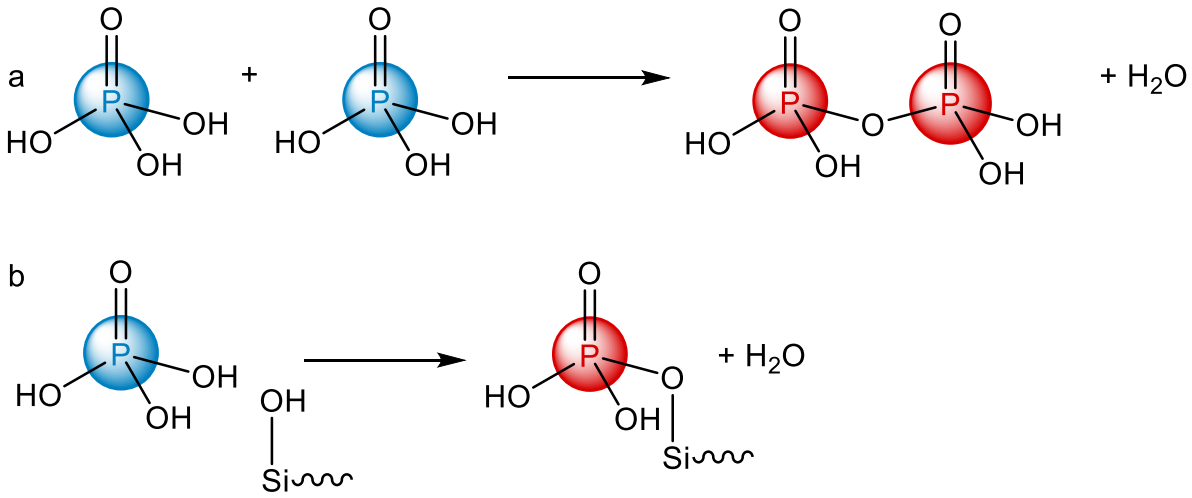

Scheme 5.1 Reaction of the orthophosphoric acid sites (Q^0) to (a) pyrophosphoric acid or (b) framework-bound sites (both of which show signals in the Q^1 region).

Spectral deconvolutions of each spectrum of P-BEA-27 collected different temperatures showed that the linewidths of the peaks increase (Figure 5.2b). Additionally, the chemical shift anisotropy (CSA) of Q^1 is also increasing shown by the more intense spinning sideband patterns at elevated temperatures (Figure 5.2c). The decrease in the linewidth and the CSA values both indicate lower mobility at higher temperatures, which is counterintuitive. The decrease in the mobility is a consequence of condensation of the POH groups in Q^0 and Q^1 with the SiOH in the framework to form framework-bound and "mixed" sites, described in previous studies on P-SPP-27 and P-BEA-27.[10] Thus, more condensed sites form at higher temperatures, which have lower mobility and higher CSAs. In this case, a framework bound Q^1 site has lower mobility than oligomeric Q^1, and therefore results in a stronger CSA pattern and broader linewidth. Signals may also appear in the Q^2 region, however, they overlap with the spinning sidebands of Q^1.

At temperatures relevant to reaction conditions (~150 °C), the amount of Q^1 is greater than Q^0. This likely has consequences for the activity of the catalyst since Q^1 is more acidic than Q^0. Thus, P-site distribution as a function of water, as well as temperature, and may also be dependent on the reaction conditions, which was explored using operando NMR. However, in previous studies on the catalytic activity and selectivity, P-BEA (Si/P = 3) showed optimal results, likely because of the higher stability of P-sites in the framework and the higher P content. Therefore, for the *operando* NMR studies, P-BEA-3 was chosen as the catalyst.

Initial P-site speciation in dehydrated P-BEA-3 (thermally treated at 450 °C for 12 h under dynamic vacuum $<10^{-4}$ Torr) is different than that of dehydrated P-BEA-27 (Figure 5.3a). The most striking difference lies in the appearance of a sharp peak at -43 ppm superposed on the broad Q^3 signals. The sharp peak does not have spinning sidebands. In

previous studies this sharp peak was attributed to a silicophosphate phase $Si_5O(PO_4)_6$ which was associated with three ^{29}Si resonances at -217.0, -213.3 and -119.1 ppm using ^{31}P-^{29}Si HMQC and ^{31}P-^{29}Si CP MAS NMR measurements.[28,29] Thus, higher P-loading results in the formation of a crystalline silicophosphate phase. In its hydrolyzed state, P-BEA-3 in also shows predominantly Q^0 and a minor fraction of Q^1 sites (Figure 5.3b), indicating that the silicophosphate phase also hydrolyzes. When the temperature is increased to 50 °C, as observed in P-BEA-27, the fraction of Q^0 sites decreases while Q^1 sites increase and plateau off after 150 °C is reached. The relative proportions of the Q^0 and Q^1 sites differ, i.e. P-BEA-3 contains a higher ratio of Q^0/Q^1, which could be likely due to its state of hydrolysis in the beginning. The linewidths of the peaks corresponding to sites in this material are relatively narrower compared to P-BEA-27, likely to the formation of more P-O-P oligomers at a higher P-loading. P-site distribution is thus dependent on the water content, temperature as well as the P-content.

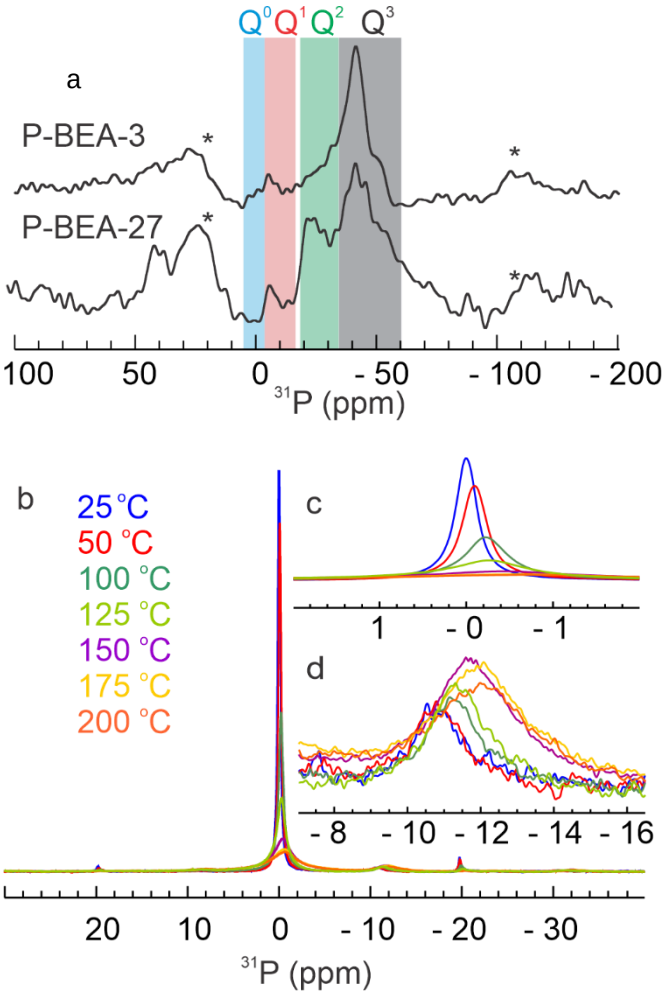

Figure 5.3. ^{31}P MAS NMR spectra of P-BEA. (a) changes in the P-site distribution as an effect of P-loading observed in dehydrated P-BEA-27 and P-BEA-3. The spectra were recorded at 18.8 T at 20 kHz MAS using liquid N_2 boiloff for both bearing and spinning gases. (b) ^{31}P MAS NMR spectra of hydrolyzed P-BEA (Si/P = 27) (a) acquired at variable temperatures as indicated. (c) and (d) show the peaks corresponding to Q^0 and Q^1 sites, respectively. The spectra were recorded at 11.75 T under 4 kHz MAS.

5.2.2 Changes in P-site distribution in the presence of a reactant

P-site distribution was investigated under operando conditions. ^{13}C labelled-2-propanol was transferred by vapor phase onto hydrolyzed P-BEA and the resulting sample was sealed in a WHiMS rotor under inert conditions and its ^{31}P NMR spectrum recorded.[22] At 25 °C, Q^0 and Q^1 sites are both observed (Figure 5.4), which at elevated temperatures, broaden as observed previously in Figure 5.1 and 5.2. In this case, sharp upfield shifted shoulders are also observed. The upfield shifted shoulders at -2.5 and -14 ppm are likely due to the presence of 2-propanol, and it was hypothesized that 2-propanol could undergo a reaction with the phosphoric acid sites to form phosphate esters, resulting in the sharp signals. For instance, isopropyl phosphate esters typically show sharp peaks between 0 to -2.6 ppm (Scheme 5.2b).[30,31]

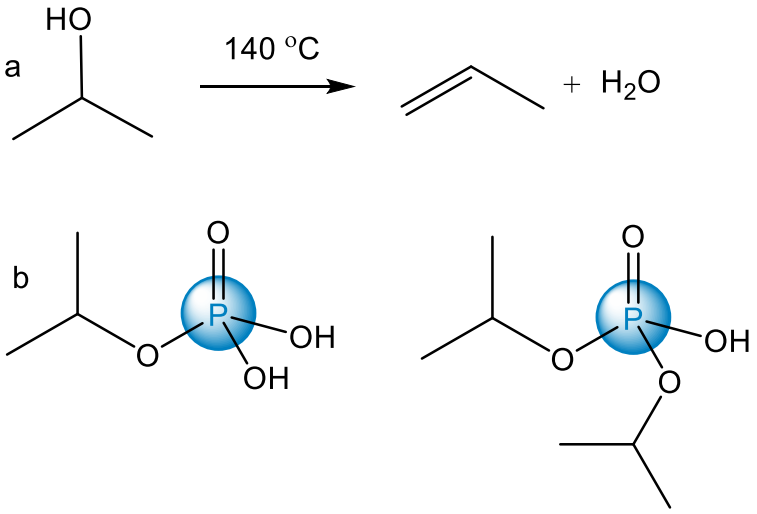

Scheme 5.2 (a) The conversion of 2-propanol to propene at 140 °C with the release of H_2O as a byproduct. (b) Suggested phosphate esters that may be forming during the reaction (left: isopropyl dihydrogen phosphate, right: diisopropyl hydrogen phosphate).

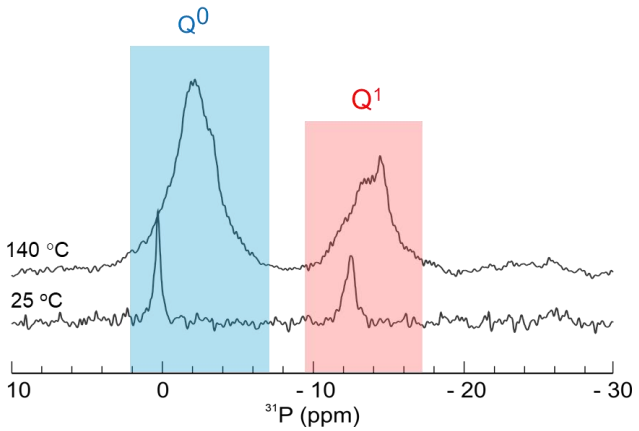

Figure 5.4. ^{31}P MAS NMR spectra of hydrolyzed P-BEA (Si/P = 3) at 25 (bottom) and 140 (top) °C mixed with ^{13}C labelled-2-propanol. The spectra were recorded at 11.75 T under 4 kHz MAS.

As the reaction progresses, sharp new peaks emerge in the Q^0 region (Figure 5.5a), while the peaks in the Q^1 region become more resolved. Assessing the changes in the peak areas, sites in the Q^0 region decrease over the reaction time, while those in Q^1 sites off after the first 100 min of the reaction (Figure 5.5b). The peak areas of the Q^2 signals remain constant, although the resolution improves. The contributions of different components to the Q^0 and Q^1 signals are plotted as a function of reaction time in Figure 5.5c. Three peaks are eventually observed in the Q^0 region at 0, -1.5 and -2.5 ppm. The peak at -1.5 ppm increases at first, and decreases after 150 min. Simultaneously, the peak at -2.5 ppm decreases, and plateaus off after the first 100 min. On the other hand, the peak at 0 ppm increases as the reaction progresses. These changes likely suggest the conversion of the phosphate ester giving rise to the peak at -1.5 ppm to that corresponding to the peak at -2.5 ppm, for instance, the conversion of isopropyl dihydrogen phosphate to diisopropyl hydrogen phosphate). In the case of Q^1 signals, two peaks are observed at -12.5 and -14 ppm. The peak at -14 ppm which has

very low intensity to begin with, remains constant, while the peak at -12.5 ppm also does not change significantly in intensity, and in fact remains constant after the first 100 min, suggesting that this phosphate ester does not undergo any further changes.

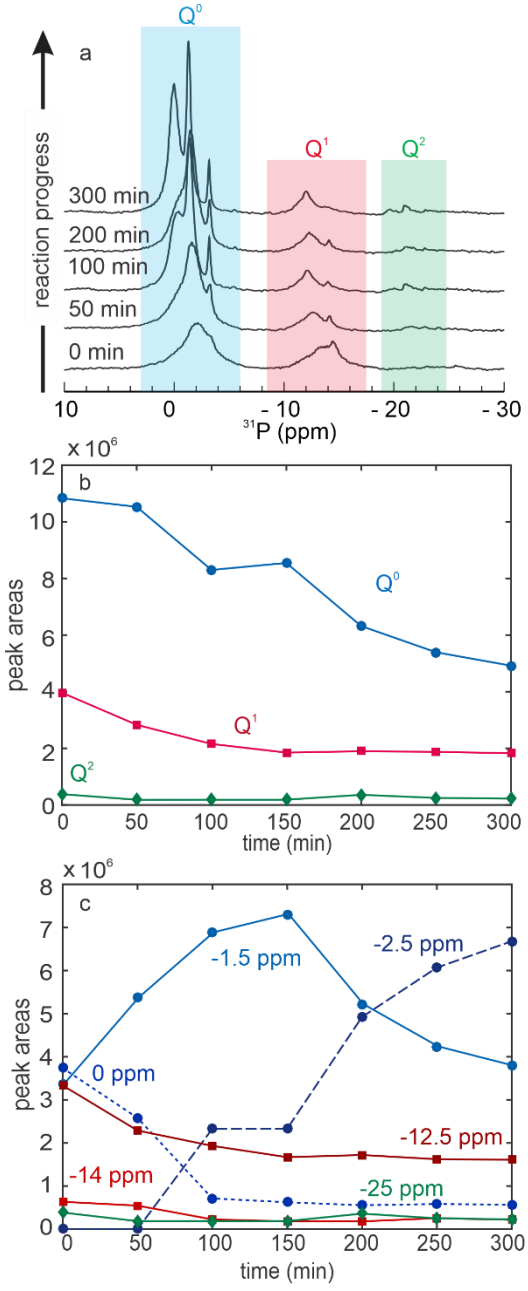

Figure 5.5 ^{31}P MAS NMR spectra of 100 μL of 2-propanol transferred by vapor phase onto 40 mg hydrolyzed P-BEA (Si/P = 3) at increasing reaction times from 0 to 300 min. The spectra were recorded at 140 °C, in a magnetic field of 11.75 T under 4 kHz MAS spinning conditions. (a) ^{31}P MAS NMR spectra showing evolution of the P-site distribution. (b) Changes in the peak areas of the signals corresponding to Q^0, Q^1 and Q^2. (c) Changes in the peak areas of each component in the Q^0 and Q^1 signals. Representative spectral deconvolutions are shown in Figure A5.2.

5.2.3 Monitoring the evolution of reactants and products under reaction conditions

As the reaction progresses, the P-site distribution varies and phosphate esters are likely formed. The changes in the reactant and product distribution, enabled by ^{13}C MAS NMR was also investigated (Figure 5.6). 2-propanol dehydration results in the formation of propene and H_2O and could also form 2-propan-2-yloxypropane as a side-product. In the beginning of the reaction, two peaks (a broad one at 62 ppm and a narrow one at 59 ppm) in the region of 2-propanol appear. The two peaks may indicate different environments of the 2-propanol, i.e. a more confined 2-propanol site could give rise to a broad peak. Another broad peak is observed at 69 ppm, which has been assigned to methylene carbons participating in a phosphate-ester linkage in the polymerization of ethylene isopropyl phosphate.[31]

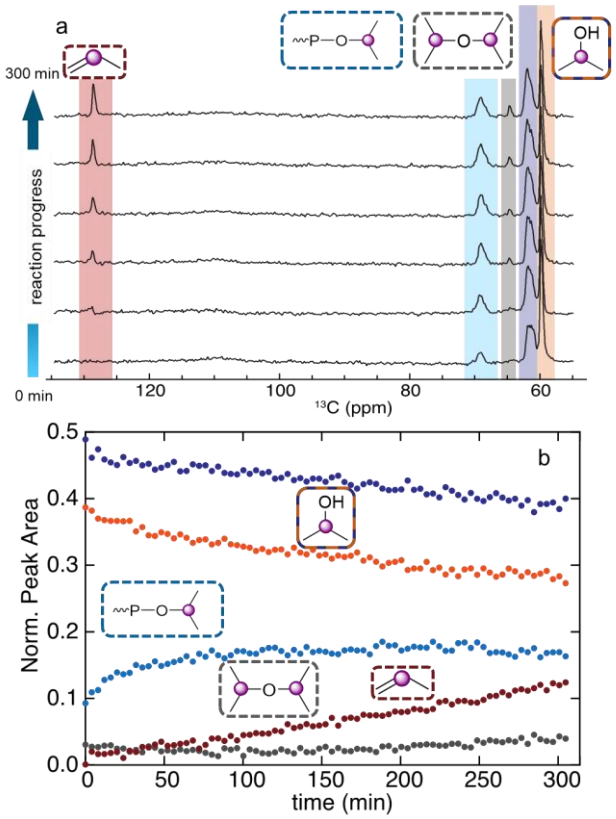

Figure 5.6. Representative ^{13}C MAS NMR (a) spectra and (b) peak areas obtained from each signal, of 40 mg hydrolyzed P-BEA (Si/P = 3) onto which 100 μL of 2-propanol was transferred via vapor phase at increasing reaction times from 0 to 300 min. The spectra were recorded at 140 °C, in a magnetic field of 11.75 T under 4 kHz MAS using a recycle delay of 10 s. The sites corresponding to each signal are also indicated.

After several minutes of the reaction, a peak at -136 ppm is observed which increases linearly. Another peak at 64.5 ppm, which increases with reaction time is also observed, and it corresponds to 2-propan-2-yloxypropane, a side-product observed in this reaction.[32] The peak at 69 ppm increases and plateaus off, indicating that the sites corresponding to this peak, i.e. the phosphate esters remain stable over time. Thus, operando NMR enables monitoring of

the 2-propanol dehydration reaction and the evolution of reactants, products and side-products.

5.3 Conclusions

P-distribution evolves under reaction conditions, which occurs at elevated temperatures and releases water as a by-product. At elevated temperatures, more condensed sites form, although water is also released as a by-product. Under reaction conditions, a more complex distribution of P-sites is observed and the ^{31}P and ^{13}C NMR both suggest the formation of phosphate esters. Thus, operando NMR enables the observation of the consumption of liquid-phase 2-propanol and evolution of gas-phase propene, in the presence of a solid P-zeosil catalyst.

5.4 Experimental

5.4.1 Sample preparation and handling

All-silica self-pillared pentasil (SPP), dealuminated zeolite BEA, and their P-modified analogs (P-SPP and P-BEA, each with a Si/P ratio of 27), were synthesized following previously described procedures.[8,33] Each dehydrated material was dried at 450 °C under dynamic vacuum ($<10^{-4}$ Torr) for 12 h before use. NMR samples were packed and sealed 3.2-mm zirconia rotors inside a N_2-filled glove-box.

5.4.2 Direct excitation solid-state MAS-NMR spectroscopy

^{31}P MAS-NMR measurements were performed at room temperature on a Bruker AVANCE III Ultrashield Plus 18.8 T Spectrometer (corresponding to ^{31}P frequency of 323.85 MHz) at MAS frequencies of 20 kHz ^{31}P NMR measurements were made in 3.2-mm rotors using a single 90 ° excitation pulse of length 7 μs on the ^{31}P channel. An aqueous phosphoric acid solution (1 M) provided the chemical shift reference.

5.4.3. ^{13}C and ^{31}P Operando MAS NMR spectroscopy

^{13}C and ^{31}P MAS NMR experiments were performed on Bruker AVANCE III Ultrashield Plus 11.7 T Spectrometer operating at 125.7747 MHz for the ^{13}C channel and xx for the ^{31}P channel, equipped with a 5 mm triple resonance HXY probe from Revolution NMR. A 40 mg portion of the sample was loaded into a 5 mm ZrO_2 rotor customized for high-temperature experiments and spun at 4 kHz. The ramp from room temperature to the desired reaction temperature usually required ca. 10 min. To perform experiments under reaction conditions, 100 μL of 2-Propanol-2-^{13}C was transferred by vapor phase onto 40 mg of the sample.

In ^{13}C direct polarization experiments, a 35 kHz ^{1}H decoupling field was employed with an acquisition time of 300 ms. The ^{13}C spectral width was 50 kHz, and 15008 data points were acquired per transient, using a relaxation delay of 15 s to ensure quantitative analysis. Each transient spectrum was acquired by averaging 64 scans. Temperature calibration of the high-pressure system was accomplished by acquiring ^{207}Pb NMR spectra of lead nitrate in the rotor as a function of spectrometer temperature setting.^{13}C chemical shifts were referenced to

TMS via a secondary standard, adamantane (37.48 ppm). Spectrum deconvolution was performed using the CSA model in TopSpin 4.0.6.

5.5 References

(1) Sievers, C.; Scott, S. L.; Noda, Y.; Qi, L.; Albuquerque, E. M.; Rioux, R. M. Phenomena Affecting Catalytic Reactions at Solid−Liquid Interfaces. *ACS Catal.* **2016**, *6* (12). https://doi.org/10.1021/acscatal.6b02532.

(2) Muraza, O.; Galadima, A. Isomerization and Alkylation of Biomass-Derived Compounds in Aqueous Media over Hydrophobic Solid Acid Catalysts: A Mini Review. *Ind. Eng. Chem. Res.* **2014**, *53* (46), 17869–17877. https://doi.org/10.1021/IE503310P.

(3) Zhang, L.; Pham, T. N.; Faria, J.; Resasco, D. E. Improving the Selectivity to C4 Products in the Aldol Condensation of Acetaldehyde in Ethanol over Faujasite Zeolites. *Appl. Catal. A Gen.* **2015**, *504*, 119–129. https://doi.org/10.1016/j.apcata.2014.11.018.

(4) Zhu, X.; Lobban, L. L.; Mallinson, R. G.; Resasco, D. E. Bifunctional Transalkylation and Hydrodeoxygenation of Anisole over a Pt/HBeta Catalyst. *J. Catal.* **2011**, *281* (1), 21–29. https://doi.org/10.1016/j.jcat.2011.03.030.

(5) Ausavasukhi, A.; Huang, Y.; To, A. T.; Sooknoi, T.; Resasco, D. E. Hydrodeoxygenation of M-Cresol over Gallium-Modified Beta Zeolite Catalysts. *J. Catal.* **2012**, *290*, 90–100. https://doi.org/10.1016/j.jcat.2012.03.003.

(6) Caratzoulas, S.; Davis, M. E.; Gorte, R. J.; Gounder, R.; Lobo, R. F.; Nikolakis, V.; Sandler, S. I.; Snyder, M. A.; Tsapatsis, M.; Vlachos, D. G. Challenges of and Insights into Acid-Catalyzed Transformations of Sugars. *J. Phys. Chem. C* **2014**, *118* (40),

22815–22833. https://doi.org/10.1021/jp504358d.

(7) Cheng, Y.-T.; Jae, J.; Shi, J.; Fan, W.; Huber, G. W. Production of Renewable Aromatic Compounds by Catalytic Fast Pyrolysis of Lignocellulosic Biomass with Bifunctional Ga/ZSM-5 Catalysts. *Angew. Chemie* **2012**, *124* (6), 1416–1419. https://doi.org/10.1002/ange.201107390.

(8) Cho, H. J.; Ren, L.; Vattipalli, V.; Yeh, Y.-H.; Gould, N.; Xu, B.; Gorte, R. J.; Lobo, R.; Dauenhauer, P. J.; Tsapatsis, M.; Fan, W. Renewable *p* -Xylene from 2,5-Dimethylfuran and Ethylene Using Phosphorus-Containing Zeolite Catalysts. *ChemCatChem* **2017**, *9* (3), 398–402. https://doi.org/10.1002/cctc.201601294.

(9) Abdelrahman, O. A.; Park, D. S.; Vinter, K. P.; Spanjers, C. S.; Ren, L.; Cho, H. J.; Vlachos, D. G.; Fan, W.; Tsapatsis, M.; Dauenhauer, P. J. Biomass-Derived Butadiene by Dehydra-Decyclization of Tetrahydrofuran. *ACS Sustain. Chem. Eng.* **2017**, *5* (5), 3732–3736. https://doi.org/10.1021/acssuschemeng.7b00745.

(10) Jain, S. K.; Tabassum, T.; Li, L.; Ren, L.; Fan, W.; Tsapatsis, M.; Caratzoulas, S.; Han, S.; Scott, S. L. P-Site Structural Diversity and Evolution in a Zeosil Catalyst. *J. Am. Chem. Soc.* **2021**, *143* (4), 1968–1983. https://doi.org/10.1021/jacs.0c11768.

(11) Ravenelle, R. M.; Schübler, F.; Damico, A.; Danilina, N.; Van Bokhoven, J. A.; Lercher, J. A.; Jones, C. W.; Sievers, C. Stability of Zeolites in Hot Liquid Water. *J. Phys. Chem. C* **2010**, *114* (46), 19582–19595. https://doi.org/10.1021/jp104639e.

(12) Yang, H.; Coolman, R. J.; Karanjkar, P.; Wang, H.; Xu, Z.; Chen, H.; Moutziaris, T. J.; Huber, G. W. The Effect of Steam on the Catalytic Fast Pyrolysis of Cellulose. *Green Chem.* **2015**, *17* (5), 2912–2923. https://doi.org/10.1039/c5gc00026b.

(13) Chen, K.; Damron, J.; Pearson, C.; Resasco, D.; Zhang, L.; White, J. L. Zeolite

Catalysis: Water Can Dramatically Increase or Suppress Alkane C-H Bond Activation. *ACS Catal.* **2014**, *4* (9), 3039–3044. https://doi.org/10.1021/cs500858d.

(14) Wang, H.; Hou, Y.; Sun, W.; Hu, Q.; Xiong, H.; Wang, T.; Yan, B.; Qian, W. Insight into the Effects of Water on the Ethene to Aromatics Reaction with HZSM-5. *ACS Catal.* **2020**, *10* (9), 5288–5298. https://doi.org/10.1021/acscatal.9b05552.

(15) Zapata, P. A.; Faria, J.; Ruiz, M. P.; Jentoft, R. E.; Resasco, D. E. Hydrophobic Zeolites for Biofuel Upgrading Reactions at the Liquid-Liquid Interface in Water/Oil Emulsions. *J. Am. Chem. Soc.* **2012**, *134* (20), 8570–8578. https://doi.org/10.1021/ja3015082.

(16) Chen, K.; Kelsey, J.; White, J. L.; Zhang, L.; Resasco, D. Water Interactions in Zeolite Catalysts and Their Hydrophobically Modified Analogues. *ACS Catal.* **2015**, *5* (12), 7480–7487. https://doi.org/10.1021/acscatal.5b02040.

(17) Oliver, F. G.; Munson, E. J.; Haw, J. F. High-Temperature in-Situ Magic Angle Spinning NMR Studies of Chemical Reactions on Catalysts. *J. Phys. Chem.* **2002**, *96* (20), 8106–8111. https://doi.org/10.1021/j100199a052.

(18) Foley, D. A.; Bez, E.; Codina, A.; Colson, K. L.; Fey, M.; Krull, R.; Piroli, D.; Zell, M. T.; Marquez, B. L. NMR Flow Tube for Online NMR Reaction Monitoring. *Anal. Chem.* **2014**, *86* (24), 12008–12013. https://doi.org/10.1021/ac502300q.

(19) Zhi Hu, J.; A. Sears, J.; S. Mehta, H.; J. Ford, J.; Hun Kwak, J.; Kake Zhu; Yong Wang; Jun Liu; W. Hoyt, D.; F. Peden, C. H. A Large Sample Volume Magic Angle Spinning Nuclear Magnetic Resonance Probe for in Situ Investigations with Constant Flow of Reactants. *Phys. Chem. Chem. Phys.* **2012**, *14* (7), 2137–2143. https://doi.org/10.1039/c1cp22692d.

(20) Surface, J. A.; Skemer, P.; Hayes, S. E.; Conradi, M. S. In Situ Measurement of Magnesium Carbonate Formation from CO2 Using Static High-Pressure and -Temperature 13C NMR. *Environ. Sci. Technol.* **2012**, *47* (1), 119–125. https://doi.org/10.1021/es301287n.

(21) Qi, L.; Alamillo, R.; Elliott, W. A.; Andersen, A.; Hoyt, D. W.; Walter, E. D.; Han, K. S.; Washton, N. M.; Rioux, R. M.; Dumesic, J. A.; Scott, S. L. Operando Solid-State NMR Observation of Solvent-Mediated Adsorption-Reaction of Carbohydrates in Zeolites. *ACS Catal.* **2017**, *7* (5), 3489–3500. https://doi.org/10.1021/acscatal.7b01045.

(22) Walter, E. D.; Qi, L.; Chamas, A.; Mehta, H. S.; Sears, J. A.; Scott, S. L.; Hoyt, D. W. Operando MAS NMR Reaction Studies at High Temperatures and Pressures. *J. Phys. Chem. C* **2018**, *122* (15), 8209–8215. https://doi.org/10.1021/acs.jpcc.7b11442.

(23) Jaegers, N. R.; Mueller, K. T.; Wang, Y.; Hu, J. Z. Variable Temperature and Pressure Operando MAS NMR for Catalysis Science and Related Materials. *Acc. Chem. Res.* **2020**, *53* (3), 611. https://doi.org/10.1021/acs.accounts.9b00557.

(24) Zhao, Z.; Shi, H.; Wan, C.; Hu, M. Y.; Liu, Y.; Mei, D.; Camaioni, D. M.; Hu, J. Z.; Lercher, J. A. Mechanism of Phenol Alkylation in Zeolite H-BEA Using In Situ Solid-State NMR Spectroscopy. **2017**. https://doi.org/10.1021/jacs.7b02153.

(25) Vjunov, A.; Hu, M. Y.; Feng, J.; Camaioni, D. M.; Mei, D.; Hu, J. Z.; Zhao, C.; Lercher, J. A. Following Solid-Acid-Catalyzed Reactions by MAS NMR Spectroscopy in Liquid Phase--Zeolite-Catalyzed Conversion of Cyclohexanol in Water. *Angew. Chem. Int. Ed. Engl.* **2014**, *53* (2), 479–482. https://doi.org/10.1002/anie.201306673.

(26) Zhi Hu, J.; Y. Hu, M.; Zhenchao Zhao; Suochang Xu; Aleksei Vjunov; Hui Shi; M.

Camaioni, D.; F. Peden, C. H.; A. Lercher, J. Sealed Rotors for in Situ High Temperature High Pressure MAS NMR. *Chem. Commun.* **2015**, *51* (70), 13458–13461. https://doi.org/10.1039/c5cc03910j.

(27) Thomas R. Krawietz; Ping Lin; Karen E. Lotterhos; Paul D. Torres; Dewey H. Barich; Abraham Clearfield, A.; Haw*, J. F. Solid Phosphoric Acid Catalyst: A Multinuclear NMR and Theoretical Study. *J. Am. Chem. Soc.* **1998**, *120* (33), 8502–8511. https://doi.org/10.1021/ja9813461.

(28) Lejeune, C.; Coelho, C.; Bonhomme-Coury, L.; Azaïs, T.; Maquet, J.; Bonhomme, C. Studies of Silicophosphate Derivatives by 31P→29Si CP MAS NMR. *Solid State Nucl. Magn. Reson.* **2005**, *27* (4), 242–246. https://doi.org/10.1016/j.ssnmr.2005.02.001.

(29) Coelho, C.; Azais, T.; Bonhomme-Coury, L.; Maquet, J.; Massiot, D.; Bonhomme, C. Application of the MAS-J-HMQC Experiment to a New Pair of Nuclei {29Si,31P}: Si5O(PO4)6 and SiP2O7 Polymorphs. *J. Magn. Reson.* **2006**, *179* (1), 114–119. https://doi.org/10.1016/j.jmr.2005.11.015.

(30) Wagner, G. W.; Bartram, P. W. Reactions of the Nerve Agent Simulant Diisopropyl Fluorophosphate with Self-Decontaminating Adsorbents. A 31P MAS NMR Study. *J. Mol. Catal. A Chem.* **1999**, *144* (3), 419–424. https://doi.org/10.1016/S1381-1169(98)00343-4.

(31) Wen, fie; Zhuo, R.-X. Enzyme-Catalyzed Ring-Opening Polymerization of Ethylene Isopropyl Phosphate. **1998**, *19*, 641442. https://doi.org/10.1002/(SICI)1521-3927(19981201)19:12.

(32) Kumar, G.; Ren, L.; Pang, Y.; Li, X.; Chen, H.; Gulbinski, J.; Dauenhauer, P. J.; Tsapatsis, M.; Abdelrahman, O. A. Acid Sites of Phosphorus-Modified Zeosils. *ACS*

Catal. **2021**, 9933–9948. https://doi.org/10.1021/ACSCATAL.1C01588.

(33) Zhang, X.; Liu, D.; Xu, D.; Asahina, S.; Cychosz, K. A.; Agrawal, K. V.; Wahedi, Y. Al; Bhan, A.; Hashimi, S. Al; Terasaki, O.; Thommes, M.; Tsapatsis, M. Synthesis of Self-Pillared Zeolite Nanosheets by Repetitive Branching. *Science (80-.).* **2012**, *336* (6089), 1684–1687. https://doi.org/10.1126/science.1221111.

5.6 Appendix

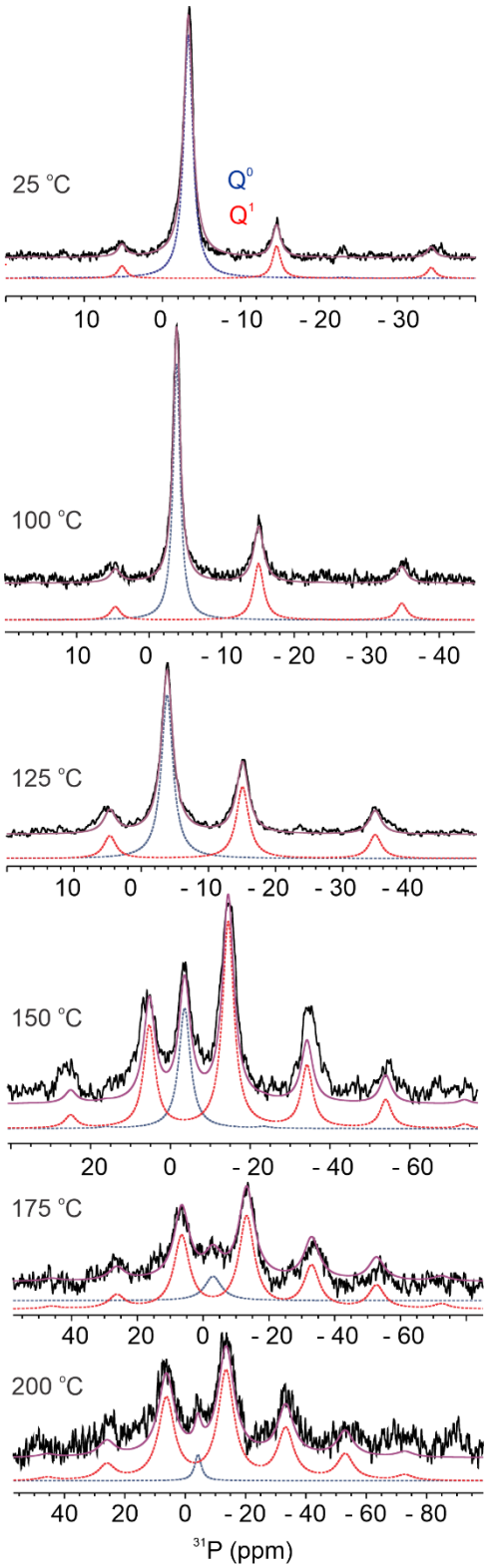
25 °C
Q0
Q1
10 0 - 10 - 20 - 30
100 °C
10 0 - 10 - 20 - 30 - 40
125 °C
10 0 - 10 - 20 - 30 - 40
150 °C
20 0 - 20 - 40 - 60
175 °C
40 20 0 - 20 - 40 - 60
200 °C
40 20 0 - 20 - 40 - 60 - 80
31P (ppm)

Figure A5.1 ^{31}P MAS NMR of hydrolyzed P-BEA with Si/P = 27 acquired at different temperatures as indicated (black) and the corresponding simulations (purple) that include contributions for Q^0 and Q^1 components. Spectra were recorded at 11.7 T, using 4 kHz MAS. Simulations were performed using the CSA model in Topspin 4.0.6. Deconvolution of the spectrum of P-BEA into its Q^n components is shown in dotted spectra, which are offset vertically.

Table A5.1 Chemical shift parameters obtained for P-BEA, acquired by fitting simulated spectra to the experimental data at each temperature [a]

Temperature	Q^0			Q^1		
(°C)	cs_{iso} (ppm)	CSA (ppm)	FWHM (Hz)	cs_{iso} (ppm)	CSA (ppm)	FWHM (Hz)
25	-3.3	x	285	-14.6	-37	250
100	-3.8	x	240	-15.1	-40	340
125	-2.9	x	420	-15.1	-35	450
150	-3.6	x	700	-14.5	-42	700
175	-5.0	x	1240	-13.2	-50	1140
200	-4.2	x	900	-13.5	-50	1300

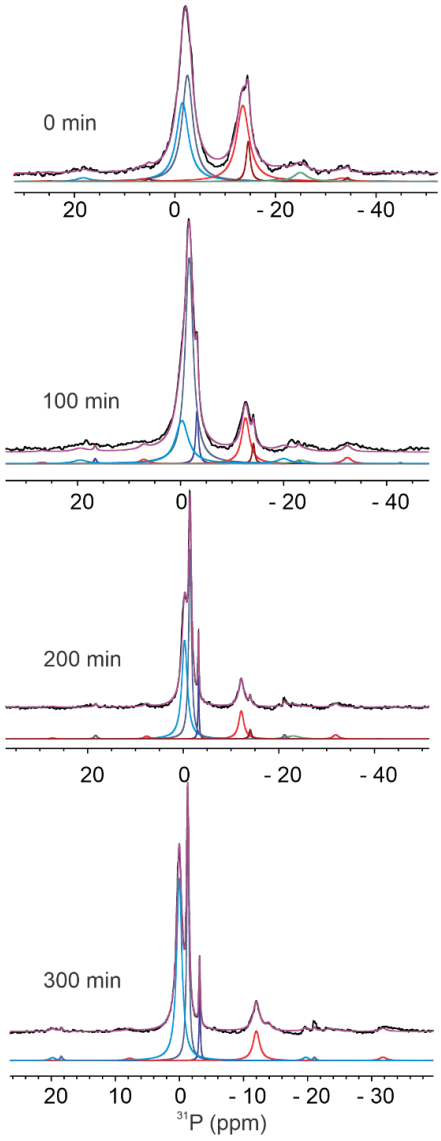

Figure A5.2 ^{31}P MAS NMR of hydrolyzed P-BEA with Si/P = 3 (40 mg) with ^{13}C labelled-2-propanol acquired at different reaction times as indicated (black) and the corresponding simulations (purple) that include contributions for Q^0, Q^1 and Q^2 components. Spectra were recorded at 11.7 T, using 4 kHz MAS, at 140 °C. Simulations were performed using the CSA model in Topspin 4.0.6. Deconvolution of the spectrum of P-BEA into its Q^n components which are shown in different shades of blue (Q^0) and red (Q^1) and a shade of green (Q^2).

Chapter 6: Conclusions

6.1 Major findings

Dehydroxylation of non-porous and mesoporous silicas at 500 ^{o}C, results in surface hydroxyl groups that are closely associated with one another. When VCl_4 is reacted with these hydroxyls, spin-spin coupled $\equiv SiOVCl_3$ sites are formed, which results in increased electron relaxation and EPR signals that are broadened beyond detection at room temperature. At temperatures below 20 K, the lineshape is predominantly Lorentzian, confirming the dominance of spin-spin interactions. Changing the coordination number of the V(IV) center results in regeneration of the EPR signals at room temperature. Dilution of the V(IV) center also regenerates the signals, however, even at low loadings of V (8 % surface silanol coverage), approximately 50 % of the EPR spectrum arises from a broad component, indicating clustered V(IV) sites. Increasing the loading further increases the contribution from the clustered V(IV) sites. This insight can be used to approximately determine that the silanols exist in cluster sizes of approximately 10, which are still present after thermal treatment of the silica at 500 °C. The absence of EPR signals at room temperatures is also observed in other mesoporous silicas as well non-porous silica treated at 700 °C.

DNP-enhanced solid-state NMR spectroscopy, including ^{RESPIRATION}CP NMR, ^{29}Si-filtered ^{31}P DCP NMR, and 2D ^{31}P-^{31}P correlation NMR, in combination with DFT calculations was used to probe the nature of P-sites in a phosphorus-modified self-pillared pentasil (P-SPP). Two types of fully-condensed P-sites are present in dry P-SPP: mononuclear (Q^3_3) and oligomeric (most likely dinuclear, Q^3_2-Q^3_2). Although neither is acidic, the NMR results confirm that both are surface-bound, confirmed by ^{29}Si-filtered ^{31}P DCP correlation

NMR spectroscopy. The mononuclear site undergoes hydrolysis of a P-O-Si linkage to form a Q_2^2 site, before eventually being converted to H_3PO_4 (Q^0), presumably via an unstable Q_1^1 intermediate. Frequency-selective detection using $^{\text{RESPIRATION}}$CP suggests the presence of additional dinuclear P-sites containing both P-O-Si and P-O-P linkages in dry P-SPP. The P-O-Si linkages in this type of site also hydrolyze first, converting surface bound Q_2^3-Q_2^3 to non-surface-bound Q_0^1-Q_0^1, in which the P-O-P linkage eventually hydrolyses to form Q^0. This study reveals that the Brønsted acidity in P-SPP arises from a diverse mixture of partly-hydrolyzed surface-bound and non-surface-bound mononuclear and dinuclear sites, even at low P-loadings (P/Si = 27).

The impact of water on the zeosil frameworks and the P-site distribution was compared in P-SPP and P-modified dealuminated zeolite BEA (P-BEA). SPP has a higher hydroxyl content relative to BEA, as determined by quantification using ultra-fast ^{1}H MAS NMR, and is thus more hydrophobic. Improved resolution achieved through ultra-fast MAS shows a distribution of different types of SiOH groups in the two zeosils. ^{31}P MAS NMR of dehydrated P-BEA shows that it has fewer framework-bound sites, on average, (such as $Q_2^3 - Q_1^3$, $Q_1^2 - Q_0^1$ and $Q_0^1 - Q_0^1$) which are acidic, in contrast to the Q_3^3 and $Q_2^3 - Q_2^3$ sites predominantly present in dehydrated P-SPP. Ambient exposure of the material shows that P-sites in P-BEA are more resistant to hydrolysis and persist over longer timescales compared to those in P-SPP. ^{1}H MAS NMR shows that this is likely due to the nature of the zeosil framework. The BEA framework results in a population of P-sites which are in slow exchange with water as observed. On the other hand, the open architecture of the SPP framework results in more water-accessible P-sites. Thus, the accessibility of the water to P-sites as well as the higher

fraction of P-O-P linkages in P-BEA, makes the sites less susceptible to hydrolysis; P-SPP hydrolyzes faster.

Investigation of P-sites under reaction conditions demonstrates that they condense to form framework-bound and/or oligomeric sites at elevated temperatures between 25 to 200 °C. Under reaction conditions, i.e. at 140 °C and in the presence of a 2-propanol as a reactant, phosphate esters are generated in the reaction as suggested by the ^{31}P and ^{13}C operando NMR.

6.2 Future directions

Site-specific information on the silanol distribution in silicas and siliceous zeosils is important in determining structure-property relationships. Grafted paramagnetic probe molecules on the surface of silica experience spin-spin coupling due to the spatial proximity of surface silanols which are likely in pairs or form clusters. Thus, these silanols cannot be described as well-isolated. Expanding the scope of the study to other materials (such as organic mesoporous silicas with systematically varying hydrophobicities, and all- and high-silica zeolites) containing different silanol densities would help address the question on whether all types of silicas, regardless of the synthesis procedure and the presence of micro- and mesopores contain silanol pairs or clusters. Furthermore, spin dilution studies on these silicas would provide insight on whether the cluster sizes vary for each silica. For instance, observing whether the cluster size varies as a function of hydrophobicity in organic mesoporous silicas would be interesting, and thus shed light onto controlling the isolation of catalytically active grafted metallic precursors which could impact their stability, selectivity and activity.

The studies on P-zeosils have demonstrated using existing and novel NMR techniques, such as advanced pulse sequences, DNP, ultra-fast and operando capabilities, to probe the nature of P-sites. The precise identities of the active sites in P-zeosils are yet to be established, and must be evaluated under reaction conditions. The formation of stable phosphate esters and its effect on the 2-propanol dehydration reaction can be further explored by observing the effect of the reaction temperature, catalyst amount and reactant concentration, in addition to the hydration state of the catalyst in the beginning of the reaction. The formation of the phosphate esters, as well as the release of water, obscures determination of the precise identity of the active P-site. Therefore, the evolution of P-sites using a simpler probe reaction, such as the Hofmann elimination of *tert*-butylamine generating isobutene and ammonia, can be explored, and used to determine the active P-site.

An important attribute that must be investigated is the Brønsted acid site distribution in the P-zeosils, which determines the activity and selectivity of the catalysts. The Brønsted acid site distribution and strength, as a function of the different hydration states of the P-zeosils, can be quantified by using trimethylphosphine oxide as a probe molecule, which is known to adsorb preferentially on the acid sites on solid catalysts. By using advanced 2D NMR correlation experiments (^{31}P- ^{31}P) in combination with selective detection of P-sites using selective ^{31}P $^{\text{RESPIRATION}}$CP, the acidity as a function of the hydration state can be correlated. The findings from the operando NMR experiments can be related with the acid site distribution. The scope of these experiments can be further broadened to other P-modified silicas (such as crystalline silicophosphates and solid phosphoric acid catalysts) and zeolites (containing Al) with different P-content, that show differences in catalytic activity, selectivity and stability.